Master Thesis, Department of Geosciences

Imaging reservoir quality of Knurr and Stø Formations in the Hammerfest Basin and Ringvassøy-Loppa Fault Complex, Norwegian Barents Sea

Dechen Zhang

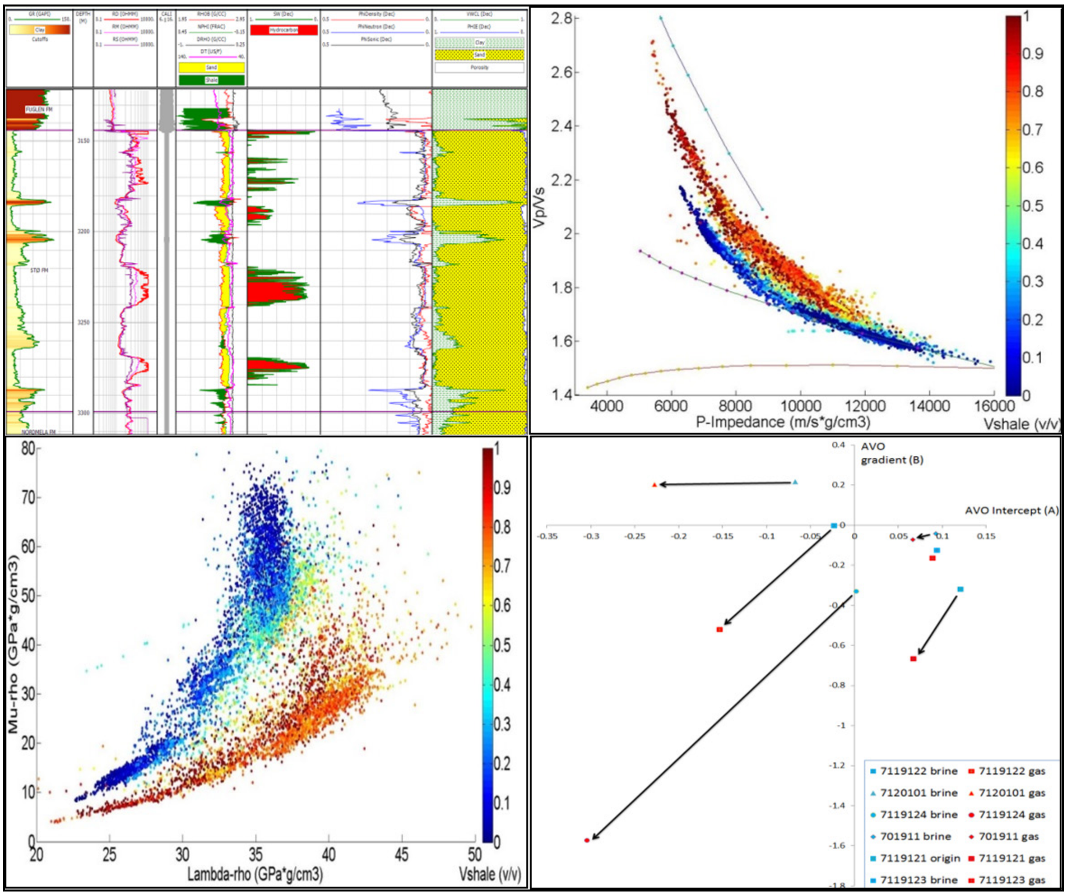

UNIVERSITY OF OSLO

FACULTY OF MATHEMATICS AND NATURAL SCIENCES

Imaging reservoir quality of Knurr and Stø Formations in the Hammerfest Basin and Ringvassøy-Loppa Fault Complex, Norwegian Barents Sea

Dechen Zhang

Master Thesis in Geosciences

Discipline: Petroleum Geology and Petroleum Geophysics

Department of Geosciences

Faculty of Mathematics and Natural Sciences

University of Oslo

02.06.2014

© Dechen Zhang, 2014

This work is published digitally through DUO – Digitale Utgivelser ved UiO

http://www.duo.uio.no

It is also catalogued in BIBSYS (http://www.bibsys.no/english)

All rights reserved. No part of this publication may be reproduced or transmitted, in any form or by any means, without permission.

Preface

This thesis is part of the ‘‘BarRock’’ (Barents Sea Rock Properties) project and is submitted to the Department of Geosciences, University of Oslo (UiO), in candidacy of the M.Sc. in Petroleum Geology and Petroleum Geophysics.

This research has been performed at the Department of Geosciences, University of Oslo, during the period of January 2014 - May 2014 under the supervision of Nazmul Haque Mondol, Associate Professor, Department of Geosciences, University of Oslo, Norway.

Acknowledgments

I would like to express special appreciation to my supervisor Nazmul Haque Mondol for his patience and continuous support. Discussions with him have always been motivating and instrumental.

I wish to express my special gratitude to Oluwakemi Yetunde Ogebule for her unpublished data and suggestions for further improvement of the thesis. My sincere thanks also go to PhD candidates Irfan Baig, Mohammad Koochak Zadeh, Mohsen Kalani, and Sirikarn Narongsirikul. The meetings every week with them are constructive and valuable.

Last but not the least; I am thankful to my wife, my parents and other members in my family for their support and wishes for successful completion of my research project. All my helpful and caring friends and classmates deserve special thanks for their emotional supports.

Abstract

The Barents Sea is a prospective area in terms of hydrocarbon resources with high ratio of discovery wells. This study focuses on reservoir quality of two sandstone reservoirs of Knurr and Stø Formations in the Hammerfest Basin and Ringvassøy-Loppa Fault Complex in the Norwegian Barents Sea. The study methods include petrophysics analysis, rock physics diagnostics and AVO modelling. Seven exploration wells from the study area are analysed to investigate the reservoir quality of two target reservoirs. The studied reservoir sandstones are buried at different depth levels from approximately 1400 m to 3300 m (RKB). Therefore, this database provides a perfect profile for sandstone compaction and diagenetic studies.

A comparison of Vp-depth trends in studied wells and published Vp-depth trends for normally subsided basins shows that the Vp in the study area are much higher than expected. The calculated average porosity values of the reservoirs are much lower than published porosity-depth trends. Regional uplift and erosion is attributed as the main reason for these anomalous values. The estimated average uplift in the study area is about 900 m. The exhumation decrease to the north-west direction. After estimation of uplift, the present depth is corrected to a maximum burial depth. New depth data are subsequently used to calculate maximum burial temperatures for the reservoirs. The maximum temperatures show that the sediments have experienced much higher thermal exposures than what is interpolated from bottom hole temperatures. All the reservoirs in the studied wells are within the zone of chemical compaction.

It is clear from petrophysical analysis that the reservoir quality of the Knurr Formation is poorer compared to the Stø Formation. The Knurr Formation is deposited in a submarine fan system while the Stø Formation is deposited in a coastal environment. Different sedimentary environments result in different reservoir parameters, like net-to-gross ratio, shale volume and porosity.

Rock physics templates work well for estimating quartz cement content and for distinguishing different lithologies and pore fluids. Even the shallowest buried sandstones (around 1200 meters below sea floor) in well 7119/12-2 contain cements between the grains according to rock physics diagnostic results. This is also confirmed by published literatures. Secondary porosity is also common in the studied wells. A clear trend of rock properties with increasing depth is observed in all of the rock physics templates used. Lamda-Rho versus Mu-Rho cross plot works better than Vp/Vs versus IP cross plot for discriminating the lithology and fluid in the studied wells. Due to the complex compaction and diagenetic history, the shear wave velocity measured in well 7119/12-4 is abnormally high. These high shear wave velocities result false gas effect in rock physics templates (e.g. Vp/Vs versus IP and LMR).

The AVO modelling results agree reasonably well with the classical AVO theory. The gas-bearing data points deviate from the background trend at both the top and bottom interfaces of the reservoirs. An impedance inversion with increasing depth is observed in the AVO modelling for the Stø Formation sandstones. With increasing depth, the “soft” sandstones turn into “hard” sandstones compared to the overlying shale. The AVO modelling results are sensitive to many factors, like water saturation, wavelet and block size. The measured Vs values in well 7119/12-4 also result false gas effect in AVO modelling.

Table of Contents

Preface i

Acknowledgments iii

Abstract v

Table of Contents vii

List of Figures x

List of Tables xvi

Chapter 1 Introduction 1

- 1.1 Background 1
- 1.2 Motivation and research objectives 2
- 1.3 Study area and database 3
- 1.4 Limitations 4
- 1.5 Chapter descriptions 5

Chapter 2 Geological settings 7

- 2.1 Regional tectonic and geological evolution 7
- 2.2 Structural elements 9
  - 2.2.1 Hammerfest Basin 9
  - 2.2.2 Ringvassøy-Loppa Fault Complex (RLFC) 9
  - 2.2.3 Tromsø Basin 10
- 2.3 Stratigraphy 10
  - 2.3.1 Kapp Toscana Group 11
  - 2.3.2 Adventdalen Group 13
- 2.4 Petroleum systems 16
  - 2.4.1 Source rocks 16
  - 2.4.2 Reservoir rocks 18
  - 2.4.3 Traps 21
- 2.5 Tectonic uplift 21
  - 2.5.1 Effects of tectonic uplift on petroleum system 21
  - 2.5.2 Uplift estimations 22
- 2.6 Geothermal gradient estimation 25

Chapter 3 Research methodologies and theoretical background 27

- 3.1 Work flow 27
- 3.2 Petrophysical analysis 28
  - 3.2.1 Lithology discrimination and net-to-gross estimation 28
  - 3.2.2 Shale volume calculation 30
  - 3.2.3 Porosity calculation 33

3.2.4 Water saturation and pay zone identification 36
3.2.5 Determination of Rw 38
3.2.6 Determination of Rmf and Sxo 39
3.3 Rock physics diagnostics 39
3.3.1 The rock physics cement models 39
3.3.2 Vs prediction 40
3.3.3 Calculation of elastic parameters 42
3.3.4 Construction of rock physics templates 43
3.4 AVO modelling 45
3.4.1 Generation of synthetic seismogram 45
3.4.2 Gassmann fluid substitution 46
3.4.3 Angle dependent reflection coefficient 47
3.4.4 AVO classification of reservoirs 48
Chapter 4 Petrophysical analysis 49
4.1 Results 49
4.1.1 Knurr Formation 49
4.1.2 Stø Formation 52
4.2 Discussion 53
4.2.1 Knurr Formation 53
4.2.2 Stø Formation 55
4.3 Uncertainty analysis 58
4.3.1 Vsh estimation using Gamma Ray log 58
4.3.2 Porosity calculation 58
4.3.3 Sw estimation 58
Chapter 5 Rock physics diagnostics 61
5.1 Results 61
5.1.1 The rock physics cement models 61
5.1.2 Vs and density prediction 64
5.1.3 Construction of rock physics templates 66
5.2 Discussion 69
5.2.1 The rock physics cement models 69
5.2.2 Vs and density prediction 70
5.2.3 Construction of rock physics templates 73
5.3 Uncertainty analysis 74
Chapter 6 AVO modelling 75
6.1 Results 75
6.1.1 AVO signature of Knurr Formation 75
6.1.2 AVO signature of Stø Formation top surface 76
6.1.3 AVO signature of Stø Formation bottom surface 77

6.2 Discussions 79
6.2.1 Knurr Formation 79
6.2.2 Stø Formation 79
6.3 Sensitivity analysis 82
6.3.1 Effects of water saturation 82
6.3.2 Effects of wavelet 84
6.3.3 Effects of block size 86
6.4 Uncertainty analysis 88
Chapter 7 Summary and conclusion 91
Reference 95
Appendix 103

List of Figures

Figure 1.1 Structural elements in and around the Barents Sea area. The study area is shown by red rectangle (modified from Henriksen et al. (2011b)). 1

Figure 1.2 Structural elements of Southwestern Barents Sea and Norwegian Continental Shelf. Study area is in red rectangle (modified from NPD factmaps (2013d)). 2

Figure 1.3 Studied wells in Ringvassøy-Loppa Fault Complex (green), Hammerfest Basin (blue) and Troms-Finnmark Fault Complex (dark green) (modified from NPD (2013d)). 3

Figure 2.1 Major structural features, platforms and basins in the Western Barents Sea, with study area in red rectangle (modified from Faleide et al. (2008))........ 7

Figure 2.2 Different uplift tectonic mechanisms in different areas in the Barents Sea (Dimakis et al., 1998)........ 8

Figure 2.3 Detailed structural elements of SW Barents Sea. The study area is marked by the red rectangle (modified from Gabrielsen (1984)). 9

Figure 2.4 A cross section along the Tromsø Basin, RLFC and Hammerfest Basin (modified from Gabrielsen et al. (1990)). 10

Figure 2.5 Mesozoic and Cenozoic lithostratigraphy of the SW Barents Sea (modified from Glørstad-Clark et al. (2010)). 11

Figure 2.6 Hekkingen Shale (left), Knurr Formation sandstone (middle) and Stø Formation sandstone (right) (from NPD (2013c)). 12

Figure 2.7 Sedimentological log (Walderhaug and Bjørkum, 2003) and sequence stratigraphy analysis (Hübert et al., 2004) for Stø Formation in Hammerfest Basin. 13

Figure 2.8 Well correlation of all seven wells included in this study. 15

Figure 2.9 Carboniferous to Cretaceous source rock properties (Ohm et al., 2008)........ 17

Figure 2.10 Maturity map and maturation history of 3 major source rocks in 6 different regions (Duran et al., 2013)........ 18

Figure 2.11 The distribution map of Triassic plays in the Barents Sea (bru-1, bru-2, brl, rm-4 and rm-5 are names of all the plays). Study area is in red rectangle (modified from NPD (2013e)). 19

Figure 2.12 The distribution map of Lower to Middle Jurassic plays in Barents Sea. JM-5, JM-6, JM-7 and BJL are names of the plays. Study area is in red rectangle (modified from NPD (2013a)). 19

Figure 2.13 Structural cross section through well 7119/12-1 (modified from Olaussen et al. (1984)). 20

Figure 2.14 The distribution map of Upper Jurassic to Lower Cretaceous plays in Barents Sea (bju, bku-1 and kl-3 are names of the plays). Study area is in red rectangle (modified from NPD (2013b)). 20

Figure 2.15 Barents Sea Jurassic play in a rotated fault block (left) and Cretaceous play in a submarine fan (right) (modified from Blaich and Ersdal (2011)). 21

Figure 2.16 Uplift map of Barents Sea (black lines) with subsurface fluid flows (Pink points), (modified from Vadakkepuliyambatta et al. (2013)). 22

Figure 2.17 The comparison between calculated average porosity of reservoir sandstones and porosity- depth trend (Ramm and Bjørlykke, 1994). 23

Figure 2.18 Velocity-depth cross plot of shales in all the wells before (left) and after correction (right) 25

Figure 3.1 Flow chart describing the steps involved in the study. 27

Figure 3.2 Composite log plot of well 7119/12-3. 28

Figure 3.3 Composite log plot for Stø Formation in 7120/10-1. Notice the high Neutron porosity values of the whole section due to logging equipment error. 29

Figure 3.4 The Depth - GR plot of both Knurr Formation (left) and Stø Formation (right) in all wells, the reservoir is shallowest in 7119/12-2, and deepest in 7119/12-3. 32

Figure 3.5 Composite log plot of Stø Formation in well 7119/12-2. Notice the high Neutron porosity values of the whole section due to logging equipment error. 33

Figure 3.6 Density-NPHI cross plot (colour coded by GR) of all the Knurr and Stø Formations data from 7 studied wells. 35

Figure 3.7 Components of the gross rock (bulk), individual components are not to scale (Eslinger and Pevear, 1988). 36

Figure 3.8 Composite log plot of Stø Formation in well 7019/1-1. 37

Figure 3.9 Pickett plot of Stø Formation in well 7119/12-2 (left) and 7119/12-1 (right), coloured by GR. 38

Figure 3.10 Friable, contact and constant cement models (Avseth et al., 2009; Avseth et al., 2000) 40

Figure 3.11 The relationship between Vp and Vs (Castagna et al., 1985). 42

Figure 3.12 Vp/Vs versus IP template (Ødegaard and Avseth, 2003). 44

Figure 3.13 LMR plot from Goodway (2001) and Perez and Tonn (2003). 44

Figure 3.14 The convolution process for generating synthetic seismogram (Schroeder, 2006). 45

Figure 3.15 Wavelet used for AVO modelling in this study. 46

Figure 3.16 AVO classification for gas sands (Castagna and Swan, 1997). 48

Figure 4.1 Composite log plot of Knurr Formation in well 7120/10-1. 50

Figure 4.2 Composite log plot of Knurr Formation in well 7120/10-2. 51

Figure 4.3 Composite log plot of Knurr Formation in well 7019/1-1. 51

Figure 4.4 Neutron-Density cross plot of Knurr Formation in all the available wells. 52

Figure 4.5 Neutron-Density cross plot of Stø Formation in all the available wells. 53

Figure 4.6 Lower Cretaceous sandstone play of well 7120/10-1, 7120/10-2(left) and 7019/1-1(right) (modified from Seldal (2005)). 54

Figure 4.7 Well correlation for Knurr Formation, the depth going deeper from left to right, with top flattened in this picture. 54

Figure 4.8 Well correlation of Stø Formation from west to east, flatten on the top of Stø Formation. 55

Figure 4.9 Composite log plot for Stø Formation in 7119/12-1, core porosity data are showed as red dots. Notice the separation between density porosity and sonic porosity at high porosity zones. 56

Figure 4.10 Diagenetic model of Stø Formation (Olaussen et al., 1984). 57

Figure 5.1 Vp-Porosity cross plot for Knurr and Stø Formation sandstone (Vshale<=0.3) for all the wells available. 61

Figure 5.2 Vp-Porosity cross plot for Knurr and Stø Formation sandstone, coloured by Vshale (Vshale<=0.3), (A: 7119/12-2, B: 7120/10-1, C: 7119/12-4, D: 7019/1-1, E: 7119/12-1, F: 7119/12-3). 62

Figure 5.3 Vs-Porosity cross plot of 7119/12-4 Stø Formation (include sandstone and shale), (A: Vs-Density and Neutron average porosity, B: Vs-Density porosity, C: Vs-Neutron porosity, D: Vs-Sonic porosity). 63

Figure 5.4 Vs-Porosity cross plot of Stø Formation from well 7119/12-4, A: Vs values derived from Mud rock equation (Castagna et al., 1985), B: Vs values derived from Krief et al. (1990) equation, C: Vs values derived from Greenberg and Castagna (1992) equation, D: Vs values derived from Han et al. (1986) equation. 64

Figure 5.5 Vp-Vs cross plot in well 7119/12-4, the data are coloured by Neutron porosity. .. 65

Figure 5.6 Vp-Density cross plot of Kunrr formation and Stø Formation in all the wells, the data are coloured by shale volume. 65

Figure 5.7 Vp-Porosity cross plot for Knurr and Stø Formation sandstone (Vshale<=0.4) in all the wells available, with Han's equation at 40 Mpa (left) and 20 Mpa (right). 66

Figure 5.8 Vp/Vs-Ip cross plot for Knurr and Stø Formations from 7 wells colour-codded by shale volume (left) and well name (right). 67

Figure 5.9 Vp/Vs-Ip cross plot for Stø Formation of well 7119/12-4, measured Vs data (left) and estimated Vs from Mud rock equation (right), colour-codded by shale volume.............. 67

Figure 5.10 LMR plot for Knurr and Stø Formation of all the wells available, coloured by shale volume (left) and well name (right). 68

Figure 5.11 LMR plot derived from measured Vs (left) and estimated Vs from Mudrock equation (right) for Stø Formation from well 7119/12-4. Notice the different scale between the two pictures. 69

Figure 5.12 Vp-Porosity cross plot for Knurr and Stø Formations sandstone (Vshale<=0.3) for all the wells available, colour coded by depth. 70

Figure 5.13 Measured and estimated Vs curves in Stø Formation of well 7119/12-4. 71

Figure 5.14 Vs-GR cross plot of Stø, Nordmela, Tubåen and Fruholmen formations of well 7119/12-4. 72

Figure 5.15 Vp-Density cross plot of Kunrr formation and Stø Formation in all the wells, the data are coloured well names. 73

Figure 5.16 LMR plot for Knurr and Stø Formation for all wells (coloured by deep resistivity). 74

Figure 6.1 A comparison between well logs and synthetic seismogram (using Ricker wavelet), red curves are original well log data with gas saturated in the reservoir, bule curves are the logs after fluid substituition (brine saturated situation). 75

Figure 6.2 AVO cross plot for the top of Knurr Formation (both brine and gas saturated situations). 76

Figure 6.3 AVO intercept (A) versus gradient (B) for the top of Stø Formation in 6 wells (both brine and gas saturated situations). 76

Figure 6.4 The zero-offset reflected amplitude values for the top of Stø Formation in 6 wells (both brine and gas saturated situation). Notice the near-zero value of brine saturated situation in well 7119/12-4. 77

Figure 6.5 AVO intercept (A) versus gradient (B) for the bottom of Stø Formation in 6 wells (both brine and gas saturated situation).. 78

Figure 6.6 The zero-offset reflected amplitude values for the bottom of Stø Formation in 6 wells (both brine and gas saturated situation). 78

Figure 6.7 AVO cross plot from Castagna et al. (1998), Gardner's equation and linear Vp/Vs ralationship (Mudrock equation) are assumed. 79

Figure 6.8 Schematic depth trends of sand and shale impedances, notice the "cross-over" (Avseth et al., 2005). 80

Figure 6.9 Average Vp and density values of Stø reservoir sandstones and Fuglen Formation cap rocks in wells 7119/12-2 (A and B) and 7119/12-3 (C and D). 81

Figure 6.10 AVO intercept (A) versus gradient (B) at the top of the Stø Formation in the shallowest well 7119/12-2 with different saturation scenarios. 82

Figure 6.11 Elastic parameters at top of the Stø Formation in wells 7119/12-2 (left) and 7119/12-3 (right) with different water saturation scenarios, data from Table 6.1 and 6.2....... 83

Figure 6.12 AVO intercept (A) versus gradient (B) at top of the Stø Formation in well 7119/12-3 with different water saturation scenarios. 84

Figure 6.13 The time-amplitude cross plots of Bandpass 1 (A), Bandpass 2 (C) and Ricker (E) wavelets and corresponding frequency-amplitude cross plots of Bandpass 1 (B), Bandpass 2 (D) and Ricker (F) wavelets. 85

Figure 6.14 AVO intercept (A) versus gradient (B) at top of the Stø Formation in 7120/10-1 (left) and 7119/12-1 (right) using three different wavelets. 86

Figure 6.15 AVO responses at top of the Stø Formation in well 7119/12-2 with four different block sizes. 86

Figure 6.16 AVO intercept (A) and gradient (B) at top of the Stø Formation in well 7119/12-4 with different block size and saturation. 87

Figure 6.17 AVO intercept (A) versus gradient (B) at top of the Stø Formation in well 7119/12-3 with different block sizes and fluid saturation. 88

Figure 6.18 The AVO modelling at top of the Stø Formation in well 7119/12-4 saturated with gas.. 88

Appendix

Figure Appendix-1 Neutron-Density cross plot of Knurr Formation in well 7019/1-1. 103

Figure Appendix-2 Neutron-Density cross plot of Stø Formation in well 7019/1-1. 103

Figure Appendix-3 Neutron-Density cross plot of Stø Formation in well 7120/10-1. 104

Figure Appendix-4 Neutron-Density cross plot of Knurr Formation in well 7120/10-2. 104

Figure Appendix-5 Neutron-Density cross plot of Stø Formation in well 7119/12-1. 105

Figure Appendix-6 Neutron-Density cross plot of Stø Formation in well 7119/12-2. 105

Figure Appendix-7 Neutron-Density cross plot of Stø Formation in well 7119/12-3. 106

Figure Appendix-8 Neutron-Density cross plot of Stø Formation in well 7119/12-4. 106

Figure Appendix-9 The density-depth cross plot of all the data in the study area. The data are colour coded by shale volume. 107

Figure Appendix-10 The Vp-depth cross plot of all the data in the study area. The data are colour coded by shale volume. 107

Figure Appendix-11 Vp-depth cross plot of well 7120/10-1 (left) and 7120/10-2 (right). All the data are shales (GR>70 API). The data are colour coded by GR values. 108

Figure Appendix-12 Vp-depth cross plot of well 7119/12-1 (left) and 7119/12-2 (right). All the data are shales (GR>70 API). The data are colour coded by GR values. 108

Figure Appendix-13 Vp-depth cross plot of well 7119/12-3 (left) and 7119/12-4 (right). All the data are shales (GR>70 API). The data are colour coded by GR values. 109

Figure Appendix-14 Vp-depth cross plot of well 7119/12-4. All the data are shales (GR>70 API). The data are colour coded by GR values. 109

Figure Appendix-15 LMR cross plot of Knurr and Stø Formation data in all the wells available. The data are coloured coded by depth. 110

Figure Appendix-16 Vp/Vs-Ip cross plot of all the formations available in well 7119/12-4. Measured Vs values are used in this plot. The data are colour coded by GR values. Stø Formation sandstones are in the black polygon. 110

Figure Appendix-17 LMR cross plot of all the formations available in well 7119/12-4. Measured Vs values are used in this plot. The data are colour coded by GR values. Stø Formation sandstones are in the black polygon. 111

Figure Appendix-18 The composite interpretation plot of well 7119/12-1. The density porosity and sonic porosity curves separate in zones with secondary porosity. 111

List of Tables

Table 1.1 Wells information in the study area (from NPD (2013c)). 4

Table 1.2 A list of available/missing/partially available log data in the studied database......... 5

Table 2.1 Petroleum system information of the study area (from NPD (2013c)). 16

Table 2.2 Uplift estimation and comparisons with published data. 24

Table 2.3 Geothermal gradient estimation of all 7 wells. 26

Table 3.1 Gamma Ray baseline values for all 7 wells. 31

Table 3.2 Parameter values for Vp and Vs relationship (Krief et al., 1990). 41

Table 3.3 Relations between elastic constants and velocities (Sheriff, 1973) 42

Table 3.4 moduli, density and velocity data of minerals (from Mavko et al. (2009)). 43

Table 3.5 AVO classification chart (Castagna and Swan, 1997). 48

Table 4.1 Reservoir and pay zones evaluation results for Knurr Formation. 49

Table 4.2 Reservoir and pay zones evaluation results for Stø Formation. 52

Table 4.3 Estimated Rw values using Rwa method 59

Table 4.4 Estimated m and Rw value from Pickett plot method 59

Table 5.1 Core sample description in Stø Formation of 7119/12-4 (from NPD website). 70

Table 5.2 The code explanation of the lithology description. 70

Table 6.1 Typical fluid substitution results at the top of Stø Formation in well 7119/12-2 82

Table 6.2 Fluid substitution results at the top of Stø Formation in well 7119/12-3 83

Chapter 1 Introduction

1.1 Background

The Barents Sea is bordered by the Norwegian and Russian coasts, the Novaya Zemlya, Franz Josef Land and Svalbard archipelagos, and the eastern margin of the deep Atlantic Ocean (Figure 1.1). The whole region covers about 1.3 million km^2 and the average water depth is about 300m. The Barents Sea has a complex geological history and is composed of different basins and platforms (Doré, 1995; Øvrebø and Talleraas, 1977; Gabrielsen, 1984; Richardsen et al., 1993; Faleide et al., 1993b; Henriksen et al., 2011b).

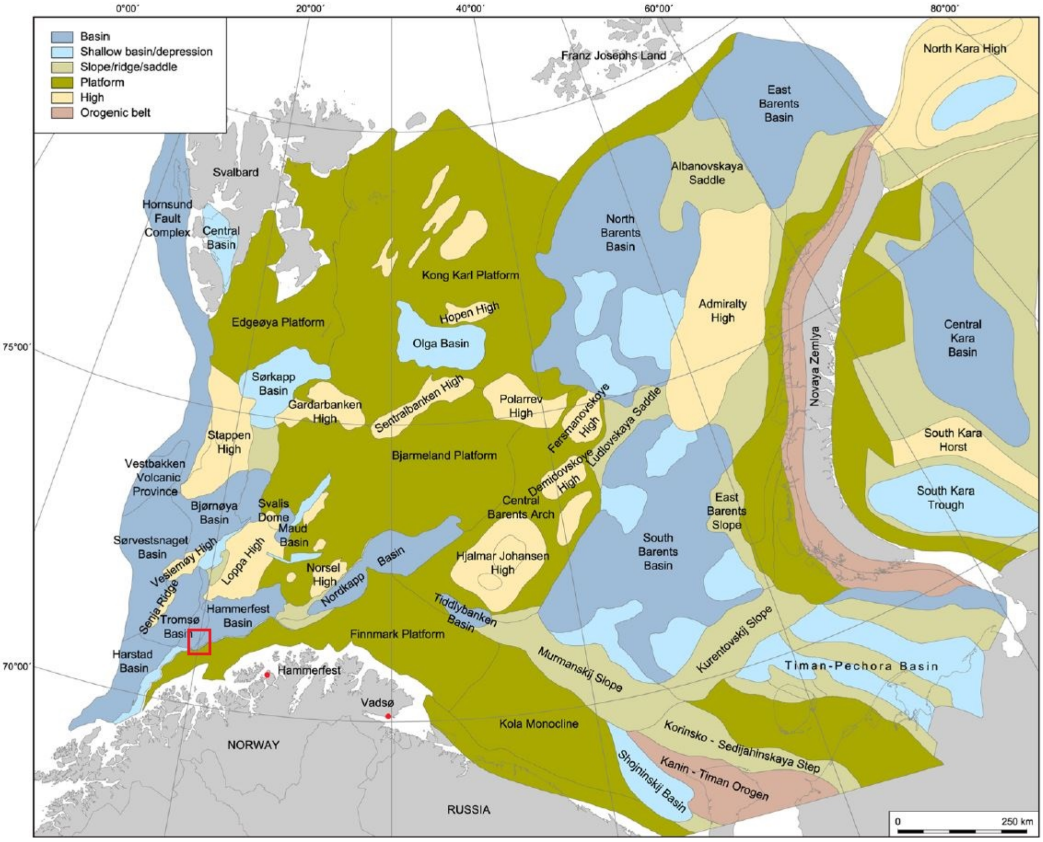
0°00´
20°00´
40°00´
60°00´
80°00´
75°00´
70°00´
Basin
Shallow basin/depression
Slope/ridge/saddle
Platform
High
Orogenic belt
Franz Josephs Land
North Kara High
East Barents Basin
Svalbard
Albanovskaya Saddle
Hornsund Fault Complex
Central Basin
North Barents Basin
Kong Karl Platform
Admiralty High
Hopen High
Edgeøya Platform
Olga Basin
Central Kara Basin
Novaya Zemlya
Sørkapp Basin
Gardarbanken High
Sentralbanken High
Polarrev High
Fersmanovskoye High
Ludlovskaya Saddle
South Kara Horst
Stappen High
Bjarmeland Platform
Vestbakken Volcanic Province
Demidovskoye High
South Kara Trough
Bjørnøya Basin
Svalis Dome
Central Barents Arch
East Barents Slope
Maud Basin
Sørvestsnaget Basin
Veslemøy High
Loppa High
Hjalmar Johansen High
South Barents Basin
Norsel High
Basin
Nordkapp
Senja Ridge
Hammerfest Basin
Tiddlybanken Basin
Kurentovskij Slope
Tromsø Basin
Finnmark Platform
Harstad Basin
Murmanskij Slope
Timan-Pechora Basin
Hammerfest
Vadsø
Kola Monocline
NORWAY
Korinsko - Sedijahinskaya Step
Kanin - Timan Orogen
Shojninskij Basin
RUSSIA
0
250 km

Figure 1.1 Structural elements in and around the Barents Sea area. The study area is shown by red rectangle (modified from Henriksen et al. (2011b)).

There have been extensive hydrocarbon exploration activities from the 1970's. More than 100 wells drilled in Norwegian Barents Sea since the first exploration well 7119/12-1 (included in this study) completed in 1980. At the beginning of the exploration, Barents Sea was supposed to be a prolific and promising hydrocarbon province because of the similarities to reservoirs and source rocks of the North Sea discoveries (Doré, 1995). There are several active petroleum systems in this region (Ohm et al., 2008). It turns out that the Norwegian Barents Sea petroleum systems are more complex compared to the North Sea. The technical success rate is high as nearly all drilled wells found hydrocarbon shows (Ohm et al., 2008), but most of the findings are gas (e.g. Snøhvit, Askeladd, Alka and Albatross shown in Figure 1.2). Cenozoic uplift and erosion is suggested as the reason for this gas-prone petroleum system (Ohm et al., 2008; Doré, 1995; Doré and Jensen, 1996; Nyland et al., 1992). Recently, more and more oil discoveries (e.g. Nucula, Johan Castberg, Wisting and Gohta) make the area a clear spotlight to oil and gas industries.

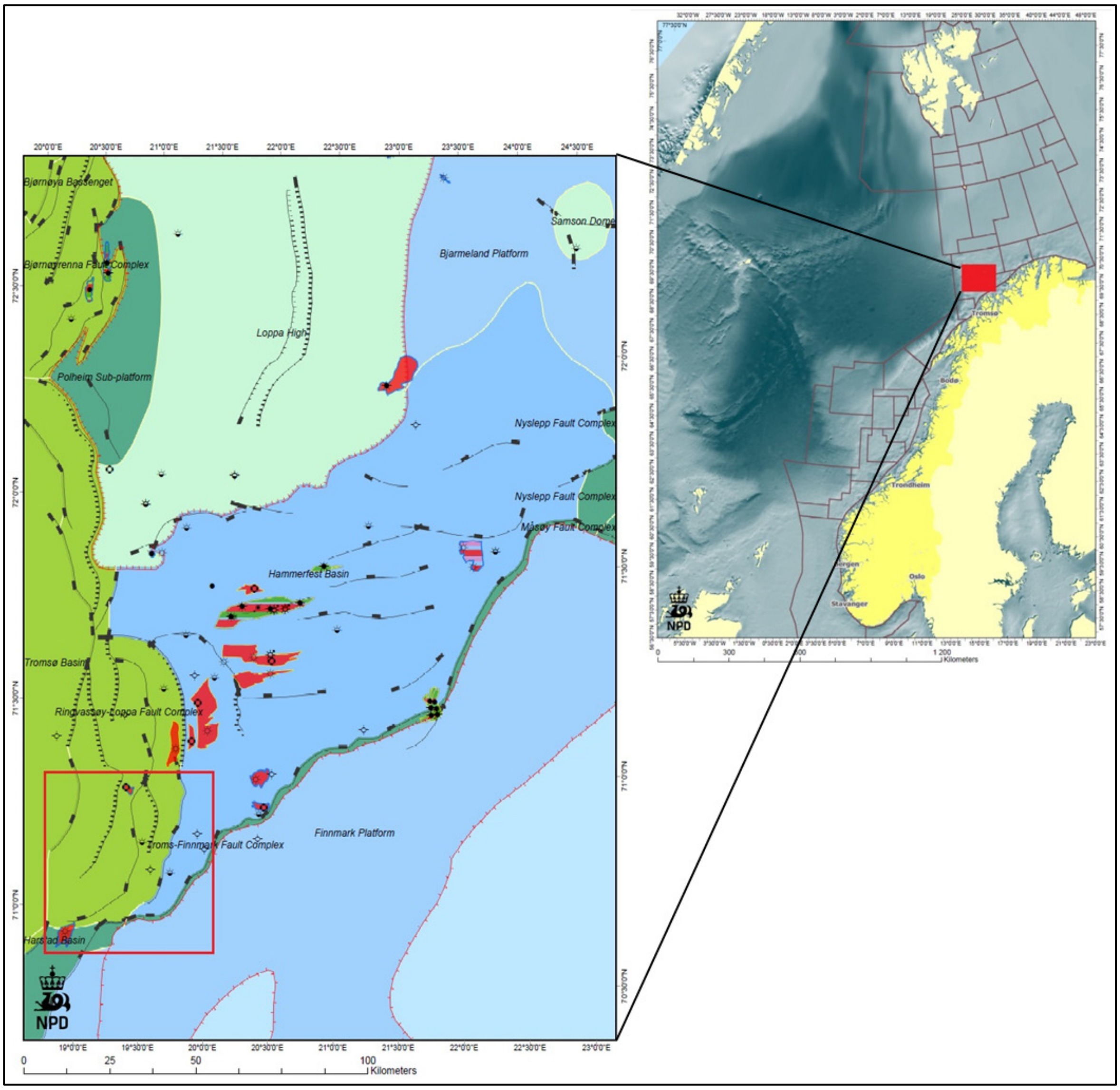
Bjørnøya Bassenget
Bjørnøyrenna Fault Complex
Polheim Sub-platform
Loppa High
Samson Dome
Bjarmeland Platform
Nyslepp Fault Complex
Nyslepp Fault Complex
Måsøy Fault Complex
Hammerfest Basin
Tromsø Basin
Ringvassøy-Loppa Fault Complex
Troms-Finnmark Fault Complex
Finnmark Platform
Harstad Basin
NPD
0
25
50
100
Kilometers
Tromsø
Bodø
Trondheim
Bergen
Oslo
Stavanger
NPD
0
300
600
1 200
Kilometers

Figure 1.2 Structural elements of Southwestern Barents Sea and Norwegian Continental Shelf. Study area is in red rectangle (modified from NPD factmaps (2013d)).

1.2 Motivation and research objectives

Reservoir properties like porosity, shale volume and net-to-gross (N/G) are key parameters to the study for exploration and production of hydrocarbon resources. These reservoir properties vary between different localities and geologic formations because of the different depositional environments and subsequent diagenetic processes. Stø and Knurr Formations are two important reservoirs in this study area. Stø Formation was deposited in prograding coastal regimes and Knurr Formation was deposited in distal open marine conditions (Dalland et al., 1988). Reservoirs at different depths have different burial history, which leads to different diagenetic processes. Furthermore, uplift and erosion in the whole region complicates the burial history and diagenetic processes. Therefore, geological models established for normal subsidence basins will be misleading if used for hydrocarbon exploration in this region. Better understanding of the reservoir qualities and seismic characters could reduce the exploration risks and costs in the uplifted and tectonically complex area.

The aim of this study is to investigate the reservoir quality of Stø and Knurr Formations using seven exploration wells (Figure 1.3 and Table 1.1). The available well log data are studied in detail using petrophysical methods, rock physics diagnostics technique and seismic AVO forward modelling. The geological processes carefully interpreted to explain the causes of variations of reservoir qualities. Using petrophysical methods, rock physics diagnostics and AVO modelling, the details of the reservoir properties are investigated. The geological processes that control the reservoir properties are also studied and to relate with seismic signatures. The uncertainties and limitations of the applied methods are discussed.

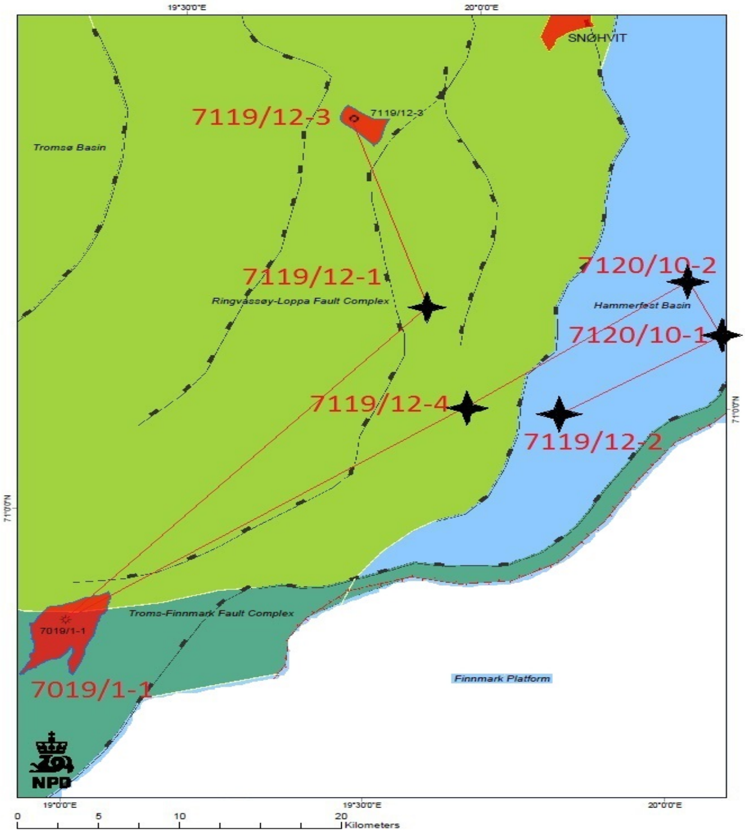
19°30'0"E
20°0'0"E
SNØHVIT
7119/12-3
7119/12-3
Tromsø Basin
7119/12-1
Ringvassøy-Loppa Fault Complex
7120/10-2
Hammerfest Basin
7120/10-1
7119/12-4
7119/12-2
71°0'0"N
71°0'0"N
Troms-Finnmark Fault Complex
7019/1-1
7019/1-1
Finnmark Platform
NPD
19°0'0"E
19°30'0"E
20°0'0"E
0
5
10
20
Kilometers

Figure 1.3 Studied wells in Ringvassøy-Loppa Fault Complex (green), Hammerfest Basin (blue) and Troms-Finnmark Fault Complex (dark green) (modified from NPD (2013d)).

1.3 Study area and database

The study area is located on the border of the Ringvassøy-Loppa Fault Complex and the Hammerfest basin, close to the Finnmark Platform in the south (Figure 1.2 and Figure 1.3). Compared with other basins (e.g. Nordkapp, Bjørnøya, Olga) in the Norwegian Barents Sea, the Ringvassøy-Loppa Fault Complex and the Hammerfest basins were the earliest petroleum exploration areas (Duran et al., 2013). The Hammerfest basin is the most petroliferous in this region (Duran et al., 2013; Ostanin et al., 2013a; Ohm et al., 2008). Decades of drilling activities already proved multiple effective petroleum systems in the study area. The N-S trending Ringvassøy-Loppa Fault Complex (RLFC) separates the Hammerfest Basin from the adjacent Tromsø Basin where same petroleum systems found at relatively shallower depth in the Hammerfest Basin compared to that of the Tromsø Basin (Ostanin et al., 2012).

A total seven exploration wells (7119/12-1, 7119/12-2, 7119/12-3, 7119/12-4, 7120/10-1, 7120/10-2 and 7019/1-1) from the Ringvassøy-Loppa Fault Complex and the Hammerfest Basin were studied (Table 1.1). Wells 7119/12-1, 7119/12-3 and 7119/12-4 are located in the Ringvassøy-Loppa Fault Complex. Well 7019/1-1 is located on the border between Ringvassøy-Loppa Fault Complex and Troms-Finnmark Fault Complex. Three other wells 7119/12-4, 7120/10-1 and 7120/10-2 are located in the Hammerfest Basin. There are two small gas discoveries (7019/1-1 and 7119/12-3) within the seven exploration wells investigated in the study area. The detail information of seven studied wells are given in Table 1.1.

Table 1.1 Wells information in the study area (from NPD (2013c)).

Wellbore name	**7119/12-1**	**7119/12-2**	**7119/12-3**	**7119/12-4**	**7120/10-1**	**7119/10-2**	**7019/1-1**
NS degrees	71° 6' 8" N	71° 0' 51.81" N	71° 14' 20.18" N	71° 1' 42.91" N	71° 3' 6.25" N	71° 5' 34.8" N	70° 55' 5.1" N
EW degrees	19° 47' 40.29" E	19° 58' 20.81" E	19° 44' 37.92" E	19° 49' 20.56" E	20° 16' 29.8" E	20° 14' 28.31" E	19° 4' 22.44" E
Completed date	10.10.1980	26.06.1981	12.09.1983	17.02.2011	08.09.1984	05.09.1990	03.12.2000
Type	Exploration	Exploration	Exploration	Exploration	Exploration	Exploration	Exploration
Content	Oil Shows	Shows	Gas/Condensate	DRY	Dry	Dry	GAS
Kelly bushing elevation [m]	25	25	29	23	25	25	24
Water depth [m]	200	180	211	192	183	186	190
Total depth (MD) [m RKB]	3088	1902	3314	2917	2000	2500	3003
Final vertical depth (TVD) [m RKB]	3087	1902	3308	2910	N/A	2497	2998
Maximum inclination [°]	4.4	2	7	8.9	8.5	7.5	7.9
Bottom hole temperature [°C]	96	62	136	105	71	63	108

The main data used in this study is the well logs from these seven wells. The information of these wells on NPD website is also very important for data analysing. Data from published literatures (e.g. uplift estimation of Barents Sea) are also used in this study. Unpublished core sample data are used to compare with calculated results.

1.4 Limitations

Many of the original well logs require editing and correction before they are available for further study and analysis. This is to correct for the following:

- Shale zone washout
- Mud filtrate invasion
- Gaps or missing data (Table 1.2)
- Shale and hydrocarbon effects

Table 1.2 A list of available/missing/partially available log data in the studied database.

Mesurement	7119/12-1	7119/12-2	7119/12-3	7119/12-4	7120/10-1	7119/10-2	7019/1-1
GR	Available	Available	Available	Available	Available	Available	Available
SP	N/A	N/A	N/A	N/A	N/A	N/A	N/A
Caliper	Available	Available	Available	Partially available	Available	Partially available	Partially available
Shallow Resistivity	Available	Available	Partially available	N/A	N/A	N/A	Partially available
Middle Resistivity	Available	Available	Available	Available	Available	Partially available	Available
Deep Resistivity	Available	Available	Available	Available	Available	Available	Available
Neutron Porosity	Partially available	Available	Partially available	Partially available	Available	Partially available	Partially available
Density	Available	Available	Available	Partially available	Available	Partially available	Partially available
Sonic log	Available	Available	Available	Partially available	Available	Partially available	Available
Pe	N/A	N/A	N/A	Partially available	N/A	N/A	Partially available
Bit size	N/A	N/A	N/A	Available	N/A	N/A	Available

Spontaneous potential (SP) log is not available in this study because of the offshore drilling condition. Some of the well logs are not available or partially available due to bad well conditions during and after drilling. The shale zone washout and mud filtrate invasion affect well logs with shallow depth of investigation, like the Density log. Normally the Density log values will decrease at shale washout zones but increase in mud filtrate zone. Sonic log values act the same as the Density log. These environmental effects lead to errors in petrophysical analysis, rock physics diagnostics and AVO modelling.

1.5 Chapter descriptions

The first chapter is a general introduction of this study. The background and exploration history of the Norwegian Barents Sea, the motivation for this research, the introduction of the study area and the database utilized in this study discussed in chapter 1.

The second chapter focuses on the structure and tectonic in the study area. The information is gathered mostly from published literatures. The regional tectonic, structural elements, depositional history, stratigraphy and petroleum systems are included in this chapter.

The third chapter is about the research methodologies and theoretical background compiled from published papers. The basic principles and well accepted equations for petrophysical methods, rock physics diagnostics and AVO modelling are discussed in this chapter.

Results from petrophysical analyses are presented and discussed in chapter 4. The lithologic discrimination, net to gross, shale volume, porosity and water saturation estimations are performed and described in detail in this chapter. The comparisons of reservoir properties between wells and the geological processes that control them are also discussed.

In Chapter 5, the rock physics diagnostics technique is performed using different established rock physics models and templates. General trends of different rock parameters (velocity, porosity, density, gamma ray etc.), transition zone from mechanical to chemical compaction, uplift estimation and sand-shale compaction trends are discussed in this chapter.

Chapter 6 includes AVO forward modelling results and sensitivity analysis. The effect of different parameters (e.g. water saturation, wavelet and block size) on AVO response for different reservoirs is explained in this chapter. The uncertainties of AVO modelling are also discussed. A summary of the present research along with concluding remarks are given in the last chapter 7.

Chapter 2 Geological settings

2.1 Regional tectonic and geological evolution

According to Henriksen et al. (2011b), the greater Barents Sea suffered three major tectonic phases from Late Paleozoic to the Paleocene. In the first phase, Paleozoic Caledonian Orogeny induced uplift to the west. In the second phase, Late Palaeozoic–Mesozoic Uralide Orogeny caused uplift to the east. In the third phase, the regional geology becomes more complex due to Late Mesozoic–Cenozoic rifting and crustal breakup.

The SW Barents Sea (focus in this study) went through three rift phases after the Caledonian Orogeny: Late Devonian-Early Carboniferous, Middle Jurassic–Early Cretaceous and Tertiary (Figure 2.1). All the phases comprise several tectonic pulses and reshape the area (Faleide et al., 1993a). The Middle – Late Jurassic was a period of regional extension and minor strike-slip movement in the SW Barents Sea. The Tromsø basin subsidence was initiated in this period.

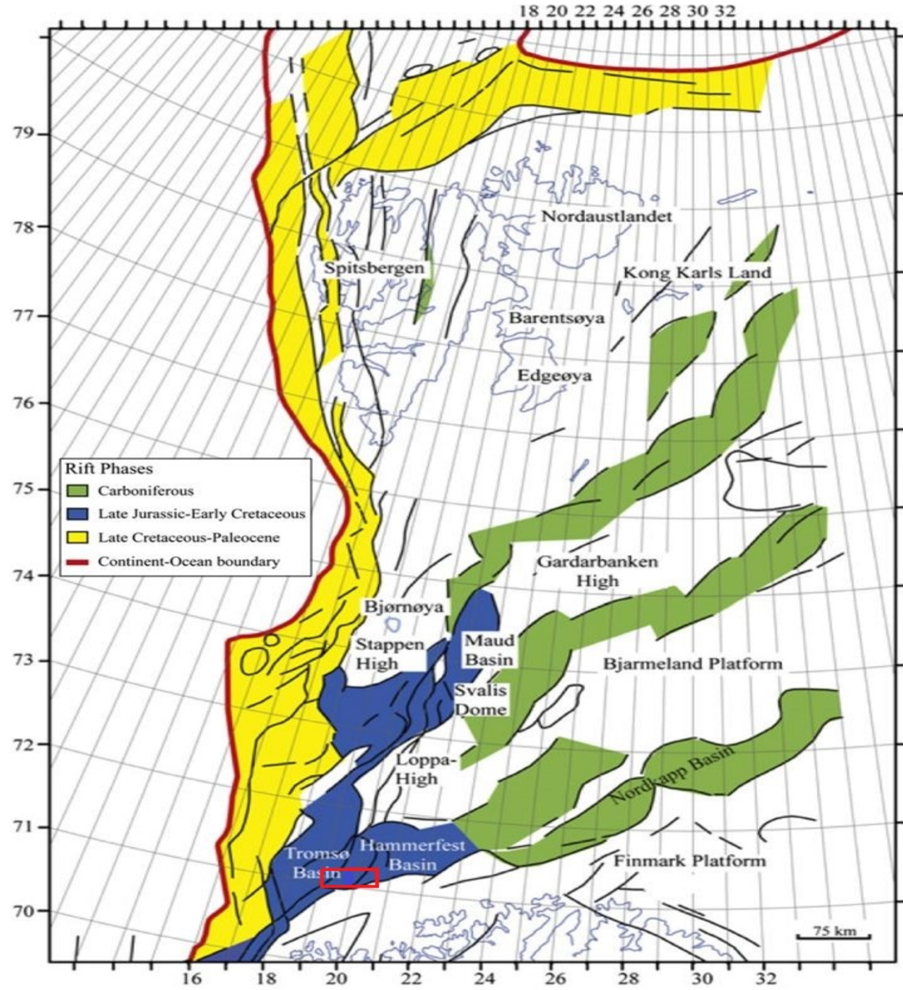
18 20 22 24 26 28 30 32
Rift Phases
Carboniferous
Late Jurassic-Early Cretaceous
Late Cretaceous-Paleocene
Continent-Ocean boundary
Nordaustlandet
Spitsbergen
Kong Karls Land
Barentsøya
Edgeøya
Gardarbanken High
Bjørnøya
Stappen High
Maud Basin
Svalis Dome
Bjarmeland Platform
Loppa-High
Nordkapp Basin
Tromsø Basin
Hammerfest Basin
Finmark Platform
75 km
79
78
77
76
75
74
73
72
71
70
81
80
79
78
77
76
75
74
73
72
71
16
18
20
22
24
26
28
30
32

Figure 2.1 Major structural features, platforms and basins in the Western Barents Sea, with study area in red rectangle (modified from Faleide et al. (2008)).

In Early Cretaceous at least three tectonic phases of extensional faulting can be recognized (Faleide et al., 1993a). The first two are Berriasian/Valanginian and Hauterivian/Barremian.

The Tromsø basin was affected much more strongly than the Hammerfest basin in these two phases. The Aptian/Albian tectonic movement was quite strong in RLFC zone, which separated the eastern stable Hammerfest basin with the western rapidly subsided Tromsø basin. These movements can be related to the opening of the Amerasia Basin and the southern North Atlantic (Faleide et al., 1993a). The Tromsø basin continued to subside during Late Cretaceous while the Hammerfest basin deposited a condensed sequence.

The entire Barents Sea went through uniform and widespread deposition in Late Paleocene (Faleide et al., 1993a). After Paleocene, two major erosion phases are proven by numerous evidences. The first might be correlated with the opening of the Norwegian Greenland Sea. The second is caused by the post Miocene glaciations (Nyland et al., 1992). Several uplift mechanisms could contribute to the uplift of the entire Barents Sea (Figure 2.2), but the thermal process is the most possible reason for the overall uplift (Dimakis et al., 1998). In Eocene, the Norwegian-Greenland Sea Floor started to spread and the western Barents Sea margin went through strike-slip movements. The transpressional forces created folding and thrusting in Svalbard region (Faleide et al., 1993a). Since the opening of the Norwegian-Greenland Sea, the entire Barents Sea experienced uplift and erosion. Rapid erosion created large volumes of sediment in huge fan systems in western and northern margins of the Barents Sea (Dimakis et al., 1998).

The glacial erosion processes include minor glaciers erosion during interglacials and interstadials, and major ice sheets erosions during peroids of peak glaciations (Elverhøi et al., 1998). Most of the Barents Sea was subaerial during interglacial and interstadial times. Isostatic uplift prolonged the period of subaerial erosion and allowed large amount of sediments to be eroded (Dimakis et al., 1998).

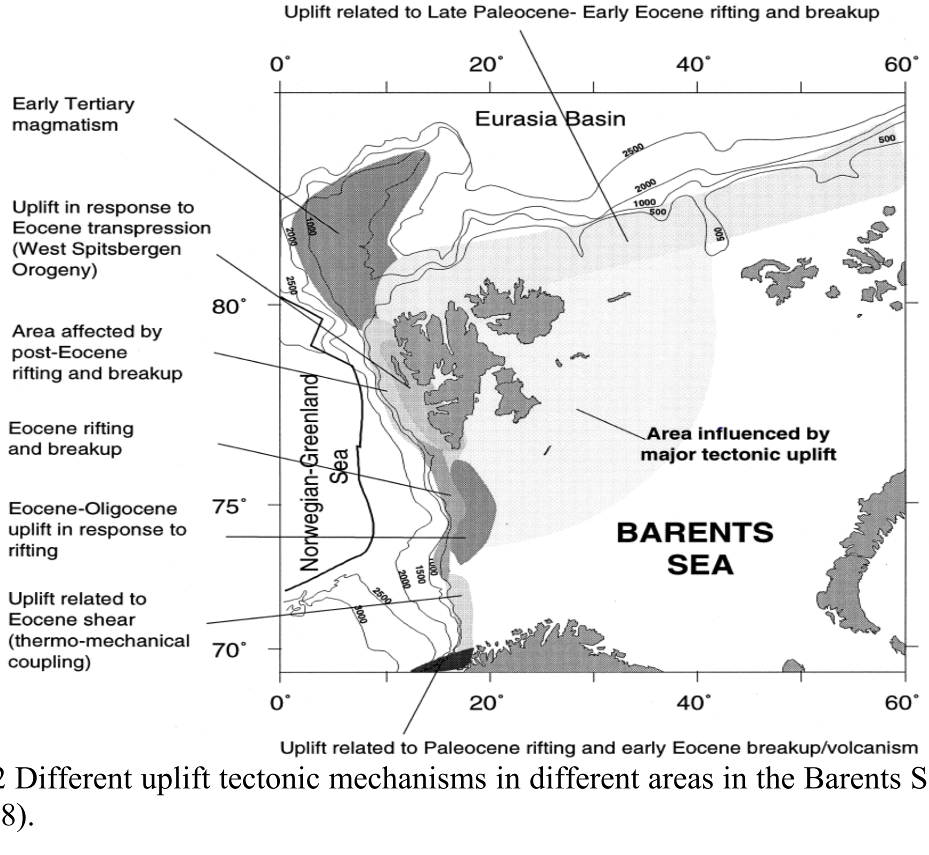
Uplift related to Late Paleocene- Early Eocene rifting and breakup
0°
20°
40°
60°
Early Tertiary magmatism
Eurasia Basin
2500
2000
1000
500
Uplift in response to Eocene transpression (West Spitsbergen Orogeny)
80°
Area affected by post-Eocene rifting and breakup
Norwegian-Greenland Sea
Area influenced by major tectonic uplift
Eocene rifting and breakup
75°
BARENTS SEA
Eocene-Oligocene uplift in response to rifting
1500
3000
Uplift related to Eocene shear (thermo-mechanical coupling)
70°
Uplift related to Paleocene rifting and early Eocene breakup/volcanism

Figure 2.2 Different uplift tectonic mechanisms in different areas in the Barents Sea (Dimakis et al., 1998).

2.2 Structural elements

2.2.1 Hammerfest Basin

The Hammerfest Basin has a striking axis of ENE-WSW (Figure 2.3). The Basin has a central dome parallel to the basin axis. The directions of the fault systems are E-W, ENE-WSW and WNW-ESE (Gabrielsen, 1984). The eastern part of the basin, which has the characteristics of a sag basin, is less affected by the faulting (Gabrielsen et al., 1990). The Hammerfest Basin is relatively shallow and the depth to basement is approximately 6-7 km from the seismic reflection data (Roufosse, 1987).

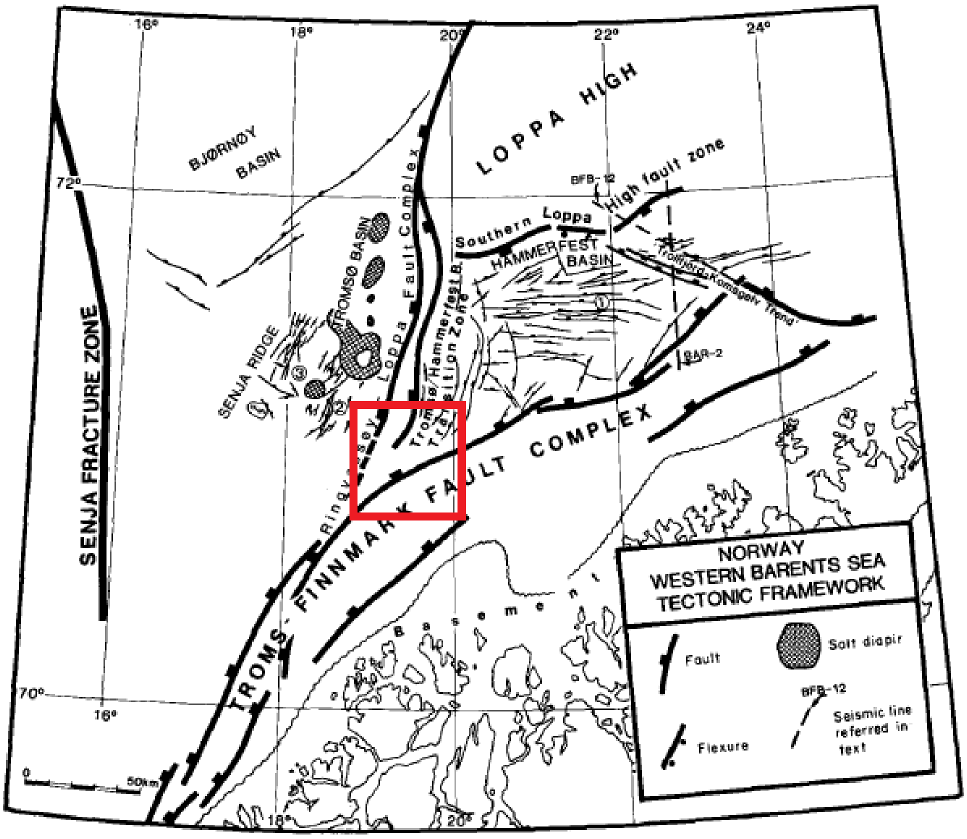
16°
18°
20°
22°
24°
72°
70°
16°
18°
20°
LOPPA HIGH
BJØRNØY BASIN
Loppa Fault Complex
Southern Loppa High fault zone
BFB-12
HAMMERFEST BASIN
Troms/Hammerfest B. Transition Zone
Trollfjord-Komagelv Trend
BAR-2
TROMSØ BASIN
SENJA RIDGE
SENJA FRACTURE ZONE
Ringvassøy
TROMS - FINNMARK FAULT COMPLEX
Basement
①
②
③
④
0
50km
NORWAY
WESTERN BARENTS SEA
TECTONIC FRAMEWORK
Fault
Salt diapir
Flexure
BFB-12
Seismic line referred in text

Figure 2.3 Detailed structural elements of SW Barents Sea. The study area is marked by the red rectangle (modified from Gabrielsen (1984)).

2.2.2 Ringvassøy-Loppa Fault Complex (RLFC)

The RLFC has a strike of N-S direction. Basement movements caused the fault complex to work as a long lived hinge line based on multiple detachments (Braut, 2012; Zalmstra, 2013). Structures related to growth faults were identified in the seismic and five active periods were established. The main subsidence along this fault complex started in Middle Jurassic and culminated in Early Cretaceous (Gabrielsen et al., 1990). In the Late Cretaceous this fault complex was reactivated and Tertiary strata were affected (Figure 2.4). The subsidence and faulting could be related to large-scale extensional rifting (Talleraas, 1979), or local movements related to salt subtraction (Øvrebø and Talleraas, 1977).

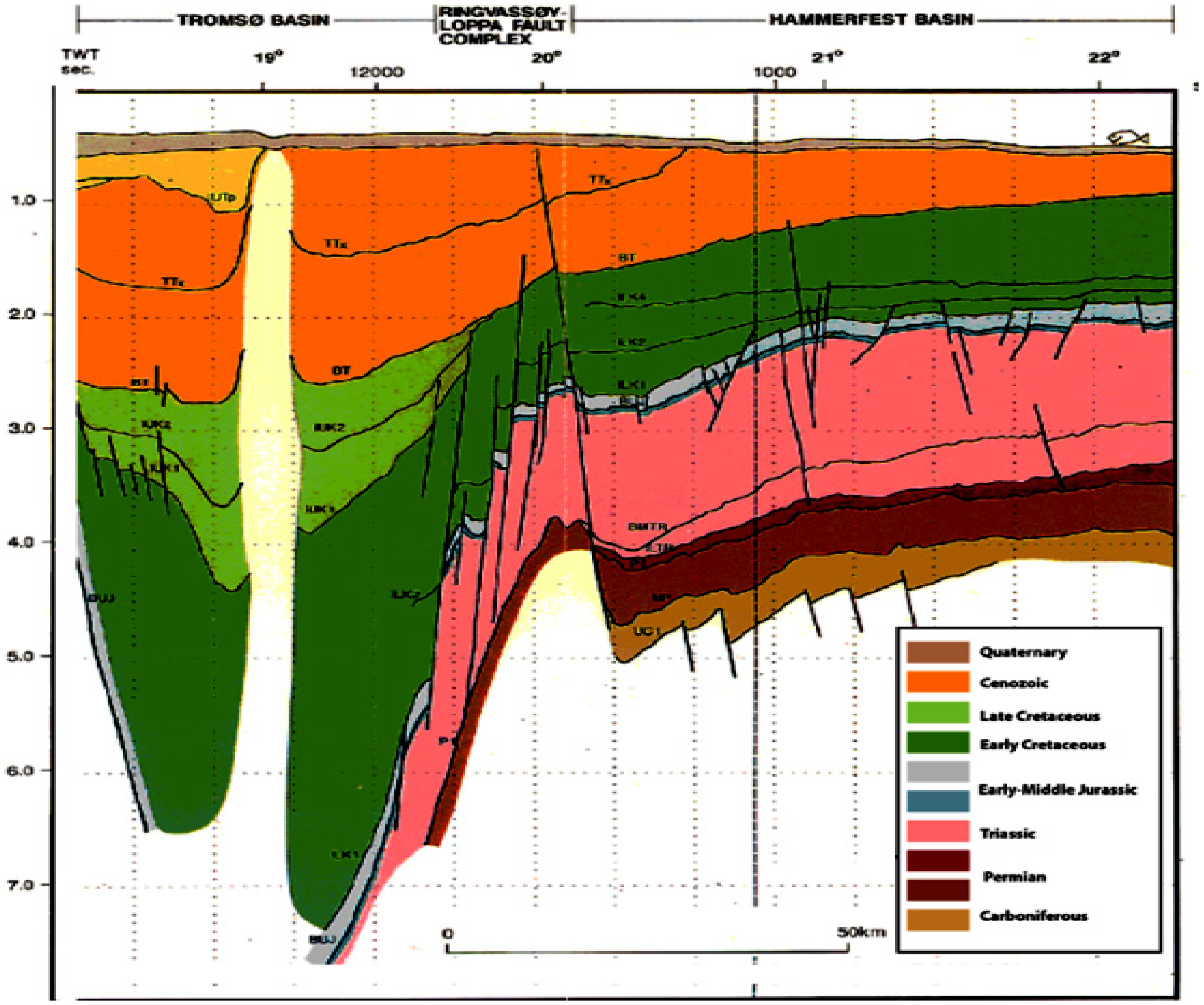
TROMSØ BASIN
RINGVASSØY-LOPPA FAULT COMPLEX
HAMMERFEST BASIN
TWT sec.
19°
12000
20°
1000
21°
22°
1.0
2.0
3.0
4.0
5.0
6.0
7.0
UTp
TTx
BT
LK2
LK1
BUJ
P
UC1
0
50km
Quaternary
Cenozoic
Late Cretaceous
Early Cretaceous
Early-Middle Jurassic
Triassic
Permian
Carboniferous

Figure 2.4 A cross section along the Tromsø Basin, RLFC and Hammerfest Basin (modified from Gabrielsen et al. (1990)).

2.2.3 Tromsø Basin

The Tromsø Basin has a NNE-SSW trending axis and thick succession of sedimentary rocks. The depth of the basement is 10-13 km (Roufosse, 1987). Thick sequence of Late Paleozoic salt formed a series of salt diapirs in the centre of the basin. Halokinesis is important in the forming of the Tromsø Basin structure (Talleraas, 1979). It could also be related to large-scale extensional (Talleraas, 1979) or shear movements.

2.3 Stratigraphy

The Mesozoic stratigraphy in the study area can be divided into Adventdalen Group and Kapp Toscana Group (Figure 2.5). The wells from the studied database did not penetrate the formations older than Fruholmen Formation in Triassic.

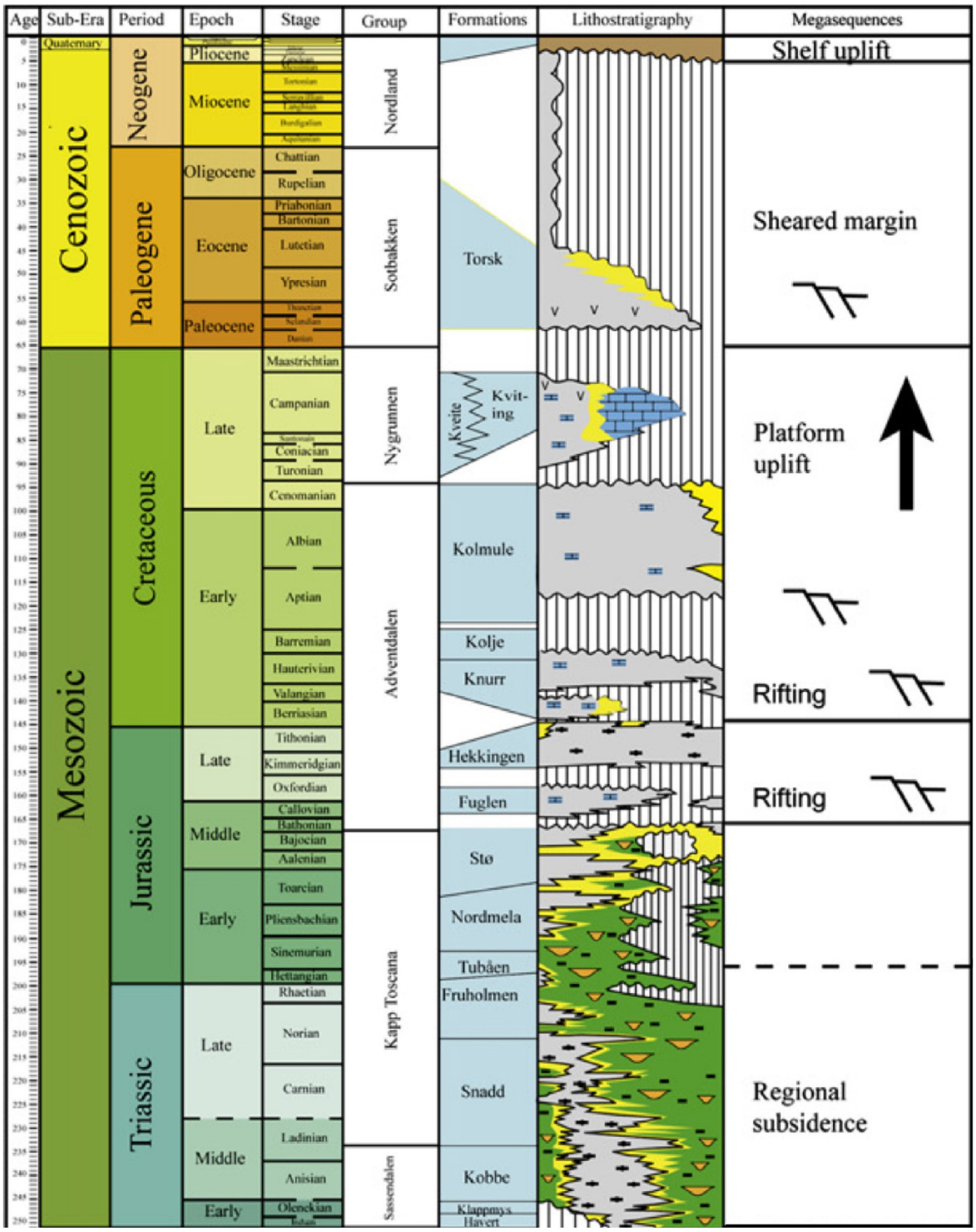
Age
Sub-Era
Period
Epoch
Stage
Group
Formations
Lithostratigraphy
Megasequences
Quaternary
Cenozoic
Mesozoic
Neogene
Paleogene
Cretaceous
Jurassic
Triassic
Pliocene
Miocene
Oligocene
Eocene
Paleocene
Late
Early
Late
Middle
Early
Late
Middle
Early
Tortonian
Serravallian
Langhian
Burdigalian
Aquitanian
Chattian
Rupelian
Priabonian
Bartonian
Lutetian
Ypresian
Thanetian
Selandian
Danian
Maastrichtian
Campanian
Santonian
Coniacian
Turonian
Cenomanian
Albian
Aptian
Barremian
Hauterivian
Valangian
Berriasian
Tithonian
Kimmeridgian
Oxfordian
Callovian
Bathonian
Bajocian
Aalenian
Toarcian
Pliensbachian
Sinemurian
Hettangian
Rhaetian
Norian
Carnian
Ladinian
Anisian
Olenekian
Induan
Nordland
Sotbakken
Nygrunnen
Adventdalen
Kapp Toscana
Sassendalen
Torsk
Kveite
Kvit-ing
Kolmule
Kolje
Knurr
Hekkingen
Fuglen
Stø
Nordmela
Tubåen
Fruholmen
Snadd
Kobbe
Klappmys
Havert
Shelf uplift
Sheared margin
Platform uplift
Rifting
Rifting
Regional subsidence

Figure 2.5 Mesozoic and Cenozoic lithostratigraphy of the SW Barents Sea (modified from Glørstad-Clark et al. (2010)).

2.3.1 Kapp Toscana Group

This group is deposited in near shore, deltaic environment and is characterized by shallow marine and coastal reworking of deltaic and fluviodeltaic sediments (Mork et al., 1982).

2.3.1.1. Fruholmen Formation

Dark shale changes gradually into interbedded sandstones, shales and coals from base to the middle of this formation. Sandstone dominates in the middle part, but the upper part is more shaly. Shale was mainly deposited in open marine condition. The sandstone is deposited in coastal and fluvial environments (Dalland et al., 1988).

2.3.1.2. Tubåen Formation

This formation is dominated by sandstones with subordinate shales and minor coals (Dalland et al., 1988). The sandstone represents high-energy marginal marine environment. Marine shale was deposited in distal setting. Coal and shale are deposited in protected back barrier lagoonal environment (Dallmann, 1999).

2.3.1.3. Nordmela Formation

This formation is mainly consisted of interbedded siltstones, sandstones, shale and mudstones with minor coals. The depositional environment is tidal flat to flood plain. Some individual sandstone represent estuarine and tidal channel environment (Dallmann, 1999).

2.3.1.4. Stø Formation

According to Dallmann (1999), the lithologies are mainly moderately to well sorted and mineralogically mature sandstones, interbedded with thin shale and siltstones (Figure 2.6). Occasionally, there is phosphatic lag conglomerates deposited in this formation. The depositional environment is prograding coastal regimes and a variety of linear clastic coastal lithofacies is represented. Shale and siltstone intervals represent regional transgressive pulses in the late Toarcian and late Aalenian.

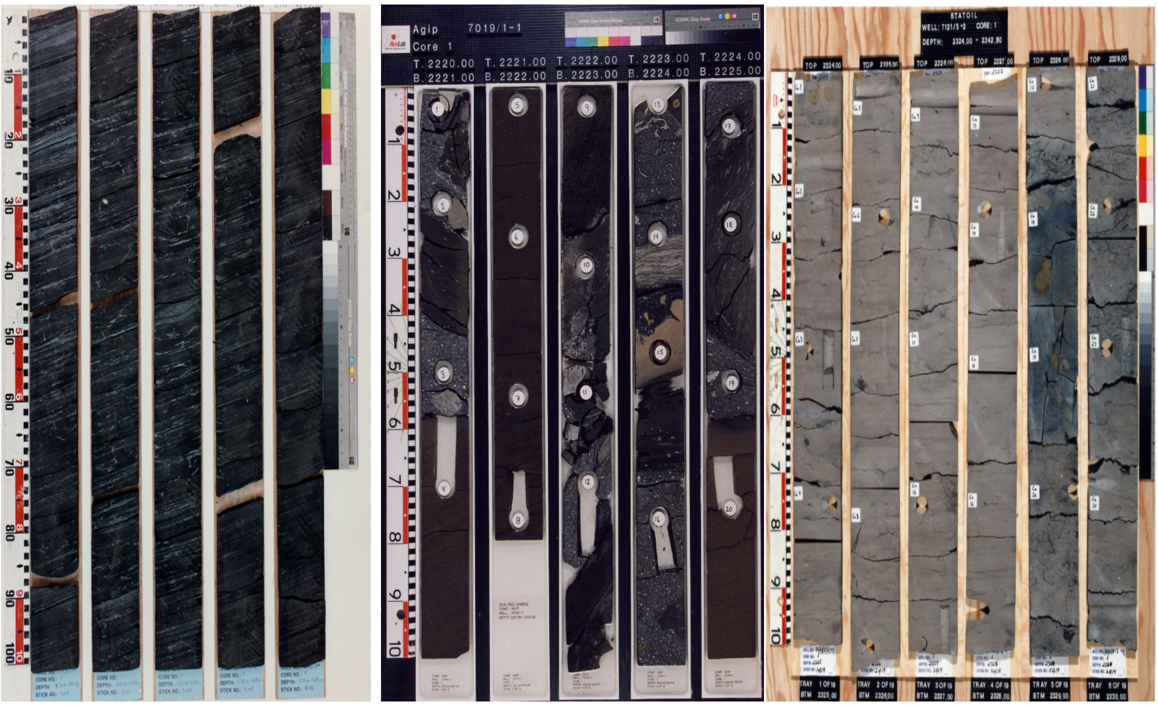

Figure 2.6 Hekkingen Shale (left), Knurr Formation sandstone (middle) and Stø Formation sandstone (right) (from NPD (2013c)).

The formation is thickest in southwestern wells, thinning generally eastwards. The entire unit can be sub-divided into three depositional sequences, with bases defined by transgressive episodes (Figure 2.7). The basal sequence is only present in the western parts of the Hammerfest Basin. The middle (late Toarcian/Aalenian) sequence represents maximum transgression in the area. The uppermost Bajocian sequence is highly variable owing to syn-depositional uplift and to later differential erosion (Dallmann, 1999).

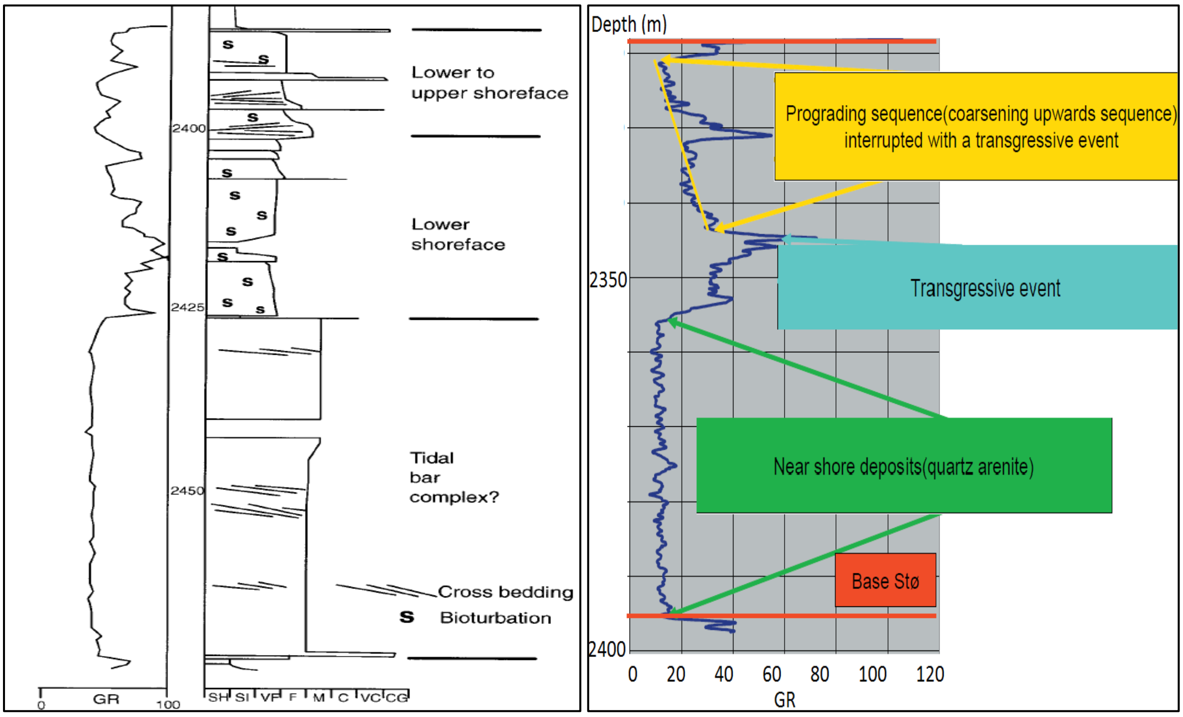

Figure 2.7 Sedimentological log (Walderhaug and Bjørkum, 2003) and sequence stratigraphy analysis (Hübert et al., 2004) for Stø Formation in Hammerfest Basin.

2.3.2 Adventdalen Group

The group is mainly composed of dark marine mudstones, but also includes deltaic and shelf sandstones of Late Jurassic to Early Cretaceous age (Dallmann, 1999). The most important hydrocarbon source rocks of Hekkingen and Fuglen Formations (Figure 2.8) were included in this group.

2.3.2.1 Fuglen Formation

The lithology is mainly dark brown pyritic mudstones, interbedded with brownish grey thin limestone (Dalland et al., 1988). The depositional environment is highstand marine shelf with low sedimentation rates (Dallmann, 1999).

2.3.2.2. Hekkingen Formation

The lithology is brownish grey to very dark grey shale and claystone. There are also limestone, dolomite, siltstone and sandstone occasionally interbeded in this formation. Low parts of the formation have very high gamma ray values. The depositional environment is anoxic deep marine (Dalland et al., 1988).

2.3.2.3. Knurr Formation

The lithology is mainly dark grey to greyish brown claystones with thin limestone and dolomite interbeds (Figure 2.6). The upper part consists of some red to yellow brown claystone. Thin sandstones can be observed in the lower part of this formation, but these sandstones disappear laterally into the Hammerfest Basin. The depositional environment is open, generally distal and locally restricted marine environment (Dalland et al., 1988).

2.3.2.4. Kolje Formation

The lithology of the Kolje Formation is mainly dark brown to dark grey shale and claystone, with minor interbeds of pale limestone and dolomite. Some thin interbeds of light grey-brown siltstone could be included in the upper part of this formation. The depositional environment is distal open, or sometimes restricted marine (Dalland et al., 1988).

2.3.2.5 Kolmule Formation

The lithlogy of this formation is predominantly dark grey to green claystone and shale. There might be siltstone interbeds and limestone and dolomite stringers. Traces of glauconite and pyrite also can be noticed. The depositional environment is open marine (Dalland et al., 1988).

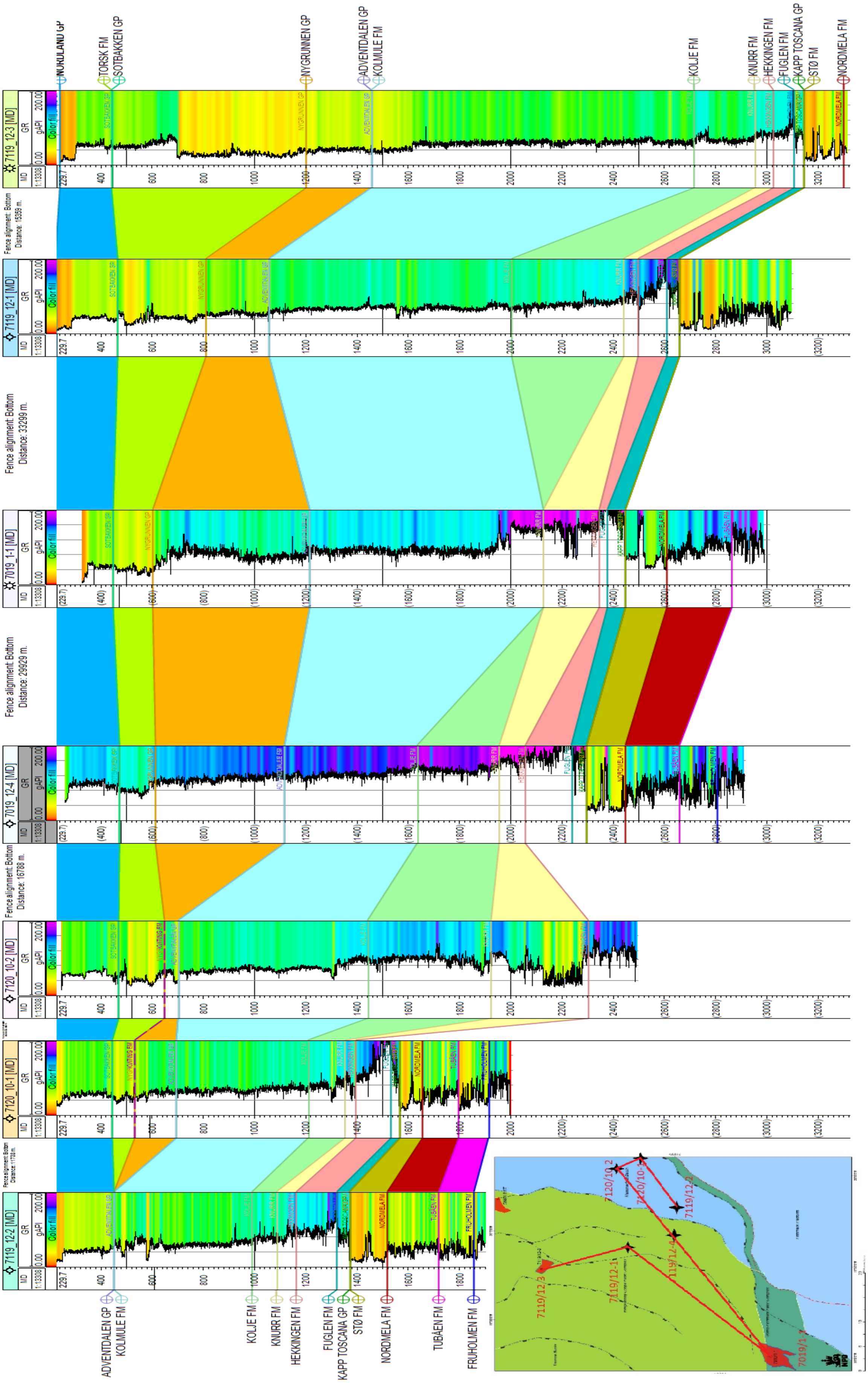

Figure 2.8 Well correlation of all seven wells included in this study.

2.4 Petroleum systems

A petroleum system includes essential elements (source rock, reservoir rock and seal/cap rock) and processes, like trap formation and generation-migration-accumulation of hydrocarbons (Magoon and Dow, 1994). Most of the petroleum found in the study area belongs to Mesozoic petroleum systems (Table 2.1).

Table 2.1 Petroleum system information of the study area (from NPD (2013c)).

Wellbore name	**7119/12-1**	**7119/12-2**	**7119/12-3**	**7119/12-4**	**7120/10-1**	**7119/10-2**	**7019/1-1**
Seismic location	738-424 &SP.484	738 418 SP: 65.	738 - 232 SP 676	3D survey : ST09M03-inline 6640 & xline 7290	E 841 - 30 SP. 630	E 841 - 09 SP. 295	94 TRM3D inline 1026 & crossline 1050
Geological location	Tromsø basin	Hammerfest basin	Tromsø basin	Tromsø basin	Hammerfest basin	Hammerfest basin	Tromsø basin
Oldest penetrated age	Early Jurassic	Late Triassic	Early Jurassic	Late Triassic	Late Triassic	Late Jurassic	Early Jurassic
Oldest penetrated formation	Stø Fm	Fruholmen Fm	Nordmela Fm	Fruholmen Fm	Fruholmen Fm	Hekkingen Fm	Tubåen Fm
Reservoir rock	Primary target was middle Jurassic sandstone. Secondary targets were Early Jurassic and Late Triassic sandstones	The primary objectivewas sandstones of Middle Jurassic age. Secondary objectives were clastics of lower Jurassic and Upper Triassic age.	Middle to Early Jurassic sandstone	The primary objective was Stø and Nordmela Formations.The secondary objective was Tubåen, Fruholmen and Snadd Formations	Middle to Early Jurassic sandstone	Valanginian submarine fan sandstones within the Knurr Formation	The primary target was to test the Middle Jurassic through Upper Triassic Stø Formation . Lower Basal clastics of the Early Cretaceous Knurr Formation were a secondary target.
Source rock	Upper Jurassic shale (Hekkingen Formation). Older source rocks may be present	Upper Jurassic shale (Hekkingen Formation).	Upper Jurassic shale (Hekkingen Formation). Older source rocks may be present	Could be Upper Jurassic shale (Hekkingen Formation	Upper Jurassic shale (Hekkingen Formation)	Upper Jurassic shale (Hekkingen Formation)	Could be Upper Jurassic shale (Hekkingen Formation)
Trap	A seismic closure (Alpha structure) on a horst block	A seismic closure (Zeta-structure)	A seismic closure	N/A	B-prospect	Up dip sand pinch out to the south and west combined with structural dip to the northeast	A seismic closure (Gamma-structure) and a stratigraphic trap of a submarine fan

2.4.1 Source rocks

A number of source rocks can be found in the Barents Sea with ages ranging from Carboniferous to Cretaceous (Ohm et al., 2008). Evidences from biomarkers and isotopes in the hydrocarbon samples indicate that most of the discovered oil and gas came from different source rocks (Ohm et al., 2008).

2.4.1.1 Source rock distribution

The standards for good source rock includes high total organic carbon (TOC), hydrocarbon generative potential (S2) and hydrogen index (HI). According to the geochemical data (Figure 2.9), the most prolific source rock is Hekkingen Formation shale from Upper Jurassic age. Middle Jurassic, Triassic (e.g. Snadd and Kobbe Formations) and Paleozoic shales also have potential to generate petroleum (Ohm et al., 2008). Because semigrabens developed in basin margin and dome developed in the basin axis, the Hekkingen Formation thins northwards to less than 100 m towards axis of the Hammerfest Basin (Dalland et al., 1988). This formation is the most widespread source rock generating petroleum in the Barents Sea. The Triassic source rocks are much patchier in lakes and estuaries (Ohm et al., 2008). The temperature gradient here is higher because of uplift and erosion. That is why the source rock maturity of Barents Sea is higher compared to Haltenbanken and North Sea (Dalland et al., 1988).

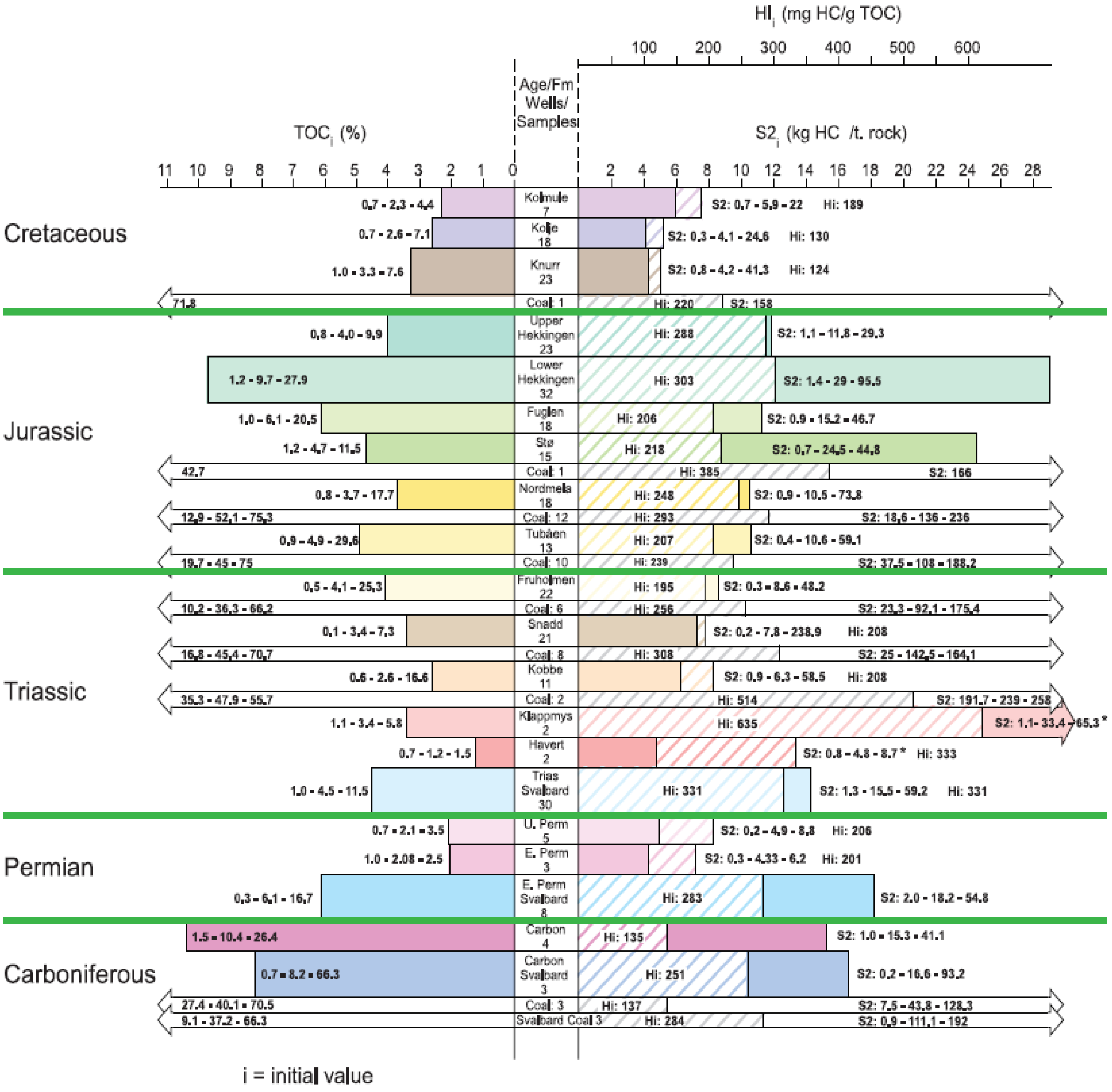

Figure 2.9 Carboniferous to Cretaceous source rock properties (Ohm et al., 2008).

2.4.1.2 Maturation and Migration

The Hammerfest Basin source rocks are less mature than Ringvassøy-Loppa Fault Complex (Figure 2.10). The deeper formations are more mature than shallower formations. The hydrocarbons from western deep basin migrated to eastern reservoirs through different kinds of migration routes (Duran et al., 2013). From the Barents Sea field data, most of the traps are not fully charged. According to Duran et al. (2013), the oil was spilled out because of the gas expansion and tilting during uplift and erosion.

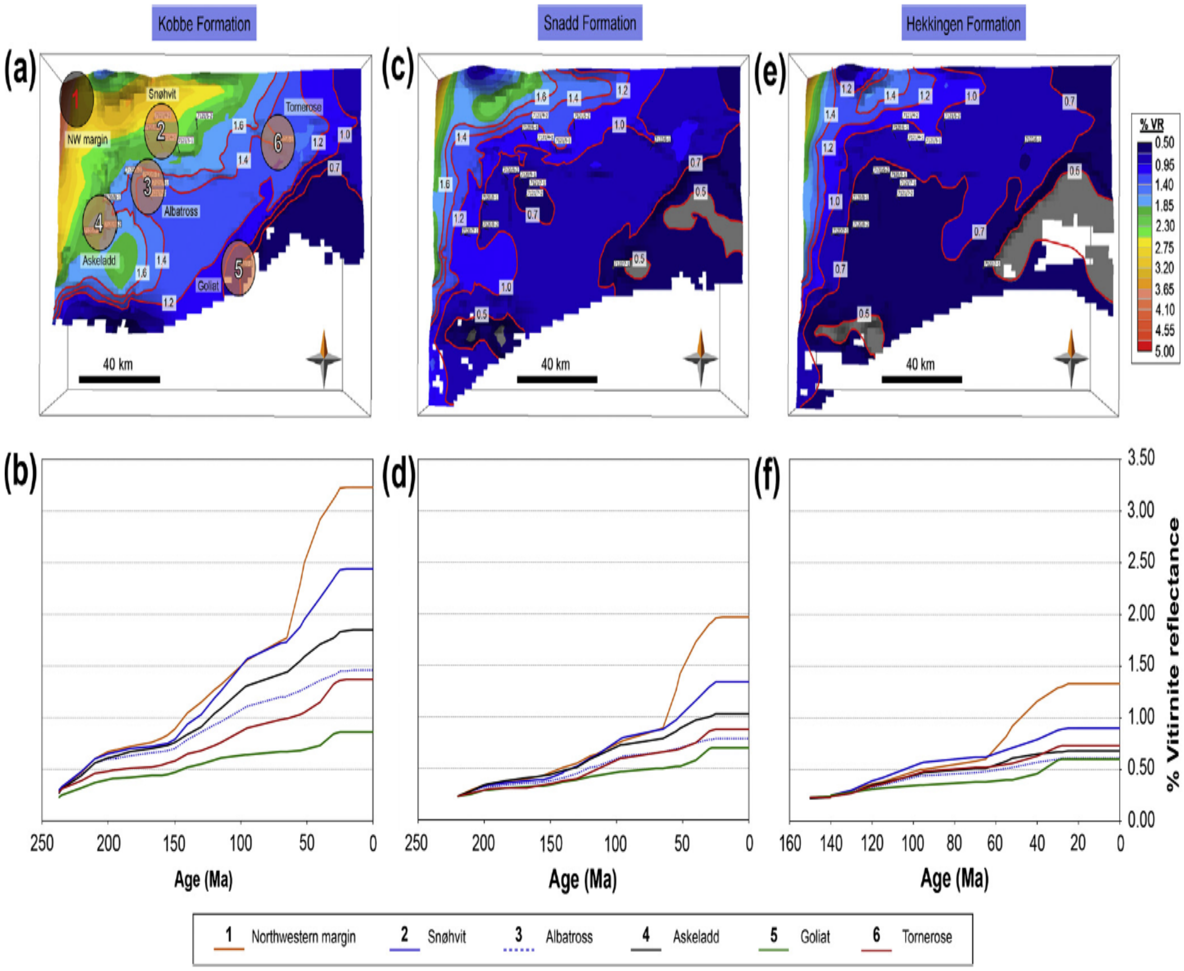

Figure 2.10 Maturity map and maturation history of 3 major source rocks in 6 different regions (Duran et al., 2013).

2.4.2 Reservoir rocks

2.4.2.1 Triassic

Triassic reservoirs were widely distributed in the whole Barents Sea region, but not in this study area (Figure 2.11). Two wells in the study area (7119/12-2 and 7120/10-1) penetrated Fruholmen Formation in Triassic age. High quality sandstones were found in the 7119/12-2, but no evidence of hydrocarbon presence. Triassic reservoirs could be important targets in Finnmark platform in the south.

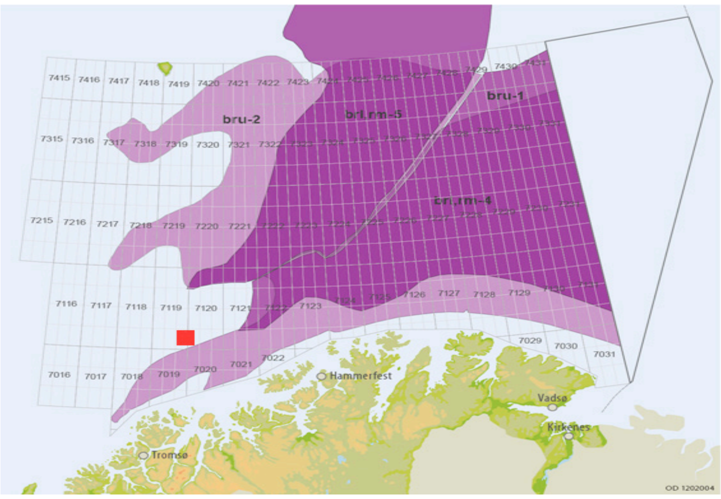
bru-2
brl,rm-5
bru-1
brl,rm-4
7415 7416 7417 7418 7419 7420 7421 7422 7423
7315 7316 7317 7318 7319 7320 7321 7322
7215 7216 7217 7218 7219 7220 7221
7116 7117 7118 7119 7120 7121 7123 7126 7127 7128 7129
7016 7017 7018 7019 7020 7021 7022 7029 7030 7031
Hammerfest
Vadsø
Kirkenes
Tromsø
OD 1202004

Figure 2.11 The distribution map of Triassic plays in the Barents Sea (bru-1, bru-2, brl, rm-4 and rm-5 are names of all the plays). Study area is in red rectangle (modified from NPD (2013e)).

2.4.2.2 Lower to Middle Jurassic

In the Norwegian Barents Sea, 90% of the hydrocarbon resources are gas and 85% of the resources are found in Lower-Middle Jurassic sandstones (e.g. Stø and Tubåen Formations, Figure 2.12) (Duran et al., 2013). Stø Formation is composed of clean sandstones with large scale cross-bedding and marine fossils. The deposition environment is high energy shallow marine shoreline including shoreface and tidal delta (Olaussen et al., 1984). The interbedded shale in this formation was deposited in transgressive offshore marine environment. The entire sequence gradually changes into distal low energy marine environments westwards (Stewart et al., 1995). This play is the major target of four wells in the study area (7119/12-1, 7119/12-2, 7119/12-3 and 7120/10-1) (Figure 2.13). All these four wells penetrated good quality sandstone reservoirs in Stø Formation. Nordmela Formation also contains a few sandstone reservoirs, but the quality is poorer than Tubåen Formation. The other reservoirs include Lower Cretaceous and Lower and Upper Triassic sandstones, etc.

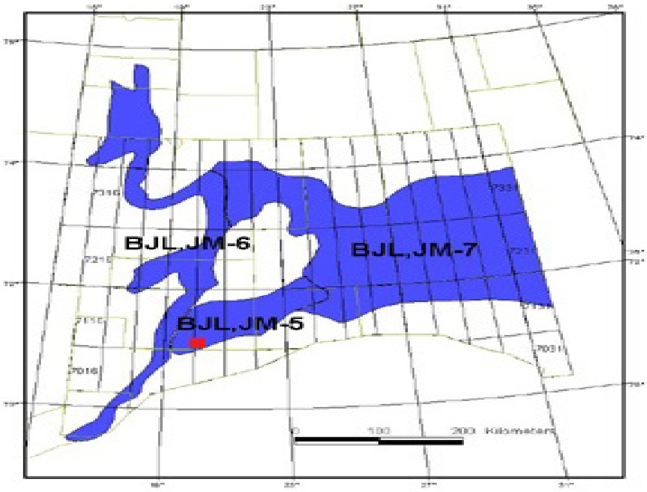
BJL,JM-6
BJL,JM-7
BJL,JM-5
7316
7215
7116
7016
7031
0 100 200 Kilometers

Figure 2.12 The distribution map of Lower to Middle Jurassic plays in Barents Sea. JM-5, JM-6, JM-7 and BJL are names of the plays. Study area is in red rectangle (modified from NPD (2013a)).

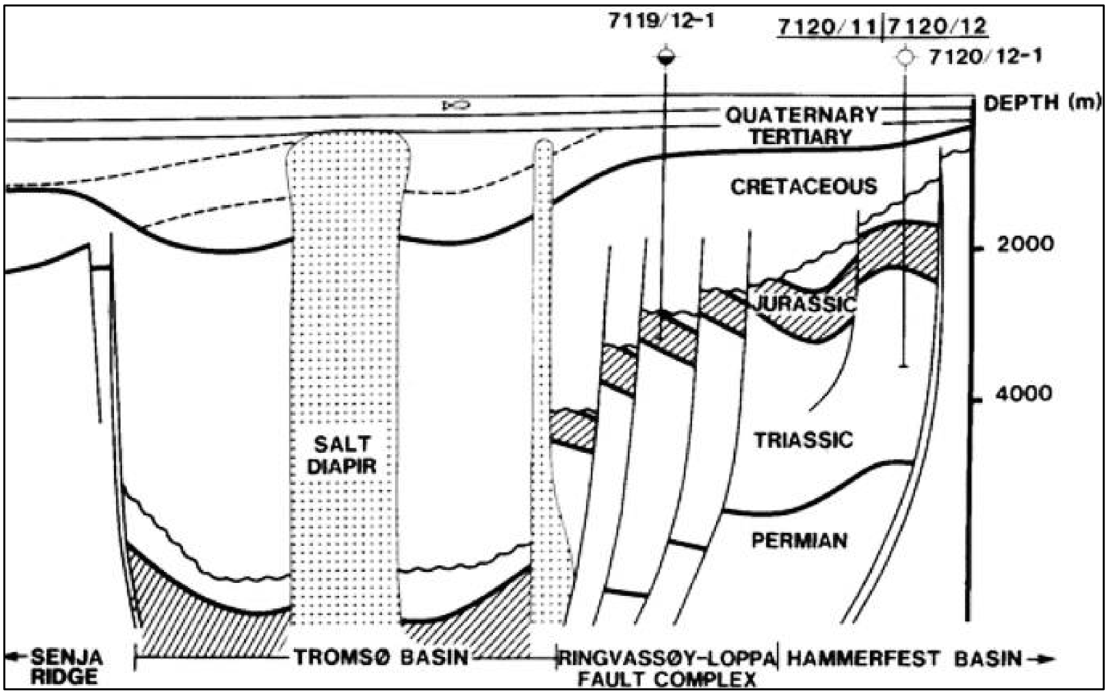
7119/12-1
7120/11
7120/12
7120/12-1
QUATERNARY
TERTIARY
DEPTH (m)
CRETACEOUS
2000
JURASSIC
4000
TRIASSIC
SALT DIAPIR
PERMIAN
SENJA RIDGE
TROMSØ BASIN
RINGVASSØY-LOPPA FAULT COMPLEX
HAMMERFEST BASIN

Figure 2.13 Structural cross section through well 7119/12-1 (modified from Olaussen et al. (1984)).

2.4.2.3 Lower Cretaceous

Lower Cretaceous wedges and mounds were ranked as secondary targets after the Jurassic structure closure (Figure 2.14).

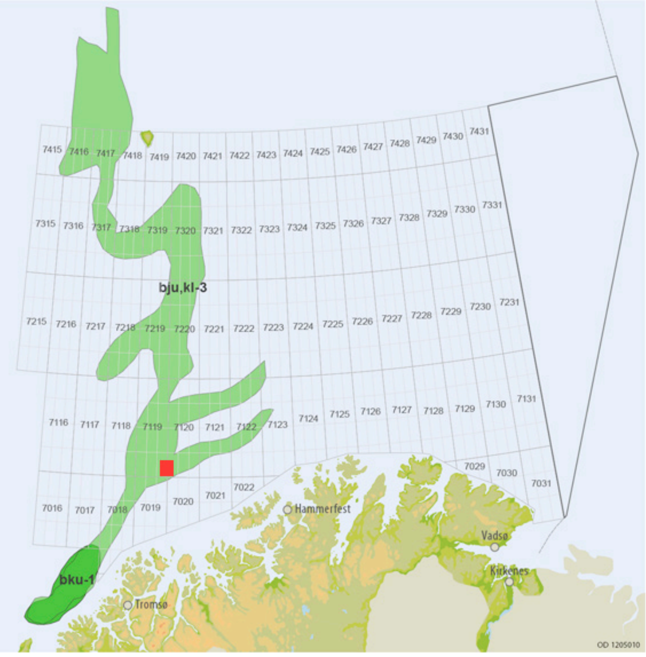
bju,kl-3
bku-1
Hammerfest
Tromsø
Vadsø
Kirkenes
OD 1205010

Figure 2.14 The distribution map of Upper Jurassic to Lower Cretaceous plays in Barents Sea (bju, bku-1 and kl-3 are names of the plays). Study area is in red rectangle (modified from NPD (2013b)).

2.4.3 Traps

The primary target in the study area is fault- bounded positive blocks, like horst structures and rotated fault blocks (Doré, 1995). The secondary target is stratigraphic trap, like submarine fan systems in Knurr Formation (Figure 2.15).

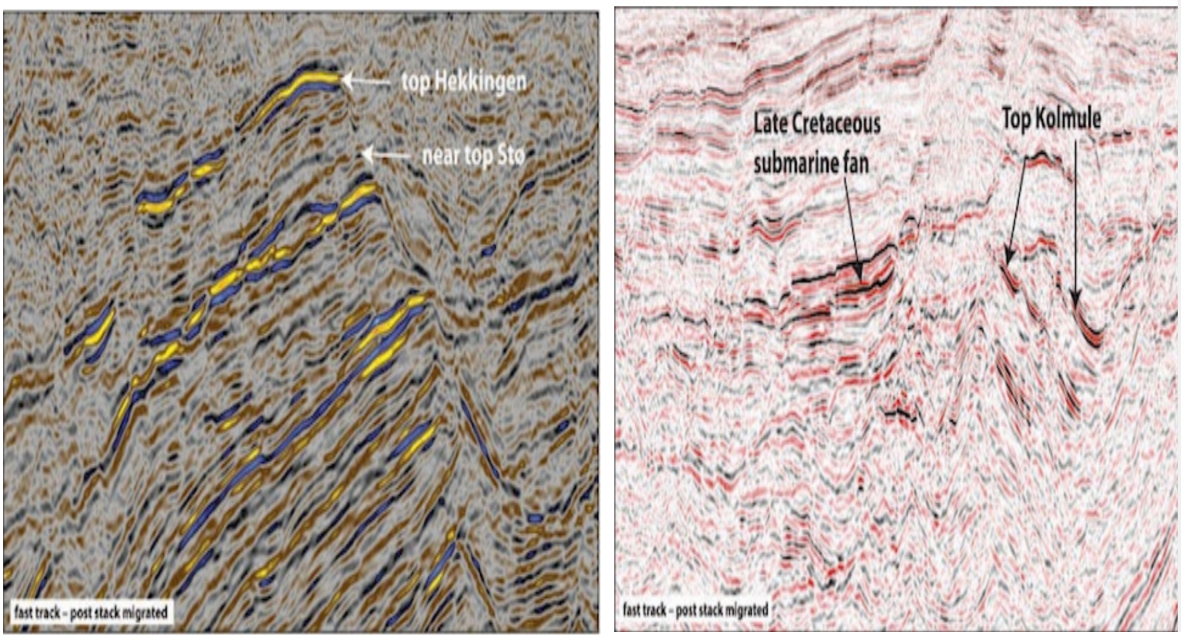
top Hekkingen
near top Stø
fast track - post stack migrated
Late Cretaceous submarine fan
Top Kolmule
fast track - post stack migrated

Figure 2.15 Barents Sea Jurassic play in a rotated fault block (left) and Cretaceous play in a submarine fan (right) (modified from Blaich and Ersdal (2011)).

2.5 Tectonic uplift

2.5.1 Effects of tectonic uplift on petroleum system

According to Ostanin et al. (2013b), uplift, tilting and rapid erosion could lead to:

- Gas expansion and oil-to-gas phase change.
- Hydrocarbon spill out.
- Seal failure.
- Suppression of hydrocarbon generation.
- Reactivation of faults.

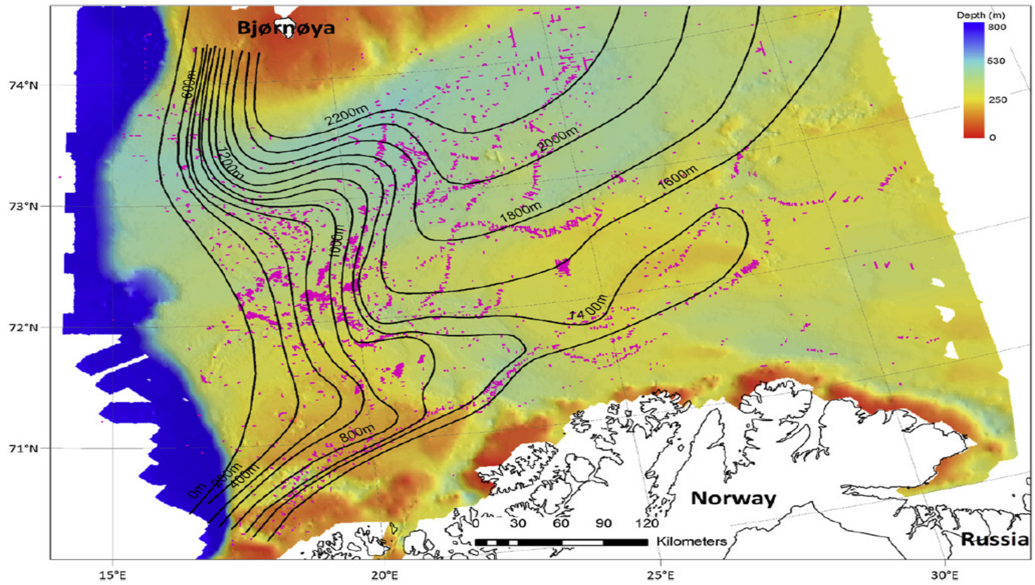

Figure 2.16 Uplift map of Barents Sea (black lines) with subsurface fluid flows (Pink points), (modified from Vadakkepuliyambatta et al. (2013)).

From Figure 2.16, Ringvassøy-Loppa Fault Complex is less uplifted than Hammerfest basin. The petroleum system in Ringvassøy-Loppa Fault Complex would be less affected by uplift effect than Hammerfest basin.

2.5.2 Uplift estimations

The method for uplift estimation includes: Maximum Temperature (T-max), Apatite Fission Track Analysis (AFTA), Vitrinite Reflectance (Ro), Sandstone Diagenesis, and Shale Compaction (Density or Sonic log) (Henriksen et al., 2011a). The method used here compares the Sonic log and porosity with published trends.

The porosity-depth models of Ramm and Bjørlykke (1994) can help to better understand the porosity-depth relationship of sediments during mechanical compaction.

$$\phi = A * e^{-(\alpha+(\beta * Cl)) * Z}$$

Where A, α and β are regression coefficients. Coefficient A is related to the initial porosity at zero burial depth. α is a framework grain stability factor. β is a factor describing the sensitivity towards increasing clay index (CI). Clay index is defined by the volume of clay relative to the total volume of stable framework grains. There is a close approximation for deep buried sandstones.

$$\phi = 45 * e^{-(0.23+(0.27 * Cl)) * Z}$$

Where $Cl > 0.1$ or $Z < 2.5$

$$\phi = 25 - 13 * (Z - 2.5)$$

Where $Cl < 0.1$ or $Z > 2.5$

In Figure 2.17, the porosity-depth trend above is compared with calculated average porosity of Knurr and Stø Formations in the wells available (Table 4.1 and Table 4.2). The big difference between the trend and calculated porosity is most likely caused by regional uplift. The depth differences are range from 1 to 2 Km. There is a clear break between the shallow 3 wells and deep 3 wells at about 2.2 Km depth below sea floor. Cementation and secondary porosity are commonly observed in the wells. Therefore, the porosity values vary complexly.

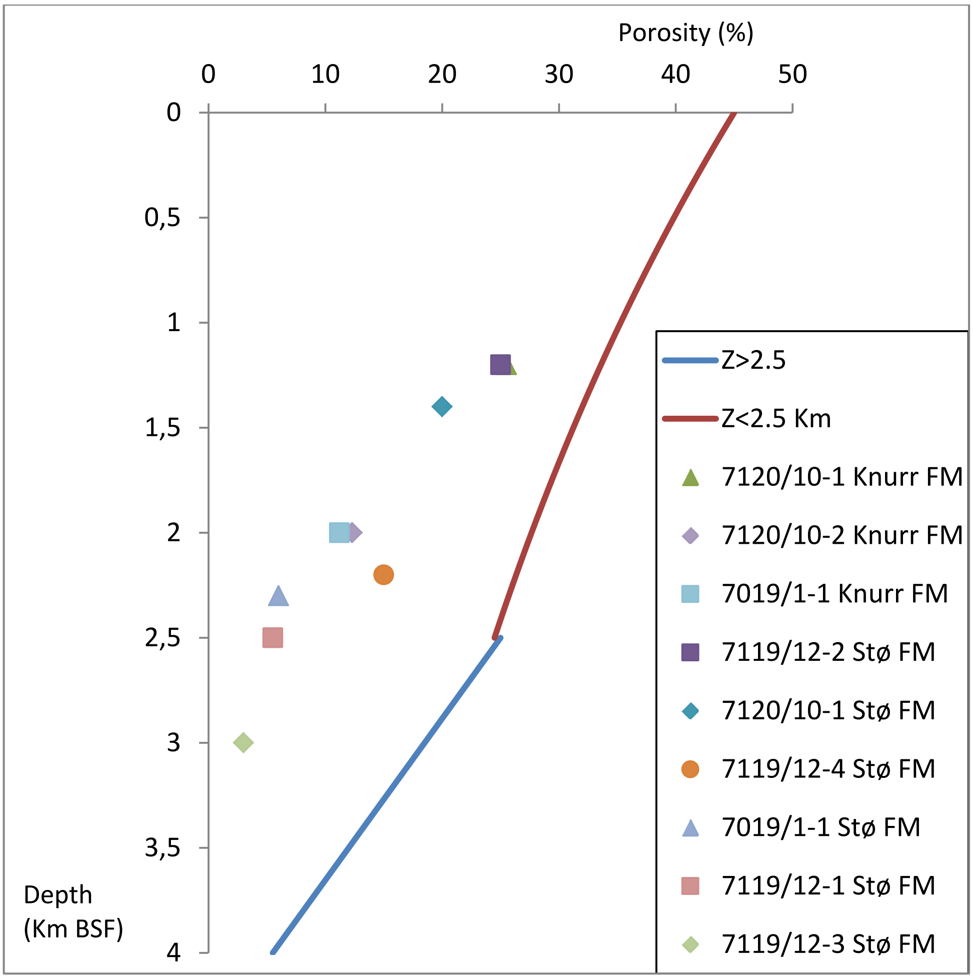

Figure 2.17 The comparison between calculated average porosity of reservoir sandstones and porosity- depth trend (Ramm and Bjørlykke, 1994).

The velocity-depth trend from Storvoll et al. (2005) was used to estimate the uplift and erosion:

$$Z = 1.76Vp - 2600$$

Where, Z = depth (meters) and Vp = velocity (meters per second).

A normal velocity-depth trend for marine Jurassic shale from Japsen (1999) is also used for a reference trend line:

$$tt = 465 * e^{-\frac{Z}{2435}} + 180$$

Where tt (transit time) =1/V (µm/s), and Z (meters) is depth below seabed.

The experimental compaction curve for kaolinite-silt (50:50) mixture suggested by Mondol (2009) is also very useful in uplift estimation (Figure 2.18). A comparison of uplift and erosion estimation of this study and data published by several authors is given in the Table 2.2.

Table 2.2 Uplift estimation and comparisons with published data.

Well name	7119/12-1	7119/12-2	7119/12-3	7119/12-4	7120/10-1	7119/10-2	7019/1-1
From this study	900	900	600	900	900	900	900
Henriksen et al. (2011a)	700	800	500	700	800	750	700
Ohm et al. (2008)	750	1050	500	750	1100	950	750
Storvoll et al. (2005)	900	N/A	N/A	N/A	N/A	N/A	N/A
Riis and Fjeldskaar (1992)	1500-2000	1500-2000	1500-2000	1500-2000	1500-2000	1500-2000	1500-2000
Nyland et al. (1992)	1000-1500	1000-1500	1000-1500	1000-1500	1000-1500	1000-1500	1000-1500
Reemst et al. (1994)	1200-1500	1200-1500	1200-1500	1200-1500	1200-1500	1200-1500	1200-1500
Rasmussen and Fjeldskaar (1996)	500-600	500-600	600-700	500-600	500-600	500-600	500-600
Doré and Jensen (1996)	750-1250	750-1250	750-1250	750-1250	750-1250	750-1250	750-1250
Dimakis et al. (1998)	750-1250	750-1250	750-1250	750-1250	750-1250	750-1250	750-1250

The reservoir quality is highly affected due to previously deeper buried sandstones and later uplift. Diagenesis in the wells with reservoir at 2600 m is comparable to diagenesis occurring at 3500-4000 m in the North Sea (Olaussen et al., 1984). The reservoir in the shallowest well 7119/12-2 have quartz grain pressue solution and quartz cementation at about 1400m (KB) and 46°C. According to Bjørlykke and Egeberg (1993), quartz cementation will start at about 70-80°C.If uplift is corrected, the corrected depth is around 2300 m (KB) and reservoir temperature is about 77°C.

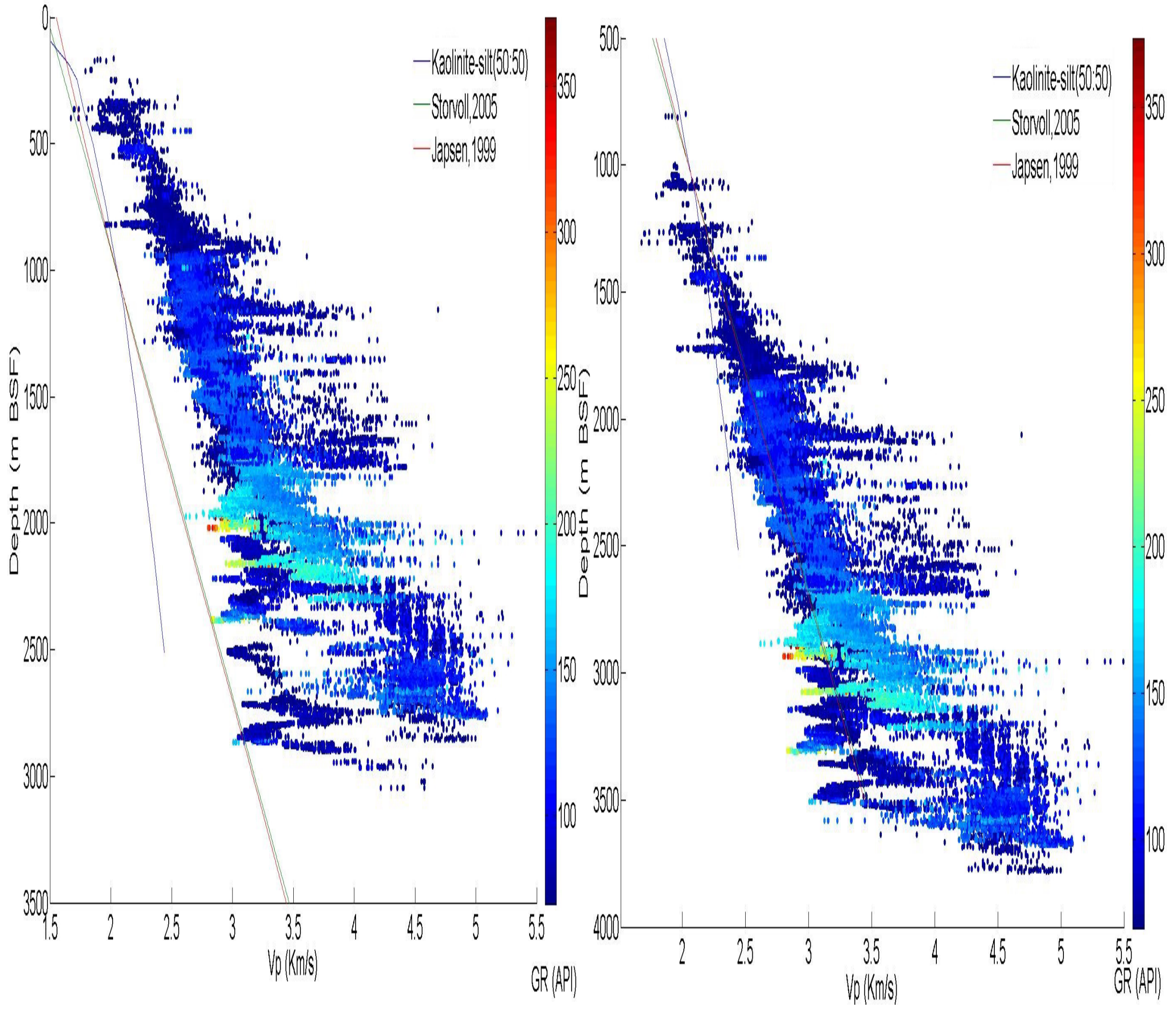

Figure 2.18 Velocity-depth cross plot of shales in all the wells before (left) and after correction (right)

2.6 Geothermal gradient estimation

Geothermal gradient plays an important role in hydrocarbon exploration for many reasons. The hydrocarbon generation is controlled by the thermal history of the source rock, and the reservoir quality is highly affected by the temperature-related diagenetic processes. Temperature also affects the resistivity measured in well logs. The temperature, with and without uplift correction at the top of the reservoir zones are estimated and given in Table 2.3. If there are two measured temperatures available in each well, the geothermal gradient can be calculated using the following formula:

$$G = \frac{T2 - T1}{Dep2 - Dep1}$$

Where G is the geothermal gradient in °C/Km, T1 and T2 are measured temperature in °C. Dep1 and Dep2 are the measured depths in Km.

Table 2.3 Geothermal gradient estimation of all 7 wells.

Well Name	Bottom Temperature (°C)	Total Depth (m_KB)	Water Depth	Geothermal Gradient (°C/Km)	Upliftment estimation	Formation	Top (m_KB)	Corrected top depth	Bottom (m_KB)	Thickness (m)	Reservoir top temperature (°C)	Corrected Reservoir top temperature (°C)
7119_12-2	62.00	1902.00	180.00	33.68	900.00	Knurr Fm	1087.00	1987.00	1163.00	76.00	36.61	66.93
						STØ FM	1372.00	2272.00	1517.00	145.00	46.21	76.52
7120_10-1	71.00	2000.00	183.00	36.87	900.00	Knurr Fm	1353.00	2253.00	1394.00	41.00	49.89	83.08
						STØ FM	1568.00	2468.00	1655.00	87.00	57.82	91.00
7120_10-2	63.00	2500.00	186.00	25.50	900.00	Knurr Fm	1922.00	2822.00	2303.00	381.00	49.01	71.95
7019_12-4	105.00	2917.00	192.00	37.06	900.00	Knurr Fm	1955.00	2855.00	2058.00	103.00	72.46	105.82
						STØ FM	2296.00	3196.00	2448.00	152.00	85.10	118.44
7019_1-1	108.00	3003.00	190.00	36.97	900.00	Knurr Fm	2127.00	3027.00	2345.00	218.00	78.64	111.91
						STØ FM	2447.00	3347.00	2610.00	163.00	90.47	123.74
7119_12-1	96.00	3088.00	200.00	31.86	900.00	Knurr Fm	2441.00	3341.00	2497.00	56.00	77.76	106.43
						STØ FM	2658.00	3558.00	3088.00	430.00	84.67	113.36
7119_12-3	136.00	3314.00	211.00	42.54	600.00	Knurr Fm	2953.00	3553.00	3026.00	73.00	125.62	151.14
						STØ FM	3144.00	3744.00	3299.00	155.00	133.74	159.27

Note that the total depth and bottom hole temperature data used in this calculation are taken from the NPD website. The water depths of all studied wells are around 200 m. The water temperatures on the sea floor for all the wells are considered to be 4°C.

Chapter 3 Research methodologies and theoretical background

3.1 Work flow

The research focuses on imaging reservoir quality by employing several techniques such as petrophysical analyses, rock physics diagnostics and AVO modelling of two reservoir horizons. The petrophysical analyses and rock physics diagnostics have been carried out by Interactive Petrophysics (IP) software and Microsoft Excel, while the AVO modelling is performed by the Hampson Russell software packages. As mentioned earlier the basic input to the petrophysical analyses, rock physics diagnostics and AVO modelling are the well log data. Shale volume, net-to-gross, porosity and water saturation are calculated using equations. Analysis of reservoir rock properties performed using standard rock physics templates. Finally, AVO modelling is carried out by generating synthetic seismic to investigate change in rock properties in response to changes in saturation in pore fluids. A flow diagram (Figure 3.1) describing the whole work flow of the thesis is given below:

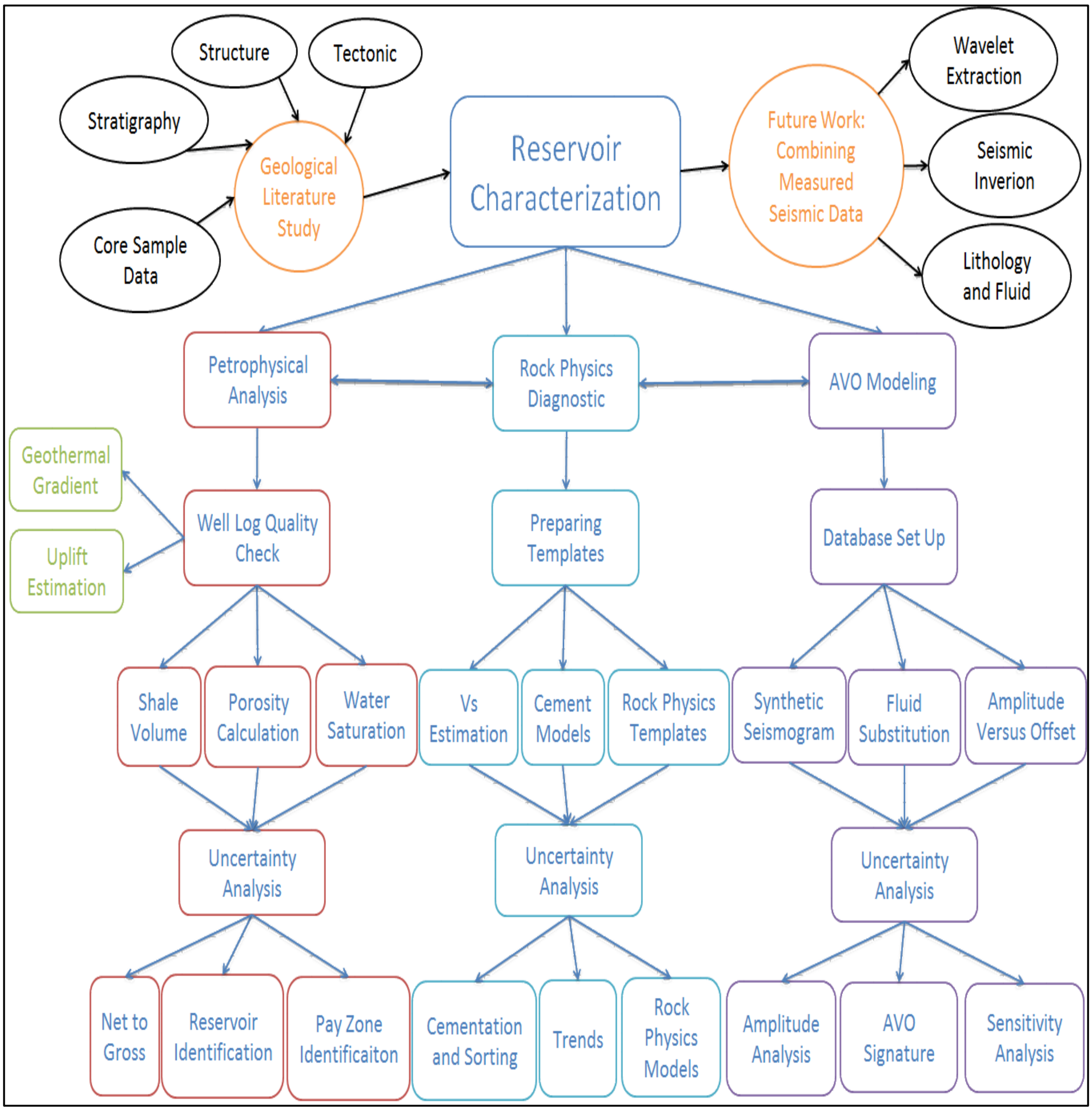
Structure
Tectonic
Stratigraphy
Geological Literature Study
Core Sample Data
Reservoir Characterization
Future Work: Combining Measured Seismic Data
Wavelet Extraction
Seismic Inverion
Lithology and Fluid
Petrophysical Analysis
Rock Physics Diagnostic
AVO Modeling
Geothermal Gradient
Uplift Estimation
Well Log Quality Check
Preparing Templates
Database Set Up
Shale Volume
Porosity Calculation
Water Saturation
Vs Estimation
Cement Models
Rock Physics Templates
Synthetic Seismogram
Fluid Substitution
Amplitude Versus Offset
Uncertainty Analysis
Uncertainty Analysis
Uncertainty Analysis
Net to Gross
Reservoir Identification
Pay Zone Identificaiton
Cementation and Sorting
Trends
Rock Physics Models
Amplitude Analysis
AVO Signature
Sensitivity Analysis

Figure 3.1 Flow chart describing the steps involved in the study.

3.2 Petrophysical analysis

The main purpose of petrophysical analysis is to evaluate reservoir parameters like shale volume (Vsh), net-to-gross ratio (N/G), porosity (Φ) and water saturation (Sw). The most common well log data are Gamma Ray (GR), Spontaneous Potential (SP), Caliper (CALI), Shallow Resistivity (Rs), Medium Resistivity (Rm), Deep Resistivity (Rd), Neutron Porosity (NPHI), Density (RHOB) and Sonic (DT) log. Each of these measurements has its special merit and demerit. Overall, these 9 log data can be divided into 3 groups in interpretation phase. The first group (GR, SP, and Cali) is used mainly for Vsh and N/G calculation. The second group (Rs, Rm and Rd) is used for reservoir fluid identification and water saturation calculation. The third group (NPHI, RHOB and DT) is used for porosity calculation (Figure 3.2).

Due to the complex geology, information from a single measurement could be ambiguous. In most cases, all logs are studied together to reduce risk and uncertainties and to improve understanding. Core data, cutting samples and gas-chromatographic analyses are also very helpful for more accurate interpretation. New logging techniques like Nuclear Magnetic Resonance, Gamma Spectrometry Log and Photoelectric Log give us additional confidence to interpret the data. Therefore, numerous kinds of logging tools are developed nearly every year to fulfill the increasing need for reservoir parameter evaluation.

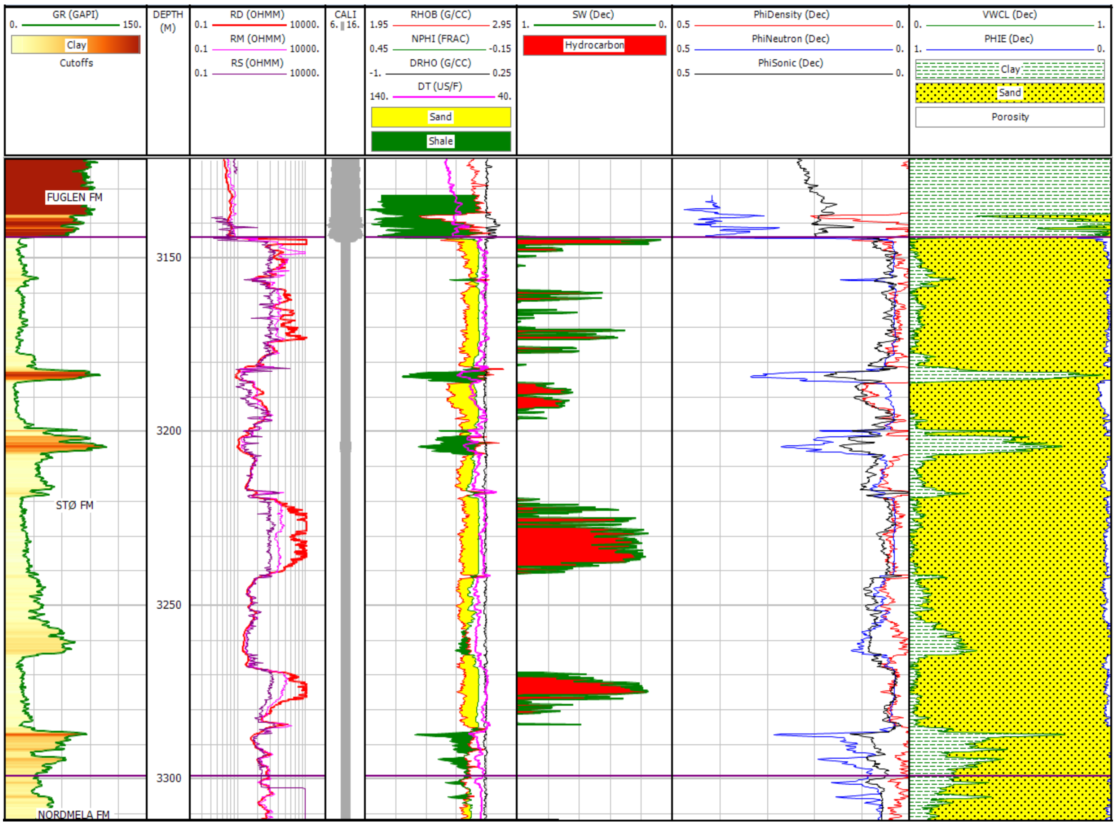

Figure 3.2 Composite log plot of well 7119/12-3.

3.2.1 Lithology discrimination and net-to-gross estimation

The term of 'lithology discrimination' here refers to classification of sedimentary rocks. The most common lithologies include sandstone, shaly sandstone, shale, limestone, dolomite, gypsum, salt, anhydrite and so on. In sandstone-shale sequence, the lithology discrimination is relatively simple. The most common method is to use Gamma Ray or SP log to identify the sandstone and calculate shale volume. In fact, all the other logs also show difference between sandstone and shale, like the crossover of Density and Neutron logs (Figure 3.3).

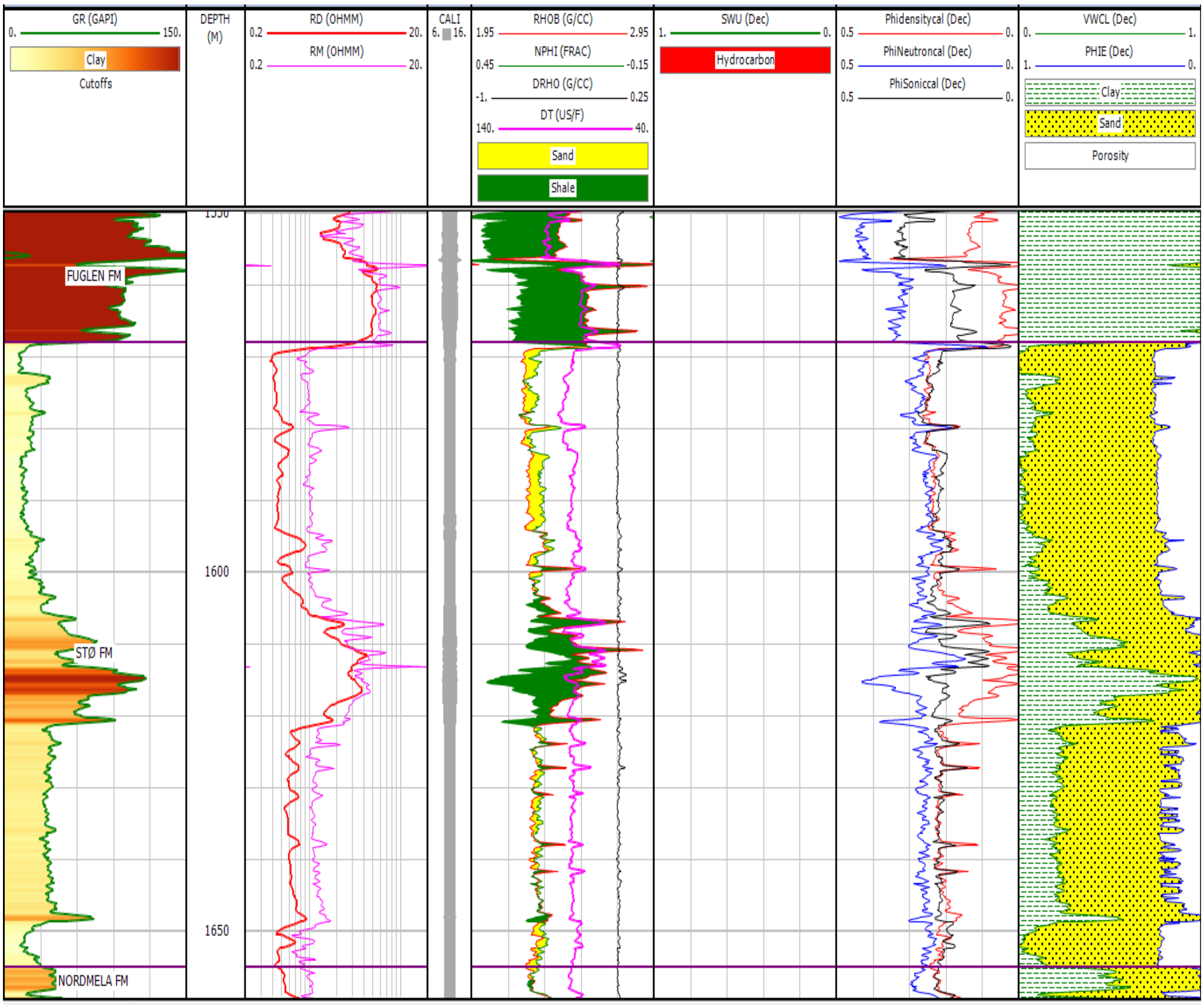

Figure 3.3 Composite log plot for Stø Formation in 7120/10-1. Notice the high Neutron porosity values of the whole section due to logging equipment error.

In a sandstone-shale-limestone scenario, using only GR or SP is not enough to discriminate the lithology. Especially when dolomite, gypsum, salt, and anhydrite are also contained in the profile, the lithology discrimination is much more complex. With the help of outcrops, cutting samples, sidewall-coring samples and core samples, we can get a quantitative idea of the mineral contents. The available petrophysical methods like Density-Neutron cross plot, M-N plot and MID plot (mineral-identification-plot) can help us to discriminate complex lithologies (Ellis and Singer, 2007).

Net reservoir interval is characterized by good reservoir quality, like high porosity and low Vsh. Gross interval is a whole sedimentary package including all reservoir zones and non-reservoir zones. Pay zones always contain commercially producible hydrocarbon, which can be quantified by petrophysical calculation. The cutoff value for reservoir zone from NPD website are: $\Phi<0.01$, $Vsh>0.40$ and $Sw>0.65$.

3.2.2 Shale volume calculation

The shale volume calculation in sandstone is important for several reasons (Ellis and Singer, 2007):

- Clays in rock affect almost all of the well log readings.
- The clay content could affect the calculated porosity and water saturation. Archie's equation is not capable for Sw calculation in shaly sandstons.
- Permeability could be reduced by even little amount of clay in the reservoir. Although permeability is not calculated in this study, it is a very important parameter for reservoir quality estimation.
- Shales can reduce net pay significantly.

The most commonly used method for Vsh determination is using Gamma Ray log. The radioactive elements (U, K and Th) are concentrated in clay minerals. Because clay minerals have large cation exchange capacities, radioactive minerals are absorbed in trace amounts from their parent igneous micas and feldspars. The combination of Density and Neutron log should be used if the formation contains organic rich materials or potassium rich minerals (e.g. mica and K-feldspar).

Shale volume is calculated in the following way: First, the Gamma Ray index (I_{GR}) is calculated from the gamma ray log data using the relationship:

$$I_{GR} = \frac{GR_{log} - GR_{min}}{GR_{max} - GR_{min}}$$

where: I_{GR} = the gamma ray index,

GR_{log} = the gamma ray reading at the depth of interest,

GR_{min} = the minimum gamma ray reading (Usually the mean minimum through a clean

sandstone or carbonate formation) ,

GR_{max} = the maximum gamma ray reading (Usually the mean maximum through a shale or

clay formation) .

There are several non-linear relationships between Gamma Ray index (IGR) and shale volume (Vsh):

Larionov (1969) for Tertiary rocks:

$$\mathrm{Vsh} = 0.083(2^{3.7\cdot \mathrm{IGR}} - 1)$$

Larionov (1969) for older rock:

$$\mathrm{Vsh} = 0.33(2^{2.0\cdot \mathrm{IGR}} - 1)$$

Stieber (1970):

$$\mathrm{Vsh} = \frac{\mathrm{I_{GR}}}{3 - 2\mathrm{I_{GR}}}$$

Clavier (1971):

$$\mathrm{Vsh} = 1.7 - \sqrt{3.38 - (\mathrm{I_{GR}} + 0.7)^2}$$

The gamma ray log measures radioactivity instead of grain size. Thus, the relationship between gamma ray log and shale content is quite empirical and need to be correlated to other data.

GR boundary lines need to be set before using GR Index method for shale volume calculation. In most of the wells in this study, the GR minimum values for the sandstones are around 15 to 25 API. For shale, the maximum values are around 100-120 API (Table 3.1). The GR values in well 7019/1-1 are obviously higher than in other wells. In sandstone zones, GR ranges from 45 to 80 API. The GR values of shales are also much higher than that in the other wells. The most possible reason for this phenomenon is that different logging equipment is used for this well. Despite the abnormal high values in this well, GR could still be used for lithology discrimination, shale volume calculation and N/G estimation (Figure 3.4).

Table 3.1 Gamma Ray baseline values for all 7 wells.

Well number	Formation	GR minimum value (API)	GR maximum value (API)
7120/10-1	Knurr Fm	15	120
	Stø Fm	15	120
7120/10-2	Knurr Fm	20	135
7119/12-1	Knurr Fm	15	120
	Stø Fm	15	120
7119/12-2	Knurr Fm	15	120
	Stø Fm	15	100
7119/12-3	Knurr Fm	15	100
	Stø Fm	15	105
7119/12-4	Knurr Fm	25	165
	Stø Fm	25	150
7019/1-1	Knurr Fm	70	175
	Stø Fm	45	185

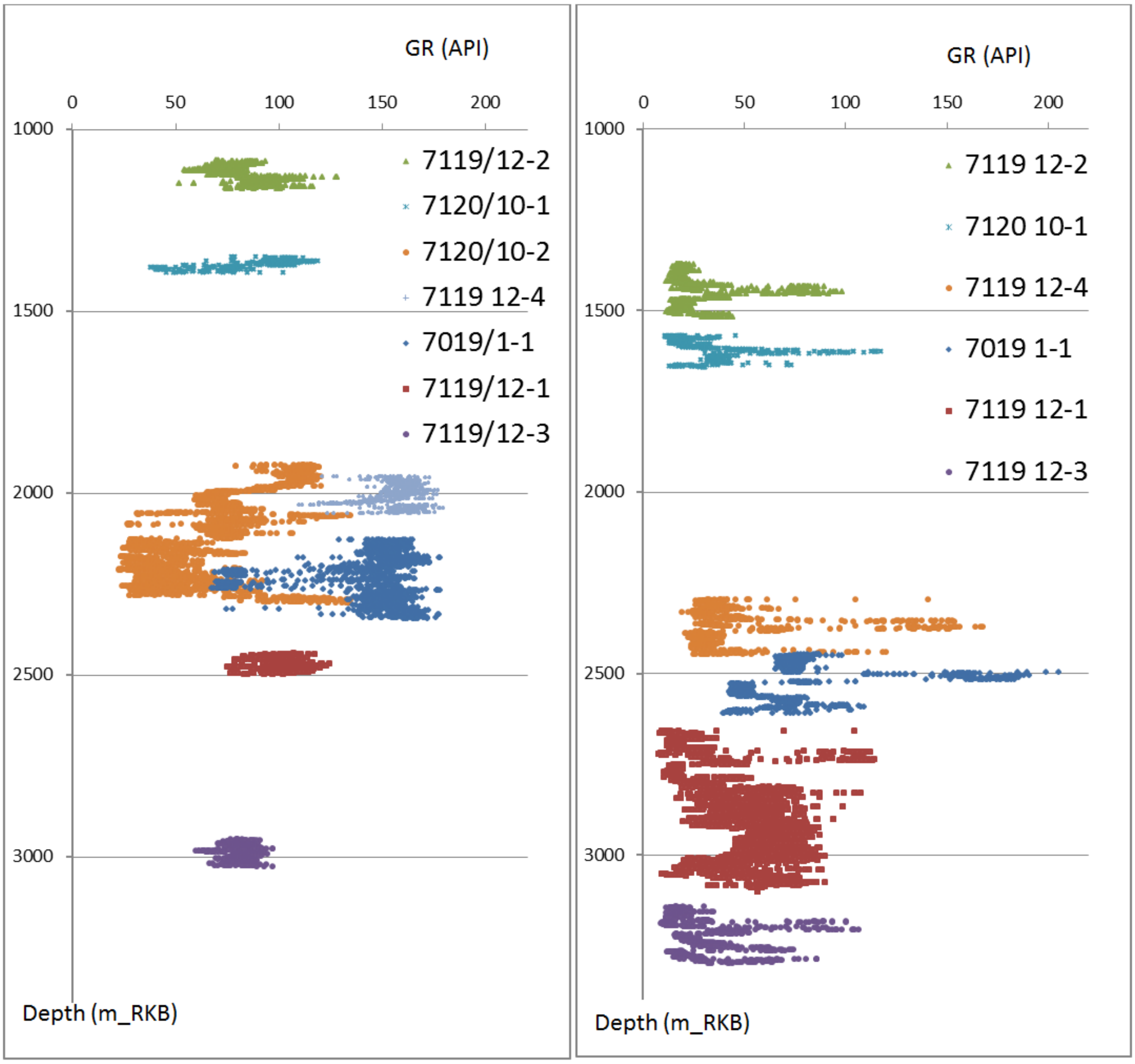

Figure 3.4 The Depth - GR plot of both Knurr Formation (left) and Stø Formation (right) in all wells, the reservoir is shallowest in 7119/12-2, and deepest in 7119/12-3.

Sometimes clay volume and shale volume means the same thing in petrophysical analysis, because they are hard to be distinguished in certain petrophysical methods. Petrophysical analysis always deals with minerals instead of particle size. Ellis and Singer (2007) mentioned that shale contains clay minerals and silt (mostly quartz and feldspar). Silt has more similar properties with sand than clay minerals, but the silt content is hard to be determined by logs. The proportion between clay mineral content and shale content can be represented by clay/shale ratio. The clay/shale ratio can vary from about 0.5 to nearly 1.0. Here in this study, clay/shale ratio is set to be 0.7.

The widely accepted method is to calculate clay volume from all the method available at certain depth. Then the minimum clay volume from all the methods will be defined as the wet clay volume for the calculated depth. The available methods include single curve method (GR, Neutron, Resistivity and SP) and double curve method (Density-Neutron, Density-Sonic and Sonic-Neutron).

3.2.3 Porosity calculation

Porosity is the fraction of space volume to total rock volume (Glover, 2011). The most useful well logs for porosity calculation are Sonic, Density and Neutron logs (Figure 3.5).

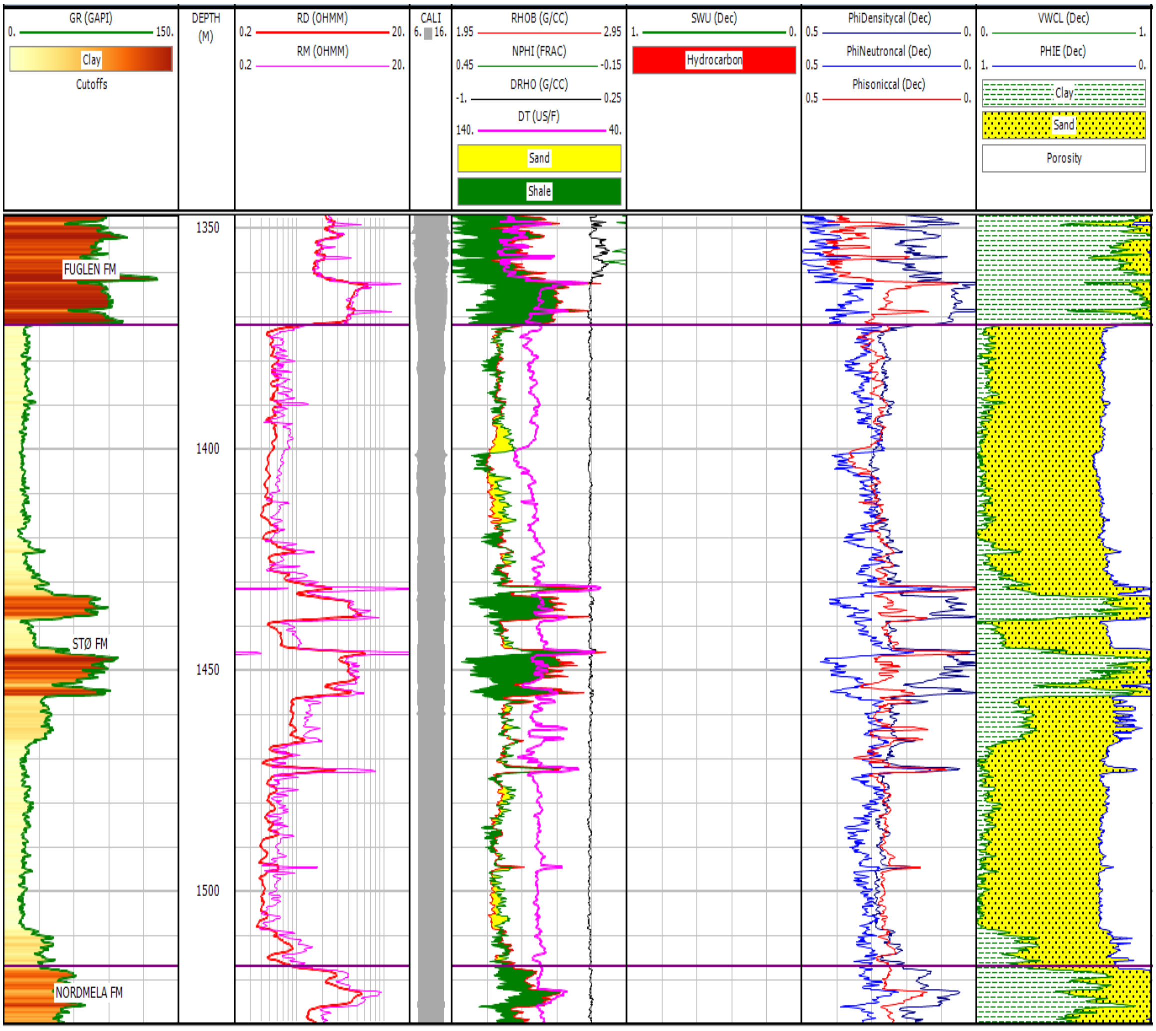

Figure 3.5 Composite log plot of Stø Formation in well 7119/12-2. Notice the high Neutron porosity values of the whole section due to logging equipment error.

3.2.3.1 Sonic porosity

The sonic log measures interval transit time (Δt) of a P-wave signal. There are two equations for the calculation of sonic porosity:

Wyllie Time-average equation:

$$\Phi s = \frac{\Delta t - \Delta t_{ma}}{(\Delta t_{fl} - \Delta t_{ma}) \cdot Cp}$$

Raymer-Hunt-Gardner equation:

$$\Phi s = \frac{5}{8} \cdot (\frac{\Delta t - \Delta t_{ma}}{\Delta t})$$

Where: Φs = calculated sonic porosity,

Δt = the sonic log reading at the depth of interest,

Δt_{ma} = the sonic log reading of rock matrix,

Δt_{fl} = the sonic log reading for formation fluid,

Cp = compaction factor, $\mathrm{Cp} = \frac{\Delta t_{\mathrm{shale}}}{100}$.

Evidence shows that sonic log only responses to primary porosity, because the acoustic signal circumvents any secondary porosity (e.g. fracture or vuggy porosity) (Merkel, 1979). In gas bearing formations, the calculated sonic porosity is higher than water bearing zone (Asquith et al., 2004).

3.2.3.2 Density porosity

Density log measures the bulk density of the rock. Density porosity can be calculated by the following equation:

$$\Phi_{\mathrm{d}} = \frac{(\rho_{\mathrm{ma}} - \rho_{\mathrm{b}})}{(\rho_{\mathrm{ma}} - \rho_{\mathrm{fl}})}$$

Where: Φ_d = calculated density porosity,

ρ_{ma} = the Density log reading of rock matrix,

ρ_{fl} = the Density log reading for formation fluid,

ρ_b = the Density log reading at the depth of interest.

In case of complex lithology and hydrocarbon effect, the density of matrix and fluid should be chosen correctly. The presence of gas causes density porosity to be higher than true porosity. The “cross-over” between Density and Neutron porosity can be gas bearing indicator.

3.2.3.3 Neutron porosity

Neutron log measures the Hydrogen Index of the rock and is calibrated into limestone porosity. Neutron–Density cross plot is the most common technique for lithology discrimination and gas identification. Neutron and Density logs are always plotted in the same track in a log plot. In most of the situations, these two logs are displayed on a limestone matrix. That is 1.95 to 2.95 g/cm^3 for the Density log and 0.45 to −0.15 for the Neutron log. In limestone intervals, these two log curves will overlay each other. In sandstone interval, these two logs shows several units mismatch. Gas effect will strengthen this kind of effect. Shale intervals would have the opposite cross-over compared to sandstone intervals (Bradley, 1987).

There is an empirical relationship between Neutron sandstone porosity (Φns) and Neutron limestone porosity directly from log (NPHI):

$$\Phi\mathrm{ns} = \mathrm{NPHI} + 0.03$$

In a known sandstone reservoir, the Density log can be scaled from 1.65 to 2.65 g/cm^3, and the Neutron log is from 0.6 to 0 porosity. These values indicate that the logs are displayed on a sandstone matrix. These two curves will overlay each other in sandstone intervals (Bradley, 1987).

3.2.3.4 Density-Neutron average porosity

As described by Bassiouni (1994), before the lithology is clearly understood, Density-Neutron average porosity can be used to estimate the porosity that is largely free of lithology effects. Both Density and Neutron porosity values should be scaled into limestone porosity, because calcite has properties that are intermediate between dolomite and quartz. After the averaging, the effects of dolomite and quartz tend to cancel out.

$$\Phi\mathrm{nd} = \frac{\Phi\mathrm{d} + \Phi\mathrm{n}}{2}$$

In gas-bearing zone, low Hydrogen content of gas leads to low Neutron reading. This phenomena is also called “excavation effect”. In Density log, the presence of gas reduces bulk density, resulting in a high apparent porosity (Bassiouni, 1994). The square-root averaging equation can be used to estimate the true porosity of gas- bearing zone:

$$\Phi\mathrm{nd} = \sqrt[2]{\frac{\Phi\mathrm{d}^2 + \Phi\mathrm{n}^2}{2}}$$

3.2.3.5 Neutron-Density cross plot

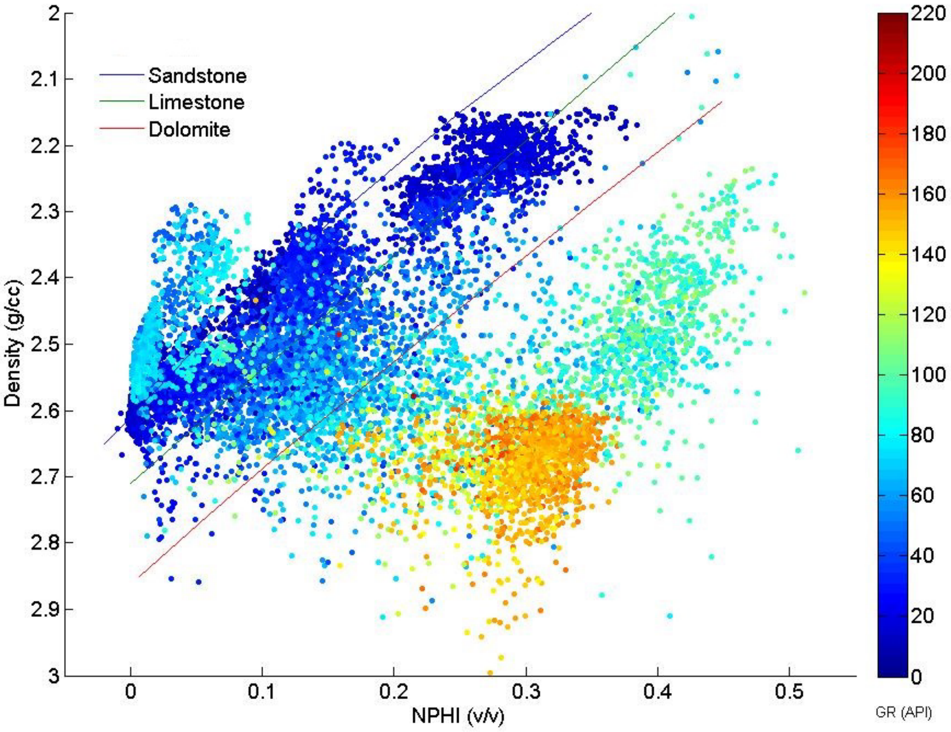

Figure 3.6 Density-NPHI cross plot (colour coded by GR) of all the Knurr and Stø Formations data from 7 studied wells.

The Neutron-Density cross plot (Figure 3.6) is a useful tool to identify the porosity and proportions of two minerals if the mineralogy is known. Pure sandstones are located on or near the sandstone line. Shale data points are far away from the sandstone line. If the sandstone log values are not falling on the sandstone line, the reason could be borehole effects, carbonate cements, high shale volume, gas effects and statistical fluctuations. In this study, the data points outside the sandstone line are caused by gas effect.

3.2.3.6 Total porosity and effective porosity

The porosity calculated in this study is the total porosity and effective porosity derived from Density log and Neutron log. The difference between total porosity and effective porosity is clay bound water. Effective porosity is the porosity that is connected to one another. Therefore, the effective porosity is used for calculating the reserve and production in petrophysical analysis. As related to rock physics, it is the total porosity that affects the stiffness of the rock. In Gassman's fluid substitution equation, it assumes that the total porosity is saturated by pore fluids.

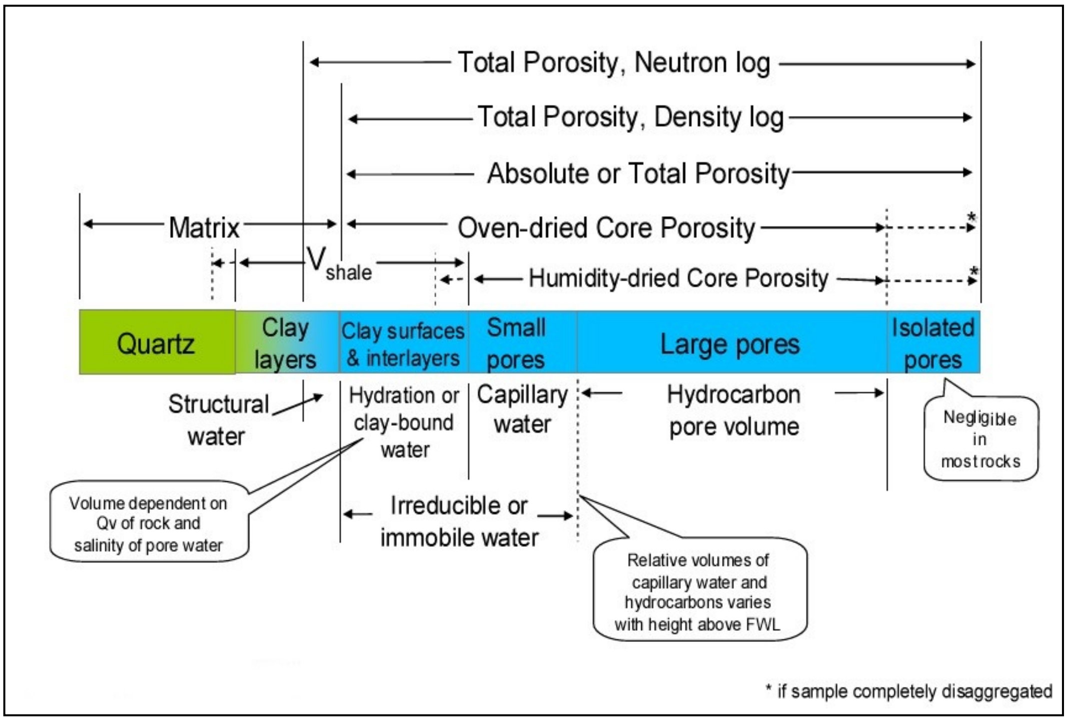
Total Porosity, Neutron log
Total Porosity, Density log
Absolute or Total Porosity
Matrix
Oven-dried Core Porosity
*
V shale
Humidity-dried Core Porosity
*
Quartz
Clay layers
Clay surfaces & interlayers
Small pores
Large pores
Isolated pores
Structural water
Hydration or clay-bound water
Capillary water
Hydrocarbon pore volume
Negligible in most rocks
Volume dependent on Qv of rock and salinity of pore water
Irreducible or immobile water
Relative volumes of capillary water and hydrocarbons varies with height above FWL
* if sample completely disaggregated

Figure 3.7 Components of the gross rock (bulk), individual components are not to scale (Eslinger and Pevear, 1988).

As shown in the Figure 3.7, Neutron porosity is larger than density porosity when the shale volume is high in the rock. Density porosity is close to laboratory measured total porosity (over-dried core porosity). In this study, the total porosity values for shale are given manually, because the shale porosity is hard to calculate without knowing clay mineral type, content and matrix parameters.

3.2.4 Water saturation and pay zone identification

Resistivity values are the major indicator for hydrocarbon in petrophysical methods (Figure 3.8). Archie's law can be used to calculate water saturation in sandstone and carbonate reservoirs in which the clay-mineral content is low (Bradley, 1987).

$$Sw = \sqrt[n]{\frac{a \cdot Rw}{Rt \cdot \Phi^{m}}}$$

Where, Sw = water saturation,

Φ = porosity,

Rw = formation water resistivity,

Rt = observed bulk resistivity,

a = tortuosity factor, varies around 1,

m = cementation exponent, varies around 2,

n = saturation exponent, generally 2.

In shaly rocks, the formation water is not the only electrically conductive medium. Clay minerals also contribute in conduction. Therefore, more complicated electrical models and equations should be used to estimate water saturation for shaly reservoirs.

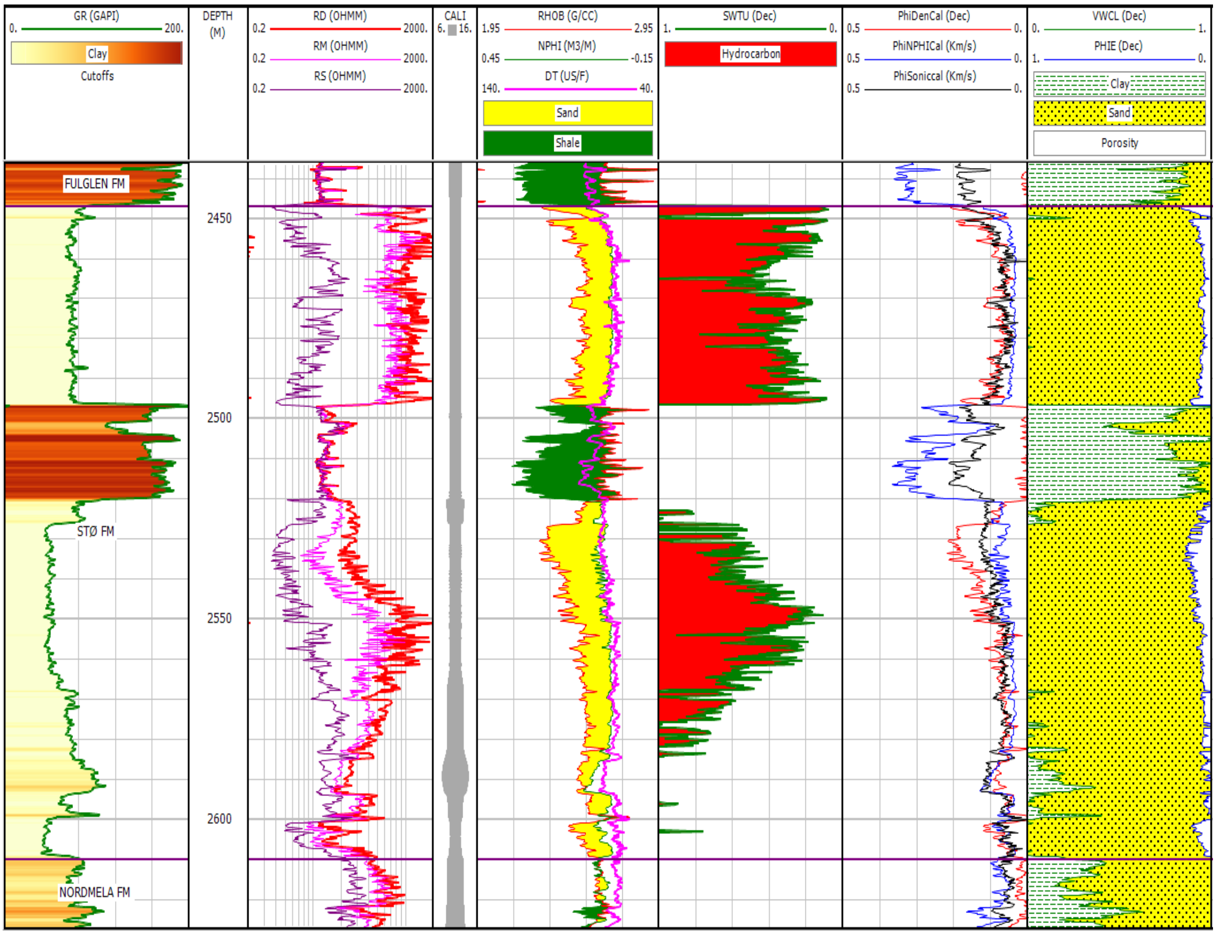

Figure 3.8 Composite log plot of Stø Formation in well 7019/1-1.

According to Bassiouni (1994), the rock resistivity is influenced by:

- Shale volume
- Porosity
- Water saturation
- Formation water resistivity (influenced by salinity, salt composition and temperature)
- Metallic mineral, like pyrite

Therefore, the formation water resistivity (Rw) is important for calculating water saturation. Usually Rw and temperature data should be provided by logging company. For example, it is always documented on the log headers. In this study, Rw is not known. Estimating Rw from SP is an acceptable method. Unfortunately, SP is not measured in wells included in this study. The method used here is Rwa (apparent Rw) method and resistivity-porosity cross plot method (Pickett Plot).

3.2.5 Determination of Rw

3.2.5.1 Rwa method

According to Archie's equation, apparent water saturation in the water zone can be defined as:

$$\mathrm{Rwa} = \mathrm{Rt} \cdot \Phi^{\mathrm{m}}$$

3.2.5.2 Resistivity-porosity cross plot method

$$\mathrm{Log(Rt)} = -\mathrm{mlog}(\Phi) + \log(\mathrm{aRw}) - \mathrm{nlog}\,(\mathrm{Sw})$$

For water zone, Sw=1,

$$\mathrm{Log(Rt)} = -\mathrm{mlog}(\Phi) + \log(\mathrm{aRw})$$

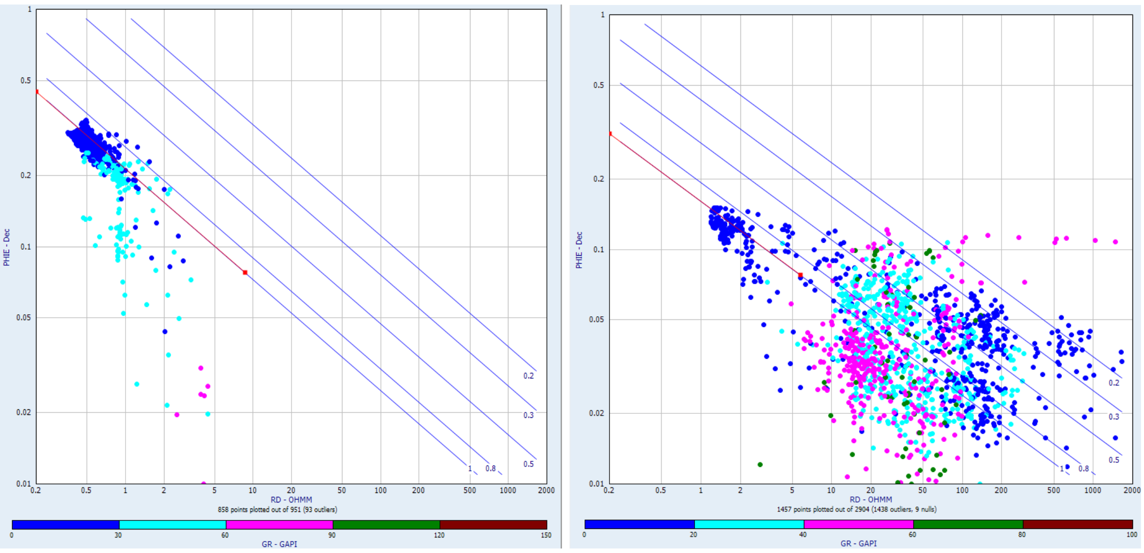

Figure 3.9 Pickett plot of Stø Formation in well 7119/12-2 (left) and 7119/12-1 (right), coloured by GR.

The Pickett plot is the logarithm cross plot between deep resistivity and effective porosity (Figure 3.9). This technique provides a, m, Rw and Sw values for input into the Archie's equation.

3.2.6 Determination of Rmf and Sxo

In the flushed zone, the movable formation fluid is replaced by drilling fluid, like mud filtrate. So, saturation of flushed zone can be calculated by the following equation:

$$\mathrm{Sxo} = \sqrt[n]{\frac{a \cdot \mathrm{Rmf}}{\mathrm{Rxo} \cdot \Phi^{m}}}$$

where, Sxo = the saturation of the flushed zone.

Rmf = the resistivity of mud filtrate.

Rxo = the resistivity of flushed zone.

If Sxo is much larger than Sw, the hydrocarbons in the flushed zone have then already been flushed by drilling fluid. In this study, the drilling mud is seawater-based with materials like barite and bentonite are added. The salty water mud has a low resistivity and the value is similar to formation water resistivity. The shallow Resistivity or MFSL log is used for flushed zone resistivity (Rxo).

3.3 Rock physics diagnostics

Rock Physics provides the connections between seismic response and rock properties like mineralogy, clay content, porosity, pore shapes, pore fluids, pore pressures, and overall architecture such as laminations and fractures (Avseth et al., 2010). Rock physics models can help to quantitatively interpret the relationship between seismic data and reservoir properties. (Avseth et al., 2005)

Rock physics diagnostic uses cross plots between the rock elastic properties (e.g. velocity, impedance and moduli) and its packing (e.g. porosity). If the data points fall close to a theoretical model line, then the textural properties of the rock are those incorporated in the theoretical effective medium model (Avseth et al., 2000). The primary goal of rock physics diagnostics is to yield robust, field-specific, effective medium models.

3.3.1 The rock physics cement models

As described by Avseth et al. (2000), reservoir sandstones can be divide into three groups: friable sands, sparsely distributed quartz cemented sands and cemented sands of cement distributed on grain contact. The velocity-porosity relationships of three sands can be explained by 3 theoretical models: Friable sand, contact cement model and constant cement model (Figure 3.10). These cement models used in this study are digitized from several published papers (Avseth, 2010; Avseth et al., 2000; Avseth et al., 2009; Avseth et al., 2005; Avseth et al., 2010).

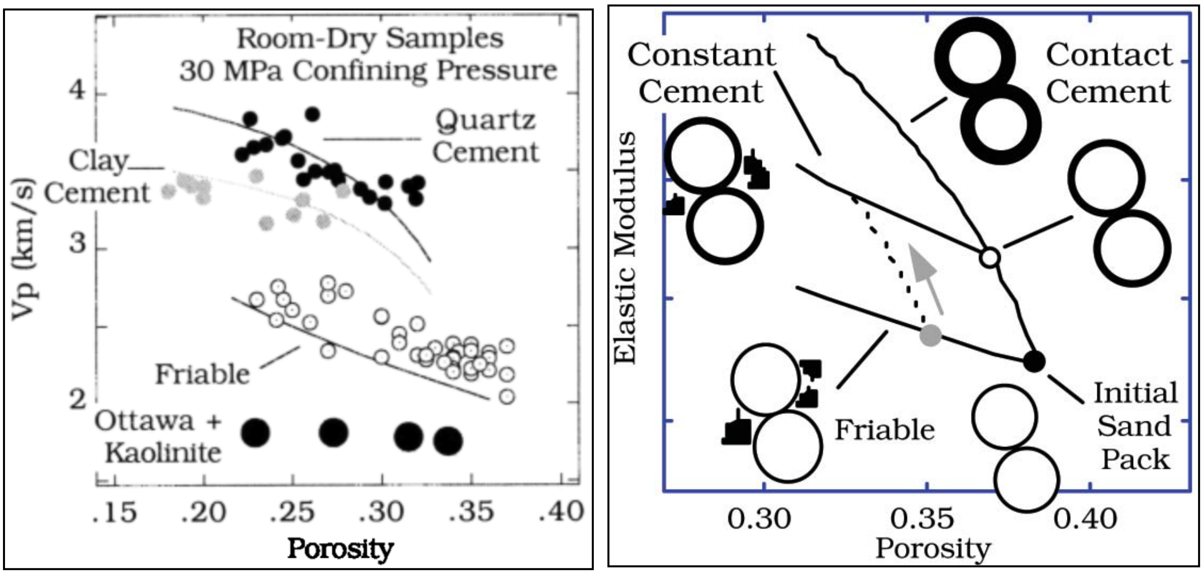

Figure 3.10 Friable, contact and constant cement models (Avseth et al., 2009; Avseth et al., 2000).

3.3.1.1 The friable-sand model

As described by Dvorkin and Nur (1996), the initial sand pack is well sorted, cement-free grains with critical porosity at about 0.4. In friable sand model, smaller grains are added into the pore space. The porosity decreases and rock stiffness slightly increases. The relatively flat trend in friable sand model is caused by depositional trends (sorting and clay content) (Avseth et al., 2000). The elastic moduli at the critical porosity point are calculated by Hertz-Mindlin theory and the values for zero porosity point (mineral point) are adapted from published mineral data. The critical porosity and the mineral points are then connected by the modified lower Hashin-Shtrikman bound (Avseth et al., 2005).

3.3.1.2 The Contact cement model

The contact cement model shows the relationship between velocity and porosity with respect to cement volume (Mavko et al., 2009). The diagenetic processes during burial will increases the cementation in sandstones. The contact cement dramatically increases the stiffness and velocity of sandstone. This steep slope relationship between elastic modulus and porosity is described as diagenetic trend (Avseth et al., 2010; Avseth et al., 2000; Avseth et al., 2009; Avseth et al., 2005).

3.3.1.3 The Constant cement model

As described by Avseth et al. (2000), in the constant cement model the data and the theoretical curve deviate from the contact cement curve because grain sorting starts to deteriorate at the cemented porosity point. This model assumes the sands have the same amount of contact cement and the porosity variation is only caused by the sorting.

3.3.2 Vs prediction

The Vp/Vs ratio for quartz and clay minerals is critical for seismic exploration and formation evaluation (Castagna et al., 1985). This ratio is described as "magic" by Avseth et al. (2005). The prediction of Vs is needed for:

- Rock physics diagnostic
- Gassman fluid substitution
- Seismic forward modelling
- Fluid and lithology prediction

Several Vp-Vs relationships suggested by many authors are summarized and described by Dvorkin (2008). The values of Vp and Vs are in Km/s:

Pickett (1963), for limestone: Vs = Vp /1.9
Pickett (1963), for dolomite: Vs = Vp /1.8
Castagna et al. (1985), Mud rock equation (Figure 3.11): Vs = 0.8621Vp -1.1724 (same as Vp= 1.16 Vs + 1.36)
Han et al. (1986), for sandstone: Vs =0.7936Vp - 0.7868
Williams (1990), for water-bearing sands from log: Vs = 0.846Vp - 1.088
Williams (1990), for shale: Vs = 0.784Vp - 0.893
Castagna and Backus (1993), for limestone: Vs = $-0.05508Vp^2 + 1.0168Vp - 1.0305$
Castagna and Backus (1993), for dolomite: Vs = 0.5832Vp - 0.0776
Castagna and Backus (1993), for clastic rock: Vs = 0.8042Vp - 0.8559
Mavko et al. (2009), for unconsolidated sands: Vs = 0.79Vp - 0.79
Mavko et al. (2009), for sandstone (Vsh<0.25): Vs = 0.754Vp - 0.657
Mavko et al. (2009), for sandstone (Vsh>0.25): Vs = 0.842Vp -1.099
Mavko et al. (2009), for sandstone (porosity<0.15): Vs = 0.853Vp - 1.137
Mavko et al. (2009), for sandstone (porosity>0.15): Vs = 0.756Vp - 0.662
Krief et al. (1990), $Vp^2=aVs^2+b$,

Table 3.2 Parameter values for Vp and Vs relationship (Krief et al., 1990).

Lithology	a	b
Sandstone (wet)	2.213	3.857
Sandstone (gas)	2.282	0.902
Sandstone (shaly)	2.033	4.894
Limestone	2.872	2.755

Greenberg and Castagna (1992),
Sandstone: Vs = 0.80416Vp - 0.85588
Limestone: Vs = $-0.05508Vp^2+1.01677Vp - 1.03049$
Dolomite: Vs = 0.58321Vp - 0.07775
Shale: Vs = 0.76969Vp - 0.86735
Fawad et al. (2011), for sandstone: Vs = 0.8249Vp − 0.9984

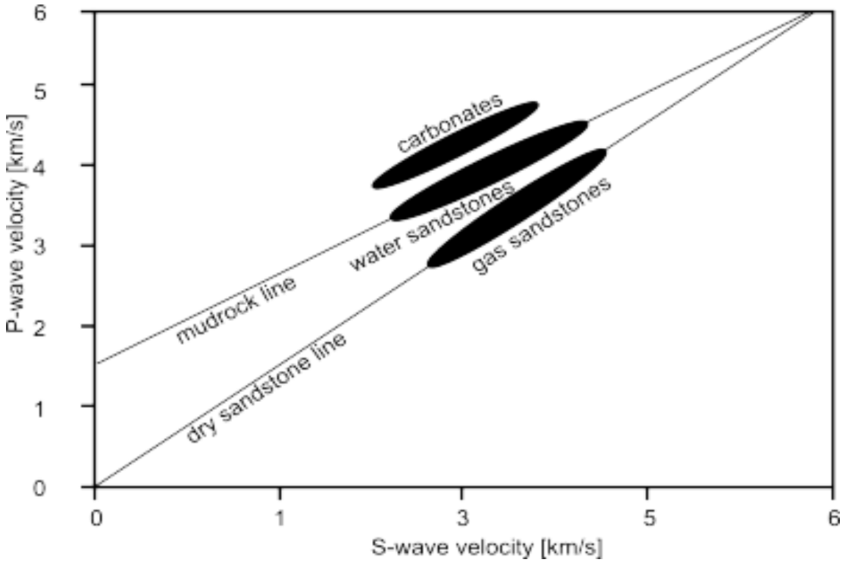

Figure 3.11 The relationship between Vp and Vs (Castagna et al., 1985).

3.3.3 Calculation of elastic parameters

In an isotropic and linear elastic medium, only two constants are needed to specify the stress–strain relation completely, like (λ, μ) or (E, ν) (Mavko et al., 2009). The other moduli can be calculated and they are always relatable to just two constants (Table 3.3).

Table 3.3 Relations between elastic constants and velocities (Sheriff, 1973)

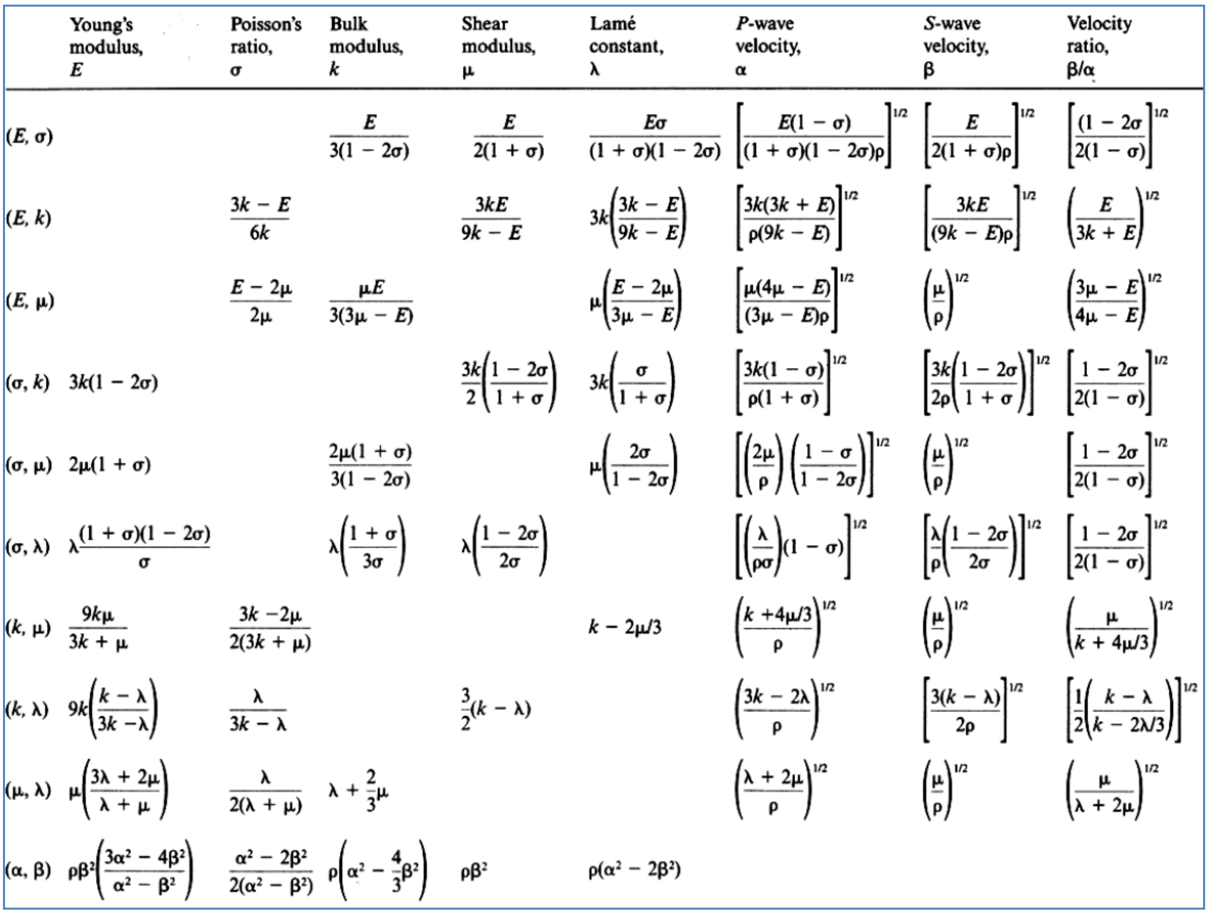

	Young's modulus, E	Poisson's ratio, σ	Bulk modulus, k	Shear modulus, μ	Lamé constant, λ	P-wave velocity, α	S-wave velocity, β	Velocity ratio, β/α
(E, σ)			$\frac{E}{3(1-2\sigma)}$	$\frac{E}{2(1+\sigma)}$	$\frac{E\sigma}{(1+\sigma)(1-2\sigma)}$	$\left[\frac{E(1-\sigma)}{(1+\sigma)(1-2\sigma)\rho}\right]^{1/2}$	$\left[\frac{E}{2(1+\sigma)\rho}\right]^{1/2}$	$\left[\frac{(1-2\sigma}{2(1-\sigma)}\right]^{1/2}$
(E, k)		$\frac{3k-E}{6k}$		$\frac{3kE}{9k-E}$	$3k\left(\frac{3k-E}{9k-E}\right)$	$\left[\frac{3k(3k+E)}{\rho(9k-E)}\right]^{1/2}$	$\left[\frac{3kE}{(9k-E)\rho}\right]^{1/2}$	$\left(\frac{E}{3k+E}\right)^{1/2}$
(E, μ)		$\frac{E-2\mu}{2\mu}$	$\frac{\mu E}{3(3\mu-E)}$		$\mu\left(\frac{E-2\mu}{3\mu-E}\right)$	$\left[\frac{\mu(4\mu-E)}{(3\mu-E)\rho}\right]^{1/2}$	$\left(\frac{\mu}{\rho}\right)^{1/2}$	$\left(\frac{3\mu-E}{4\mu-E}\right)^{1/2}$
(σ, k)	$3k(1-2\sigma)$			$\frac{3k}{2}\left(\frac{1-2\sigma}{1+\sigma}\right)$	$3k\left(\frac{\sigma}{1+\sigma}\right)$	$\left[\frac{3k(1-\sigma)}{\rho(1+\sigma)}\right]^{1/2}$	$\left[\frac{3k}{2\rho}\left(\frac{1-2\sigma}{1+\sigma}\right)\right]^{1/2}$	$\left[\frac{1-2\sigma}{2(1-\sigma)}\right]^{1/2}$
(σ, μ)	$2\mu(1+\sigma)$		$\frac{2\mu(1+\sigma)}{3(1-2\sigma)}$		$\mu\left(\frac{2\sigma}{1-2\sigma}\right)$	$\left[\left(\frac{2\mu}{\rho}\right)\left(\frac{1-\sigma}{1-2\sigma}\right)\right]^{1/2}$	$\left(\frac{\mu}{\rho}\right)^{1/2}$	$\left[\frac{1-2\sigma}{2(1-\sigma)}\right]^{1/2}$
(σ, λ)	$\lambda\frac{(1+\sigma)(1-2\sigma)}{\sigma}$		$\lambda\left(\frac{1+\sigma}{3\sigma}\right)$	$\lambda\left(\frac{1-2\sigma}{2\sigma}\right)$		$\left[\left(\frac{\lambda}{\rho\sigma}\right)(1-\sigma)\right]^{1/2}$	$\left[\frac{\lambda}{\rho}\left(\frac{1-2\sigma}{2\sigma}\right)\right]^{1/2}$	$\left[\frac{1-2\sigma}{2(1-\sigma)}\right]^{1/2}$
(k, μ)	$\frac{9k\mu}{3k+\mu}$	$\frac{3k-2\mu}{2(3k+\mu)}$			$k-2\mu/3$	$\left(\frac{k+4\mu/3}{\rho}\right)^{1/2}$	$\left(\frac{\mu}{\rho}\right)^{1/2}$	$\left(\frac{\mu}{k+4\mu/3}\right)^{1/2}$
(k, λ)	$9k\left(\frac{k-\lambda}{3k-\lambda}\right)$	$\frac{\lambda}{3k-\lambda}$		$\frac{3}{2}(k-\lambda)$		$\left(\frac{3k-2\lambda}{\rho}\right)^{1/2}$	$\left[\frac{3(k-\lambda)}{2\rho}\right]^{1/2}$	$\left[\frac{1}{2}\left(\frac{k-\lambda}{k-2\lambda/3}\right)\right]^{1/2}$
(μ, λ)	$\mu\left(\frac{3\lambda+2\mu}{\lambda+\mu}\right)$	$\frac{\lambda}{2(\lambda+\mu)}$	$\lambda+\frac{2}{3}\mu$			$\left(\frac{\lambda+2\mu}{\rho}\right)^{1/2}$	$\left(\frac{\mu}{\rho}\right)^{1/2}$	$\left(\frac{\mu}{\lambda+2\mu}\right)^{1/2}$
(α, β)	$\rho\beta^2\left(\frac{3\alpha^2-4\beta^2}{\alpha^2-\beta^2}\right)$	$\frac{\alpha^2-2\beta^2}{2(\alpha^2-\beta^2)}$	$\rho\left(\alpha^2-\frac{4}{3}\beta^2\right)$	$\rho\beta^2$	$\rho(\alpha^2-2\beta^2)$			

The moduli, density and velocity data of quartz and clay minerals in this study (Table 3.4) are used from Carmichael (1989) and Tosaya (1982):

Table 3.4 moduli, density and velocity data of minerals (from Mavko et al. (2009)).

Mineral	Bulk modulus (GPa)	Shear modulus (GPa)	Density (g/cm^3)	Vp (Km/s)	Vs (Km/s)	Poisson ratio	References
“Gulf clays”	21	7	2.6	3.41	1.64	0.35	Tosaya, (1982)
Quartz	37	44	2.65	6.05	4.09	0.08	Carmichael,(1989)

3.3.4 Construction of rock physics templates

Rock physics templates (RPTs) are important tools for predicting cementation, sorting, lithology and fluid (Avseth et al., 2005). The most widely used RPTs are porosity (ϕ) versus elastic properties (e.g. K, μ, Vp, Vs etc.), acoustic impedance (AI) versus Vp/Vs ratio and LMR ($\lambda\rho$ versus $\mu\rho$) (Ødegaard and Avseth, 2003).

3.3.4.1 Porosity versus Vp

Han et al. (1986) studied the relationship between P and S wave velocity, porosity and clay content. At confining pressure of 40 MPa and pore pressure of 1.0 MPa (differential pressure 39 Mpa), the equation is:

$$Vp=5.59-6.93\Phi-2.18C$$

At confining pressure of 20 MPa and pore pressure of 1.0 MPa (differential pressure 19 Mpa), the equation is:

$$Vp=5.49-6.94\Phi-2.17C$$

Where Vp = compressive wave velocity (Km/s),

Φ = porosity (%),

C = clay content (%).

3.3.4.2 Vp/Vs versus IP

The Vp/Vs versus IP cross-plot can be used for the fluid and lithology discrimination (Figure 3.12) (Avseth et al., 2000; Avseth et al., 2009; Avseth et al., 2005; Mavko et al., 2009; Ødegaard and Avseth, 2003). Low Vp/Vs ratios can be caused by gas, mechanical compaction or low shale volume. High acoustic impedance is usually caused by porosity loss during mechanical and chemical compaction (cementation). This method is based on Hertz-Mindlin contact theory, the lower Hashin-Shtrikman bound and the critical porosity method for the computation of the porous and solid phases (Ødegaard and Avseth, 2003).

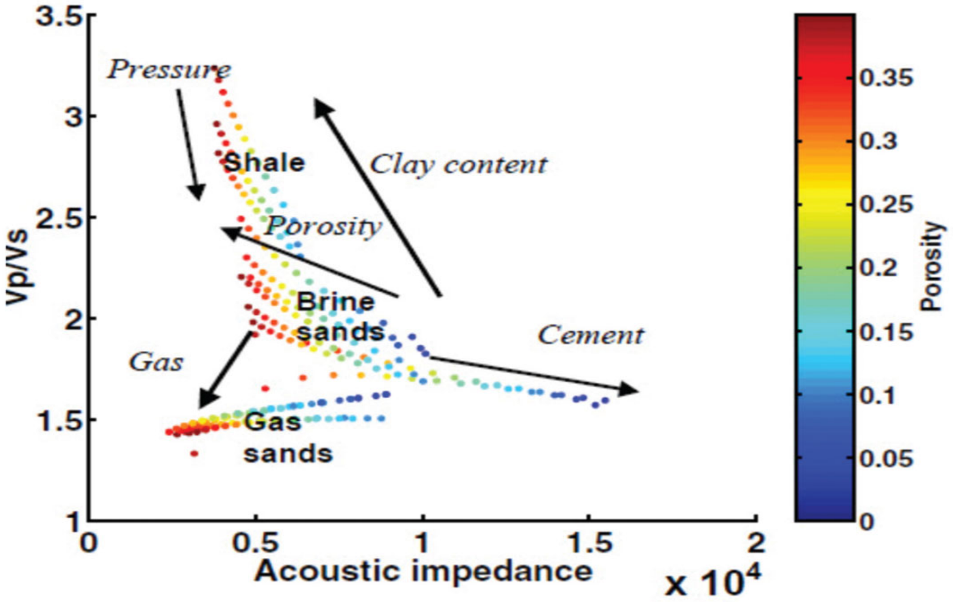

Figure 3.12 Vp/Vs versus IP template (Ødegaard and Avseth, 2003).

3.3.4.3 LMR

Goodway et al. (1997) suggested that the LMR (Lambda-Mu-Rho) cross plot is a useful tool to discriminate lithologies and pore fluids (Figure 3.13). L is the first Lamé parameter λ, M is the second Lamé parameter μ (shear modulus) and R represents density (ρ). Their relationship with Vp and Vs can be shown as:

$$\lambda\rho = I_p^{\,2} - 2I_s^{\,2}$$
$$\mu\rho = I_s^{\,2}$$

where, $I_p = V_p \cdot \rho$ and $I_s = V_s \cdot \rho$. λ is pure incompressibility (not bulk modulus K). It is the only modulus involved both the hydrostatic stress-strain relationship and pore fluid effect on acoustic wave propagation (Goodway, 2001).

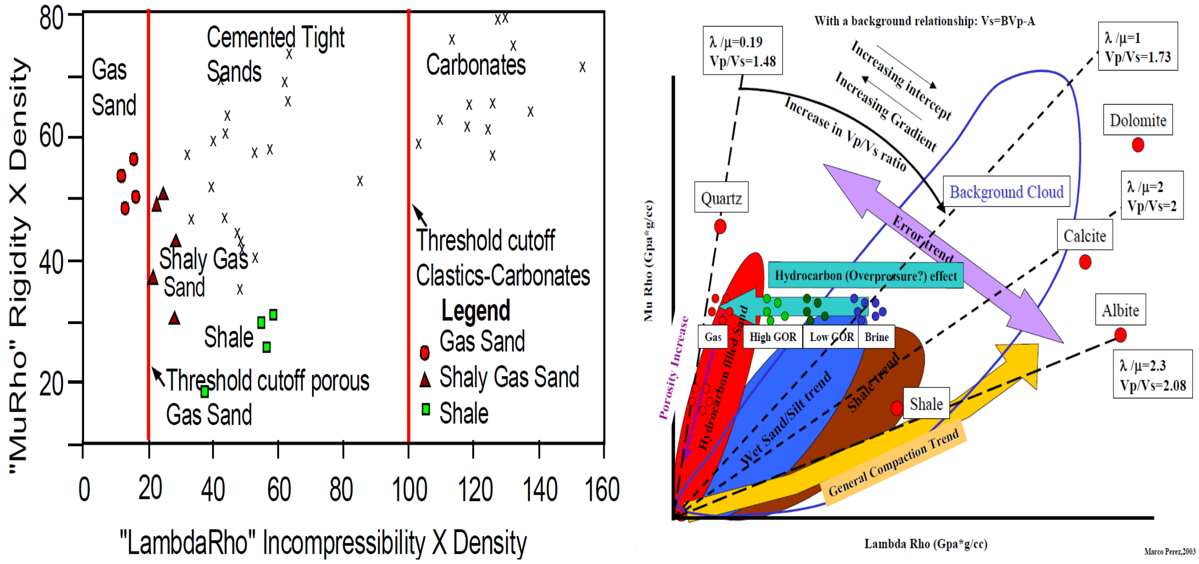

Figure 3.13 LMR plot from Goodway (2001) and Perez and Tonn (2003).

3.4 AVO modelling

AVO is a useful tool to understand the rock and fluid properties. This technique was proven to be successful worldwide, but lithological effects, tuning effects, overburden effects, data acquisition and processing effects could cause false AVO anomalies (Avseth, 2010). That is why AVO technique needs to be used carefully.

Gassmann (1951) equations predict that there will be a large decrease of Vp and small increase of Vs if only small amount of gas is containing in the pore space of a compressible sandstone (Castagna, 1993). This phenomenon changes Rp (which causes bright spot and dim spot) and Vp/Vs (which causes AVO anomalies) (Castagna, 1993).

According to Li et al. (2007), there are several modelling methodologies, like single-interface modelling, single-gather modelling, 2D stratigraphic modelling, and 2D full wave elastic modelling. Only the first method is used in this study to demonstrate the AVO characteristics of the target reservoirs.

3.4.1 Generation of synthetic seismogram

The main function of a synthetic seismogram is to provide a tie between rock properties and seismic reflection response (Schroeder, 2006). The P-wave impedance Ip is calculated by multiplying P-wave velocity and density:

$$Ip=\rho*Vp$$

The P-wave reflection coefficient Rp can be calculated by this equation:

$$Rp=\frac{Vp_2\rho_2-Vp_1\rho_1}{Vp_2\rho_2+Vp_1\rho_1}$$

The reflection coefficient series is convolved with a seismic wavelet to produce synthetic seismic data. The synthetics can be compared to real seismic traces if such data is available (Figure 3.14)

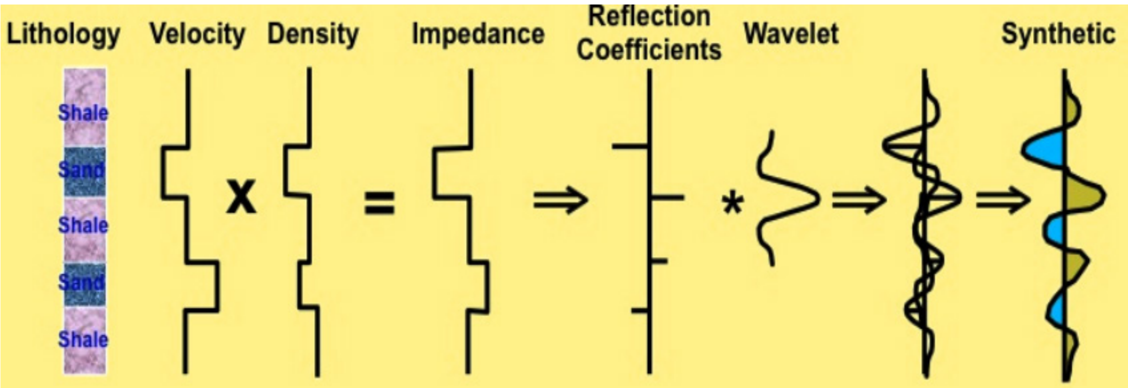

Figure 3.14 The convolution process for generating synthetic seismogram (Schroeder, 2006).

The accurate wavelet is important for both seismic forward modelling and inversion. If seismic data is available, the wavelet should be calculated by computing a filter that best shapes all the well log reflection coefficients to the input seismic (Gupta et al., 2012). It should be aware that the wavelet could be different for different depth in the seismic profile, because there is a large drop in frequency and amplitude with increasing depth. In this study, the wavelet is assumed to be constant for simplicity. The used wavelet is a bandpass wavelet with Low pass: 8 Hz, Low cut: 4 Hz, High pass: 24 Hz, High cut: 48 Hz, Phase rotation: 0, Sample rate: 2 ms, Wavelet length: 150 ms (Figure 3.15).

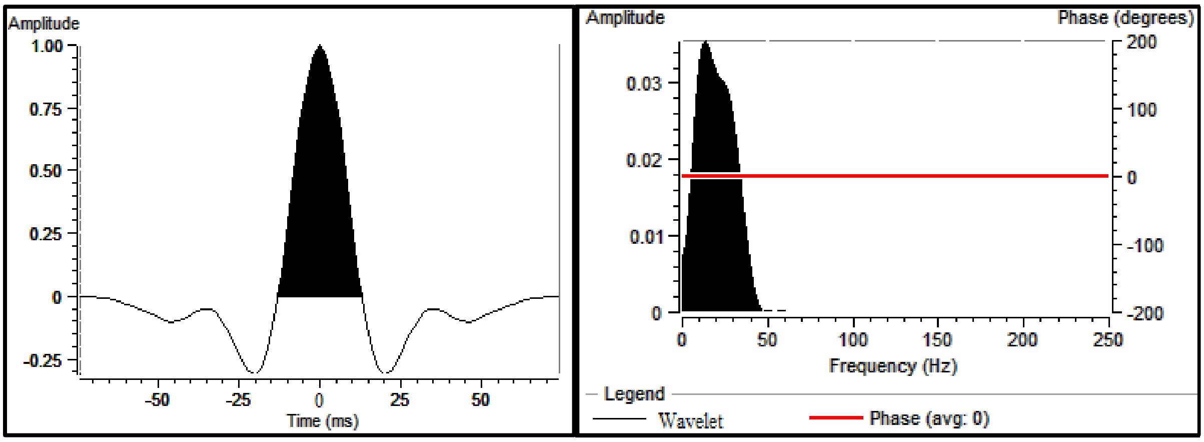

Figure 3.15 Wavelet used for AVO modelling in this study.

3.4.2 Gassmann fluid substitution

Gassmann (1951) equation can be used for estimating bulk modulus of a fluid-saturated rock with the known bulk moduli of the solid matrix (mineral part), the frame (dry rock) and the pore fluid.

$$K_{sat} = K_{dry} + K_s \frac{\left(1 - \frac{K_{dry}}{K_s}\right)^2}{1 - \frac{K_{dry}}{K_s} + \phi\left(\frac{K_s}{K_f} - 1\right)}$$

and $$\mu_{dry} = \mu_{sat}$$

where K_{sat} is saturated fluid rock bulk modulus, K_{dry} is the dry rock bulk modulus, K_s is mineral bulk modulus, K_f is the fluid bulk modulus which calculated by Reuss iso-stress model for fluid mixtures:

$$\frac{1}{K_f} = \frac{S_w}{K_w} + \frac{1 - S_w}{K_{gas}}$$

K_W and K_{gas} are the bulk modules for water and gas respectively. Φ is the rock porosity and μ is the shear modulus which is unchanged upon fluid substitution under Gassmann's theory. It can be rearranged into:

$$\frac{K_{sat}}{K_s - K_{sat}} = \frac{K_{dry}}{K_s - K_{dry}} + \frac{K_f}{\phi(K_s - K_f)}$$

In fluid substitution, Gassmann's equation assumes that dry bulk modulus does not change with different fluids. Therefore, the following equation can be used:

$$\frac{K_{sat1}}{K_s - K_{sat1}} - \frac{K_{f1}}{\phi(K_s - K_{f1})} = \frac{K_{sat2}}{K_s - K_{sat2}} - \frac{K_{f2}}{\phi(K_s - K_{f2})}$$

Gassmann's equation assumes a homogeneous mineral modulus and statistical isotropy of the pore space but is free of assumptions about the pore geometry. The basic assumptions about the porous fluid-filled rock are:

- All pores are connected and the porosity does not change with different fluids.
- All grains have the same physical properties (effective mineral grains).
- The pore fluid is homogenous and fully saturates the pore volume (effective fluid).
- Valid only for low frequencies, but can be used for seismic frequencies (10-100 Hz).

3.4.3 Angle dependent reflection coefficient

The angle dependent reflection coefficient equation, described by Aki and Richards (1980), is a linear approximation of Zoeppritz equation:

$$R(\theta) = \frac{1}{2}\left(1 - 4\frac{\beta^2}{\alpha^2}\sin^2\theta\right)\frac{\Delta\rho}{\rho} + \frac{1}{2}\frac{\Delta\alpha}{\alpha}\frac{1}{\cos^2\theta} - 4\left(\frac{\beta}{\alpha}\right)^2\left(\frac{\Delta\beta}{\beta}\right)\sin^2\theta$$

where α, β, ρ respectively are the average p-wave velocity, s-wave velocity, and density across the interface. θ is the average angle of incidence and $\Delta\alpha$, $\Delta\beta$, $\Delta\rho$ are the change in p-wave velocity, S-wave velocity and density. Shuey (1985) rearranged this equation into a more simple 3-terms equation:

$$R(\theta) = A + B\sin^2\theta + C\sin^2\theta\tan^2\theta$$

$$\text{Where, } A = R_P = \frac{1}{2}\left[\frac{\Delta V_P}{V_P} + \frac{\Delta\rho}{\rho}\right]$$

$$B = \frac{1}{2}\frac{\Delta V_P}{V_P} - 4\left(\frac{V_S}{V_P}\right)^2\frac{\Delta V_S}{V_S} - 2\left(\frac{V_S}{V_P}\right)^2\frac{\Delta\rho}{\rho}$$

If we assume that the V_P/V_S ratio is equal to 2, the gradient simplifies to:

$$B = R_P - 2R_S \text{ , where } R_S = \frac{1}{2}\left[\frac{\Delta V_S}{V_S} + \frac{\Delta\rho}{\rho}\right]$$

$$C = \frac{1}{2}\frac{\Delta V_P}{V_P}$$

C is referred to "Curvature", which is small for angles less than 30 degrees, and is usually ignored, then:

$$R(\theta) = A + B\sin^2\theta$$

B is called the Gradient and represents the slope of the line defined by the equation above. The AVO intercept “A” is the normal incidence reflectivity coefficient.

3.4.4 AVO classification of reservoirs

In the intercept-gradient cross plot, brine saturated clastic rock data usually located in the background trend. This trend can be explained with petrophysical assumptions like mudrock trend and Gardner’s relationship (Castagna and Swan, 1997).

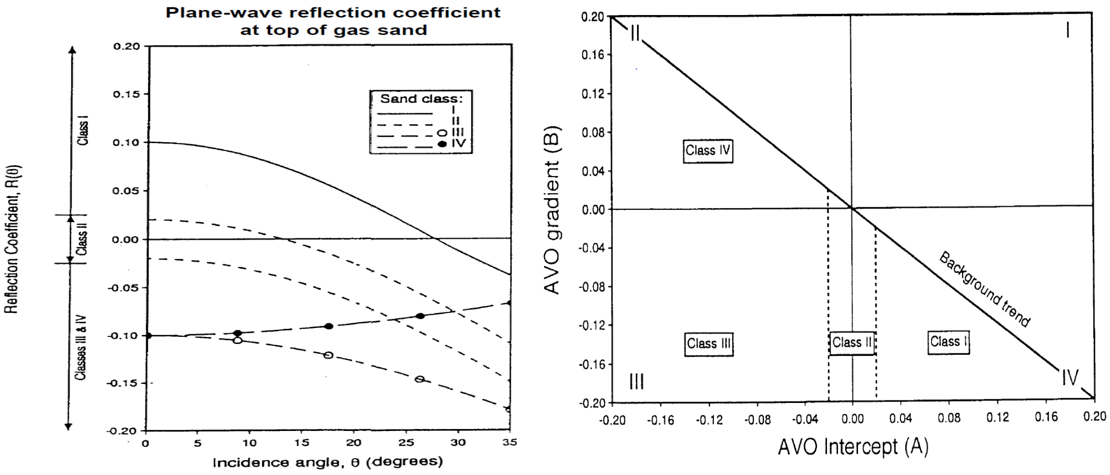

Figure 3.16 AVO classification for gas sands (Castagna and Swan, 1997).

Gas-bearing sandstones can be divided into four categories according to their AVO characteristics (Figure 3.16 and Table 3.5). The first three classifications are suggested by Rutherford and Williams (1989):

- **Class I** sands have high impedance and low Vp/Vs ratio compared with the cap-rock. They are usually found in a hard rock, onshore area.
- **Class II** sands have the similar impedance with the overlying shale. Therefore, the reflection coefficient is close to zero at the beginning. They often yield dim spots on stacked sections. The amplitude values are becoming more negative at larger offset.
- **Class III** sands have lower impedance than overlying shale. They can be found mainly in marine environment like Gulf of Mexico (Rutherford and Williams, 1989). This kind of unconsolidated sands can be easily recognized as amplitude anomalies (‘bright spots’) on stacked seismic data.
- **Class IV** sands were defined by Castagna and Swan (1997) as low impedance gas sands with positive gradient value. These are relatively rare but occur when soft sands with gas are capped by relatively stiff (very compacted or silty) shales. These stiff shales are characterized by higher Vp/Vs ratios than sandstone.

Table 3.5 AVO classification chart (Castagna and Swan, 1997).

Class	Relative Impedance	Quadrant	A	B	Amplitude vs. Offset
I	Higher than overlying unit	IV	+	-	Decreases
II	About the same as the overlying unit	II, III, or IV	+ or -	-	Increase or decrease; may change sign
III	Lower than overlying unit	III	-	-	Increases
IV	Lower than overlying unit	II	-	+	Decreases

Chapter 4 Petrophysical analysis

This chapter includes the petrophysical analysis results, discussions and uncertainties analysis. Knurr Formation and Stø Formation reservoirs are analysed separately. Key parameters (e.g. shale volume, porosity and water saturation) are shown in tables. Composite log plots and cross plots can also be found in this chapter. Combined with several literatures, the two different reservoirs are discussed respectively. The uncertainties for estimating shale volume, porosity and water saturation are discussed in details.

4.1 Results

4.1.1 Knurr Formation

A summary of interpretation of all wells for Knurr Formation is shown in Table 4.1. The detail explanations of terminologies used in Table 4.1 are given bellow:

- Net: The vertical thickness of reservoir zone read from well log data.
- Gross: The vertical thickness of the whole formation.
- N/G: Net to gross value, the proportion of reservoir rock to gross rock volume.
- Average Effective Phi: Average effective porosity of reservoir zone.
- Average Sw: Average water saturation of reservoir zone.
- Average Vcl: Average value of clay volume.
- Phi*H: Average porosity multiplied by the vertical thickness of reservoir zone. This parameter indicates the store space of reservoir zones.
- PhiSo*H: Average oil saturated porosity multiplied by the vertical thickness of reservoir zone. This parameter indicates the hydrocarbon saturated store space of reservoir zones.

Table 4.1 Reservoir and pay zones evaluation results for Knurr Formation.

Well name	Formation	Top (m_RKB)	Bottom (m_RKB)	Gross (m)	Net (m)	N/G (fraction)	Average Effective Phi (fraction)	Average Sw (fraction)	Average Vcl (fraction)	Phi*H	PhiSo*H	Result
7119/12-2	KNURR FM	1087	1163	76	0	0	N/A	N/A	N/A	N/A	N/A	No reservoir
7120/10-1	KNURR FM	1353	1394	41	3.51	0.085	0.129	1	0.308	0.45	0	Dry
7120/10-2	KNURR FM	1922	2303	381	138.07	0.362	0.123	1	0.165	16.96	0	Dry
7119/12-4	KNURR FM	1955	2058	103	0	0	N/A	N/A	N/A	N/A	N/A	No reservoir
7019/1-1	KNURR FM	2127	2345	218	24.54	0.113	0.112	0.326	0.028	2.74	1.84	Gas
7119/12-1	KNURR FM	2441	2497	56	0	0	N/A	N/A	N/A	N/A	N/A	No reservoir
7119/12-3	KNURR FM	2953	3026	73	0	0	N/A	N/A	N/A	N/A	N/A	No reservoir

The Knurr Formation is penetrated by all seven wells. The sandstones exist in three wells (7120/10-1, 7120/10-2 and 7019/1-1). According to Figure 4.1, the reservoir sandstones in well 7120/10-1 are thin (3.51 m) and shaly (Vsh = 0.308). The average effective porosity is 12.9%. The effective porosity is low because of the high shale content in the reservoir sandstones. The calculated density porosity, neutron porosity and sonic porosity values are quite different from each other.

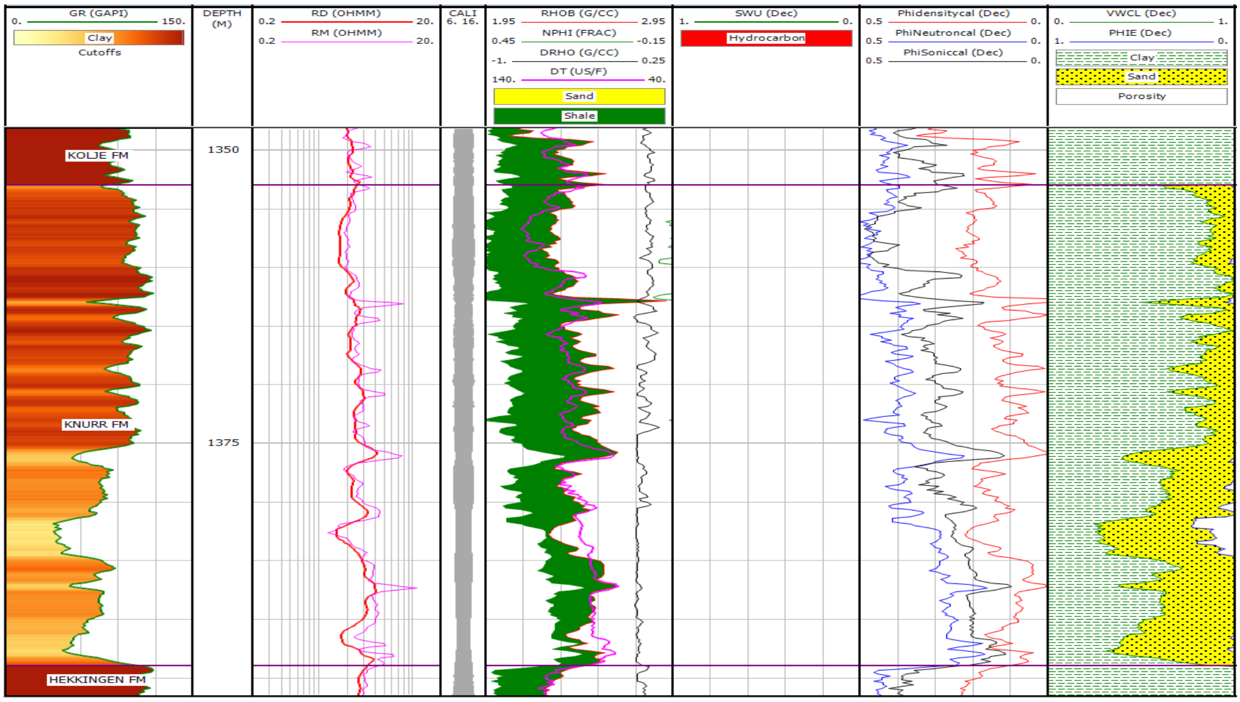

Figure 4.1 Composite log plot of Knurr Formation in well 7120/10-1.

The reservoir sandstones in well 7120/10-2 are thick (138.07 m) and relatively pure (Vsh = 0.165) according to the well logs available (Figure 4.2). In the upper section of Knurr Formation, most of the well logs are missing because of the bad borehole conditions. This well has the highest net-to-gross ratio in Knurr Formation compared to other wells (N/G = 0.362). It can be sure from the well log data that the reservoir is saturated by brine. The resistivity values of the sandstones are around 2 ohm-m, which is the same as brine saturated shales. The calculated density porosity and neutron porosity curves are similar but not cross each other.

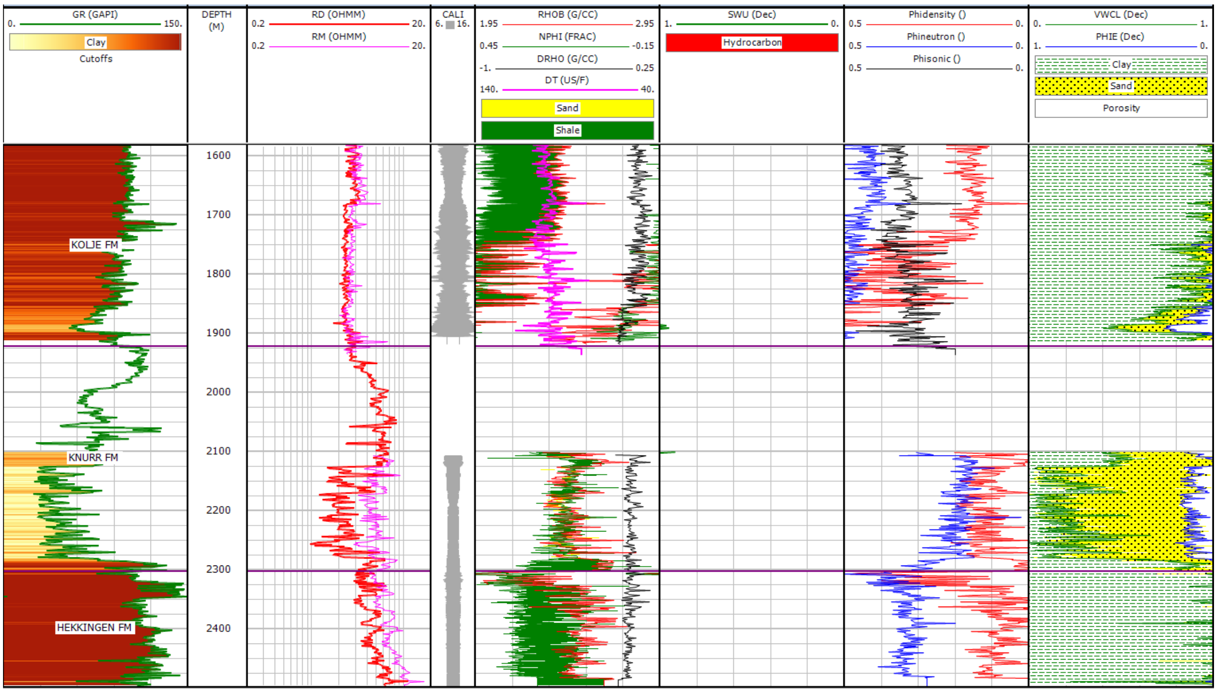

Figure 4.2 Composite log plot of Knurr Formation in well 7120/10-2.

The reservoir sandstones in well 7019/1-1 are also thin (24.54 m). The net-to-gross value is very low (0.113). This is the only well with gas in Knurr Formation (Figure 4.3). The resistivity values of reservoir sandstones are around 1000 ohm-m. There is “cross over" between calculated density porosity and neutron porosity curves.

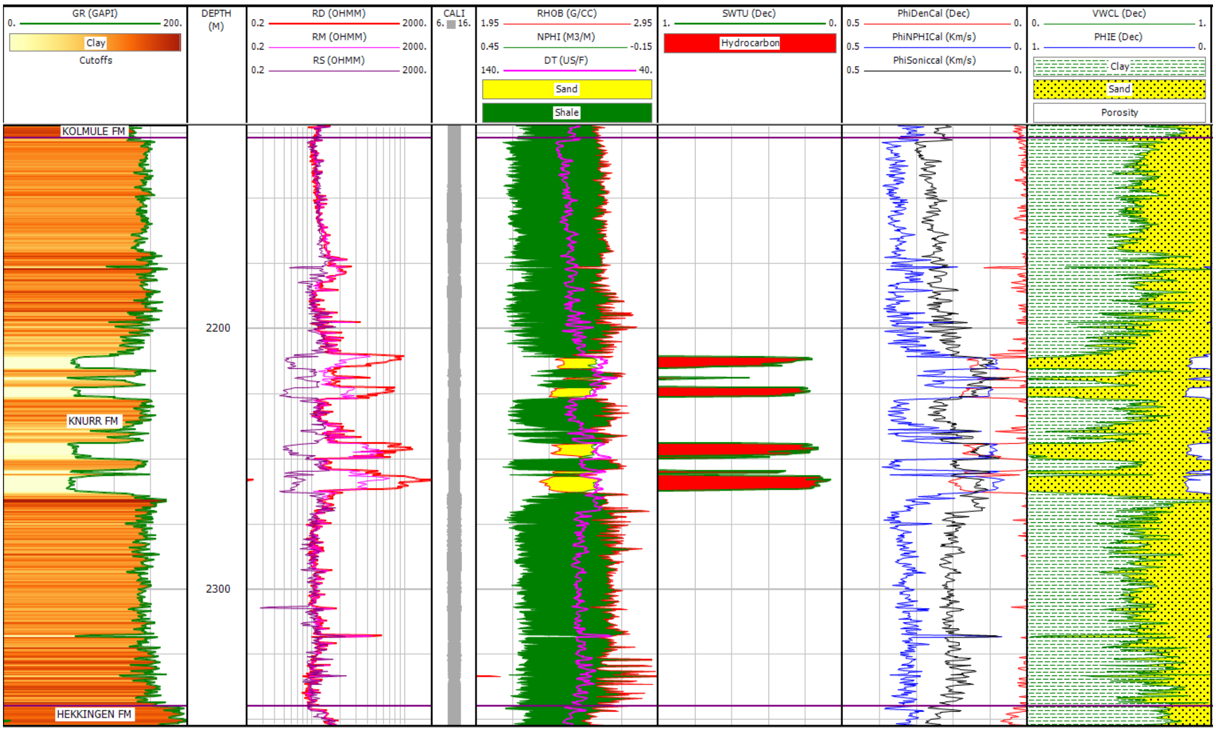

Figure 4.3 Composite log plot of Knurr Formation in well 7019/1-1.

In Figure 4.4, only the data points from well 7019/1-1 show strong gas effect. The data points of sandstone in this well are in the left of the sandstone line. Most of the data points in this figure are shale and therefore located in the right of dolomite line. The sandstone and shaly sandstone data in well 7119/10-1 and 7119/10-2 are in between the sandstone line and dolomite line.

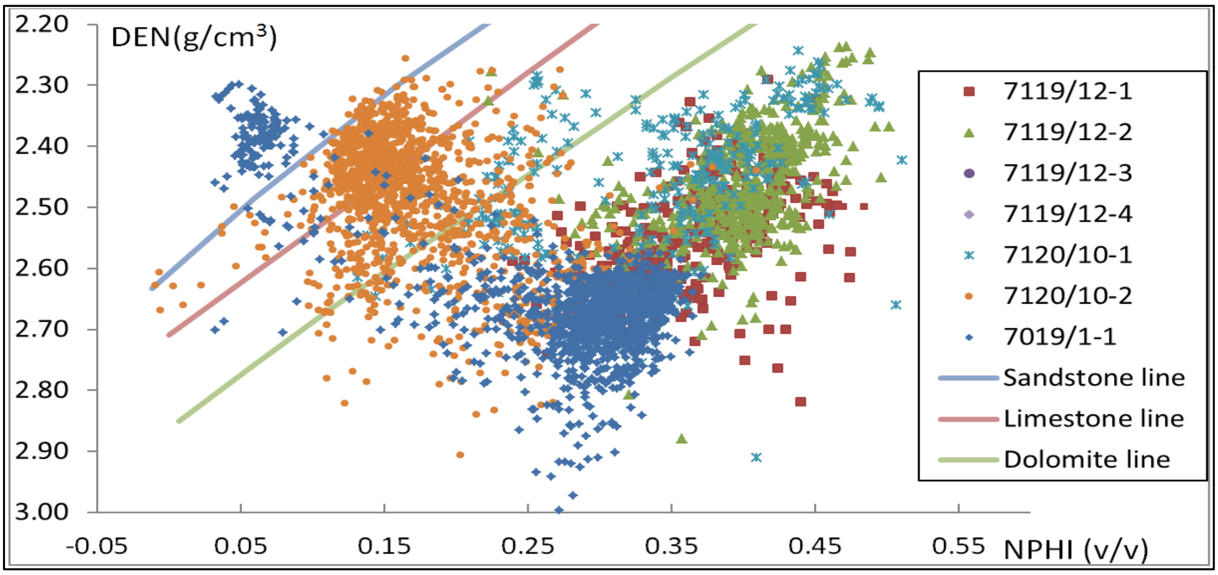

Figure 4.4 Neutron-Density cross plot of Knurr Formation in all the available wells.

4.1.2 Stø Formation

According to well correlation and literature study, the bottom of the Stø Formation in well 7119/12-1 given by NPD (3088 m KB) is misleading. It is clear from well correlation and literature (Olaussen et al., 1984) that the bottom of the Stø Formation is 2811 m (KB). The interpretation plots of Stø Formation are shown in Chaper 3 (7119/12-3 in Figure 3.2, 7120/10-1 in Figure 3.3, 7119/12-2 in Figure 3.5 and 7019/1-1 in Figure 3.8), chapter 4 (7119/12-1 in Figure 4.9) and chapter 5 (7119/12-4 in Figure 5.13). A general summary of evaluation of the Stø Formation penetrated by studied wells is shown in Table 4.2.

Table 4.2 Reservoir and pay zones evaluation results for Stø Formation.

Well name	Formation	Top (m_RKB)	Bottom (m_RKB)	Gross (m)	Net (m)	N/G (fraction)	Average effective Phi (fraction)	Average Sw (fraction)	Average Vcl (fraction)	Phi*H	PhiSo*H	Result
7119/12-2	STØ FM	1372	1517	145	126.71	0.874	0.249	1	0.116	31.53	0	Dry
7120/10-1	STØ FM	1568	1655	87	74.18	0.853	0.195	1	0.14	14.46	0	Dry
7119/12-4	STØ FM	2296	2448	152	135.36	0.891	0.147	0.974	0.029	19.94	0.52	Shows
7019/1-1	STØ FM	2447	2610	163	128.38	0.788	0.061	0.509	0.01	7.82	3.83	Gas
7119/12-1	STØ FM	2658	3088	430	18.59	0.043	0.122	0.975	0.016	2.27	0.06	Shows
7119/12-1 with new standard	STØ FM	2658	2811	153	112.78	0.737	0.055	0.798	0.043	6.18	1.25	Shows
7119/12-3	STØ FM	3144	3299	155	128.63	0.83	0.029	0.801	0.056	3.68	0.73	Gas

The Stø Formation thickness is increasing from east to west: 7120/10-1 (87m), 7119/12-2 (145m), 7119/12-4 (152m), 7119/12-1 (153m), 7119/12-3 (155m) and 7019/1-1 (163m). Most of the Stø Formation reservoirs have high N/G. The average clay volumes are low in all the wells and decreased with burial depth.

Normally the reservoir porosity will decrease with depth because of mechanical and chemical compactions. There is a clear trend of this phenomenon for Stø Formation in all the wells except 7119/12-1 (Table 4.2). The calculated porosity in most part of the reservoir in well 7119/12-1 is around 4%. There are several zones with abnormal high porosity values, like 2720.5-2726.0 (m RKB) and 2768.0-2781.5 (m RKB). The highest value of total porosity is 20% at 2721.0 (m RKB). The calculated density porosity and sonic porosity become different at these zones (Figure 4.9). This bimodality in porosity of the quartz arenites are also found in well 7019/1-1, 7119/12-3 and 7119/12-4. This phenomenon in these 3 wells is less obvious than in 7119/12-1.

The Neutron-Density cross plot can show us the gas effect in each of the wells (Figure 4.5). The results agree reasonably well with the calculated water saturation. In Stø Formation, well 7019/1-1, 7119/12-1, 7119/12-3 contains gas.

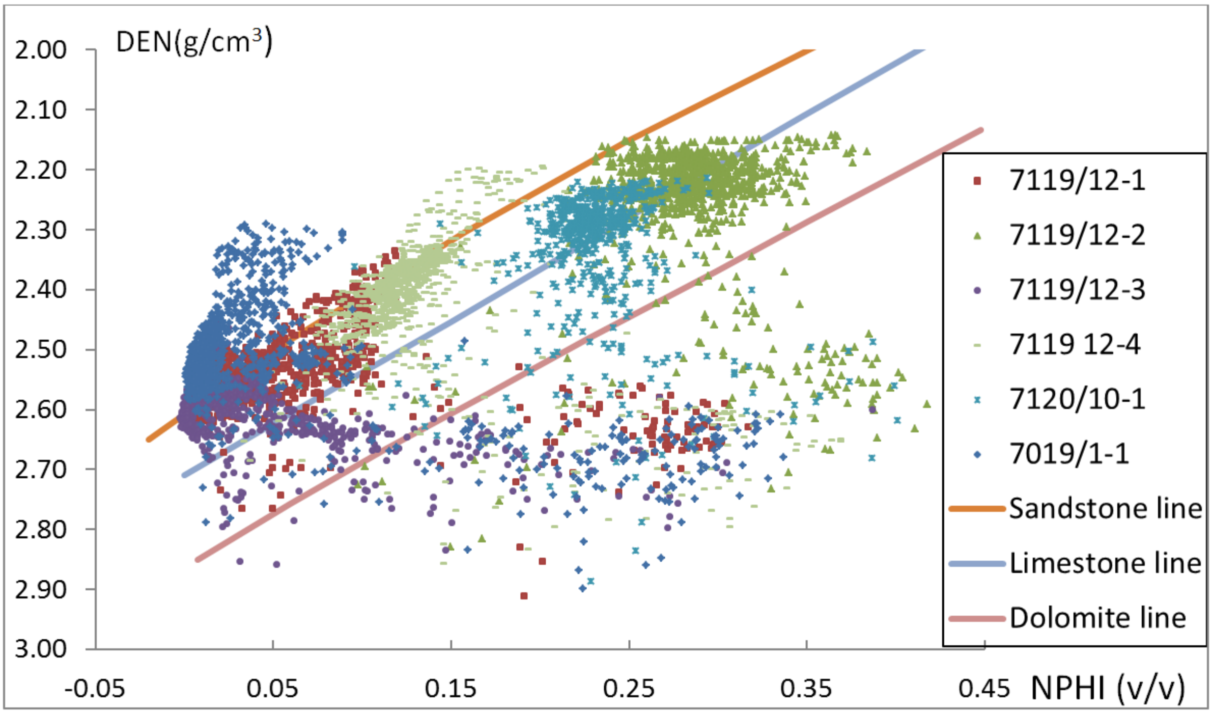

Figure 4.5 Neutron-Density cross plot of Stø Formation in all the available wells.

4.2 Discussion

4.2.1 Knurr Formation

The depositional environment of Knurr Formation is submarine fan (Figure 4.6). Therefore, the reservoir quality (e.g. N/G, Vsh and porosity) can be highly affected by sedimentary facies. The channel deposits are sand-prone. The levee deposits contain more clays and silts. The proximal facies have better reservoir qualities than the distal part of the fan lobes. It is clear from the study that parameters that controlled the reservoir quality (e.g. N/G, Vsh and porosity) are highly affected due to locations of wells within the submarine fan system. For example, the N/G are low in 7120/10-1 and 7019/1-1 because they are located in the distal part of a wedge fan (Seldal, 2005). Only thin sandstone layers are found in these two wells (Figure 4.7). Well 7120/10-2 is drilled in the middle of a spillover fan in the lower Knurr Formation (Valanginian) but the lithology of upper part (Hauterivian) of the Knurr Formation is shale dominated (Seldal, 2005). This is why the N/G of Knurr Formation is relative low (N/G=0.362). The average effective porosity of the reservoirs is around 12%, and decreases with depth. Hydrocarbon is only found in well 7019/1-1 (Sw=0.326).

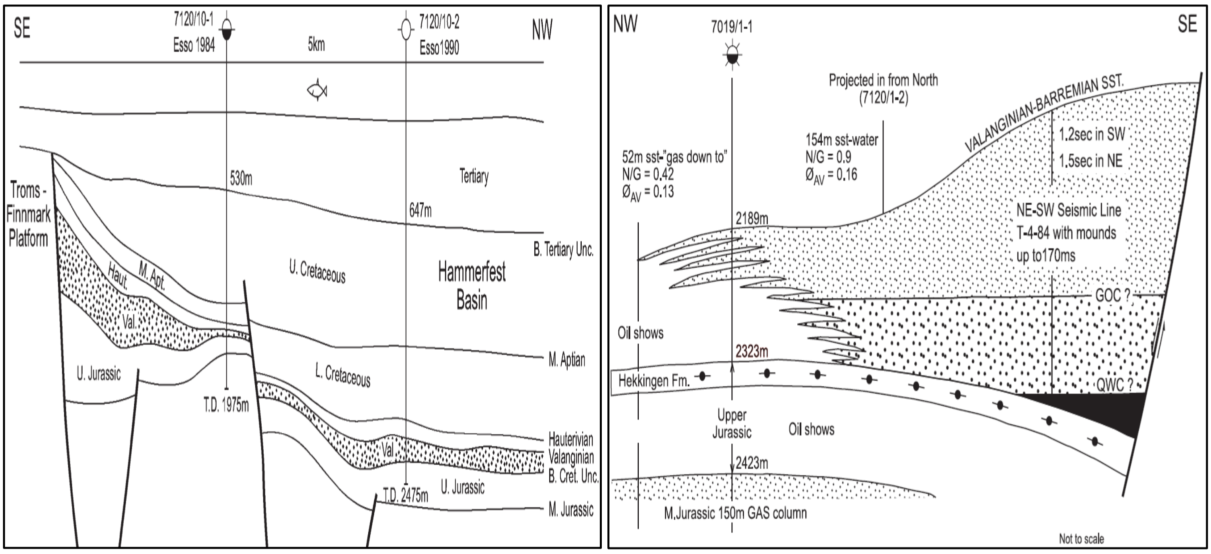
SE
7120/10-1
Esso 1984
5km
7120/10-2
Esso1990
NW
Troms - Finnmark Platform
530m
647m
Tertiary
B. Tertiary Unc.
M. Apt.
Haut.
Val.
U. Cretaceous
Hammerfest Basin
M. Aptian
U. Jurassic
T.D. 1975m
L. Cretaceous
Val.
Hauterivian
Valanginian
B. Cret. Unc.
T.D. 2475m
U. Jurassic
M. Jurassic
NW
7019/1-1
SE
Projected in from North (7120/1-2)
VALANGINIAN-BARREMIAN SST.
1.2sec in SW
1.5sec in NE
52m sst-"gas down to"
N/G = 0.42
Ø_{AV} = 0.13
154m sst-water
N/G = 0.9
Ø_{AV} = 0.16
2189m
NE-SW Seismic Line
T-4-84 with mounds
up to170ms
GOC ?
Oil shows
2323m
Hekkingen Fm.
QWC ?
Upper Jurassic
Oil shows
2423m
M.Jurassic 150m GAS column
Not to scale

Figure 4.6 Lower Cretaceous sandstone play of well 7120/10-1, 7120/10-2(left) and 7019/1-1(right) (modified from Seldal (2005)).

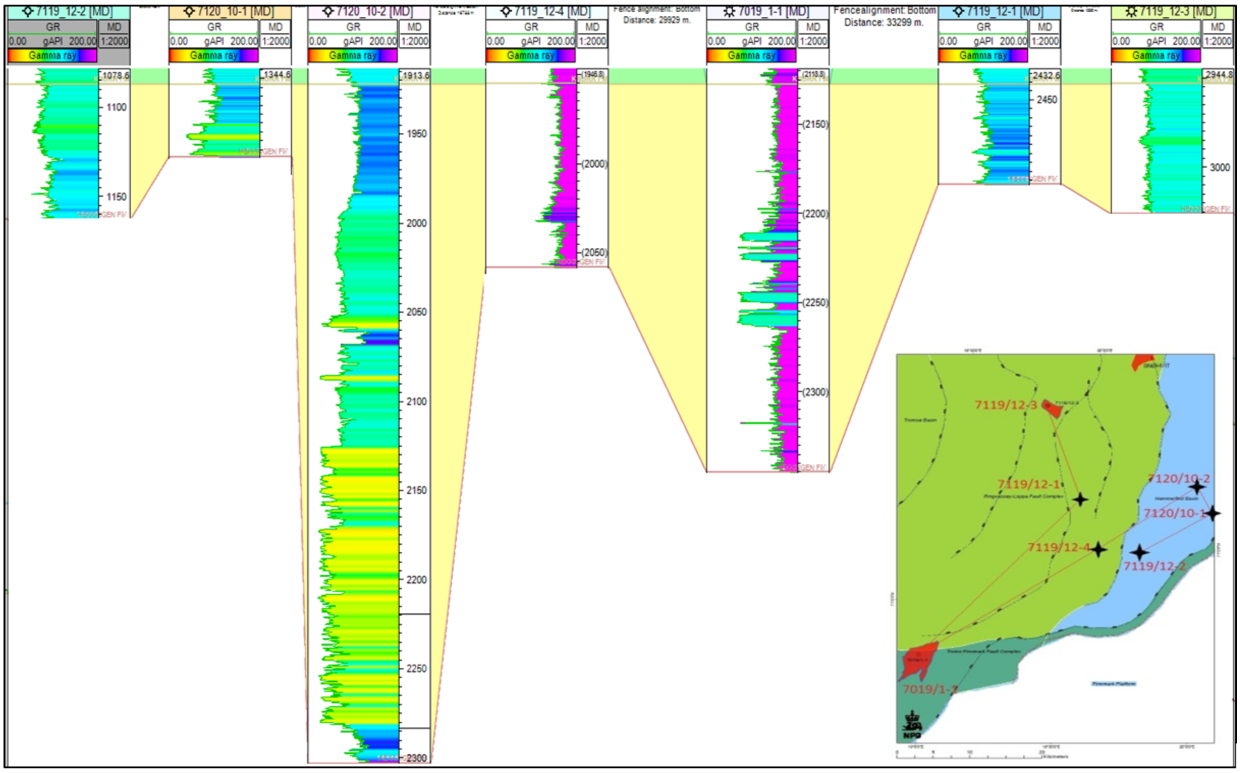

Figure 4.7 Well correlation for Knurr Formation, the depth going deeper from left to right, with top flattened in this picture.

4.2.2 Stø Formation

The high N/G in Stø Formation is due to prograding coastal regimes or shore face depositional environments. The average clay volumes are low in all the wells and decrease with burial depth. One possible reason is that complex diagenetic processes (dissolution and re-precipitation) eliminated unstable detrital and authigenic constituents (Riches et al., 1986).

Compared to the eastern Hammerfest basin, relatively thick Stø sandstones are deposited in the study area. The Stø Formation can be divided into 3 depositional sequences (Figure 4.8), with bases defined by transgressive episodes. The *basal sequence* is composed of cylindrical near shore deposits. There are prograding characteristics (coarsening upward) in the 3 western wells. The *middle transgressive event* is occasionally interrupted by sandstone deposits. The thickness of the middle sequence decreases to the east. This sequence turns into a single transgressive event in the eastern Hammerfest Basin. The *upper cylindrical deposits* are quite similar to the basal ones in this region.

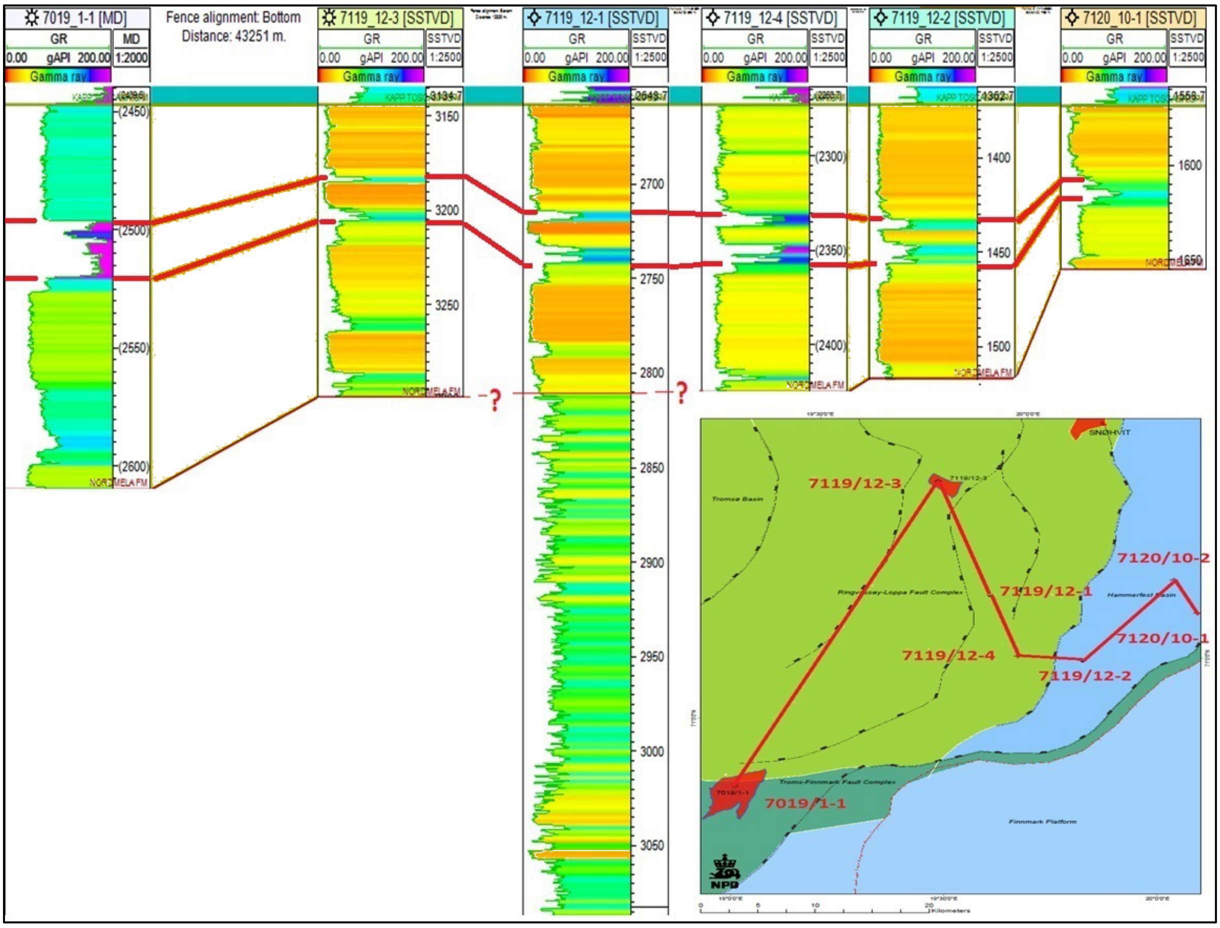

Figure 4.8 Well correlation of Stø Formation from west to east, flatten on the top of Stø Formation.

In pure sandstone zones, the log calculated total porosity values are the same with calculated effective porosity. In Figure 4.9, they are compared with point counted total porosity data (Ogebule, O.Y., personal communication). The total porosity values are quite close to the calculated ones. The misfit between calculated and point counted porosities could be explained by the limitation of the well log resolution (0.1524m). In high porosity zones, the water saturation values are close to 1. It indicates that the hydrocarbon migrated away from these high porosity zones. In these high porosity zones, the separation between density porosity and sonic porosity is observed. The Neutron and Density logs response to all sizes and all kinds of pores. Sonic log is a measure of interparticle (intergranular and intercrystalline) porosity but is largely insensitivity to secondary porosities.

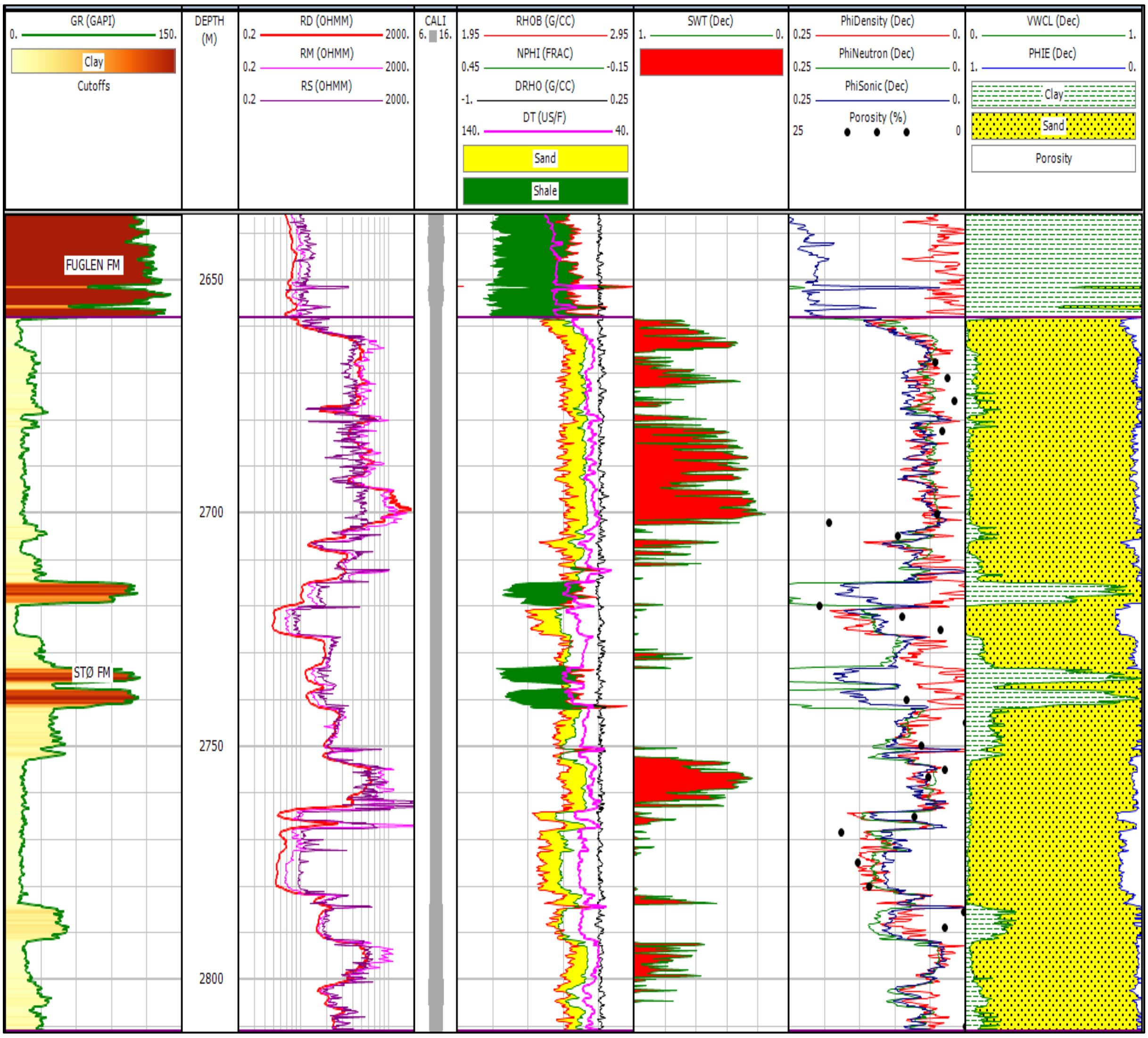

Figure 4.9 Composite log plot for Stø Formation in 7119/12-1, core porosity data are showed as red dots. Notice the separation between density porosity and sonic porosity at high porosity zones.

Bloch et al. (2002) described four possible reasons for anomalously high porosity in sandstones:

(1) Grain coats and grain rims (chlorite coats, quartz coats and clay rims).
(2) Early emplacement of hydrocarbons.
(3) Shallow development of fluid overpressure.
(4) Secondary porosity.

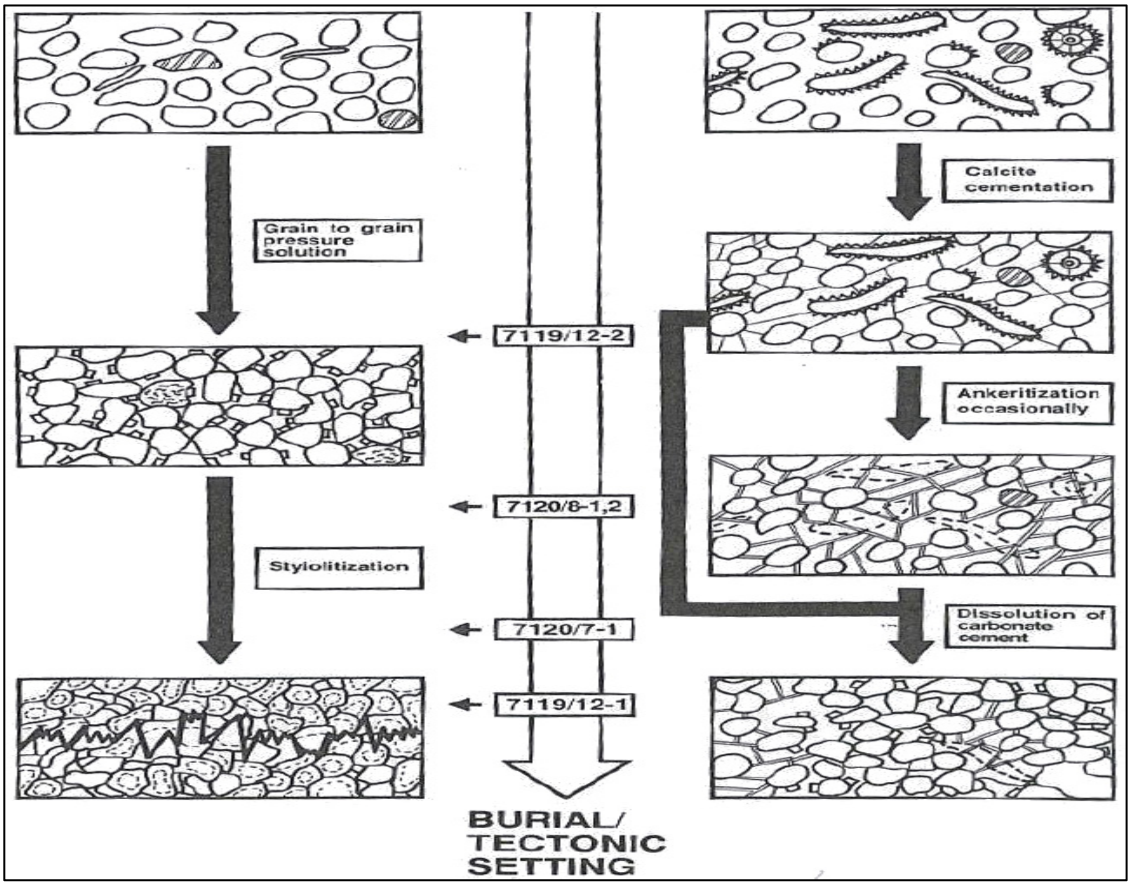

Figure 4.10 Diagenetic model of Stø Formation (Olaussen et al., 1984).

Olaussen et al. (1984) explained that carbonate cementation precipitated earlier in the sandstones may dissolve and create secondary porosity in well 7119/12-1 (Figure 4.10). Differences in textural and mineralogical composition could also be partial explanation. The similar phenomenon observed in other 3 wells (well 7019/1-1, 7119/12-3 and 7119/12-4) can be explained due to any of the above regions.

According to NPD website, the reservoir properties of Stø Formation in 7119/12-1 are poor, with only 18.5 m net sand out of 430 m, and a moderate 13.6% average porosity in the net sand. This is very close to the interpretation results of 7119/12-1 shown in the NPD website. The N/G of Stø Formation in this well (0.043) is abnormally lower than other wells in the study area (around 0.8). Two possible consequences can be explained the phenomenon. The first reason is that the gross thickness (430m) of Stø Formation is too high. Olaussen et al. (1984) suggested that the base of Stø Formation in this well is 2811.0 m instead of 3088.0m reported by NPD (Figure 4.8). From well correlation, the estimated gross thickness of Stø is 153m, which is more similar to the nearby wells. It can be concluded that NPD may miss the division between Stø and Nordmela Formations. The second possible reason could be most of the sandstones in this well are deeply buried and highly cemented. Only small parts of the sandstones meet the standards for reservoir criteria ($\Phi > 10\%$). If the cut-off value is changed to 1% as in other wells, the N/G is 0.737.

The water saturation values in well 7119/12-1 are very low comparing with other well with shows. Most of the sandstone zones are saturated by hydrocarbon according to the calculated results. Oil stains are commonly observed in the core samples of this well (Olaussen et al., 1984). It should be noticed that several sandstone zones are storm generated, for example between 2753.0 and 2763.0 m (RKB) (Olaussen et al., 1984). The zone between 2695.0 and 2702.0 m (RKB) might be the same. The coarse grain size will result in false interpretation of water saturation. The resistivity values and porosity values of these zones are high. Therefore, the water saturation from Archie's equation will be lower than the true values.

4.3 Uncertainty analysis

There are many pitfalls and uncertainties in petrophysical analysis beyond the limitations mentioned in Chapter 1. It is widely accepted that different tools and methods should be combined together to reduce the uncertainty. Uncertainties of Vsh, porosity and saturation estimations are highlighted bellow:

4.3.1 Vsh estimation using Gamma Ray log

Using Gamma Ray measurements for lithology discrimination and shale volume calculation can be misleading under certain situations.

1. Statistical fluctuations (random fluctuations) due to the random nature of the radioactive pulses reaching the detector.
2. Bad bore hole effect of Gamma Ray, like cave-in sections in shale zones.
3. Radioactive "hot shale" on top of the reservoirs causes abnormally high Gamma Ray readings, which could increase GRmax parameter and decrease calculated Vsh in the reservoir section.
4. The Gamma Ray index method for shale volume calculation assumes that the clay composition in sandstone is the same as that in the shales. This is not always correct as sandstone and shale can be deposited in different age and different sedimentary environment.

4.3.2 Porosity calculation

There are numerous methods to calculate porosity both in laboratory and in fields. As discussed in Chapter 3, using well logs (Density, Neutron and Sonic log) for porosity calculation is relatively correct despite the environmental effects. Combining different well log methods is better than using a single well log. Porosity data from laboratory are absolutely important to calibrate the log-derived porosity.

4.3.3 Sw estimation

Deep, medium and shallow resistivity log are measured in conventional well logs. They are all affected by environmental effects. After corrected, they could be used for water saturation calculation. It is difficult to determine formation water resistivity if they are not available from service companies. Rwa and Pickett plot methods could only provide limited information and heavily rely on input value of a, m and n.

4.3.3.1 Rwa method

At the interpreted water zone in each well, the cement factor m is assumed to be 2. The calculated Rw for each well is shown in Table 4.3:

Table 4.3 Estimated Rw values using Rwa method

Well Name	Water zone depth	RD (Ohmm)	Φ(%)	m (cement factor)	Rwa (Ohmm)
7119/12-2	1500	0.43	29.20	2	0.0366
7120/10-1	1588.8	0.47	14.30	2	0.0096
7120/10-2	2255.7	1.11	14.90	2	0.0246
7119/12-4	2426.9	0.65	17.60	2	0.0202
7019/1-1	2600.9	6.72	8.76	2	0.0516
7119/12-1	2776.3	1.51	12	2	0.0217
7119/12-3	3283	45.00	3.58	2	0.0577

In 7019/12-1 and 7119/12-3, the calculated Rwa is much higher than in other wells, because the sandstones in these wells are deeply buried and highly cemented. The value of cement factor m needs to be changed accordingly. Overall, the Rwa should be around 0.02 ohmm.

4.3.3.2 Resistivity-porosity cross plot method

This method works for most of the wells, but not so well in 7120/10-1 and 7120/10-2 (Table 4.4). The uncertainty of this method is largely depended on a, m and n values. This could influence the estimation due to different digenesis processes and so to pick right values of a, m and n.

Table 4.4 Estimated m and Rw value from Pickett plot method

Well Name	m (cement factor)	Rwa (Ohmm)	a	n
7119/12-2	2.14	0.030788	1.00	2.00
7120/10-1	5.56	0.000009	1.00	2.00
7120/10-2	3.49	0.001445	1.00	2.00
7119/12-4	1.99	0.020582	1.00	2.00
7019/1-1	2.99	0.004629	1.00	2.00
7119/12-1	2.42	0.008925	1.00	2.00
7119/12-3	2.16	0.033853	1.00	2.00

Chapter 5 Rock physics diagnostics

This chapter includes rock physics diagnostic results, discussions and uncertainties analysis. Knurr Formation and Stø Formation reservoirs are analysed together in each of the rock physics templates. The results and discussions are organized by the different diagnostic methods and templates used in this study. The uncertainties for the results are discussed briefly.

5.1 Results

5.1.1 The rock physics cement models

In Figure 5.1, the Vp and Porosity data from the reservoir intervals are crossplotted. The Stø Formation reservoir in 7119/12-2 is the shallowest and 7119/12-3 is the deepest. Most of the data points are plotted on the 2% constant cement model trend line. The data points from the three deepest wells are plotted close to the friable sand line.

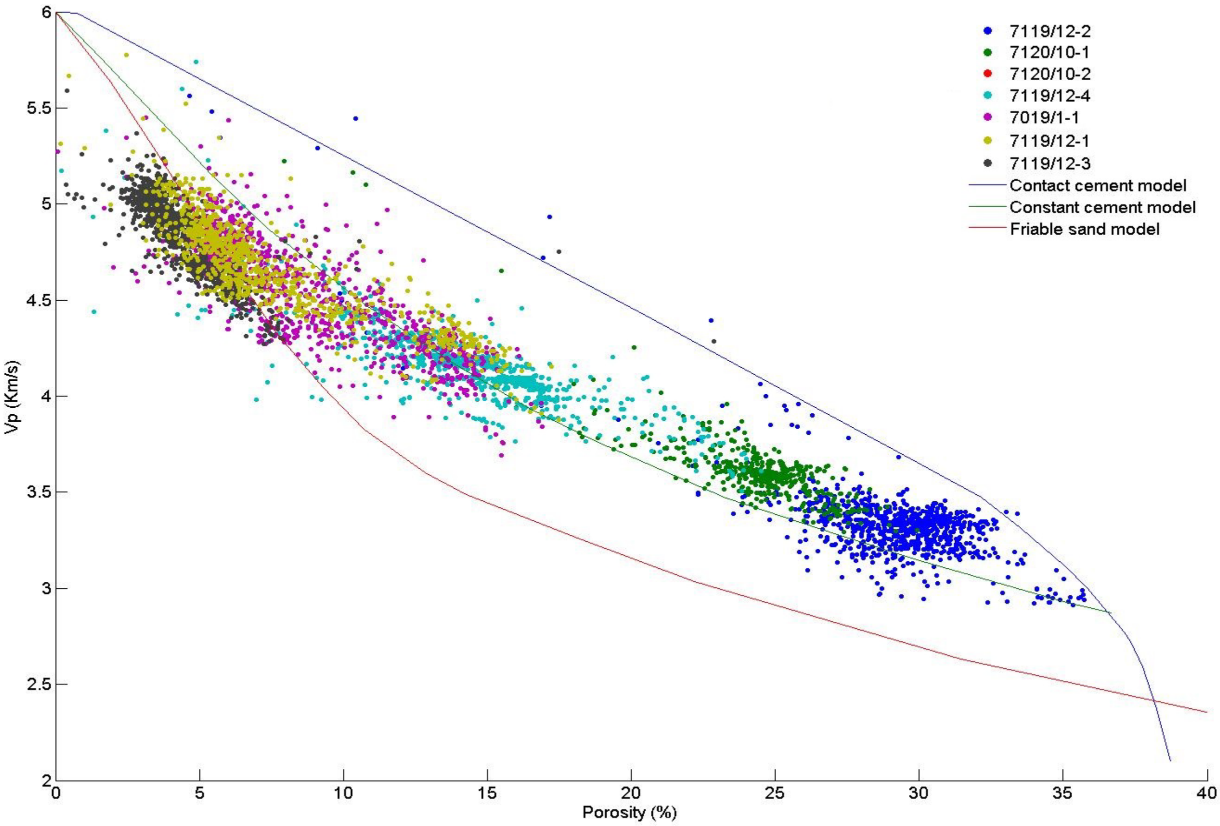

Figure 5.1 Vp-Porosity cross plot for Knurr and Stø Formation sandstone (Vshale<=0.3) for all the wells available.

In order to compare the different characteristics of each well, the individual well data are plotted seperately and coloured by shale volume in Figure 5.2. Well 7119/12-2 is the shallowest one and the total porosity varies from 25% to 35% (Figure 5.2-A). Most of the data have higher Vp values than the constant cement model curve may possibly mean there are at least 2% cement in the rreserovir sands. Well 7120/10-1 is the second shallowest well with porosity vary from 17% to 27% (Figure 5.2-B). Almost all the data points are located between the constant cement and contact cement lines. This indicates that more cement may present here than in well 7119/12-2. The shaly sandstones have less Vp than the pure sandstones in this well.

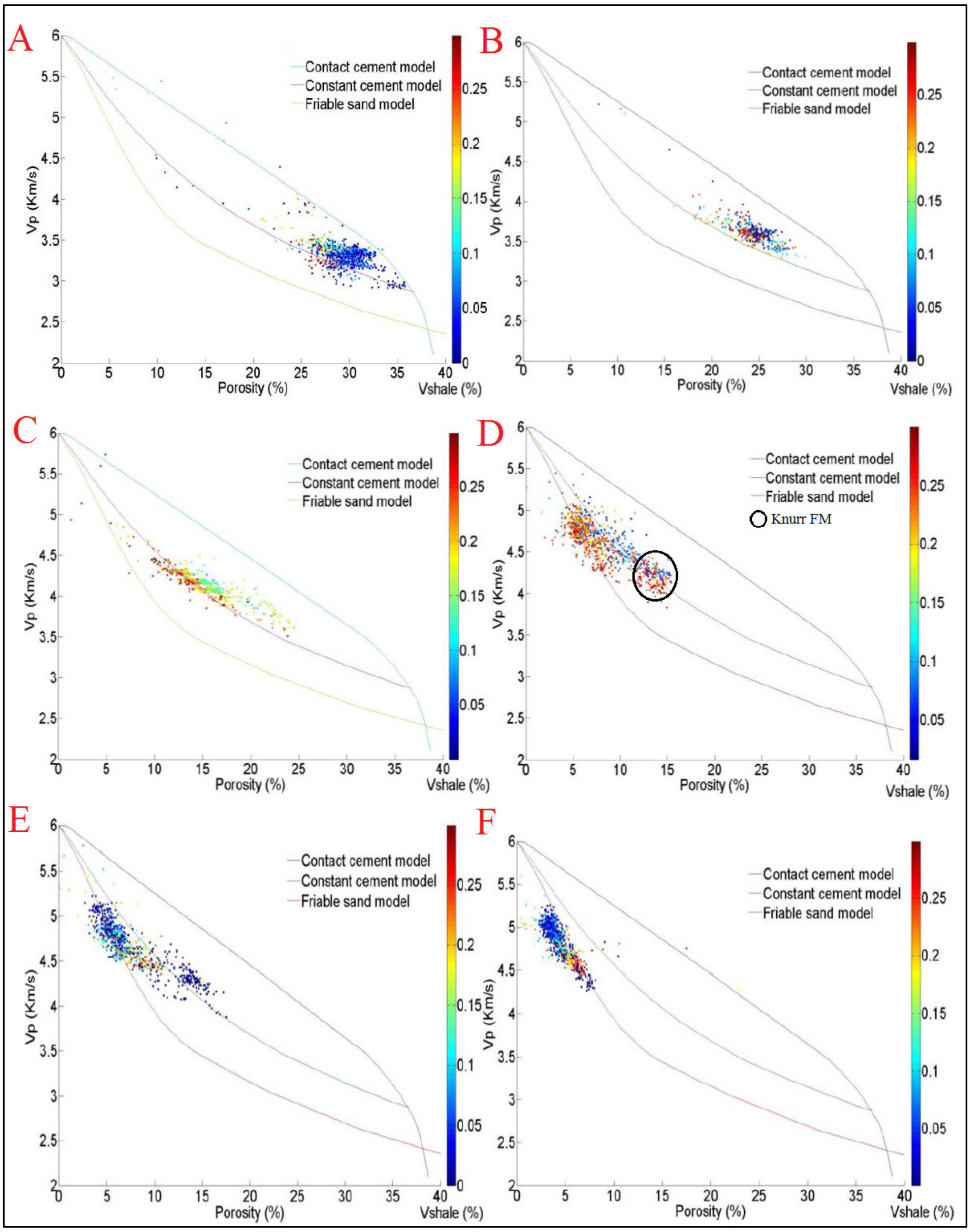

Figure 5.2 Vp-Porosity cross plot for Knurr and Stø Formation sandstone, coloured by Vshale (Vshale<=0.3), (A: 7119/12-2, B: 7120/10-1, C: 7119/12-4, D: 7019/1-1, E: 7119/12-1, F: 7119/12-3).

The Stø Formation in well 7119/12-4 has widely varying porosity values, from about 5% to 24% (Figure 5.2-C). The shaly sandstone data points are located below the constant cement line while the pure sandstone data points are above it. The Knurr Formation in well 7019/1-1 is gas saturated. The total porosity in this formation ranges from 12% to 15%. From Figure

5.2-D, the Knurr Formation data points located on the constant cement model. Considering the gas effect, there could be much more cement than expected. It is also the same for the Stø Formation (3% - 10% porosity) in this well. In Figure 5.2-E, the high porosity (8% - 18%) data points in 7119/12-1 are water saturated according to the petrophysical analysis results. They are located on the constant cement model line. The low porosity (1 - 8%) zones of the reservoir are located on the friable sand line. Almost all the data points in 7119/12-3 are located below the friable line (Figure 5.2-F).

Pore-fluid effects could be avoided if the rock-physics diagnostics are performed in the Vs - porosity domain (Avseth et al., 2010). Well 7119/12-4 is analysed as the only well with Vs measurements in this study (Figure 5.3). Four kinds of porosity calculation methods are compared here because they could lead to different results. Both sandstone and shale in Stø Formation is included in the rock physics template. The locations for shale data points change greatly due to different porosity calculation methods, but the sandstone data points are located on the contact cement model line in these four plots.

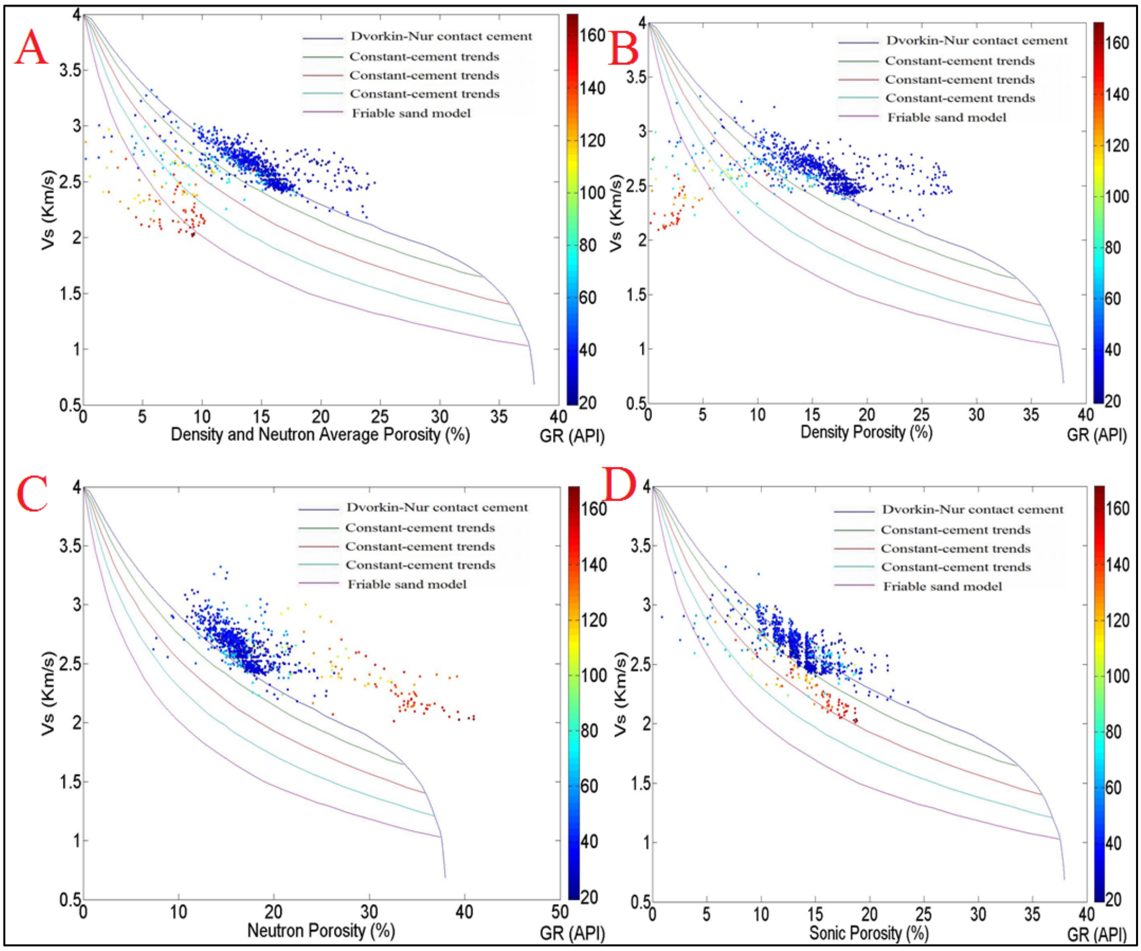

Figure 5.3 Vs-Porosity cross plot of 7119/12-4 Stø Formation (include sandstone and shale), (A: Vs-Density and Neutron average porosity, B: Vs-Density porosity, C: Vs-Neutron porosity, D: Vs-Sonic porosity).

In Figure 5.4, the cementaion and sorting are estimated by using Vs valuse drived from published Vp-Vs relationships. The data points are close to the contact cement model line. The estimated cement contents in Figure 5.4 are less than in Figure 5.3. The values derived from published papers have the ralationship as follows:

Vs from Han’s equation > Vs from Greenberg and Castagna’s equation > Vs from Krief’s equation > Vs from Mud rock equation.

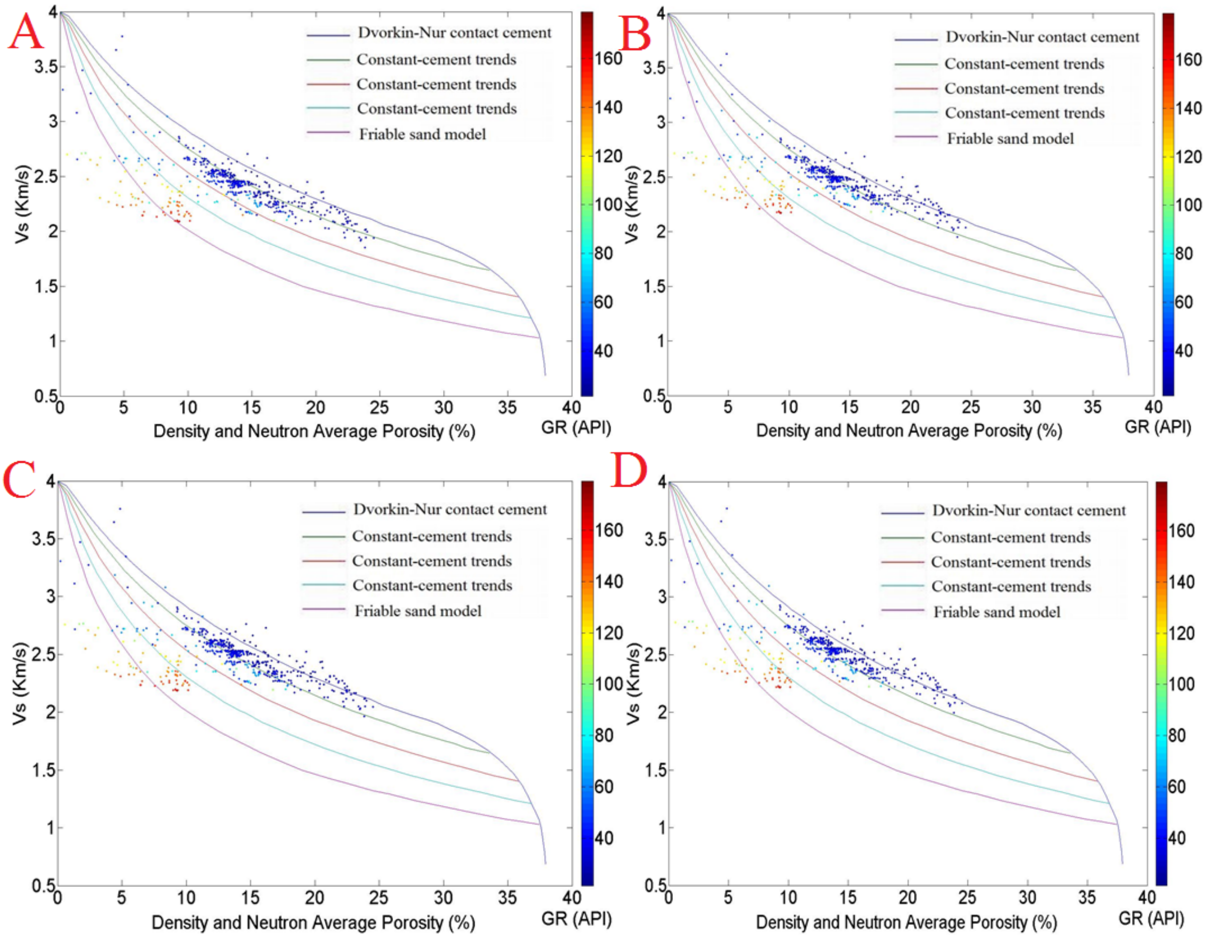

Figure 5.4 Vs-Porosity cross plot of Stø Formation from well 7119/12-4, A: Vs values derived from Mud rock equation (Castagna et al., 1985), B: Vs values derived from Krief et al. (1990) equation, C: Vs values derived from Greenberg and Castagna (1992) equation, D: Vs values derived from Han et al. (1986) equation.

5.1.2 Vs and density prediction

In Figure 5.5, the measured Vp and Vs data from different formations of well 7119/12-4 are cross plotted. The data are colour coded by NPHI. The Vs values of sandstones are much higher than that predicted from published popular equations. Most of the shale data points are on or lower than published trend lines except Hekkingen shale. Different trends for different porosity can be observed from Figure 5.5. Using calculated S-wave velocities may results in accurate predictions of reservoir properties (e.g. AVO behaviour) and ultimately guide erroneous seismic interpretations. The empirical relations obtained from data by regression analysis are as follows:

$$Vs = 0.7198*Vp-0.3024 \quad (NPHI < 0.05)$$
$$Vs = 0.6829*Vp-0.1750 \quad (0.05 < NPHI < 0.1)$$
$$Vs = 0.7399*Vp-0.4524 \quad (0.1 < NPHI < 0.15)$$
$$Vs = 0.5301*Vp+0.3963 \quad (0.15 < NPHI < 0.2)$$
$$Vs = 0.7321*Vp-0.4543 \quad (NPHI > 0.2)$$

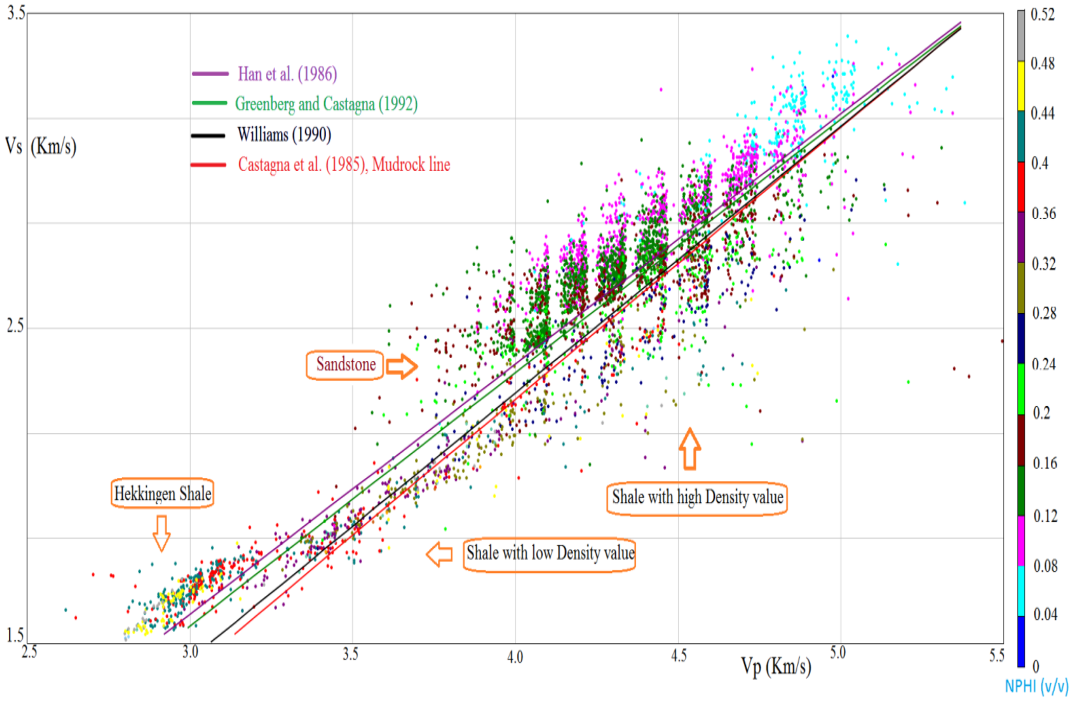

Figure 5.5 Vp-Vs cross plot in well 7119/12-4, the data are coloured by Neutron porosity.

In Figure 5.6 the Vp and density values of Knurr and Stø Formations of all wells are plotted. Shales and sandstones show two distinct trends in Vp-density domain. The Gardner's equation is also plotted in the figure for comparison. It is clearly observed that the Gardner equation does not fit most of the sandstone data, especially in high porosity/low density zones. An empirical equation for sandstone is obtained for the zones without density measurements:

$$\text{Density} = \text{Vp} * 0.23 + 1.5$$

Density is in g/cm^3 and Vp is in Km/s.

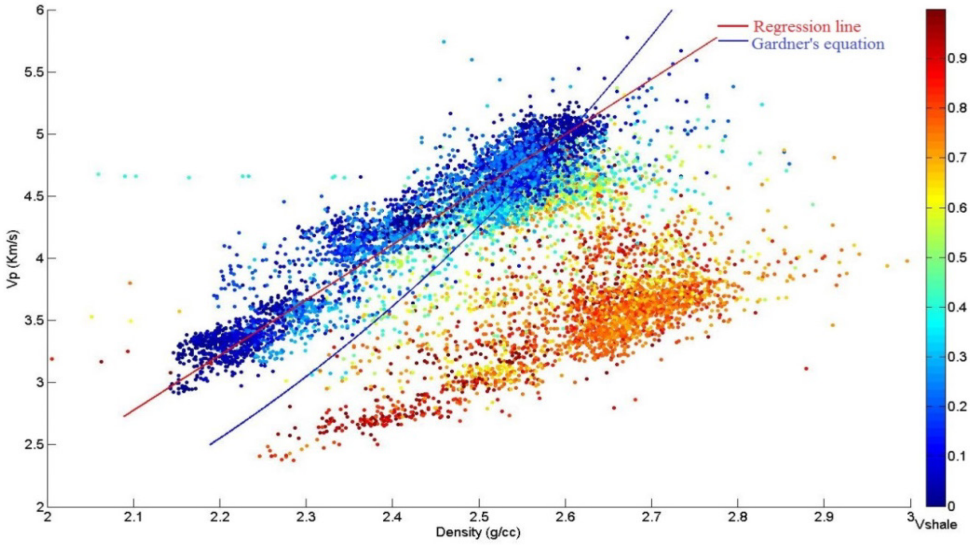

Figure 5.6 Vp-Density cross plot of Kunrr formation and Stø Formation in all the wells, the data are coloured by shale volume.

5.1.3 Construction of rock physics templates

5.1.3.1 Porosity versus Vp

Vs measurments are not available in most of the wells in this study. Therefore, the relationship between Vp and porosity is analysed here for all the wells except 7120/10-2 (Figure 5.7). There are only a few measurments in 7120/10-2 due to engineering problems. Han et al. (1986) mentioned that Vp is linearly related to porosity and clay content. In Figure 5.7, the data are plotted with Han's relationship at confining pressure of 40 MPa and 20 MPa.

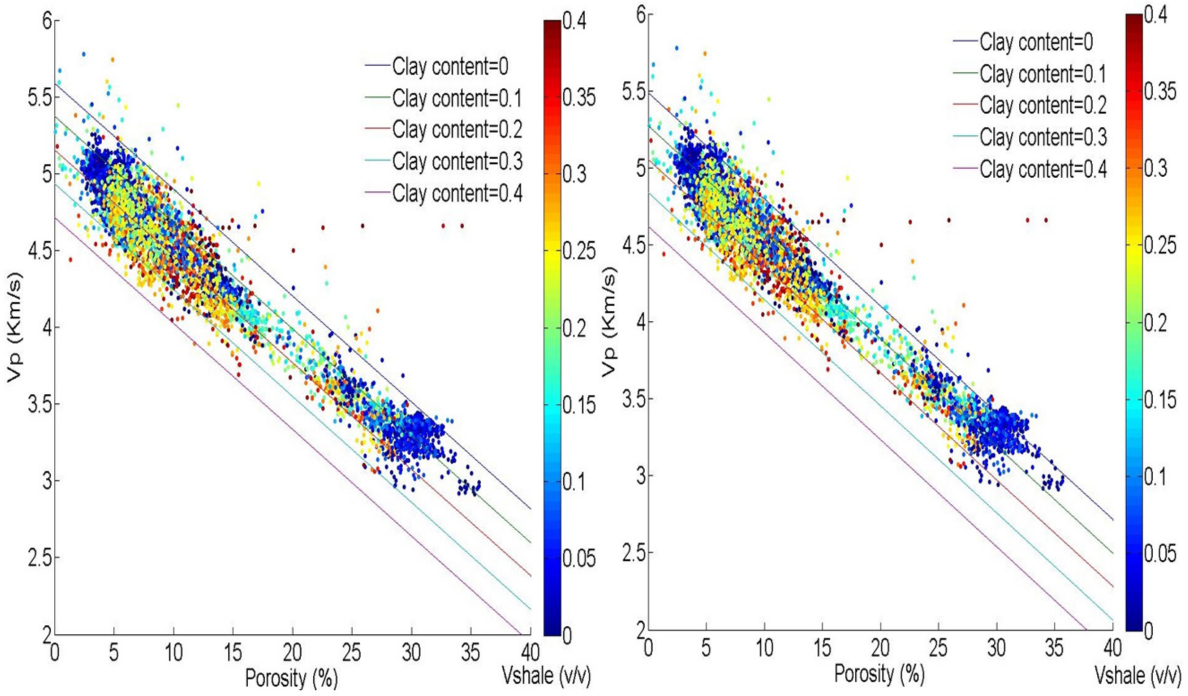

Figure 5.7 Vp-Porosity cross plot for Knurr and Stø Formation sandstone (Vshale<=0.4) in all the wells available, with Han's equation at 40 Mpa (left) and 20 Mpa (right).

5.1.3.2 Vp/Vs versus Ip

The Vs values are estimated from Mud rock equation (Castagna et al., 1985) for the Vp/Vs-IP cross plot of all the wells available (Figure 5.8). Sandstone and shale could be separated from this template, but the difference between these two lithologies is not so obvious, especially in the high P-impedance zones. The fluid effect is also not obvious in this cross plot. All the sandstone data points are on the water-saturated line.

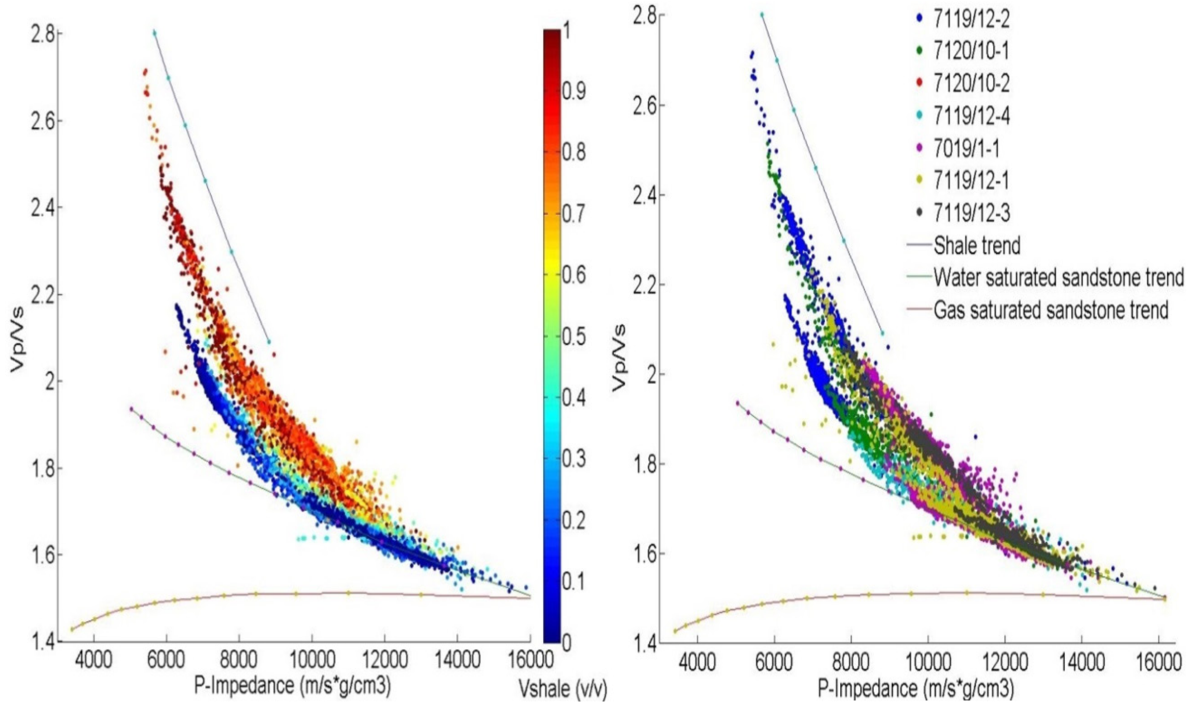

Figure 5.8 Vp/Vs-Ip cross plot for Knurr and Stø Formations from 7 wells colour-codded by shale volume (left) and well name (right).

In Figure 5.9, measured Vs data are compared with estimated Vs data in the cross plots. In the cross plot with measured Vs values, it is obvious that the sandstone and shale could be easily separated. The sandstone data points are located on the gas-saturated line. Using estimated Vs data (from Mudrock equation), shale and sandstone data points are close to each other. The sandstone data points are all located on water-saturated line.

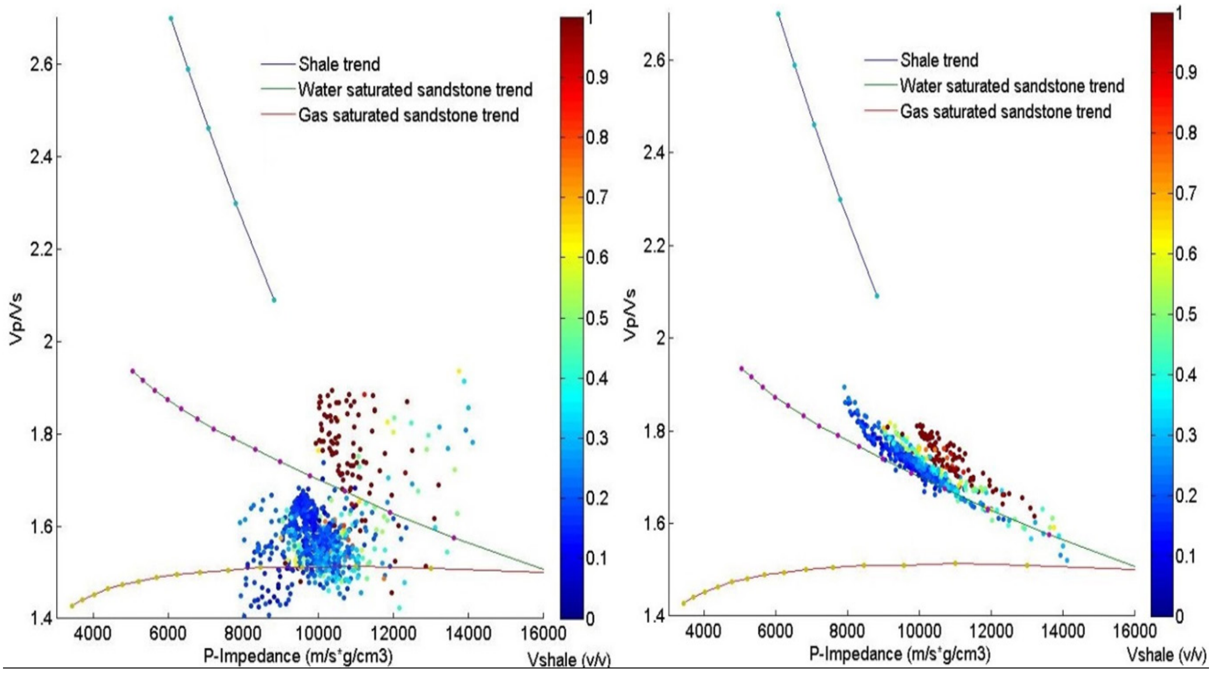

Figure 5.9 Vp/Vs-Ip cross plot for Stø Formation of well 7119/12-4, measured Vs data (left) and estimated Vs from Mud rock equation (right), colour-codded by shale volume.

5.1.3.3 LMR

In this study, the Lamé parameters are calculated from predicted Vs values from Mudrock equation (Castagna et al., 1985). The cross plot perfectly separates sandstone and shale in Figure 5.10 (left). The data points from Knurr and Stø Formations are coloured by well names, and these data can be separated by depth in Figure 5.10 (right).

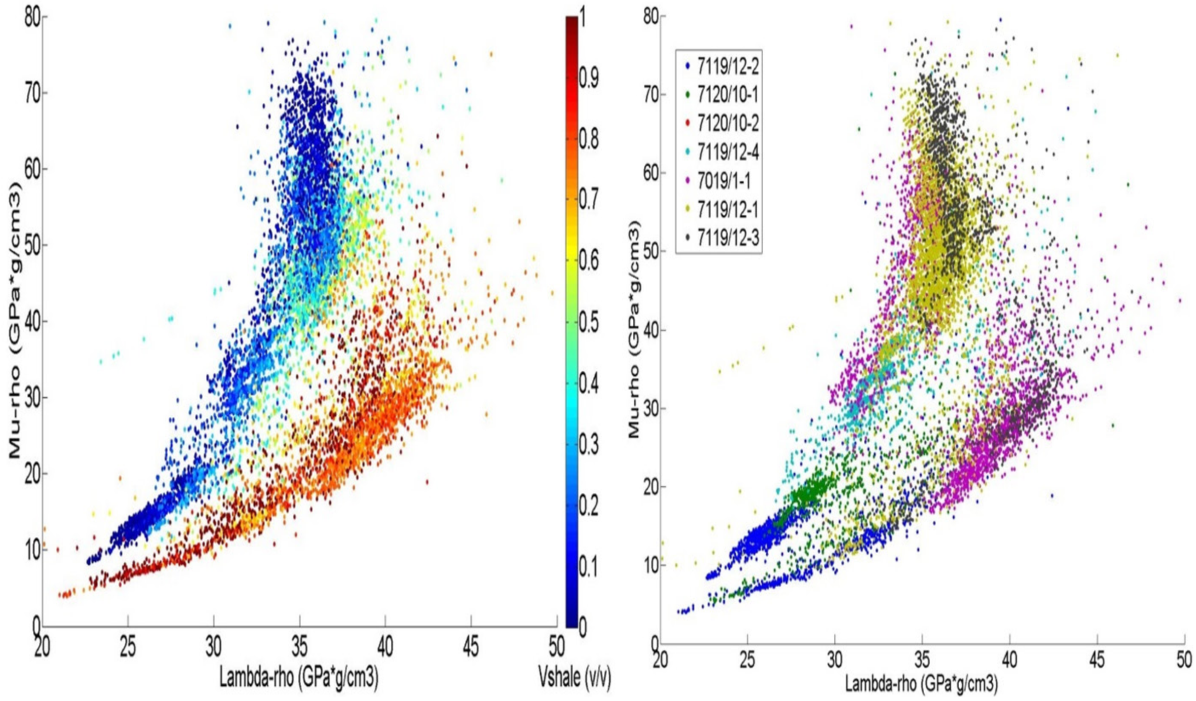

Figure 5.10 LMR plot for Knurr and Stø Formation of all the wells available, coloured by shale volume (left) and well name (right).

In order to compare the estimated Vs data with the measured Vs data, both of them are ploted together in Figure 5.11. The locations for shale are almost the same, but there is great difference between the sandstone points in these two plots. The trend of the sandstone data points are opposite to each other. The estimated Lambda-Rho (λρ) values are between 26 and 36 GPa*g/cm^3, compared to 0-26 GPa*g/cm^3 of the measured values. 0-20 GPa*g/cm^3 of λρ values are typical for gas bearing sandstones (Goodway, 2001). Therefore, the sandstone data points are mainly located in gas zones in Figure 5.11(left).

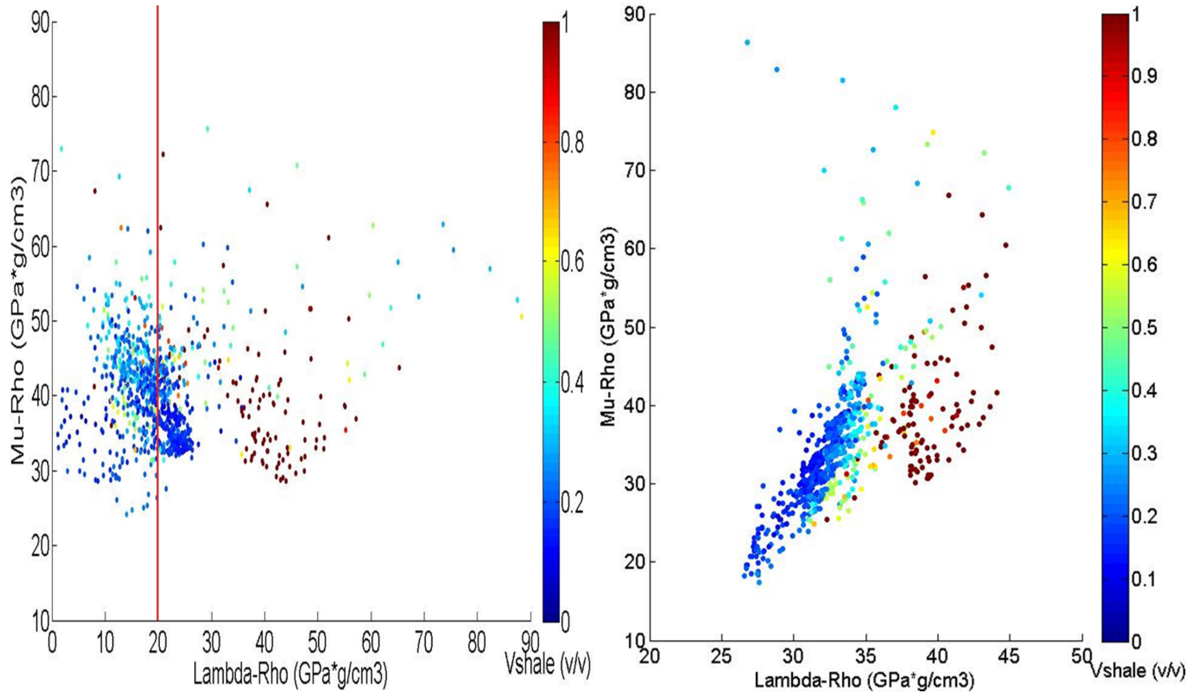

Figure 5.11 LMR plot derived from measured Vs (left) and estimated Vs from Mudrock equation (right) for Stø Formation from well 7119/12-4. Notice the different scale between the two pictures.

5.2 Discussion

5.2.1 The rock physics cement models

Based on the velocity-porosity cross plot and cement models, almost all the sandstones in Knurr and Stø Formations from all wells are cemented. In the shallowest well 7119/12-2, thin quartz overgrowths are also seen as the first stage of the quartz authigenesis (Olaussen et al., 1984). The uplift-corrected burial depth for Stø Formation top in this well 7119/12-2 is about 2272 m. Quartz cementation could have started at this depth and temperature (Bjørlykke and Egeberg, 1993). With increasing burial depth and temperature, the other wells should have more cements than 7119/12-2. The porosity values vary wildly in well 7119/12-4, 7019/1-1 and 7119/12-1 because of the complex lithology and diagenetic processes.

The low porosity (less than 8%) data points from deep wells (well 7019/1-1, 7119/12-1 and 7119/12-3) are located on the friable sand line. One of the possible reasons is that there is residual gas saturated in the sandstone pores. Thin section data and SEM data from published paper proved high amount of cement and secondary porosity in well 7119/12-1 (Olaussen et al., 1984). Another possible reason is that the sandstones deeper than 2.3 km are located in chemical compaction zones. In principle, the porosity decresed at this depth much faster than the shellower depth (Figure 5.12).

In well 7119/12-4, the different result between Vp-porosity template and Vs-porosity template could be caused by high measured Vs values (Figure 5.5).

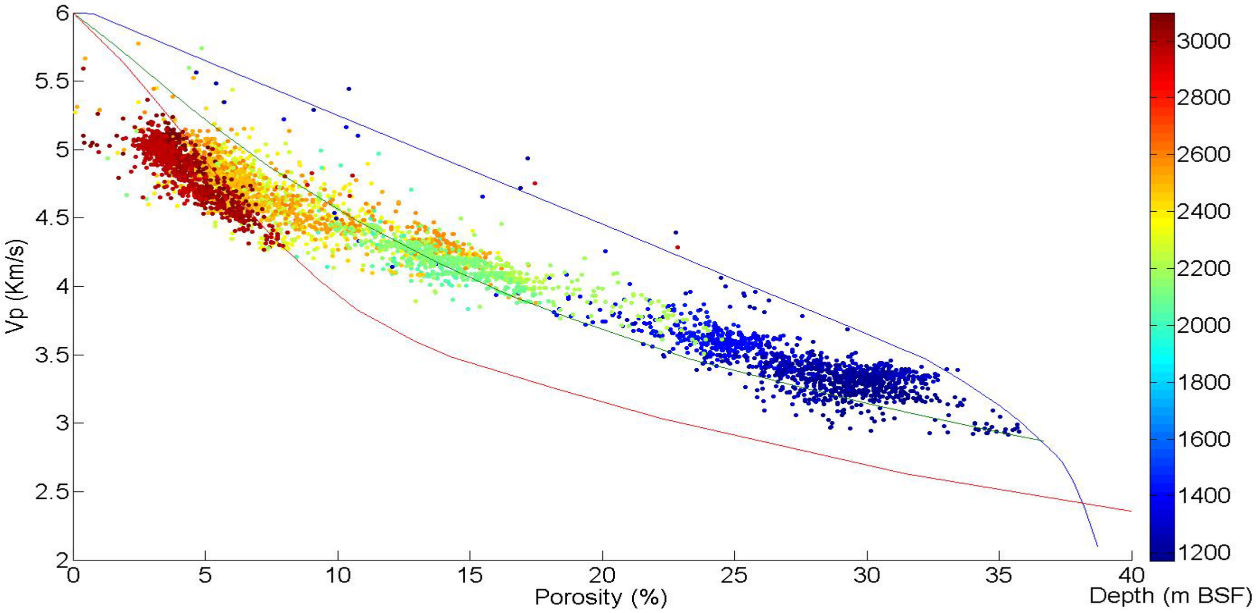

Figure 5.12 Vp-Porosity cross plot for Knurr and Stø Formations sandstone (Vshale<=0.3) for all the wells available, colour coded by depth.

5.2.2 Vs and density prediction

The Stø Formation can be divided into 4 zones based on all the information available in 7119/12-4 (Figure 5.13). The information in the red rectangle is well site geologist's description on NPD website (Table 5.1). After interpretation (Table 5.2), these core sample descriptions provide more information than the well logs.

Table 5.1 Core sample description in Stø Formation of 7119/12-4 (from NPD website).

Depth (m, RKB)	Sample type	Lithology description
2300.08	Side Wall Coring	100% SST, op-lt gy w-pl smky brn, f-md, hrd;
2365.5	Side Wall Coring	100% SST, op-lt gy w-pl smky brn, f-md, hrd ;
2387	Side Wall Coring	100% SST, op-lt gy w, congl;
2391.5	Side Wall Coring	100% SST, op-lt gy w, congl ;
2393.7	Side Wall Coring	100% SST, op-lt gy w, congl ;
2398	Side Wall Coring	100% SST, op-lt gy w, congl;
2425	Side Wall Coring	100% SST, op- lt smky gy, f-md;

The shale or shaly sandstone intervals in Stø Formation are coloured to green in the interpretation column. The measured Vs values in these intervals are quite close to the estimated Vs values. The Vp/Vs ratios are around 1.85, which is very different from the Vp/Vs of sandstones or shaly sandstones.

Table 5.2 The code explanation of the lithology description.

SST	sandstone	smky	smoky
op	opaque	brn	brown
lt	light	f	fine grain
gy	gray	md	middle grain
w	white	hrd	hard
pl	pale	congl	conglomerate

From the Figure 5.13, it is clear that the sandstones of Stø Formation can be divided into 3 categories based on Vs, porosity, resistivity and Vp/Vs ratios. The cemented sandstones are coloured to yellow in the interpretation column. The resistivity values are high and porosity values are low. The Vs values are much higher than estimated from published equations. The Vp/Vs ratios are around 1.55, which are close to dry sandstone value (1.5) and pure quartz value (1.5).

The sandstones with conglomerates (coloured in blue) are characterized by high porosity and low Vp/Vs ratios (around 1.55). The lowest value could be 1.4, which is highly questionable for quartz sandstones. The Vs values are also much higher than expected. The resistivity, porosity and Vs logs vary wildly because of the complex lithology.

The fine to medium grain sandstones (coloured in red) are not as hard as the cemented sandstones (coloured in yellow). The porosity values are high and resistivity values are low. The Vs values are close to estimated ones. The Vp/Vs ratios are around 1.65. The separation between density porosity and sonic porosity could be caused by secondary porosity, which also exists in well 7119/12-1 (Figure Appendix-18).

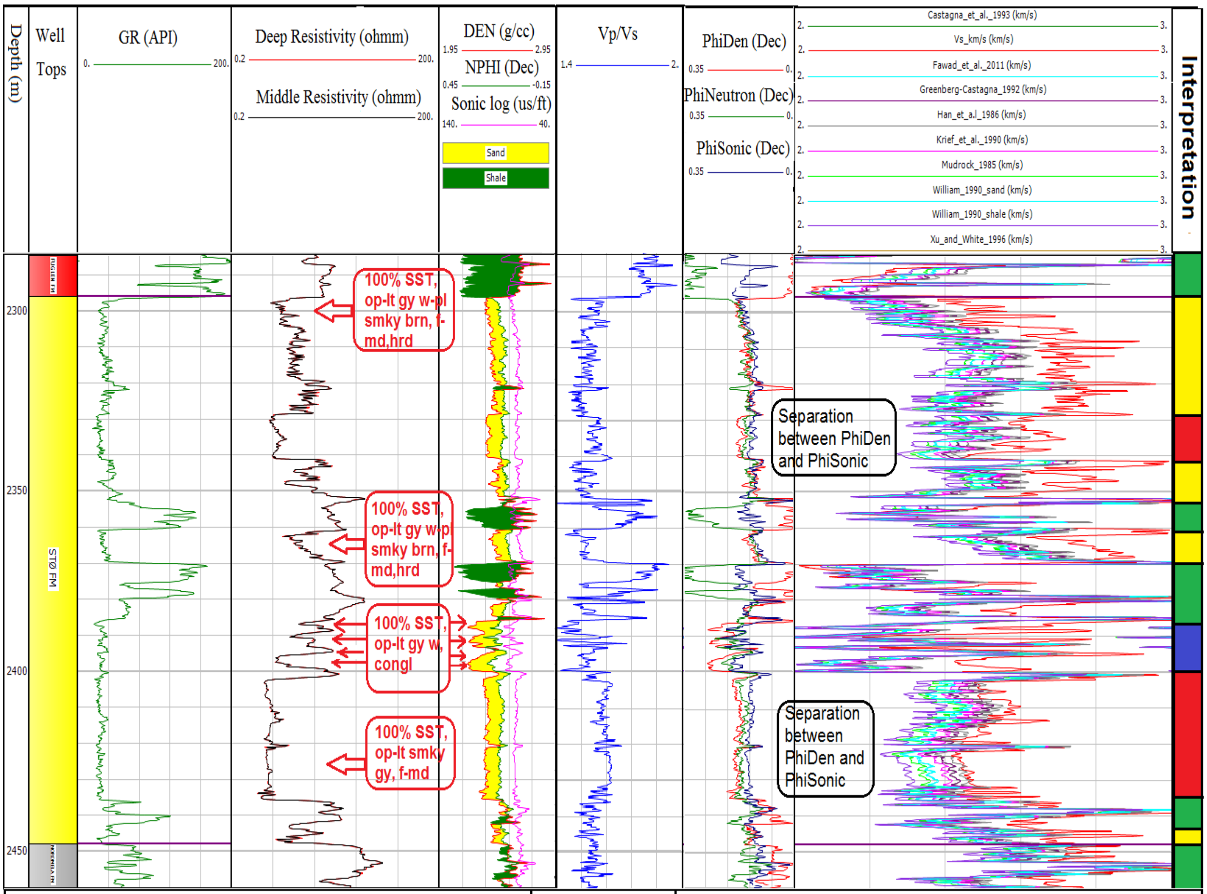

Lithology	Vp/Vs	Vs behavior
Shale or shaly sandstone	Around 1.85	Close to estimation
Fine-middle grain sandstone, cemented, hard	Around 1.55	Much higher than estimation
Sandstone with conglomerate	Around 1.55	Much higher than estimation, fluctuated wildly
Fine-middle grain sandstone	Around 1.65	Close to estimation

Figure 5.13 Measured and estimated Vs curves in Stø Formation of well 7119/12-4.

Marion et al. (1992) described the V-shape (porosity-Vshale) and inverted V-shape (Vp-Vshale) behaviour in sand-clay mixtures. The relationship between Vs and Vshale are similar to that between Vp and Vshale. This phenomenon is also found in this study (Figure 5.14).

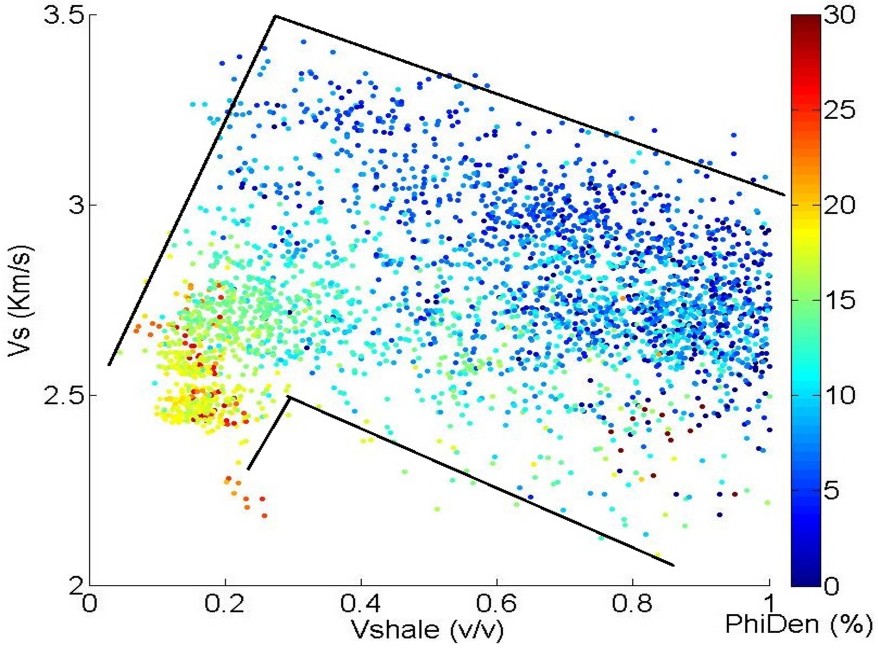

Figure 5.14 Vs-GR cross plot of Stø, Nordmela, Tubåen and Fruholmen formations of well 7119/12-4.

As discussed above, the Vs values vary with cementation, porosity, Vshale and lithology. Micro factures caused by uplift and erosion is another important factor. According to Castagna et al. (1985), the micro fractures in water saturated sandstone will decrease Vp and Vs, but the change of Vp/Vs ratio is not obvious. The other possible reasons could be related to sandstone texture (packing), pore pressure, confining pressure and logging equipment error.

In Figure 5.15, the data points deviated from the regression line are the sandstones with conglomerate in well 7119/12-4. Most of the sandstones in Stø Formation in this well have higher Vp values than expected from the regression line. There is difference between the regression line and Gardner's equation. Therefore, the local derived empirical relationship is more accurate and useful.

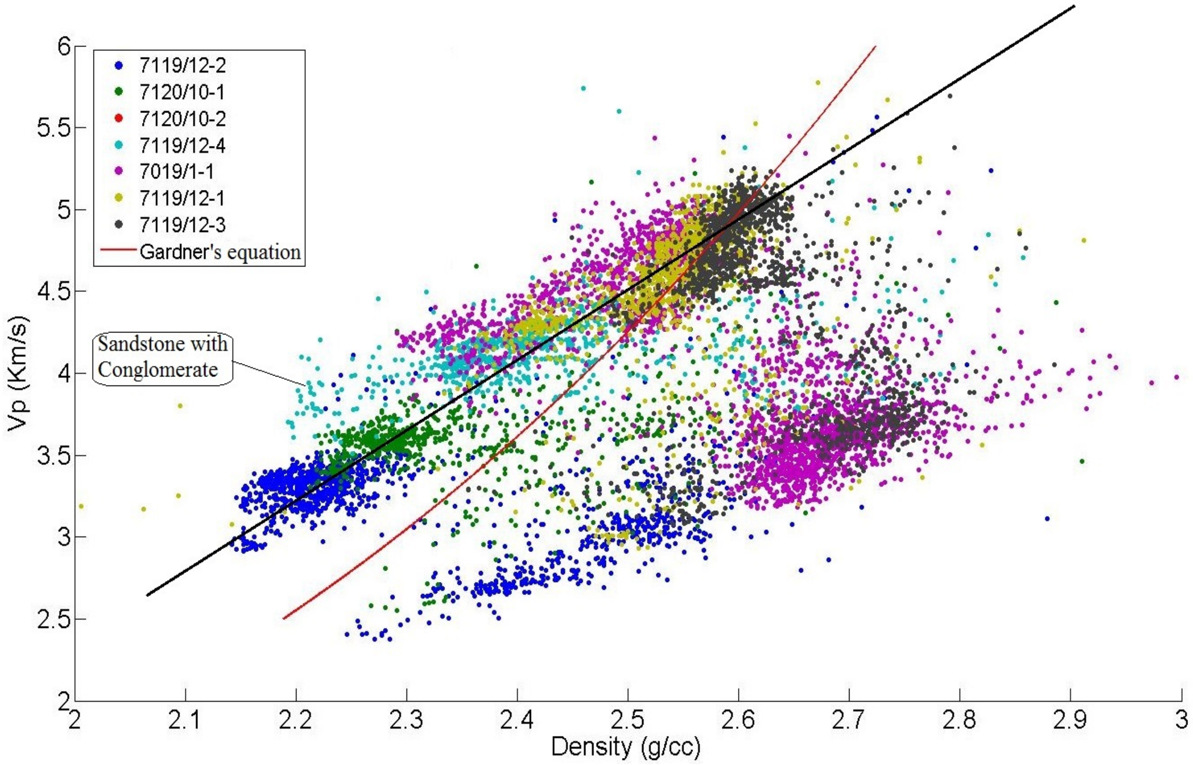

Figure 5.15 Vp-Density cross plot of Kunrr formation and Stø Formation in all the wells, the data are coloured well names.

5.2.3 Construction of rock physics templates

In Figure 5.7, Han's relationship is not matched very well with the data, especially in the low porosity region (from 2%-15%). These low porosity data are from three deeply buried wells (7019/1-1, 7119/12-1 and 7119/12-3) which are all affected by gas effect. The second reason is that the distributions of clays is not clear in these wells. Minear (1982) studied the differences between structural, laminal and suspended clay models. In the suspended clay model, clay has only a small effect on velocities, whereas both structural and laminal clays have significant and similar effects on velocities. The data points in Figure 5.7 fit Han's equation in 40 Mpa confining pressure (left) better than 20 Mpa (right), which corresponds to 4000 m burial depth., The higher Vp in sandstone than expected is caused by deep burial and latter uplift, which is similar to what we observed in Figure 2.18. Vp of sandstone is highly related to porosity. The smaller porosity values (Figure 2.17) caused higher Vp than expected.

The Vp/Vs versus Ip cross plot in Figure 5.8 shows the limit of using Mudrock equation for the construction of rock physics templates. The lithology can be barely divided and the fluid effect is not clear. Mud rock line is not a proper equation for separating shale and sandstone, because this equation is derived for both of them. Due to the absence of measured Vs, pore fluid type could not be distinguished from Figure 5.8. The lower limit of shale data points (around 1.75) is much lower than the lower limit (2.08) of calculated shale trend line. This is because in the deep wells, the Vp of shale are around 4 km/s. This value is larger than mineral value of 3.41 km/s for "Gulf clays" (Tosaya, 1982). The upper limit of sandstone points (around 2.1) is much higher than the upper limit (1.93) of calculated sandstone trend line. According to Mudrock equation, 3 Km/s Vp will corresponding to 1.41 Km/s Vs, which will lead to 2.12 of Vp/Vs (Figure 5.8). According to the data from Pickett (1963), Vp/Vs is about 1.9 for limestone and 1.8 for dolomite. Sandstones showed a variation of velocity ratio from about 1.6 to 1.75. This confirms that using Mudrock equation for high porosity sandstone could be questionable.

In the LMR cross plot coloured by depth (Figure Appendix-15), the incompressibility and rigidity are increased by depth because of compaction. There is a break of trend for sandstone data points in well 7019/1-1, 7119/12-1 and 7119/12-3. This phenomenon could be explained by Figure 5.16, in which the data points are coloured by deep resistivity. The incompressibility (λ) is decreased by the gas in pores (high resistivity values). The fluid cut-off line (in red) is deviated from the water saturated sandstone trend (in green).

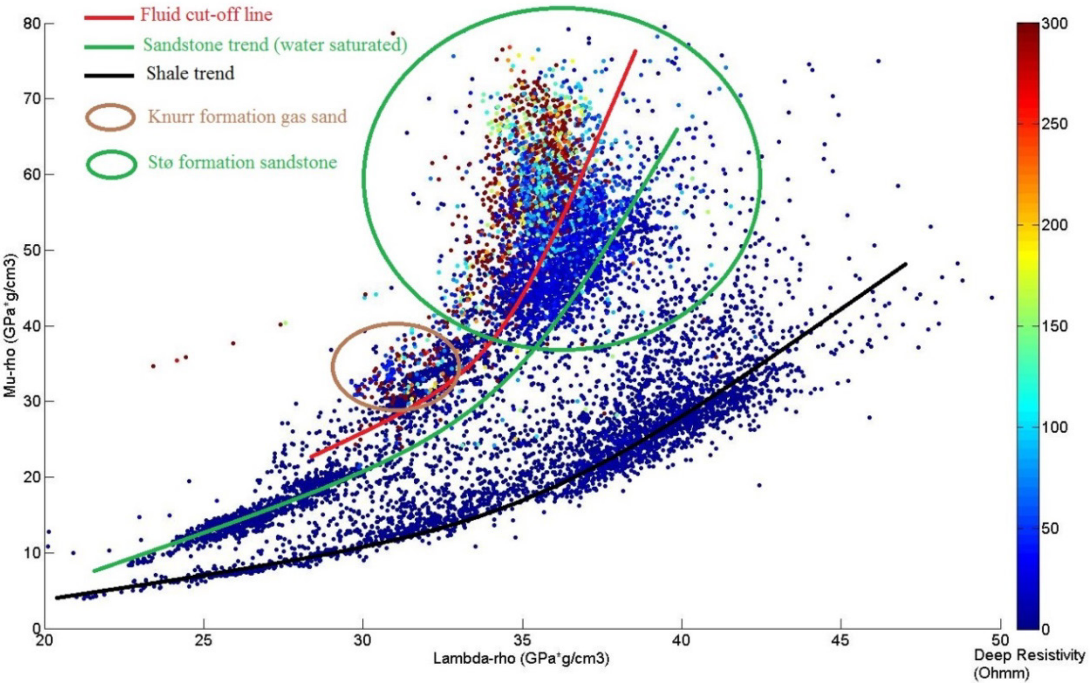

Figure 5.16 LMR plot for Knurr and Stø Formation for all wells (coloured by deep resistivity).

The interpretation results in Figure 5.16 shows that LMR cross plot are very useful for lithology and fluid discrimination. It could also give us information about the rock properties related to elastic moduli. Therefore, LMR cross plot is better in lithology and fluid discrimination than Vp/Vs versus Ip cross plot. The measured Vs data in well 7119/12-4 show "false gas effect" on both the cross plots shown above. This is caused by the higher Vs values and lower Vp/Vs ratios than expected.

5.3 Uncertainty analysis

In the cement model analysis, the Vp values should be corrected by fluid substitution method (Gassmann, 1951). The measured Vs values in 7119/12-4 might be questionable as they are higher than expected. This would definitely affect the rock physics diagnostic results and AVO modelling. The moduli, density and velocity data of "Gulf clays" in Table 3.4 are not suitable for the construction of the rock physics templates, but could be a useful reference in the absence of a better choice. The use of Mudrock equation for high porosity sandstones might be again questionable.

Chapter 6 AVO modelling

This chapter includes the AVO modelling results, discussions, sensitivity analysis and uncertainty analysis. Knurr Formation and Stø Formation are analysed and discussed separately. Different water saturation, wavelets and block sizes are used to examine their effects to AVO modelling. The uncertainties for the results are discussed briefly.

6.1 Results

6.1.1 AVO signature of Knurr Formation

The Sonic and Density logs for Knurr Formation reservoirs are only available in well 7019/1-1. The comparison between well logs and synthetic seismogram (before and after the fluid substitution) are shown in Figure 6.1. The P-impedance increases at the boundary of the cap and reservoir rocks (around 2000 m below sea floor). The reflections are peaks at this boundary on the synthetic seismograms. The Vp/Vs ratio of gas saturated situation is smaller than that of brine saturated scenario (Figure 6.1).

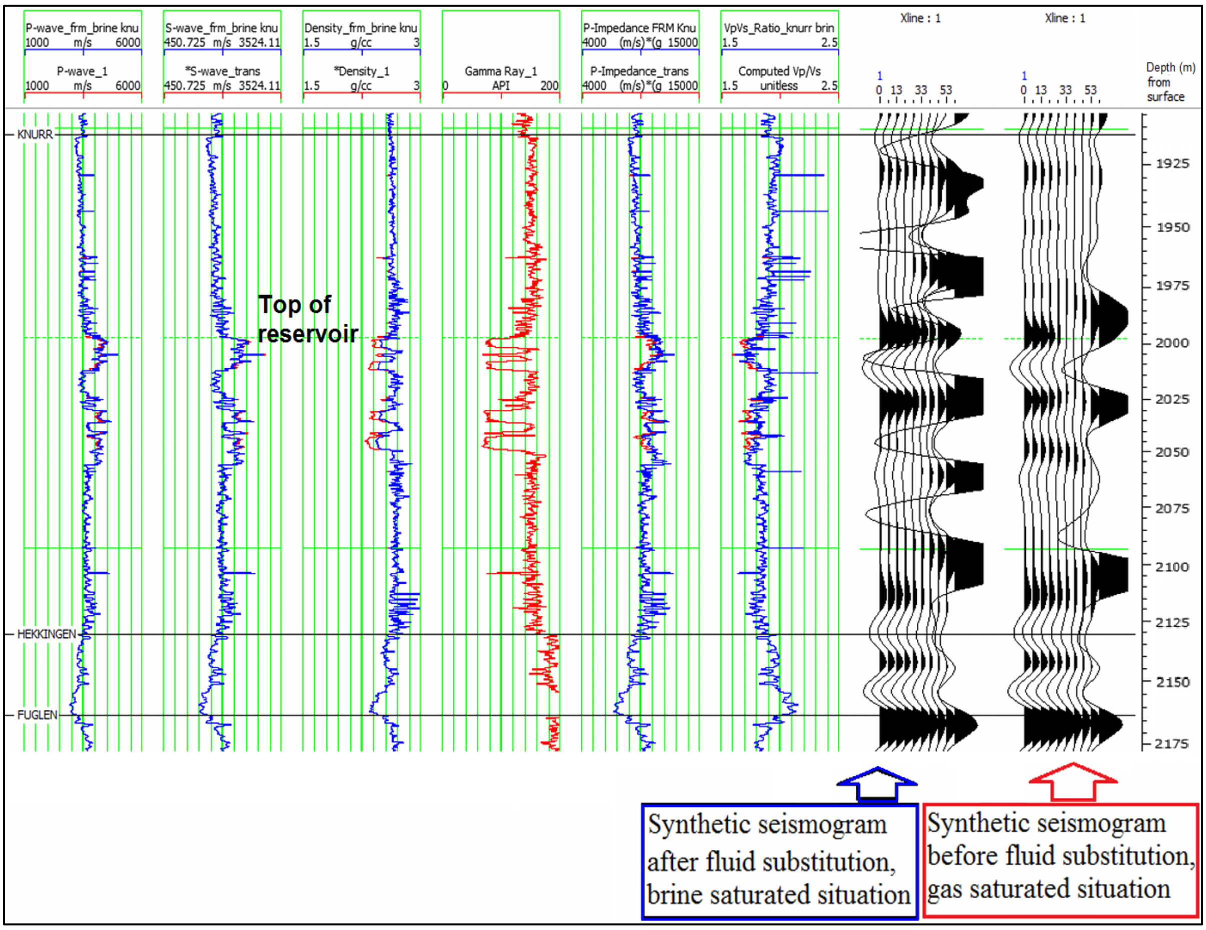

Figure 6.1 A comparison between well logs and synthetic seismogram (using Ricker wavelet), red curves are original well log data with gas saturated in the reservoir, bule curves are the logs after fluid substituition (brine saturated situation).

With the help of fluid substitution, gas saturated situation are compared with brine saturated situation in Figure 6.2. In both situations Class I AVO anomalies observed according to the classification standards (Castagna et al., 1998). The red spot (gas-saturated situation) is in the lower left direction compared to the blue spot (brine-saturated situation) in intercept-gradient crossplot.

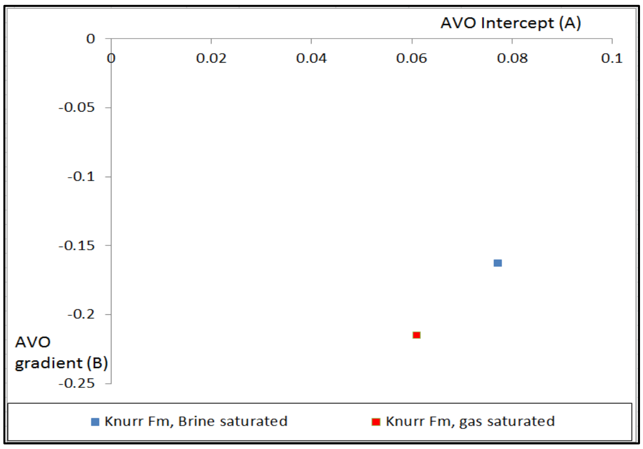

Figure 6.2 AVO cross plot for the top of Knurr Formation (both brine and gas saturated situations).

6.1.2 AVO signature of Stø Formation top surface

In order to compare the AVO signature of brine- and gas-saturated reservoirs, the fluid substitution (Gassmann, 1951) are performed for all the 6 wells that penetrated the Stø Formation. The results of I-G analysis are shown in Figure 6.3, with blue dots representing brine-saturated reservoirs and red dots representing gas-saturated reservoirs. All the AVO classes (Class I, II, III and IV) are observed in 6 studied wells (Figure 6.3). All the gas saturated reservoirs show cluster that fall in the lower left corner compared to the brine-saturated data points (blue dots). This is not very obvious for deep wells like 7019/1-1, 7119/12-1 and 7119/12-3.

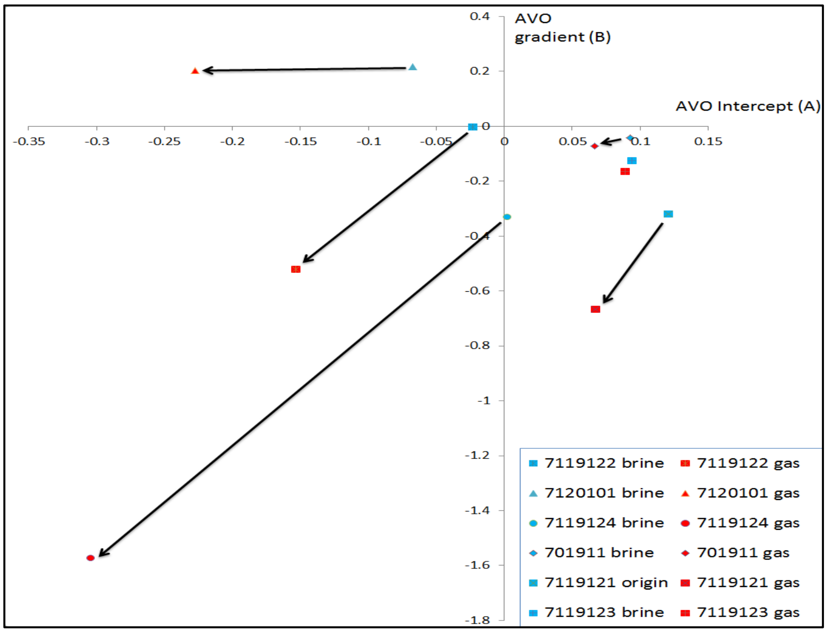

Figure 6.3 AVO intercept (A) versus gradient (B) for the top of Stø Formation in 6 wells (both brine and gas saturated situations).

The values of zero-offset reflection amplitude calculated by Zoeppritz (1919) equation are showed in Figure 6.4. In the 3 shallow wells (7119/12-2, 7120/10-1 and 7119/12-4), the reflection amplitude values are negative and get stronger when the pores are saturated with gas. That means the Stø Formation sandstones in these 3 wells have lower impedance than overlying shales.

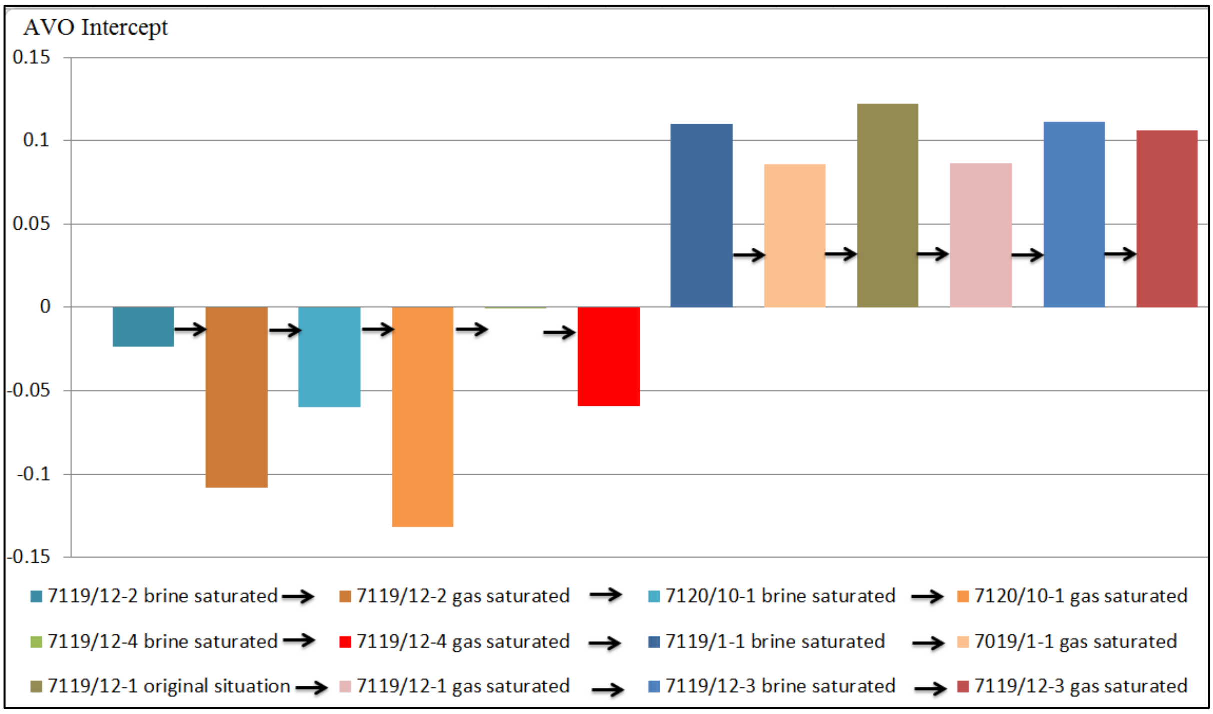

Figure 6.4 The zero-offset reflected amplitude values for the top of Stø Formation in 6 wells (both brine and gas saturated situation). Notice the near-zero value of brine saturated situation in well 7119/12-4.

In the 3 deep wells (7019/1-1, 7119/12-1 and 7119/12-3), the reflection amplitude values are positive and these become smaller when the pores are saturated by gas. In these 3 deep wells, the Stø Formation sandstones have higher impedance than overlying shales.

6.1.3 AVO signature of Stø Formation bottom surface

The AVO signatures of the Stø Formation bottom are displayed in Figure 6.5. The data from well 7119/12-3 is not shown here, because the depth of Stø Formation bottom is not specified. As expected, the gas saturated sandstone data points are deviating from the background brine trend. The AVO signatures of the Stø reservoir bottom are like a mirror of the reservoirs top. The deviation trends to the upper right direction, which is the opposite of the reservoir top.

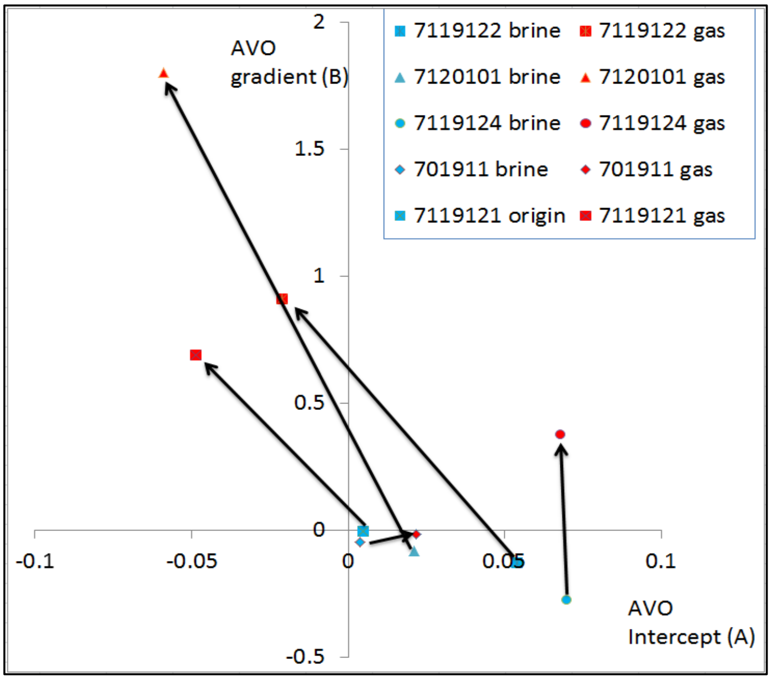

Figure 6.5 AVO intercept (A) versus gradient (B) for the bottom of Stø Formation in 6 wells (both brine and gas saturated situation).

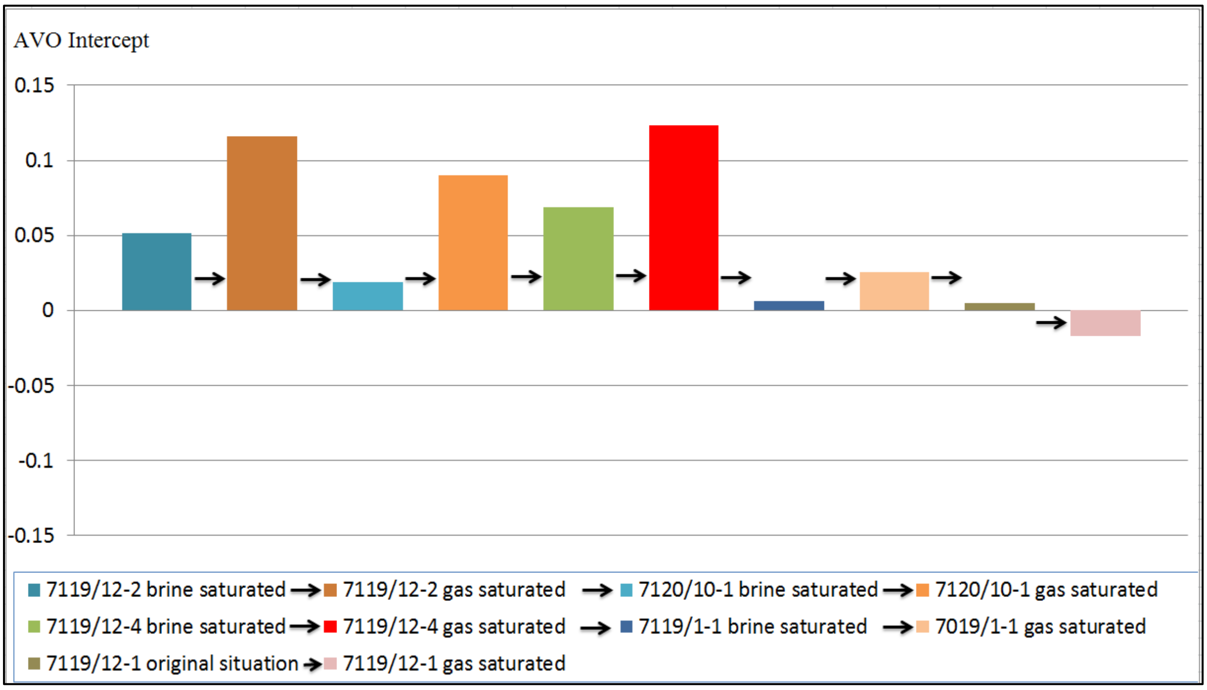

Figure 6.6 The zero-offset reflected amplitude values for the bottom of Stø Formation in 6 wells (both brine and gas saturated situation).

The calculated AVO intercept (A) parameters in Figure 6.5 are quite different from the Zoeppritz zero-offset reflected amplitude values in Figure 6.6. This will be discussed at the end of this chapter. Most of the reflected amplitude values are positive in Figure 6.6. The gas saturated reservoir scenarios have higher reflected amplitude than brine saturated scenarios.

6.2 Discussions

6.2.1 Knurr Formation

In Figure 6.7, Gardner's equation and linear Vp/Vs ralationship (Mudrock equation) are assumed. If Vp/Vs ratios increase and Vp decrease, the back ground trend will rotate counterclockwise (Castagna et al., 1998). Vp is the average of Vp across the interface $[(Vp_2+Vp_1)/2]$. Vs is the average of Vs across the interface $[(Vs_2+Vs_1)/2]$. Figure 6.1 and Figure 6.7 together explains what can be observed in Figure 6.2. In Knurr Formation sandstones (Figure 6.1), The Vp/Vs ratio of gas-saturated situation is smaller than that of brine-saturated condition. Low Vp/Vs ratio in gas-saturated situation causes both AVO intercept (A) and gradient (B) more negative than for the corresponding brine-saturated scenario. The Vp/Vs ratio decreases if the burial depth increase or the hydrocarbon saturation increase. This phenomenon can also be observed from Vp/Vs versus Ip template (Figure 5.8).

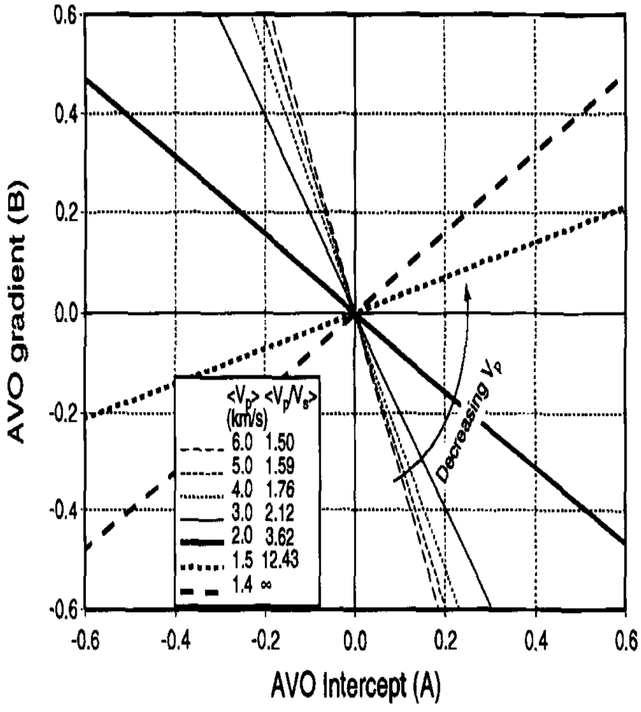

Figure 6.7 AVO cross plot from Castagna et al. (1998), Gardner's equation and linear Vp/Vs ralationship (Mudrock equation) are assumed.

6.2.2 Stø Formation

According to Castagna and Swan (1997), brine saturated sandstones will follow a well-defined "background" trend on AVO cross plots. Deviations from this background trend could be related to hydrocarbons or lithologic factors. This theory works well in this study (Figure 6.3).

When comparing Figure 6.4 with Figure 6.3, it should be noted that there are some differences between the "A" values used in the cross plot and the zero-offset reflected amplitude calculated by Zoeppritz (1919) equation. Sometimes the intercept of the regression line is not equal to the original zero-offset reflected amplitude value. Therefore, the Aki and Richards (1980) two term approximation may not be the same as Zoeppritz (1919) equation results.

According to SEG polarity standard, the reflections of Stø Formation top are negative troughs in the 3 shallow wells (7119/12-2, 7120/10-1 and 7119/12-4). The Stø Formation sandstones are “soft” events in these 3 shallow wells. As expected, the Vp and density decreased in gas-saturated condition compared to brine-saturated scenario. Therefore, the P impedance is lower and the reflection coefficient is higher when the pores are gas saturated (Figure 6.4).

The Stø Formation sandstones turn into “hard” events in the 3 deep wells (7019/1-1, 7119/12-1 and 7119/12-3). According to SEG polarity standard, the top of Stø Formation changes into a positive peak in these 3 wells (Figure 6.8). By adding gas into the pore system, Vp and density is decreased. Therefore, the reflection coefficient is also decreased.

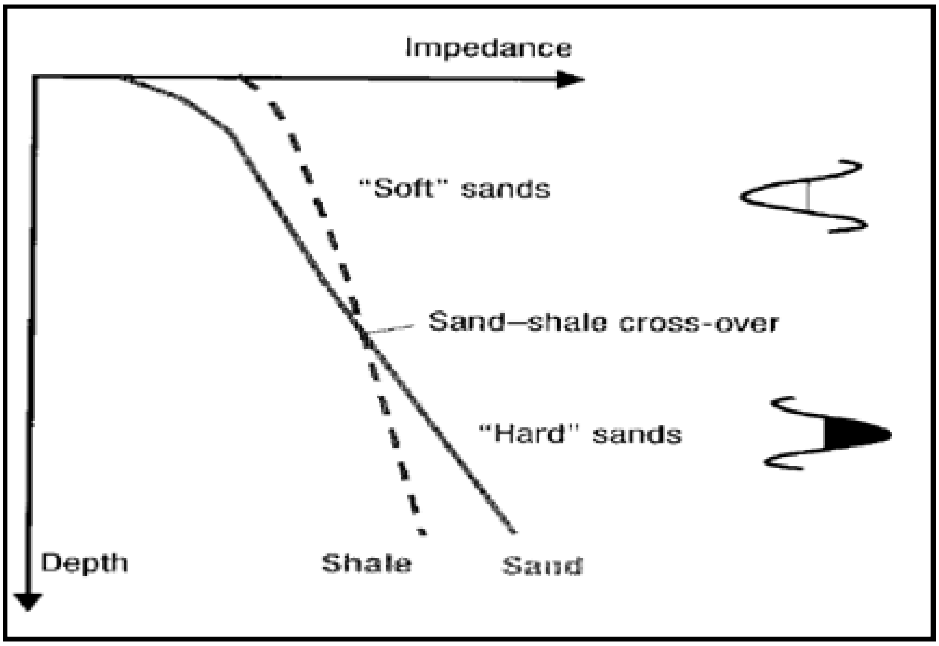

Figure 6.8 Schematic depth trends of sand and shale impedances, notice the “cross-over” (Avseth et al., 2005).

Average values of Vp and density are displayed in Figure 6.9. These values could explain the amplitude characters shown in Figure 6.4. Both the Fuglen Formation shale and Stø Formation reservoir are brine saturated in A and C subplots in Figure 6.9. In B and D subplots the reservoirs are gas saturated. It should be noticed that the parameters in Figure 6.9 are not the exact values at the interface of Stø Formation top. Therefore, there are differences between the calculated results in Figure 6.9 and the Zoeppritz zero-offset reflected amplitude in Figure 6.4.

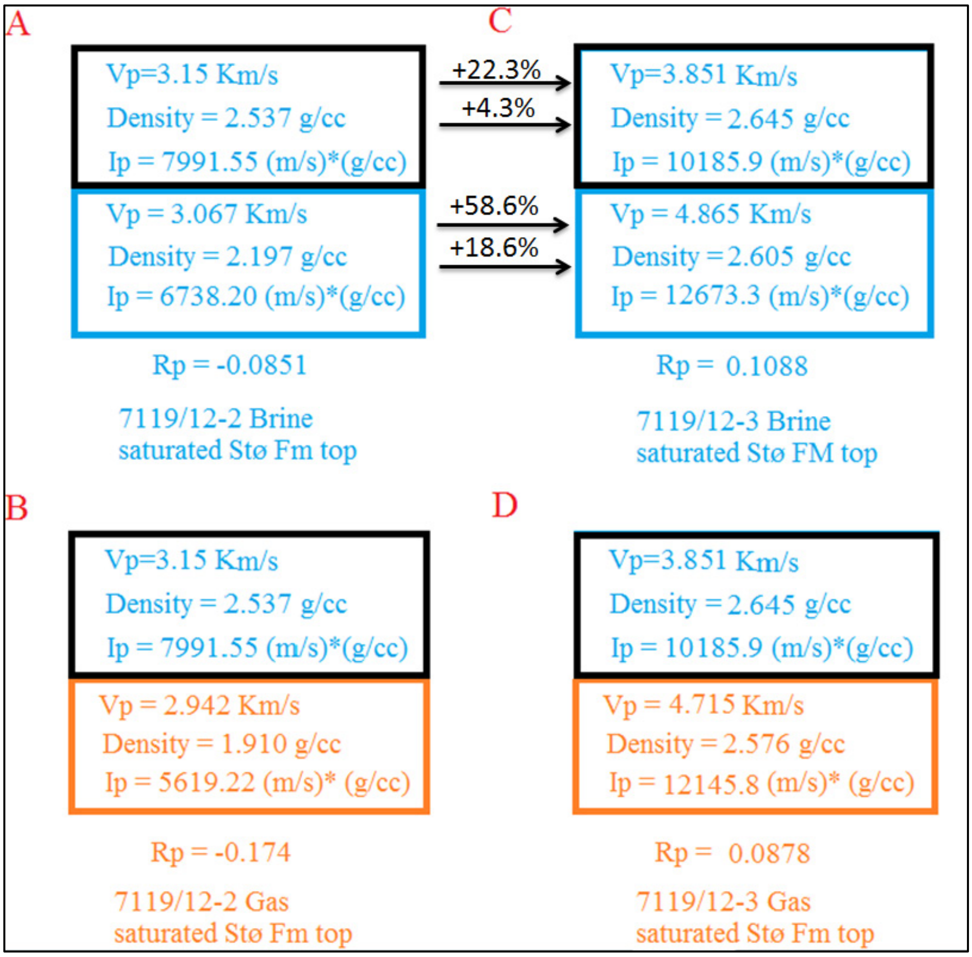
A
Vp=3.15 Km/s
Density = 2.537 g/cc
Ip = 7991.55 (m/s)*(g/cc)
Vp = 3.067 Km/s
Density = 2.197 g/cc
Ip = 6738.20 (m/s)*(g/cc)
Rp = -0.0851
7119/12-2 Brine saturated Stø Fm top
C
+22.3%
+4.3%
+58.6%
+18.6%
Vp=3.851 Km/s
Density = 2.645 g/cc
Ip = 10185.9 (m/s)*(g/cc)
Vp = 4.865 Km/s
Density = 2.605 g/cc
Ip = 12673.3 (m/s)*(g/cc)
Rp = 0.1088
7119/12-3 Brine saturated Stø FM top
B
Vp=3.15 Km/s
Density = 2.537 g/cc
Ip = 7991.55 (m/s)*(g/cc)
Vp = 2.942 Km/s
Density = 1.910 g/cc
Ip = 5619.22 (m/s)* (g/cc)
Rp = -0.174
7119/12-2 Gas saturated Stø Fm top
D
Vp=3.851 Km/s
Density = 2.645 g/cc
Ip = 10185.9 (m/s)*(g/cc)
Vp = 4.715 Km/s
Density = 2.576 g/cc
Ip = 12145.8 (m/s)* (g/cc)
Rp = 0.0878
7119/12-3 Gas saturated Stø Fm top

Figure 6.9 Average Vp and density values of Stø reservoir sandstones and Fuglen Formation cap rocks in wells 7119/12-2 (A and B) and 7119/12-3 (C and D).

The compaction effects is also shown in two wells 7119/12-2 and 7119/12-3 (Figure 6.9). The shale in Fuglen formation caused an increase of Vp (22.3%) and density (4.3%). The elastic parameters in Stø Formation increased much more than Fuglen formation. The Vp is increased by 58.6% and density is increased by 18.6%.

In 7119/12-2, Vp value decreased by 4.1% and density value decreased by 13.1% after fluid substitution. In 7119/12-3, the Vp value in the gas saturated formation was increased by 3.1% and density value was increased by 1.1% after fluid substitution. The big difference between the density behaviour is caused by the porosity differences in these two wells.

At the bottom of Stø Formation, most of the reflected amplitude values are positive (Figure 6.6). It means that the Nordmela formation have higher impedance than Stø Formation in the studied area. The gas-saturated reservoir scenarios have higher reflected amplitude than brine-saturated scenarios. In overlying gas saturated reservoir, the Vp, density and Ip values are decreased. Therefore, the reflection coefficient between the two formations is increased.

6.3 Sensitivity analysis

6.3.1 Effects of water saturation

The sensitivity study due to saturation change is performed using a shallowest well (7119/12-2) and a deepest one (7119/12-3). The typical average values of Vp, Vs, ρ, Ip, Is and Vp/Vs ratio of these two wells are shown in tables Table 6.1 and Table 6.2 to explain how these parameters changed due to saturation change.

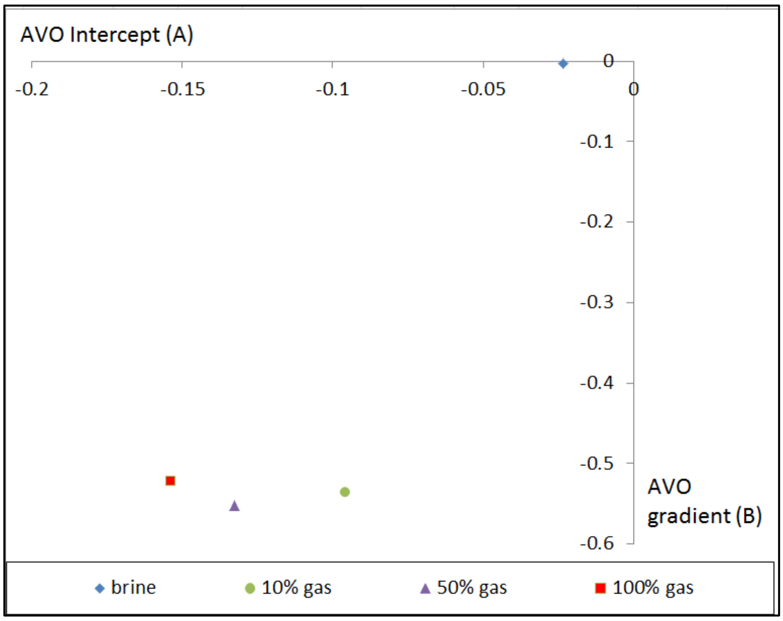

Figure 6.10 AVO intercept (A) versus gradient (B) at the top of the Stø Formation in the shallowest well 7119/12-2 with different saturation scenarios.

The AVO intercept and gradient decrease with increasing gas saturation in the pore of the Stø Formation in well 7119/12-2. As shown in Figure 6.10, a classical "Bright Spot" can be observed in this well. The three data points with different gas saturations are deviated far from the brine saturated data point. These three data points can be easily separated by AVO analysis due to less compacted, high porosity Stø reservoir sandstones in this shallowest well.

Table 6.1 Typical fluid substitution results at the top of Stø Formation in well 7119/12-2

Water saturation	Vp (Km/s)	Vs (Km/s)	ρ (g/cc)	Ip (Km/s*g/cc)	Is (Km/s*g/cc)	Vp/Vs
1	3.208	1.593	2.203	7.067	3.509	2.014
0.9	2.963	1.604	2.175	6.445	3.489	1.847
0.5	3.022	1.647	2.061	6.228	3.394	1.835
0	3.128	1.707	1.919	6.003	3.276	1.832

In Table 6.1, the density, Ip, Is and Vp/Vs gradually increase with increasing water saturation. Vs values decrease gradually with increasing water saturation. The relationship between Vs, density, Is and water saturation are linear. The relationship between Vp and water saturation is more complex (Figure 6.11, left). With decreasing water saturation, the Vp values decrease in the beginning and then increase. That is because P-wave velocity depends on the ratio of elastic modulus to density. The saturated bulk modulus for a rock is dependent on the relationship between dry rock bulk modulus, mineral grain bulk modulus, fluid bulk modulus and porosity (Gassmann, 1951). Fluid bulk modulus can be calculated by Reuss iso-stress model for fluid mixtures.

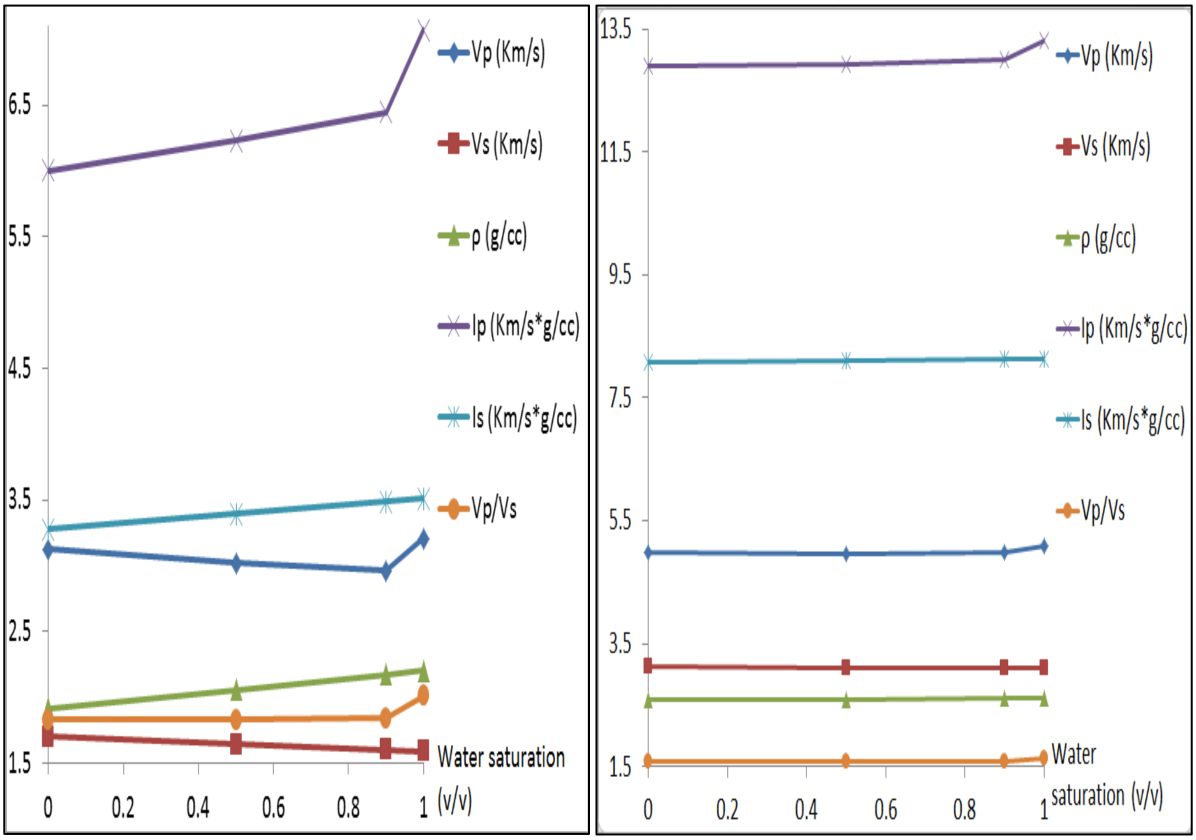

Figure 6.11 Elastic parameters at top of the Stø Formation in wells 7119/12-2 (left) and 7119/12-3 (right) with different water saturation scenarios, data from Table 6.1 and 6.2.

The relationships between the elastic parameters and water saturation in the deepest well 7119/12-3 are same as we observed in the shallow well 7119/12-2 (Figure 6.11, right) but the magnitude is much lower (Table 6.2). That is why all the data points on AVO cross plot are very close to each other (Figure 6.12).

Table 6.2 Fluid substitution results at the top of Stø Formation in well 7119/12-3.

Water saturation	Vp (Km/s)	Vs (Km/s)	ρ (g/cc)	Ip (Km/s*g/cc)	Is (Km/s*g/cc)	Vp/Vs
1	5.096	3.107	2.613	13.316	8.119	1.640
0.9	4.976	3.109	2.611	12.992	8.118	1.601
0.5	4.972	3.114	2.601	12.932	8.100	1.597
0	4.981	3.121	2.590	12.901	8.083	1.596

The green, purple and red dots on Figure 6.12 are overlapping with each other. It means that the AVO signature of 10%, 50% and 100% gas bearing Stø Formation sandstones are almost the same. There are certain distances between these three dots and the brine-saturated dot. It indicates that AVO analysis can distinguish brine and gas bearing formations in the deepest well with less confidence compared to the shallow well.

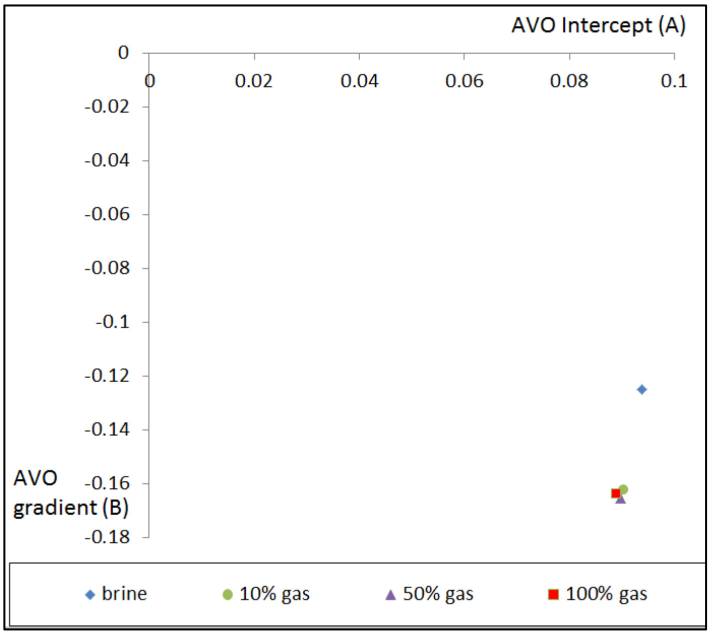

Figure 6.12 AVO intercept (A) versus gradient (B) at top of the Stø Formation in well 7119/12-3 with different water saturation scenarios.

6.3.2 Effects of wavelet

Wavelet is the link between seismic response and rock properties, but the phase of the wavelet can change both laterally (spatially) and vertically (with time) (Avseth et al., 2005). Normally the wavelet of processed seismic data remains in mixed phase. The optimum wavelet derived from seismic, well log and VSP data are commonly used for AVO analysis and seismic modelling (Srivastava et al., 2006).

In this study, three zero phase wavelets were used to check sensitivity of AVO modelling: Band pass 1 (Figure 6.13 A and B), Band pass 2 (Figure 6.13 C and D) and Ricker wavelet (Figure 6.13 E and F). The parameters of Band pass 2 are described in Chapter 3. The parameters for Band pass 1 are Low cut: 5 Hz, Low pass: 10 Hz, High cut: 60 Hz, High pass: 50 Hz, Phase rotation: 0, Sample Rate: 2 ms, Wavelet length: 400 ms. The parameters of Ricker wavelet are Domain frequency: 45 Hz, Phase rotation: 0, Sample Rate: 2 ms, Wavelet length: 150 ms.

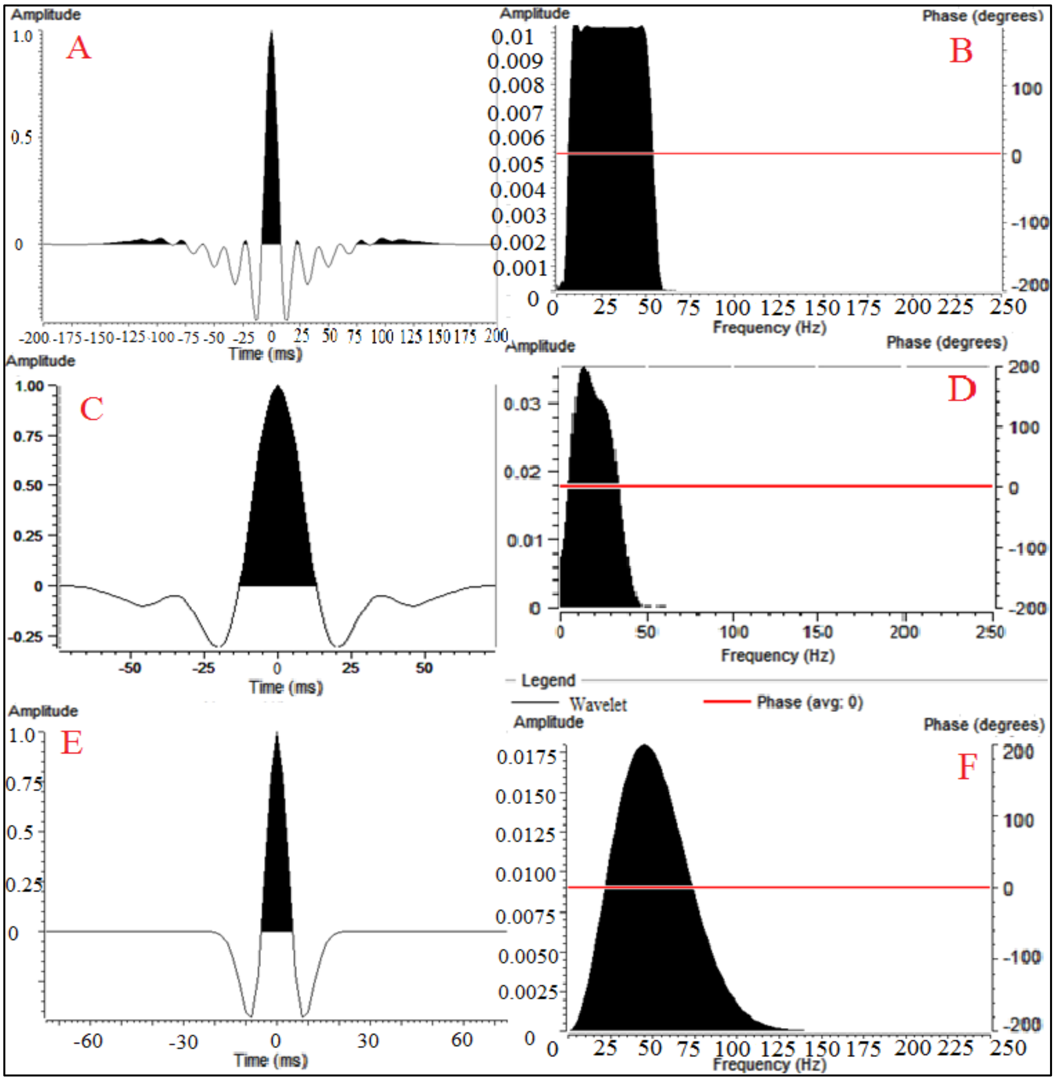

Figure 6.13 The time-amplitude cross plots of Bandpass 1 (A), Bandpass 2 (C) and Ricker (E) wavelets and corresponding frequency-amplitude cross plots of Bandpass 1 (B), Bandpass 2 (D) and Ricker (F) wavelets.

Different frequency spectrum and wavelet length between 3 wavelets result in different AVO responses (Figure 6.14). In well 7120/10-1, the AVO intercepts change dramatically while the AVO gradients remain almost the same (Figure 6.14, left). The opposite results are found in well 7119/12-1, the AVO gradients changes dramatically while the AVO intercepts remain almost the same (Figure 6.14, right).

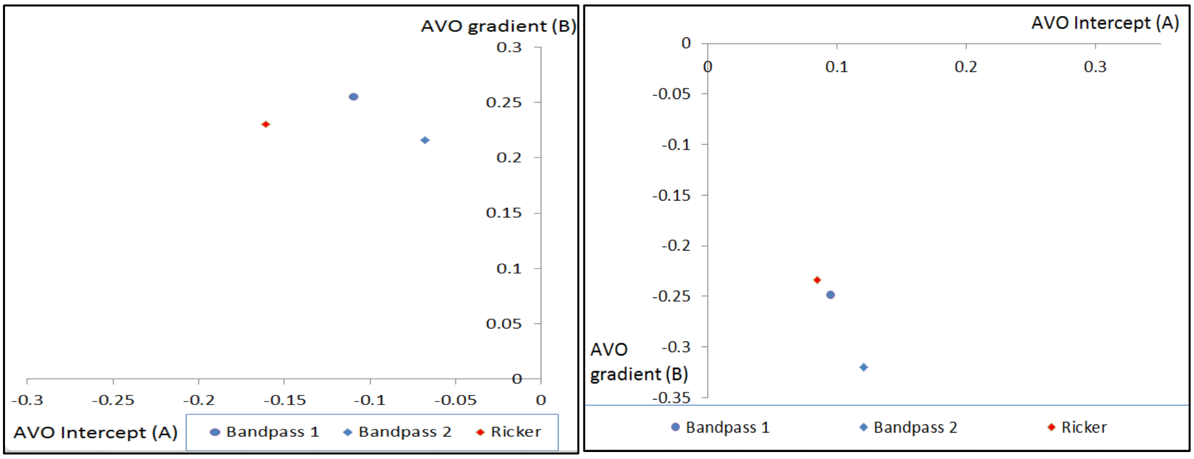

Figure 6.14 AVO intercept (A) versus gradient (B) at top of the Stø Formation in 7120/10-1 (left) and 7119/12-1 (right) using three different wavelets.

The difference of wavelet frequency would results in different superpositon of overlapping primary reflection. The constructive or destructive interference between the reflections could change the reflection at top of the Stø Formation. The data points are all in the same quadrant although different wavelets are used. The different positions of the data points on AVO cross plot could be misleading for AVO analysis.

6.3.3 Effects of block size

Due to the low vertical resolution of seismic compared to well logs, upscaling is essential for modelling the correct AVO responses using high frequency well log data. Backus (1962) averaging is used to model a finely stratified medium as a single homogeneous medium when the wavelength is large enough compared to the layer thickness. The average results are weighted by their volumetric proportions (Mavko et al., 2009). In this study, travel time (slowness) averaging method is used for simplicity.

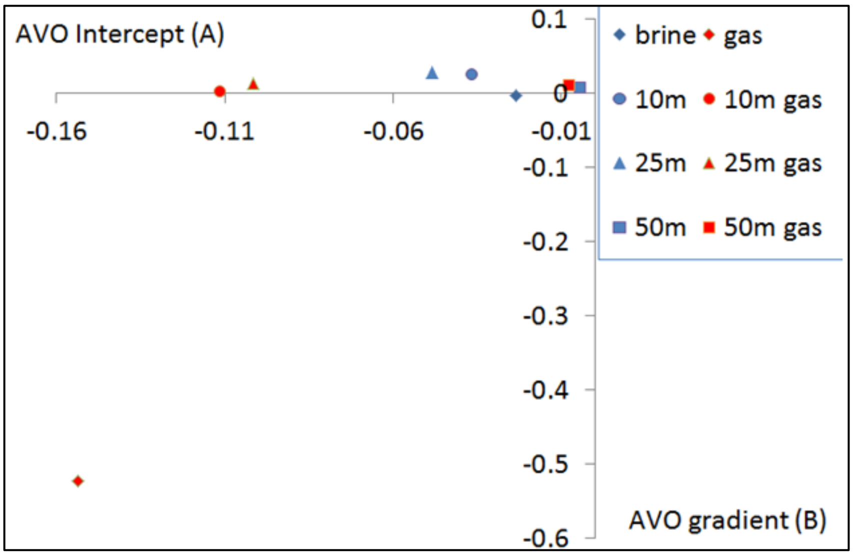

Figure 6.15 AVO responses at top of the Stø Formation in well 7119/12-2 with four different block sizes.

Different block sizes will result in different reflection coefficient on the target surface, because the averaging depth intervals during blocking are different. This phenomenon can be seen in Figure 6.15 where the well logs are blocked by 0m, 10m, 25m and 50m. The difference between the brine saturated and gas saturated data points are decreasing with the increasing block size. AVO gradient of the data points are around zero except the data point where the Stø Formation is saturated by gas and is not applied any blocking (0 m).

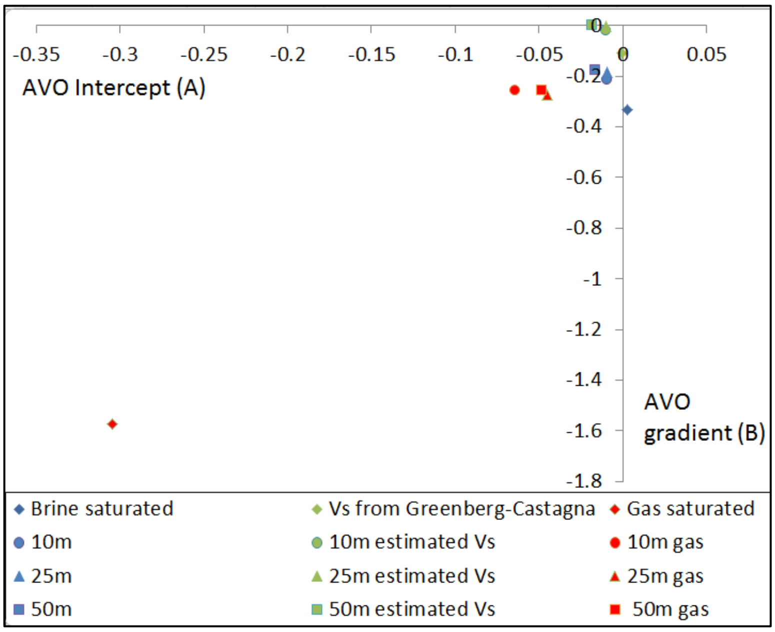

Figure 6.16 AVO intercept (A) and gradient (B) at top of the Stø Formation in well 7119/12-4 with different block size and saturation.

The differences for block sizes are not obvious for the top of the Stø Formation in well 7119/12-4 except one data point where the Stø Formation is saturated by gas and without blocking (0 m). The other data points are relatively close to each other (Figure 6.16). The water saturated data points could be classified as Class II according to Rutherford and Williams (1989) classification. The gas saturated Stø Formation will be classified as Class III AVO signature. The difference between the brine saturated and gas saturated data points decrease with increasing block size.

The measured Vs is also used in the modelling instead of the calculated Vs data using Greenberg and Castagna (1992) relationship (Figure 6.16). The AVO signatures of measured Vs data from well log tend to be gas bearing because the data points cluster in quadrant III.

The modelling results of well 7119/12-3 using different block sizes are different with that in well 7119/12-2 and 7119/12-4. The AVO intercept increases with increasing block size and gradient is decreasing with increasing block size (Figure 6.17). The difference between gas saturated and water saturated Stø Formation reflection signature are not obvious.

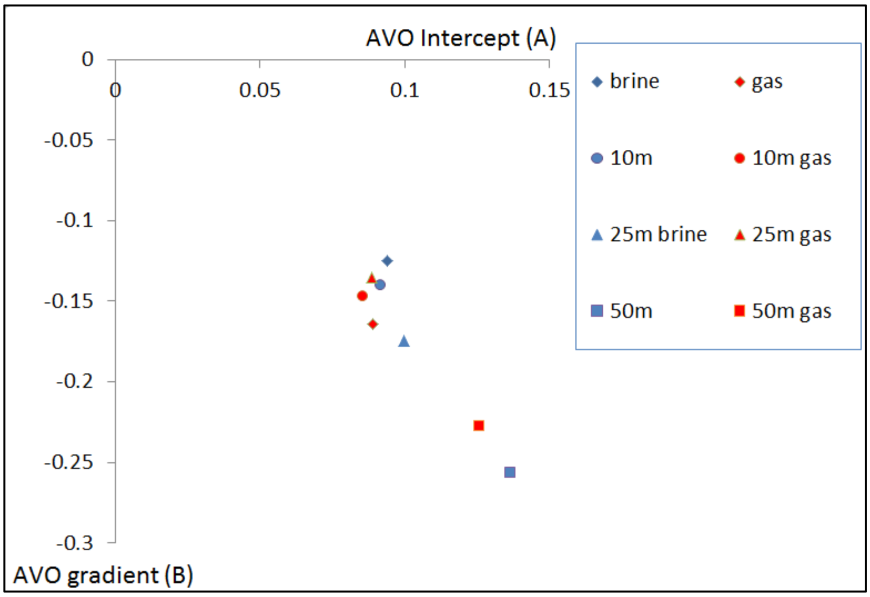

Figure 6.17 AVO intercept (A) versus gradient (B) at top of the Stø Formation in well 7119/12-3 with different block sizes and fluid saturation.

6.4 Uncertainty analysis

The method used here for AVO modelling is plane-wave analysis and Aki and Richards (1980) two term linear approximations of the Zoeppritz (1919) equations. Small incidence angles (less than 30 degree) are the prerequisites for the linear approximations. Analysing in small angle (less than 15 degree) and large angle (more than 45 degree) would result in very different results. The blue curve in Figure 6.18 is the two-term approximation of 13 degree offset. The black curve represents 40 degree approximation and red curve is 60 degree approximation.

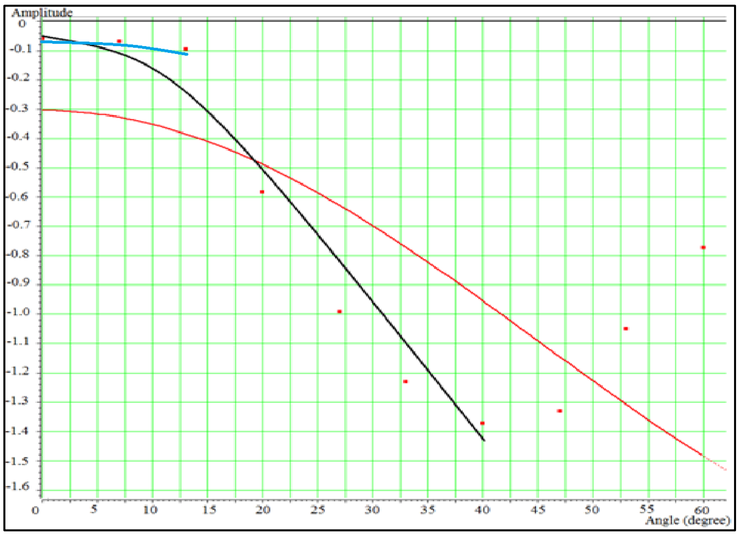

Figure 6.18 The AVO modelling at top of the Stø Formation in well 7119/12-4 saturated with gas.

The modelling result in Figure 6.19 is worse than in Figure 6.18. The A value is negative while the zero offset reflection coefficient is positive. This phenomenon shows that under certain conditions, Aki and Richards (1980) two term linear approximations do not fit well with Zoeppritz (1919) equations even at a small angle (30 degree).

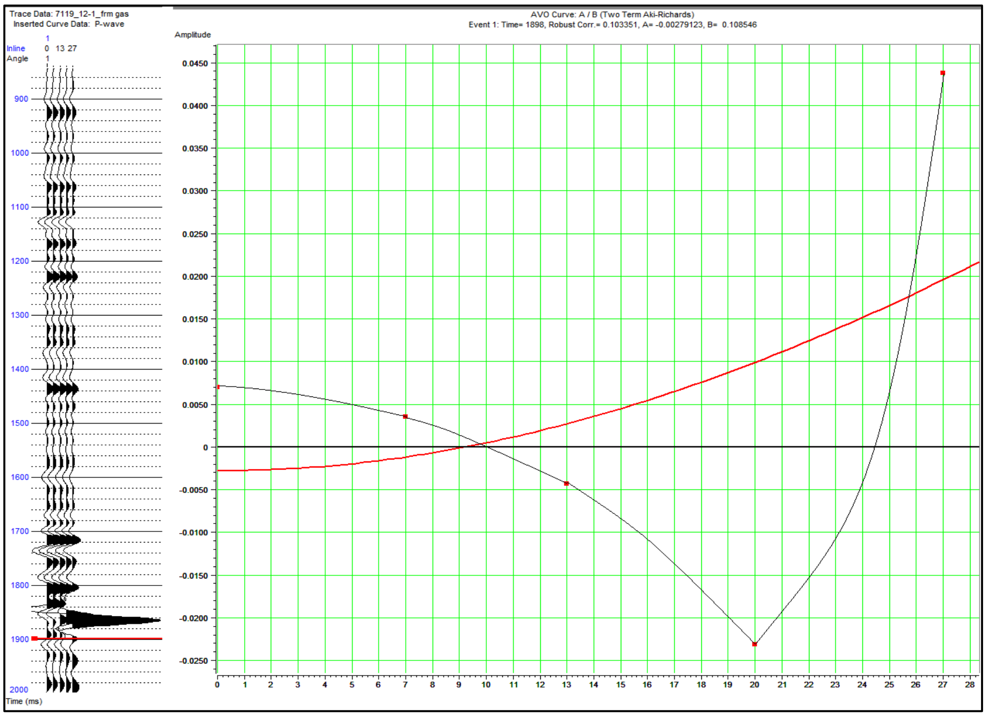

Figure 6.19 The AVO modelling at bottom of the Stø Formation in well 7119/12-4 saturated with gas.

Another uncertainty is that the estimated Vs data used in AVO modelling that derived from Vp using empirical relations (Greenberg and Castagna, 1992). As shown in Figure 6.16, there are clear differences of AVO signatures between measured and estimated Vs used in AVO modelling.

The bedding thickness of the target zone is very important because thin-layered reservoirs will cause tuning effect. The reflections at top and base of the reservoir interfere with each other when the thickness is less than a quarter of the wavelength. The Stø Formation is thick enough (87-163 m) in this study, but the shale in the middle part of Stø Formation could trigger possible interference between layers.

Chapter 7 Summary and conclusion

The Greater Barents Sea is an area bordered by the north Norwegian and Russian coasts in the south, Novaya Zemlya in the east, Franz Josef Land in the north-east, Svalbard archipelagos in the north-west and Mid-Atlantic margin in the west (Doré, 1995). Over 100 wells have been drilled in the Norwegian Barents Sea and many hydrocarbon discoveries have been reported. Most of the discoveries are gas such as Snøhvit, Askeladd, Alka and Albatross. So far, Goliat is the only oil field in developing phase. Recently, more and more oil discoveries (e.g. Nucula, Johan Castberg, Wisting and Gohta) make the area a clear spotlight to oil and gas industries.

The study area is located near the border of the Hammerfest Basin and Ringvassøy-Loppa Fault Complex of the Norwegian Barents Sea. Seven exploration wells have been drilled in the study area. These include wells 7119/12-1, 7119/12-2, 7119/12-3, 7119/12-4, 7120/10-1, 7120/10-2 and 7019/1-1. Hydrocarbon shows are documented in wells 7119/12-1 and 7119/12-2, while gas and gas/condensate are present in wells 7019/1-1 and 7119/12-3 respectively. The other three wells are dry. The aim of this study is to investigate the reservoir quality of Jurassic and Cretaceous sandstones. Reservoirs present in the study area include Tubåen, Nordmela, Stø, and Knurr Formations in order of decreasing stratigraphic age. However, this study focusses only on Knurr and Stø Formations. All available well log data have been analysed in detail using petrophysical methods, rock physics diagnostics technique and seismic AVO forward modelling.

The whole Barents Sea area has experienced tectonic uplift in Cenozoic. The amount of uplift is estimated in this study by comparing the sonic logs to published shale compaction trends (Storvoll et al., 2005; Japsen, 1999; Mondol, 2009). The uplift estimations are in close agreement with the literature data (Henriksen et al., 2011a; Ohm et al., 2008; Storvoll et al., 2005; Riis and Fjeldskaar, 1992; Nyland et al., 1992; Reemst et al., 1994; Rasmussen and Fjeldskaar, 1996; Doré and Jensen, 1996; Dimakis et al., 1998). The calculated average porosity values of the reservoirs are compared with published porosity-depth trend (Ramm and Bjørlykke, 1994). The maximum temperatures that the reservoir sandstones have experienced are estimated using corrected maximum burial depths and current geothermal gradient.

The qualities of the well logs are cross-checked. Well 7119/12-2 and 7120/10-1 show obvious higher neutron porosities than normal. The gamma ray values of well 7019/1-1 were abnormally high. These phenomena are possibly due to inaccurate logging calibration.

The net-to-gross, shale volume, porosity and water saturation are calculated for both the Knurr and Stø Formations. Significant variations of reservoir rock properties are observed in studied wells. The sediments of the Knurr and Stø Formations are composed of shale and sandstone. Therefore, Gamma Ray log is used for lithology discrimination and shale volume calculation.

Density, Neutron and Sonic logs are used to calculate different kinds of porosity models (density and neutron average porosity, density porosity, neutron porosity, sonic porosity and effective porosity). Neutron-Density cross plots are used for porosity calculation, shale volume estimation, lithology and fluid discrimination. In well 7119/12-1, unpublished porosity data from core samples are compared with calculated values from well logs. Unexpected high porosities observed at some depths may be attributed to secondary porosity as supported by Olaussen et al. (1984). The separation between density porosity and sonic porosity is observed at the secondary porosity zones. The same phenomenon is also observed in other wells like 7119/12-4 and 7019/1-1.

Water saturation of the reservoirs are calculated by Archie's equation, in which parameters such as a, m, n and Rw are used. Rwa method and Pickett plot are used to determine these values, but the results are not dependable in some wells.

Rock physics diagnostics are carried out by using templates like P-wave velocity (Vp) versus porosity, Vp/Vs versus IP and Lamda-Rho versus Mu-Rho cross plots. The Vs values are calculated from Castagna's Mudrock equation. Three cement models (contact cement, constant cement and friable sand), using Vp versus porosity cross plots, are used for evaluating the type and contents of cement between the sandstone grains. These cement models are digitized from published literatures (Avseth et al., 2009; Avseth et al., 2005). Vp/Vs versus IP and Lamda-Rho versus Mu-Rho cross plots are used for lithology and fluid discriminations. Brine-saturated shale trend, brine-saturated sandstone trend and gas-saturated sandstone trend are calculated in the Vp/Vs versus IP cross plot using typical values of sand, clay and fluids (water and gas) suggested in the literature (Mavko et al., 2009).

Vs measurements are valuable for evaluating rock properties, but they are only available in well 7119/12-4. The Vs log is compared with estimated Vs from published Vp-Vs relationships, like Mudrock equation and so on. The Vs values are found to be higher than all the estimates from published papers (Castagna et al., 1985; Castagna and Backus, 1993; Mavko et al., 2009; Krief et al., 1990; Greenberg and Castagna, 1992; Fawad et al., 2011; Han et al., 1986; Pickett, 1963; Williams, 1990). The reasons for abnormally high Vs measurements are discussed in detail. Vs-porosity cross plots of cement models are constructed using different porosity models (density and neutron average porosity, density porosity, neutron porosity and sonic porosity) and different Vs models (Measured Vs, Vs from Mudrock equation, Krief's relationship, Greenberg and Castagna's relationship and Han's relationship). Measured Vs values are also used to construct Vp/Vs versus IP, and Lamda-Rho versus Mu-Rho cross plots in well 7119/12-4. The rock physics diagnostic results using measured Vs are compared with that using estimated Vs.

AVO modelling for both the top and bottom of the reservoirs are performed in all the wells available. Fluid substitution is used to compare the "in-situ" and "what-if" scenarios. Gas and water are assumed to be the fluid present in the reservoir. Four different water saturations (0%, 50%, 90% and 100%), three different wavelets and four different averaging sizes (0m, 10m, 25m and 50m) are studied for sensitivity analysis to see their effect on AVO modelling. In these modelling, Vs values are estimated from published Vp-Vs relationships in all the wells including 7119/12-4. The difference between measured Vs and estimated Vs are studied in well 7119/12-4.

Limitations and uncertainties exist in this study and these are discussed with respect to the different study approaches in chapters 2, 4, 5 and 6.

Based on petrophysical analysis, rock physics diagnostics and AVO modelling the following conclusions are drawn from this study:

- It is clear from this study that the Vp-depth trends observed in all the studied wells are generally higher compared to the published Vp-depth trends suggested by various authors for normally subsided basins. The calculated average porosity values of the reservoirs are much lower than published porosity-depth trend. The reason is that the study area have been deeply buried and uplifted at later stage. The estimated average uplift in the study area is about 900 m. The estimation of uplift decreases to north-west direction. Vp of the sandstones vary widely because of lithologic variations, compaction and diagenetic processes.

- According to the uplift estimation, the maximum temperatures that the sediments have experienced is much higher than the present temperature that interpolated from bottom hole temperatures. All the reservoirs in the studied wells have been through chemical compaction processes. This is proven by quartz overgrowth in the shallowest buried sandstones of well 7119/12-2. The higher velocity-depth gradient than the published trends could be caused by long burial history within the chemical compaction zone.

- The thickness of the Knurr Formation reservoir is not uniform across all the wells, because the reservoir is deposited in a submarine fan system, whereas the Stø Formation is deposited in a coastal environment and has good reservoir quality in all the wells. The Stø Formation reservoir is characterized by relatively similar net and gross thickness (high N/G and very low shale volume). The thickness of the Stø Formation increases from east to west.

- The average porosity values in this study range from 25% at about 1200m (BSF) to 3% at about 3000m (BSF). The average porosity values are much lower than expected because of the effect of uplift placing the rocks at shallower depth than they have been. The calculated porosity values from well logs fit reasonably well with that measured from core samples in well 7119/12-1. Secondary porosity is common in deeply buried sandstones in the study area. The reservoirs with high secondary porosity could be important exploration targets in the future.

- In Knurr Formation, gas is found only in well 7019/1-1, whereas the Stø Formation in 7019/1-1 and 7119/12-3 are gas-bearing. Shows are documented in wells 7119/12-1 and 7119/12-4. Coarse-grained sandstones deposited in storm environments will result in wrong water saturation results. In some of the sections, the literature data of parameters (a, m, n and Rw) used in Archie's equation are not suitable in this area because of the complex tectonic history and diagenetic processes of reservoir sandstones.

- Rock physics templates work well in the studied wells for quartz cement estimation, lithology and fluid discrimination. A clear trend of rock properties with increasing depth can be observed in all of the rock physics templates. The cement models in the Vp-porosity cross plots work better for shallow wells (less than 2100m (BSF)) than the deeper wells. Lamda-Rho versus Mu-Rho cross plot is better than Vp/Vs versus IP cross plot for discriminating the lithology and fluids in the studied wells.

- The Vs values measured for sandstones in well 7119/12-4 are abnormally high that result false gas effect in rock physics analysis (e.g. Vp/Vs versus IP and LMR crossplots). In Vs-porosity cross plot with overlaid cement model lines, the estimated cement amount are more than estimated in Vp-porosity cross plot. The cement amount in shaly sandstones show a large variation when different porosity models are used (density and neutron average porosity, density porosity, neutron porosity and sonic porosity). In Vp/Vs versus Ip cross plot, all the sandstone data points are located in the gas-saturated zone. In Lamda-Rho versus Mu-Rho cross plot, most of the sandstone data points are located in the gas zones. The Vs measurements for shale in this well are normal compared to estimated Vs using published Vp-Vs relationships. An integration of well log data with core samples' analysis show that Vs values vary with cementation, porosity, shale volume and lithology in well 7119/12-4. Regional uplift might be the reason for abnormally high Vs values measured in the Stø Formation sandstones in this well. The other possible reasons include efficient packing, contact cement or error from logging equipments.

- The AVO modelling results fit well with the classical AVO theory. A clear deviation of the gas-bearing data points from background trend is observed for both the top and bottom interfaces of the reservoir. An impedance inversion with increasing depth is observed in the results of AVO modelling for top of the Stø Formation sandstones in the studied wells. With increasing depth, the "soft" sandstones turn into "hard" sandstones compared to the overlying shale. The transition depth is close to that of the top of Stø Formation in well 7119/12-4, which is around 2100 m (BSF). The water saturated Stø formation sandstone in this well will be "invisible" on seismic reflection data. The gas effect in the AVO cross plot is not obvious for wells deeper than that of the top of Stø Formation in well 7019/1-1, which is around 2200 m (BSF).

- The AVO modelling results are sensitive to many factors, like water saturation, wavelet and block sizes of well logs used in seismogram generation. A gas saturation of 10% is enough to distinctly separate the data point from a brine-saturated scenario, whereas the difference between 10% gas saturation and 100% gas saturation is small. The difference becomes even smaller with increasing depth and decreasing porosity values. The measured Vs values in 7119/12-4 result a false gas effect in the AVO modelling results.

Reference

AKI, K. & RICHARDS, P. G. 1980. *Quantitative seismology*, Freeman San Francisco.

ASQUITH, G. B., KRYGOWSKI, D. & GIBSON, C. R. 2004. *Basic well log analysis*, American Association of Petroleum Geologists.

AVSETH, P. 2010. Explorational Rock Physics – The Link Between Geological Processes and Geophysical Observables. *Petroleum Geoscience.* Springer Berlin Heidelberg.

AVSETH, P., DVORKIN, J., MAVKO, G. & RYKKJE, J. 2000. Rock physics diagnostic of North Sea sands: Link between microstructure and seismic properties. *Geophysical Research Letters,* 27**,** 2761-2764.

AVSETH, P., JØRSTAD, A., VAN WIJNGAARDEN, A.-J. & MAVKO, G. 2009. Rock physics estimation of cement volume, sorting, and net-to-gross in North Sea sandstones. *The Leading Edge,* 28**,** 98-108.

AVSETH, P., MUKERJI, T. & MAVKO, G. 2005. *Quantitative seismic interpretation: Applying rock physics tools to reduce interpretation risk*, Cambridge University Press.

AVSETH, P., MUKERJI, T., MAVKO, G. & DVORKIN, J. 2010. Rock-physics diagnostics of depositional texture, diagenetic alterations, and reservoir heterogeneity in high-porosity siliciclastic sediments and rocks—A review of selected models and suggested work flows. *Geophysics,* 75**,** 75A31-75A47.

BACKUS, G. E. 1962. Long-wave elastic anisotropy produced by horizontal layering. *Journal of Geophysical Research,* 67**,** 4427-4440.

BASSIOUNI, Z. 1994. Theory, measurement, and interpretation of well logs: SPE Textbook Series Vol. 4. *Society of Petroleum Engineers, Texas*.

BJØRLYKKE, K. & EGEBERG, P. 1993. Quartz cementation in sedimentary basins. *AAPG bulletin,* 77**,** 1538-1548.

BLAICH, O. A. & ERSDAL, G. A. 2011. Three hydrocarbon plays and considerable potential are identified by the South West Barents Sea (SWB) dataset. ***Geoexpro**,* 8**,** 57-58.

BLOCH, S., LANDER, R. H. & BONNELL, L. 2002. Anomalously high porosity and permeability in deeply buried sandstone reservoirs: Origin and predictability. *AAPG bulletin,* 86**,** 301-328.

BRADLEY, H. B. 1987. Petroleum engineering handbook.

BRAUT, H. L. 2012. Analogue modeling of detachment zones and structural analysis of the Ringvassøy-Loppa Fault Complex, SW Barents Sea.

CARMICHAEL, R. S. 1989. *Practical handbook of physical properties of rocks a nd minerals*, CRC press.

CASTAGNA, J. P. 1993. AVO analysis-tutorial and review. *Offset-dependent reflectivity: theory and practice of AVO analysis*, 3-36.

CASTAGNA, J. P. & BACKUS, M. M. 1993. *Offset-dependent reflectivity: Theory and practice of AVO analysis*, SEG Books.

CASTAGNA, J. P., BATZLE, M. L. & EASTWOOD, R. L. 1985. Relationships between compressional-wave and shear-wave velocities in clastic silicate rocks. *Geophysics,* 50, 571-581.

CASTAGNA, J. P. & SWAN, H. W. 1997. Principles of AVO crossplotting. *The Leading Edge,* 16, 337-344.

CASTAGNA, J. P., SWAN, H. W. & FOSTER, D. J. 1998. Framework for AVO gradient and intercept interpretation. *Geophysics,* 63, 948-956.

DALLAND, A., WORSLEY, D. & OFSTAD, K. 1988. *A Lithostratigraphic Scheme for the Mesozoic and Cenozoic and Succession Offshore Mid-and Northern Norway*, Oljedirektoratet.

DALLMANN, W. 1999. *Lithostratigraphic lexicon of Svalbard*, Norwegian Polar Institute.

DIMAKIS, P., BRAATHEN, B. I., FALEIDE, J. I., ELVERHØI, A. & GUDLAUGSSON, S. T. 1998. Cenozoic erosion and the preglacial uplift of the Svalbard–Barents Sea region. *Tectonophysics,* 300, 311-327.

DORÉ, A. 1995. Barents Sea geology, petroleum resources and commercial potential. *Arctic*, 207-221.

DORÉ, A. & JENSEN, L. 1996. The impact of late Cenozoic uplift and erosion on hydrocarbon exploration: offshore Norway and some other uplifted basins. *Global and Planetary Change,* 12, 415-436.

DURAN, E. R., DI PRIMIO, R., ANKA, Z., STODDART, D. & HORSFIELD, B. 2013. Petroleum system analysis of the Hammerfest Basin (southwestern Barents Sea): comparison of basin modelling and geochemical data.

DVORKIN, J. & NUR, A. 1996. Elasticity of high-porosity sandstones: Theory for two North Sea data sets. *Geophysics,* 61, 1363-1370.

DVORKIN, J. P. 2008. Yet another V s equation. *Geophysics,* 73, E35-E39.

ELLIS, D. V. & SINGER, J. M. 2007. *Well logging for earth scientists*, Springer.

ELVERHØI, A., HOOKE, R. L. & SOLHEIM, A. 1998. Late Cenozoic erosion and sediment yield from the Svalbard–Barents Sea region: implications for understanding erosion of glacierized basins. *Quaternary Science Reviews,* 17, 209-241.

ESLINGER, E. & PEVEAR, D. R. 1988. *Clay minerals for petroleum geologists and engineers*, Society of Economic Paleontologists and Mineralogis ts.

FALEIDE, J., VÅGNES, E. & GUDLAUGSSON, S. Late Mesozoic–Cenozoic evolution of the southwestern Barents Sea. Geological Society, London, Petroleum Geology Conference series, 1993a. Geological Society of London, 933-950.

FALEIDE, J. I., TSIKALAS, F., BREIVIK, A. J., MJELDE, R., RITZMANN, O., ENGEN, O., WILSON, J. & ELDHOLM, O. 2008. Structure and evolution of the continental margin off Norway and Barents Sea. *Episodes,* 31**,** 82-91.

FALEIDE, J. I., VÅGNES, E. & GUDLAUGSSON, S. T. 1993b. Late Mesozoic-Cenozoic evolution of the south-western Barents Sea in a regional rift-shear tectonic setting. *Marine and Petroleum Geology,* 10**,** 186-214.

FAWAD, M., MONDOL, N. H., JAHREN, J. & BJØRLYKKE, K. 2011. Mechanical compaction and ultrasonic velocity of sands with different texture and mineralogical composition. *Geophysical Prospecting,* 59**,** 697-720.

GABRIELSEN, R. 1984. Long-lived fault zones and their influence on the tectonic development of the southwestern Barents Sea. *Journal of the Geological Society,* 141**,** 651-662.

GABRIELSEN, R. H., FAERSETH, R. B. & JENSEN, L. N. 1990. *Structural Elements of the Norwegian Continental Shelf. Pt. 1. The Barents Sea Region*, Norwegian Petroleum Directorate.

GASSMANN, F. 1951. Elasticity of porous media: Über die Elastizität poröser Medien: Vierteljahrsschrift der Naturforschenden Gesselschaft in Zurich. Heft.

GLOVER, D. P. 2011. Petrophysics MSc Course Notes. *Clay/Shale Effects on Porosity and Resistivity Logs*.

GLØRSTAD-CLARK, E., FALEIDE, J. I., LUNDSCHIEN, B. A. & NYSTUEN, J. P. 2010. Triassic seismic sequence stratigraphy and paleogeography of the western Barents Sea area. *Marine and Petroleum Geology,* 27**,** 1448-1475.

GOODWAY, B., CHEN, T. & DOWNTON, J. Improved AVO Fluid Detection And Lithology Discrimination Using Lamé Petrophysical Parameters;"λρ", μρ, λμ Fluid Stack", From P And S Inversions. 1997 SEG Annual Meeting, 1997.

GOODWAY, W. 2001. AVO and Lamé constants for rock parameterization and fluid detection. *CSEG Recorder,* 26**,** 39-60.

GREENBERG, M. & CASTAGNA, J. 1992. SHEAR-WAVE VELOCITY ESTIMATION IN POROUS ROCKS: THEORETICAL FORMULATION, PRELIMINARY VERIFICATION AND APPLICATIONS1. *Geophysical prospecting,* 40**,** 195-209.

GUPTA, S. D., CHATTERJEE, R. & FAROOQUI, M. 2012. Rock physics template (RPT) analysis of well logs and seismic data for lithology and fluid classification in Cambay Basin. *International Journal of Earth Sciences,* 101**,** 1407-1426.

HAN, D.-H., NUR, A. & MORGAN, D. 1986. Effects of porosity and clay content on wave velocities in sandstones. *Geophysics,* 51**,** 2093-2107.

HENRIKSEN, E., BJØRNSETH, H., HALS, T., HEIDE, T., KIRYUKHINA, T., KLØVJAN, O., LARSSEN, G., RYSETH, A., RØNNING, K. & SOLLID, K. 2011a. Uplift and erosion of the greater Barents Sea: impact on prospectivity and petroleum systems. *Geological Society, London, Memoirs,* 35**,** 271-281.

HENRIKSEN, E., RYSETH, A., LARSSEN, G., HEIDE, T., RØNNING, K., SOLLID, K. & STOUPAKOVA, A. 2011b. Tectonostratigraphy of the greater Barents Sea: implications for petroleum systems. *Geological Society, London, Memoirs,* 35**,** 163-195.

HÜBERT, L., SELNES, A., DVORKIN, J., CARR, M. & HOFFMANN, J. Rock Physics Diagnostics, Effective Medium Models, and AVO Analysis of the Stø Formation, Hammerfest Basin, Norway. 66th EAGE Conference & Exhibition, 2004.

JAPSEN, P. 1999. Overpressured Cenozoic shale mapped from velocity anomalies relative to a baseline for marine shale, North Sea. *Petroleum Geoscience,* 5**,** 321-336.

KRIEF, M., GARAT, J., STELLINGWERFF, J. & VENTRE, J. 1990. A petrophysical interpretation using the velocities of P and S waves (full-waveform sonic). *Log Analyst,* 31**,** 355-369.

LI, Y., DOWNTON, J. & XU, Y. 2007. Practical aspects of AVO modeling. *The Leading Edge,* 26**,** 295-311.

MAGOON, L. B. & DOW, W. G. 1994. *The petroleum system*, American Association of Petroleum Geologists.

MARION, D., NUR, A., YIN, H. & HAN, D.-H. 1992. Compressional velocity and porosity in sand-clay mixtures. *Geophysics,* 57**,** 554-563.

MAVKO, G., MUKERJI, T. & DVORKIN, J. 2009. *The rock physics handbook: Tools for seismic analysis of porous media*, Cambridge University Press.

MERKEL, R. H. 1979. Well log formation evaluation.

MINEAR, J. W. Clay models and acoustic velocities. SPE Annual Technical Conference and Exhibition, 1982. Society of Petroleum Engineers.

MONDOL, N. H. Porosity and permeability development in mechanically compacted silt-kaolinite mixtures. 2009 SEG Annual Meeting, 2009. Society of Exploration Geophysicists.

MORK, A., KNARUD, R. & WORSLEY, D. 1982. Depositional and diagenetic environments of the Triassic and Lower Jurassic succession of Svalbard.

NPD 2013a. Norwegian Petroleum Directorate Topics *http://npd.no/Templates/OD/Article.aspx?id=931&epslanguage=en,* (accessed Janurary 2014).

NPD 2013b. Norwegian Petroleum Directorate Topics *http://npd.no/en/Topics/Geology/Geological-plays/Barents-Sea/Upper-Jurassic-to-Lower-Cretaceous/,* (accessed Janurary 2014).

NPD 2013c. Norwegian Petroleum Directorate Fact-pages of Exploration Wellbores. http://factpages.npd.no/factpages/Default.aspx?culture=en, (accessed November 2013).

NPD 2013d. Norwegian Petroleum Directorate FactMaps of Exploration Wellbores. http://npdmap1.npd.no/website/npdgis/viewer.htm, (accessed November 2013).

NPD 2013e. Norwegian Petroleum Directorate Topics. http://npd.no/en/Topics/Geology/Geological-plays/Barents-Sea/Triassic/, (accessed Janurary 2014).

NYLAND, B., JENSEN, L., SKAGEN, J., SKARPNES, O. & VORREN, T. 1992. Tertiary uplift and erosion in the Barents Sea: magnitude, timing and consequences. *Structural and tectonic modelling and its application to petroleum geology*, 153-162.

OHM, S. E., KARLSEN, D. A. & AUSTIN, T. J. F. 2008. Geochemically driven exploration models in uplifted areas: Examples from the Norwegian Barents Sea. *Aapg Bulletin,* 92**,** 1191-1223.

OLAUSSEN, S., DALLAND, A., GLOPPEN, T. & JOHANNESSEN, E. 1984. Depositional environment and diagenesis of Jurassic reservoir sandstones in the eastern part of Troms I area. *Petroleum Geology of the North European Margin.* Springer.

OSTANIN, I., ANKA, Z., DI PRIMIO, R. & BERNAL, A. 2012. Identification of a large Upper Cretaceous polygonal fault network in the Hammerfest basin: Implications on the reactivation of regional faulting and gas leakage dynamics, SW Barents Sea. *Marine Geology,* 332**,** 109-125.

OSTANIN, I., ANKA, Z., DI PRIMIO, R. & BERNAL, A. 2013a. Hydrocarbon plumbing systems above the Snohvit gas field: Structural control and implications for thermogenic methane leakage in the Hammerfest Basin, SW Barents Sea. *Marine and Petroleum Geology,* 43**,** 127-146.

OSTANIN, I., ANKA, Z., DI PRIMIO, R. & BERNAL, A. 2013b. Hydrocarbon plumbing systems above the Snøhvit gas field: structural control and implications for thermogenic methane leakage in the Hammerfest Basin, SW Barents Sea. *Marine and Petroleum Geology*.

PEREZ, M. A. & TONN, R. 2003. Reservoir Modelling and Interpretation with Lamé's Parameters: A Grand Banks Case Study. *Interpretation Templates, EnCana Corporation*.

PICKETT, G. 1963. Acoustic character logs and their applications in formation evaluation. *Journal of Petroleum Technology,* 15**,** 659-667.

RAMM, M. & BJØRLYKKE, K. 1994. Porosity/depth trends in reservoir sandstones: Assessing the quantitative effects of varying pore-pressure, temperature history and mineralogy, Norwegian Shelf data. *Clay minerals,* 29**,** 475-490.

RASMUSSEN, E. & FJELDSKAAR, W. 1996. Quantification of the Pliocene-Pleistocene erosion of the Barents Sea from present-day bathymetry. *Global and Planetary Change,* 12**,** 119-133.

REEMST, P., CLOETINGH, S. & FANAVOLL, S. 1994. Tectonostratigraphic modelling of Cenozoic uplift and erosion in the south-western Barents Sea. *Marine and Petroleum Geology,* 11**,** 478-490.

RICHARDSEN, G., VORREN, T. O. & TORUDBAKKEN, B. O. 1993. **Post-Early Cretaceous Uplift And Erosion In The Southern Barents Sea - A Discussion Based On Analysis Of Seismic Interval Velocities**. *Norsk Geologisk Tidsskrift,* 73**,** 3-20.

RICHES, P., TRAUB-SOBOTT, I., ZIMMERLE, W. & ZINKERNAGEL, U. 1986. Diagenetic peculiarities of potential Lower Jurassic reservoir sandstones, Troms 1 area, off northern Norway, and their tectonic significance. *Clay Miner,* 21**,** 565-584.

RIIS, F. & FJELDSKAAR, W. 1992. On the magnitude of the Late Tertiary and Quaternary erosion and its significance for the uplift of Scandinavia and the Barents Sea. *Structural and tectonic modelling and its application to petroleum geology,* 1**,** 163-185.

ROUFOSSE, M. 1987. The formation and evolution of sedimentary basins in the Western Barents Sea. *Petroleum Geology of North West Europe, Graham and Trotman, London***,** 1149-1161.

RUTHERFORD, S. R. & WILLIAMS, R. H. 1989. Amplitude-versus-offset variations in gas sands. *Geophysics,* 54**,** 680-688.

SCHROEDER, F. W. 2006. Well-Seismic Ties. *AAPG Slide resources 7* http://www.aapg.org/slide_resources/schroeder/7/.

SELDAL, J. Lower Cretaceous: the next target for oil exploration in the Barents Sea? Geological Society, London, Petroleum Geology Conference series, 2005. Geological Society of London, 231-240.

SHERIFF, R. E. 1973. *Encyclopedic dictionary of exploration geophysics*, Society of Exploration Geophysicists Tulsa, OK.

SHUEY, R. 1985. A simplification of the Zoeppritz equations. *Geophysics,* 50**,** 609-614.

SRIVASTAVA, A., SINGH, V., TIWARY, D. & RANGACHARI, V. 2006. Impact of Phase Variations on Quantitative AVO Analysis. *6th International Conference & Exposition on Petroleum Geophysics "Kolkata 2006".*

STEWART, D., BERGE, K. & BOWLIN, B. 1995. Exploration trends in the southern Barents Sea. *Norwegian Petroleum Society Special Publications,* 4**,** 253-276.

STORVOLL, V., BJRLYKKE, K. & MONDOL, N. H. 2005. Velocity-depth trends in Mesozoic and Cenozoic sediments from the Norwegian Shelf. *AAPG bulletin,* 89**,** 359-381.

TALLERAAS, E. The Hammerfest basin—an aulacogen. Norwegian Sea Symposium, Norwegian Petroleum Society, Tromso, 1979. 1-13.

TOSAYA, C. A. 1982. *Acoustical properties of clay-dearing rocks*, Dept. of Geophysics, School of Earth Sciences.

VADAKKEPULIYAMBATTA, S., BUNZ, S., MIENERT, J. & CHAND, S. 2013. Distribution of subsurface fluid-flow systems in the SW Barents Sea. *Marine and Petroleum Geology,* 43**,** 208-221.

WALDERHAUG, O. & BJØRKUM, P. A. 2003. The effect of stylolite spacing on quartz cementation in the Lower Jurassic Stø Formation, southern Barents Sea. *Journal of Sedimentary Research,* 73**,** 146-156.

WILLIAMS, D. M. The acoustic log hydrocarbon indicator. SPWLA 31 th Annual Logging Symposium, 1990. 1-22.

ZALMSTRA, H. 2013. Reactivation in the Ringvassøy-Loppa Fault Complex-the role of detachments. *Digitale utgivelser ved UiO,2013*

ZOEPPRITZ, K. 1919. Erdbebenwellen VII. *Nachrichten von der Gesellschaft der Wissenschaften zu Göttingen, Mathematisch-Physikalische Klasse,* 1919**,** 57-65.

ØDEGAARD, E. & AVSETH, P. Interpretation of elastic inversion results using rock physics templates. 65th EAGE Conference & Exhibition, 2003.

ØVREBØ, O. & TALLERAAS, E. 1977. The Structural geology of the Troms Area (Barents-Sea). *GeoJournal,* 1**,** 47-54.

Appendix

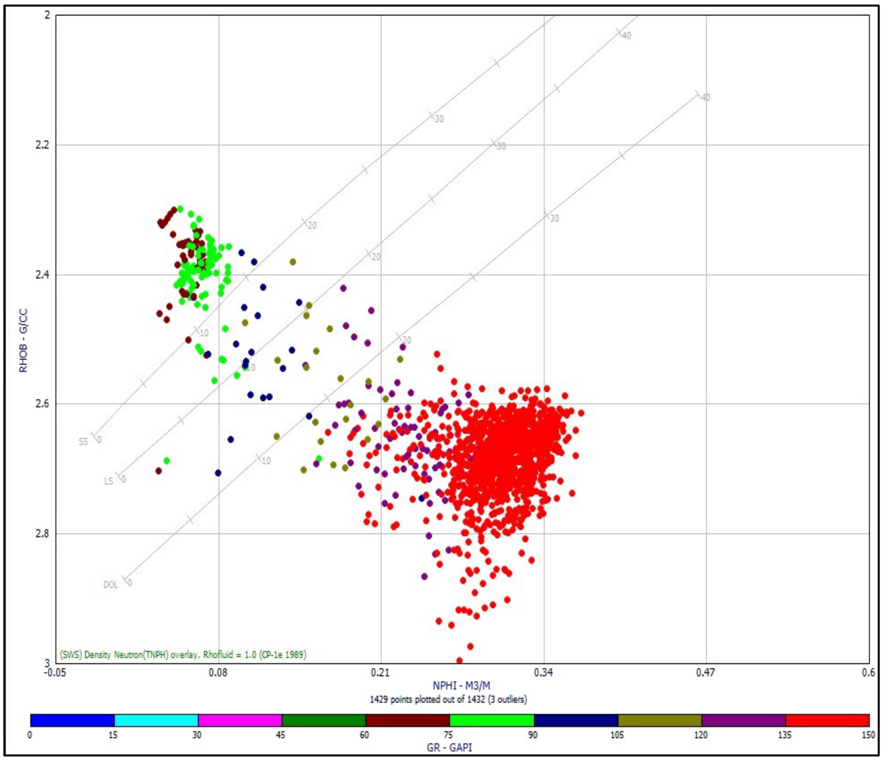

Figure Appendix-1 Neutron-Density cross plot of Knurr Formation in well 7019/1-1.

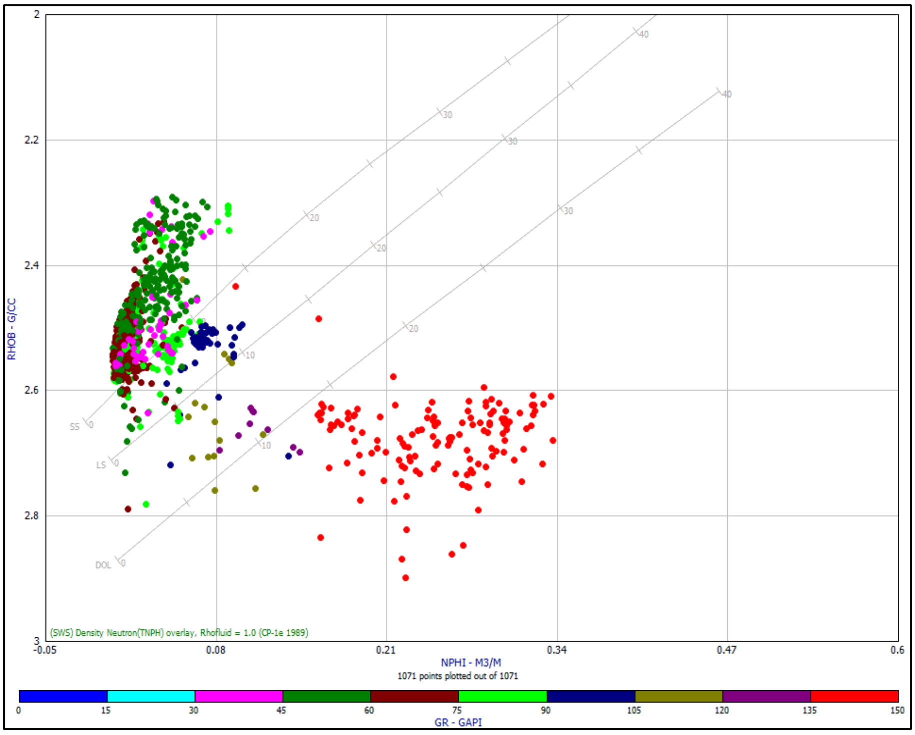

Figure Appendix-2 Neutron-Density cross plot of Stø Formation in well 7019/1-1.

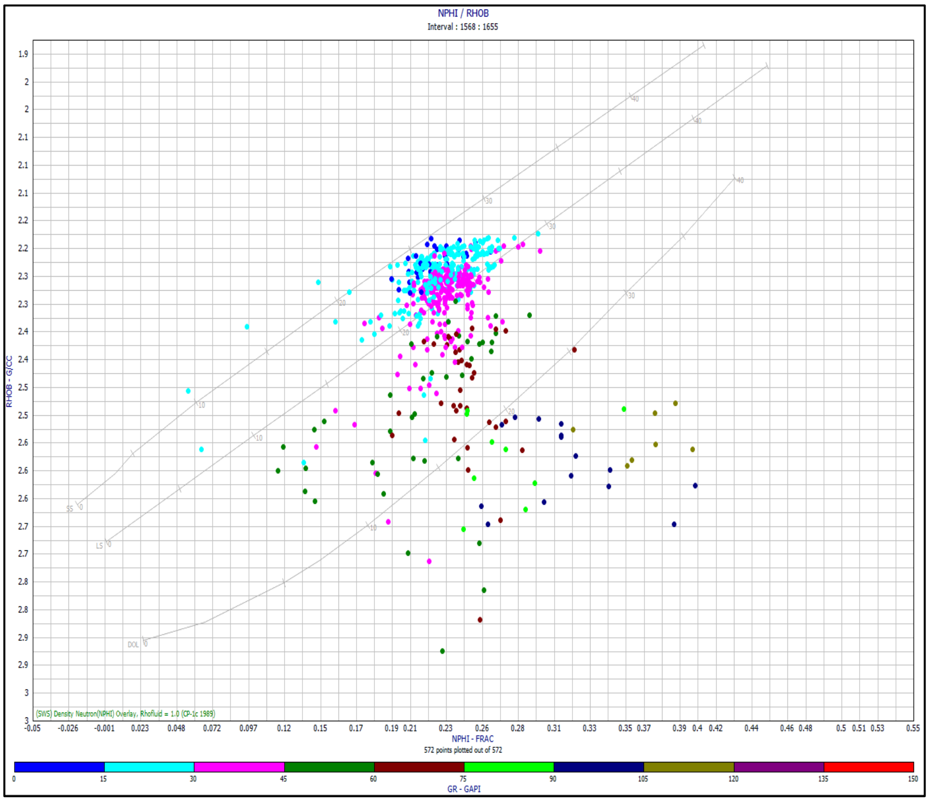

Figure Appendix-3 Neutron-Density cross plot of Stø Formation in well 7120/10-1.

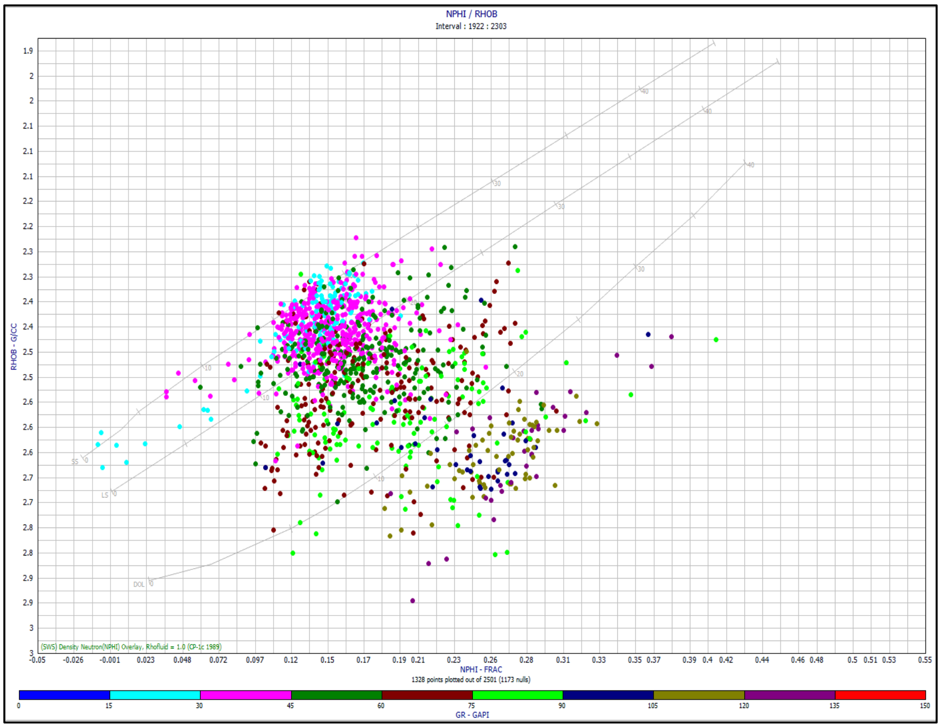

Figure Appendix-4 Neutron-Density cross plot of Knurr Formation in well 7120/10-2.

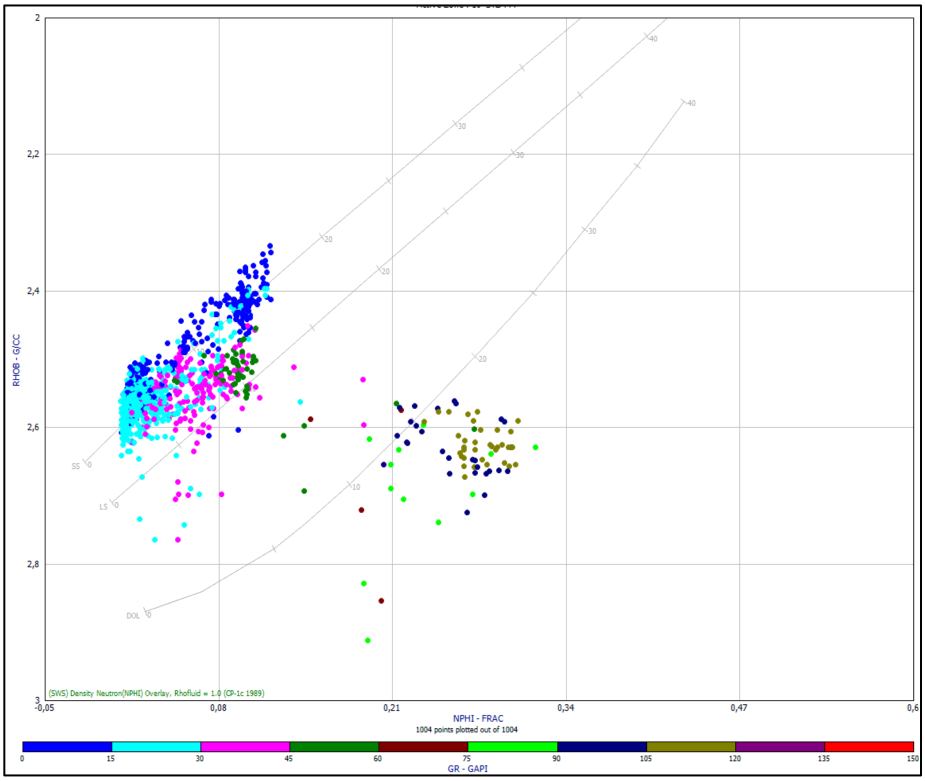

Figure Appendix-5 Neutron-Density cross plot of Stø Formation in well 7119/12-1.

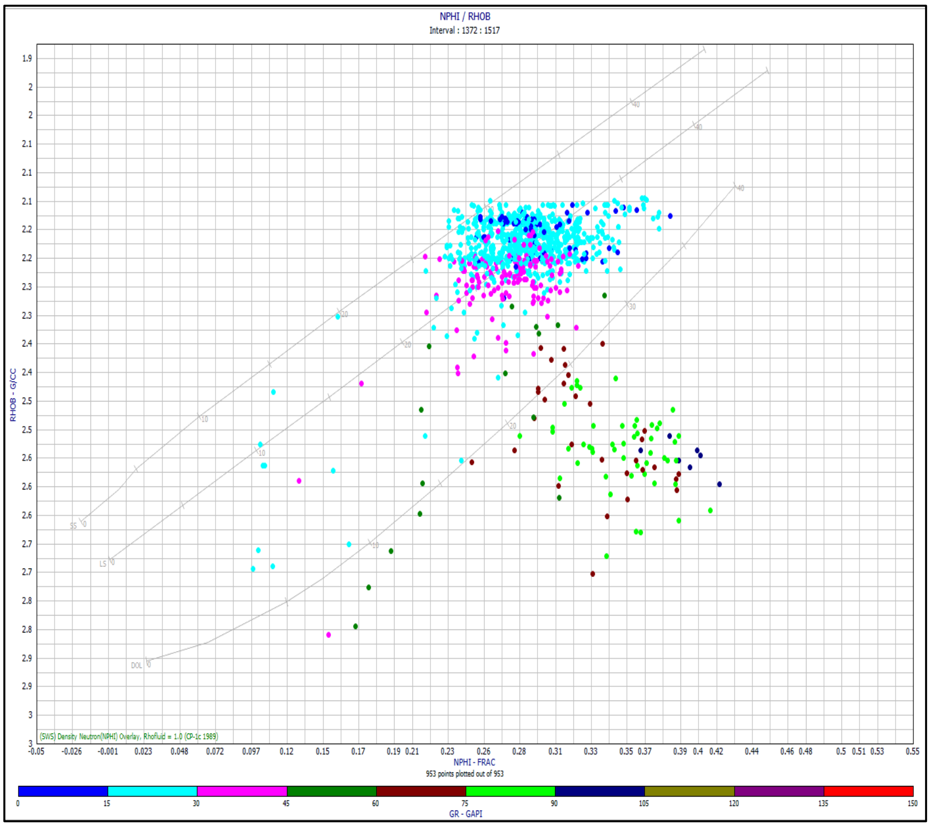

Figure Appendix-6 Neutron-Density cross plot of Stø Formation in well 7119/12-2.

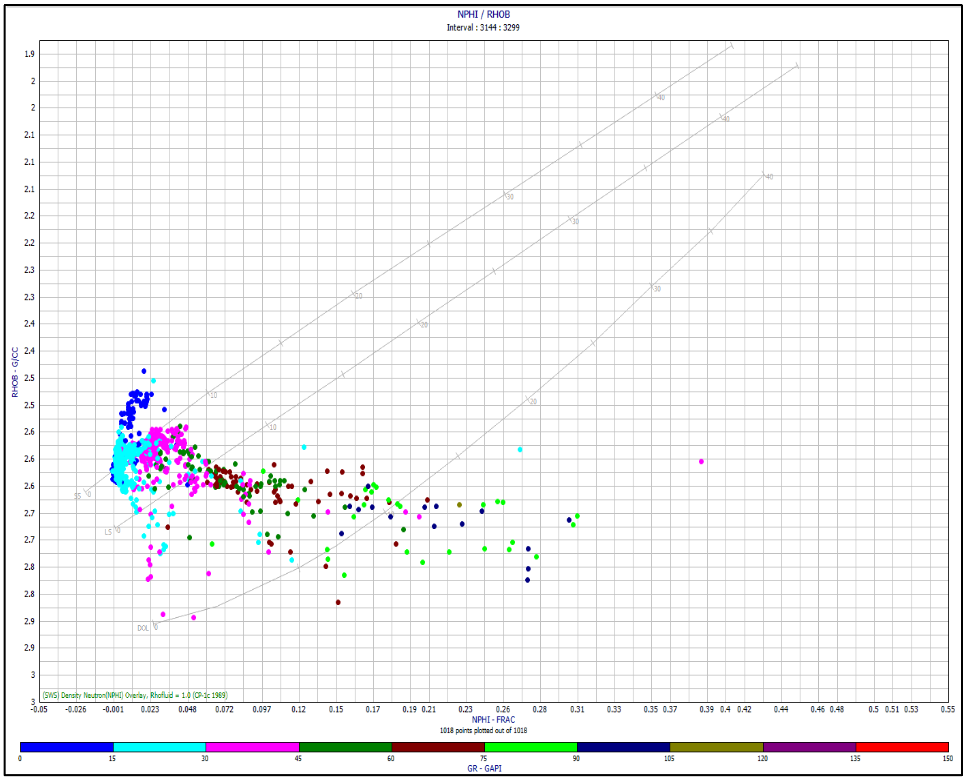

Figure Appendix-7 Neutron-Density cross plot of Stø Formation in well 7119/12-3.

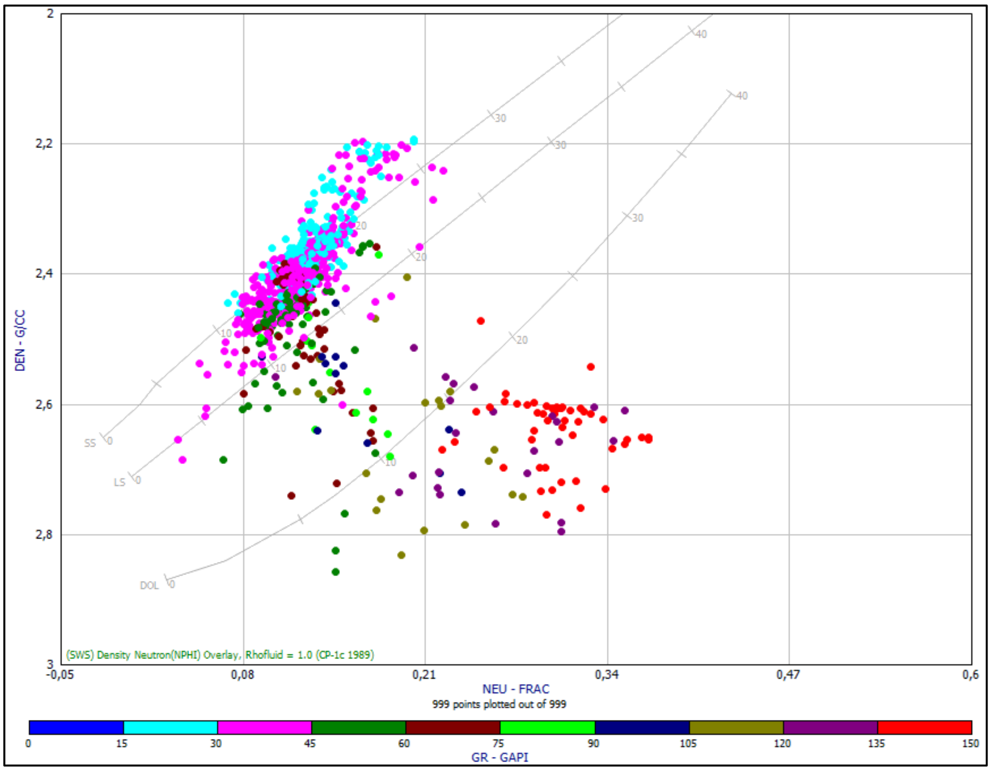

Figure Appendix-8 Neutron-Density cross plot of Stø Formation in well 7119/12-4.

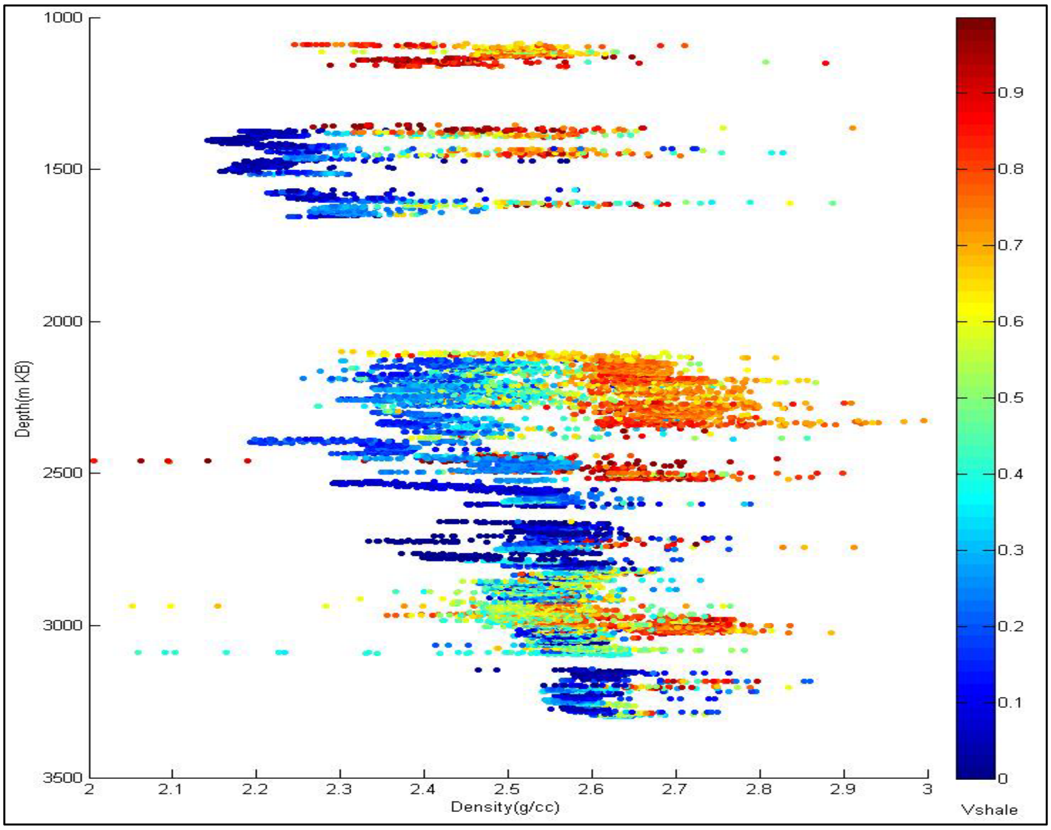

Figure Appendix-9 The density-depth cross plot of all the data in the study area. The data are colour coded by shale volume.

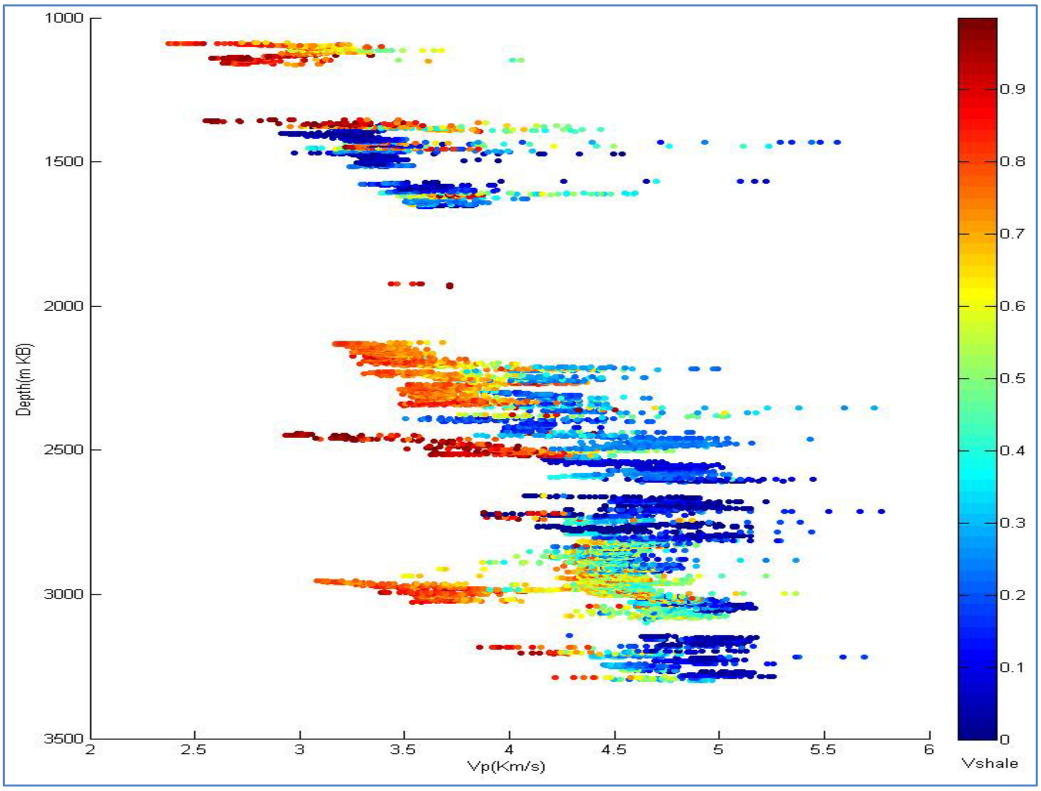

Figure Appendix-10 The Vp-depth cross plot of all the data in the study area. The data are colour coded by shale volume.

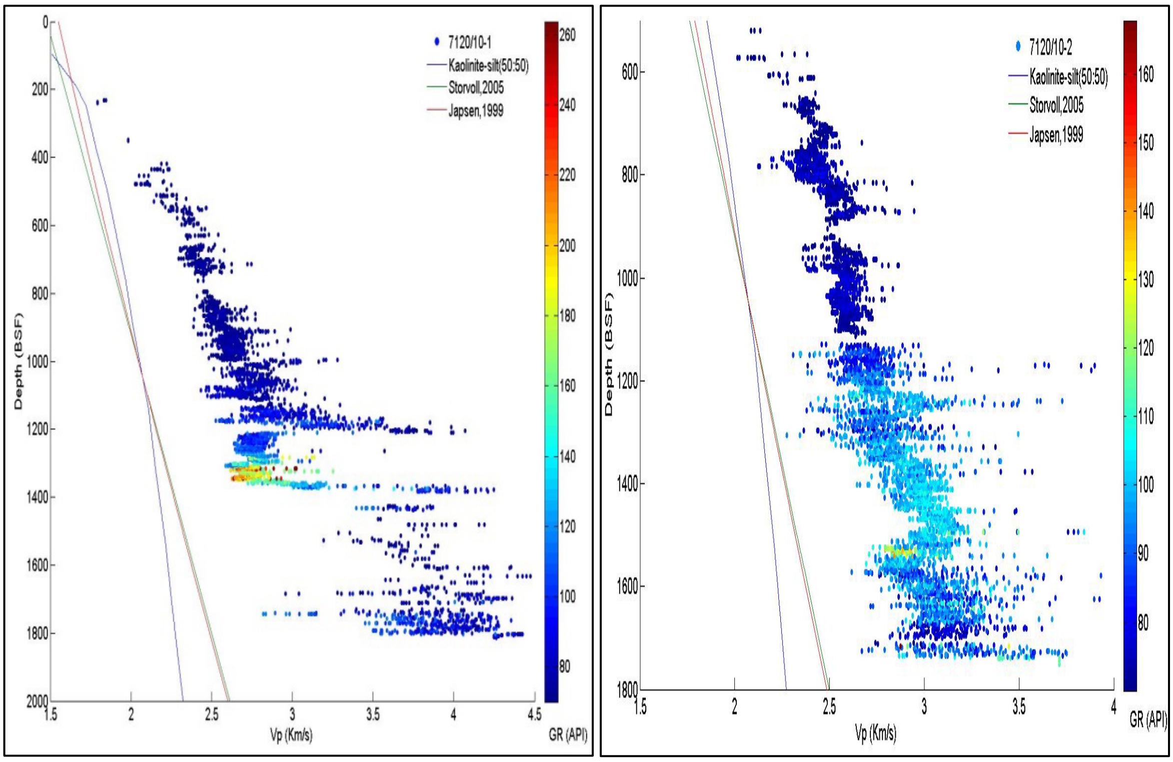

Figure Appendix-11 Vp-depth cross plot of well 7120/10-1 (left) and 7120/10-2 (right). All the data are shales (GR>70 API). The data are colour coded by GR values.

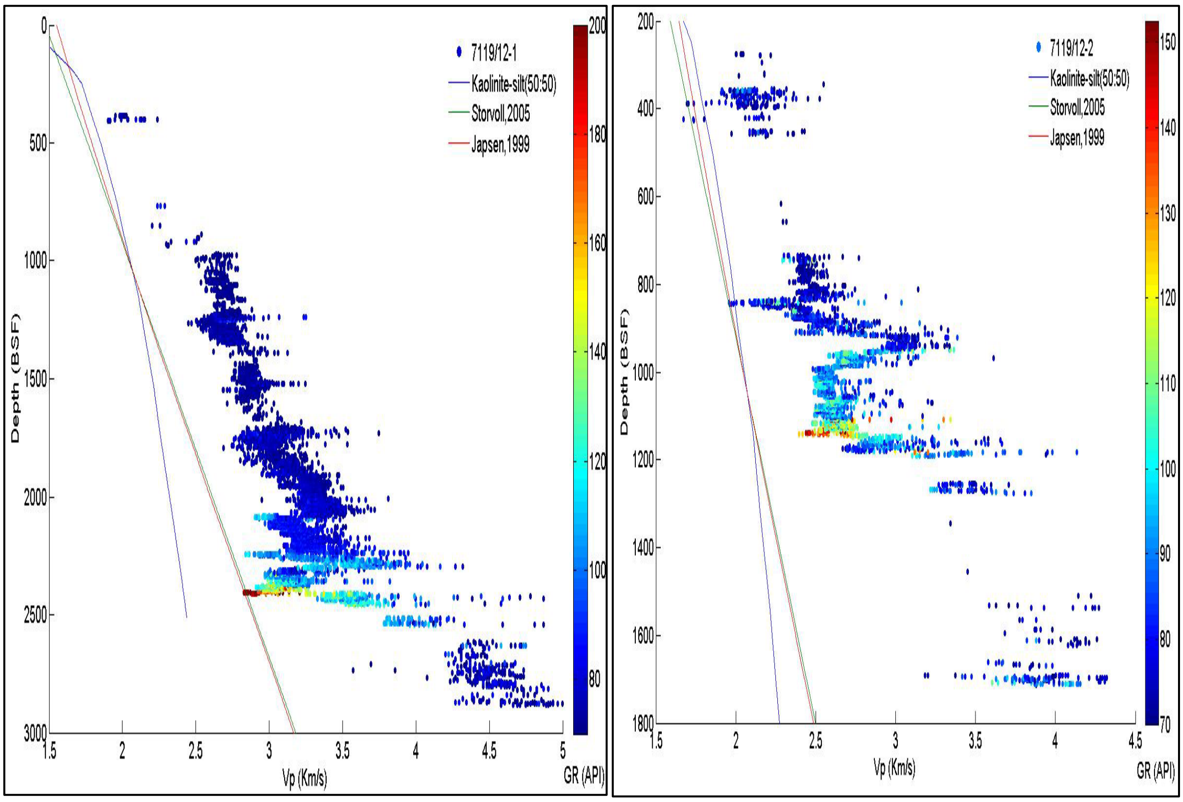

Figure Appendix-12 Vp-depth cross plot of well 7119/12-1 (left) and 7119/12-2 (right). All the data are shales (GR>70 API). The data are colour coded by GR values.

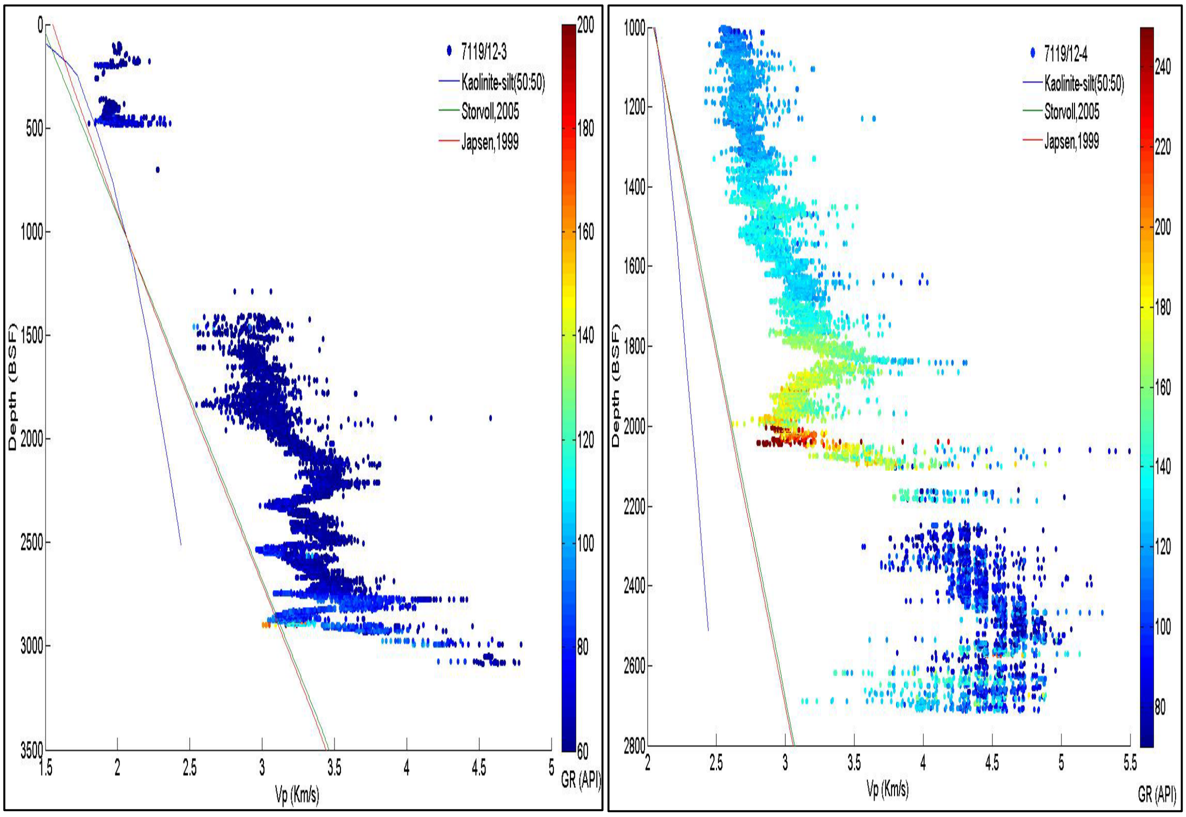

Figure Appendix-13 Vp-depth cross plot of well 7119/12-3 (left) and 7119/12-4 (right). All the data are shales (GR>70 API). The data are colour coded by GR values.

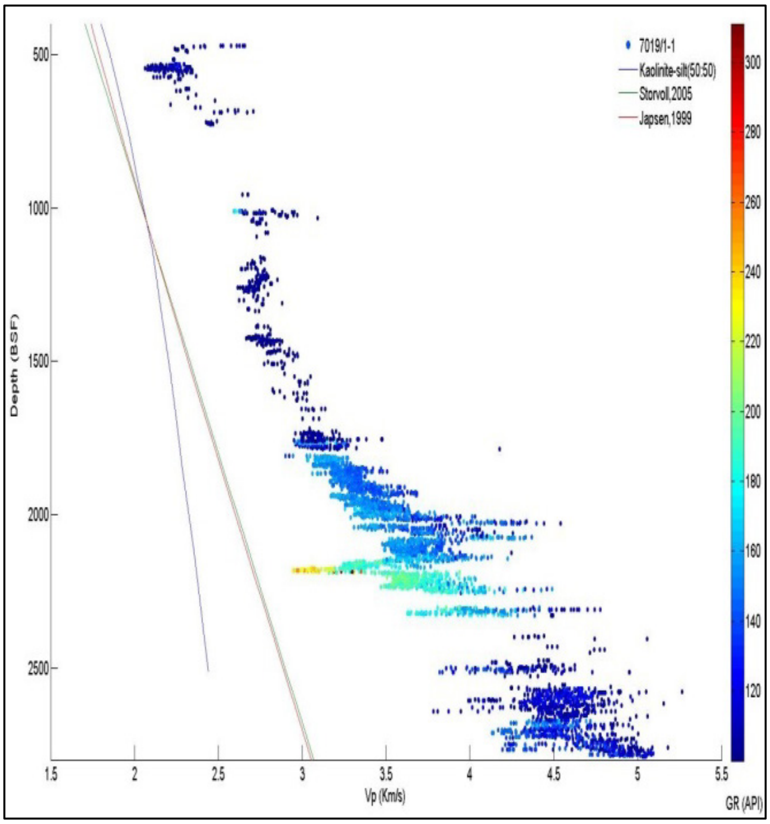

Figure Appendix-14 Vp-depth cross plot of well 7119/12-4. All the data are shales (GR>70 API). The data are colour coded by GR values.

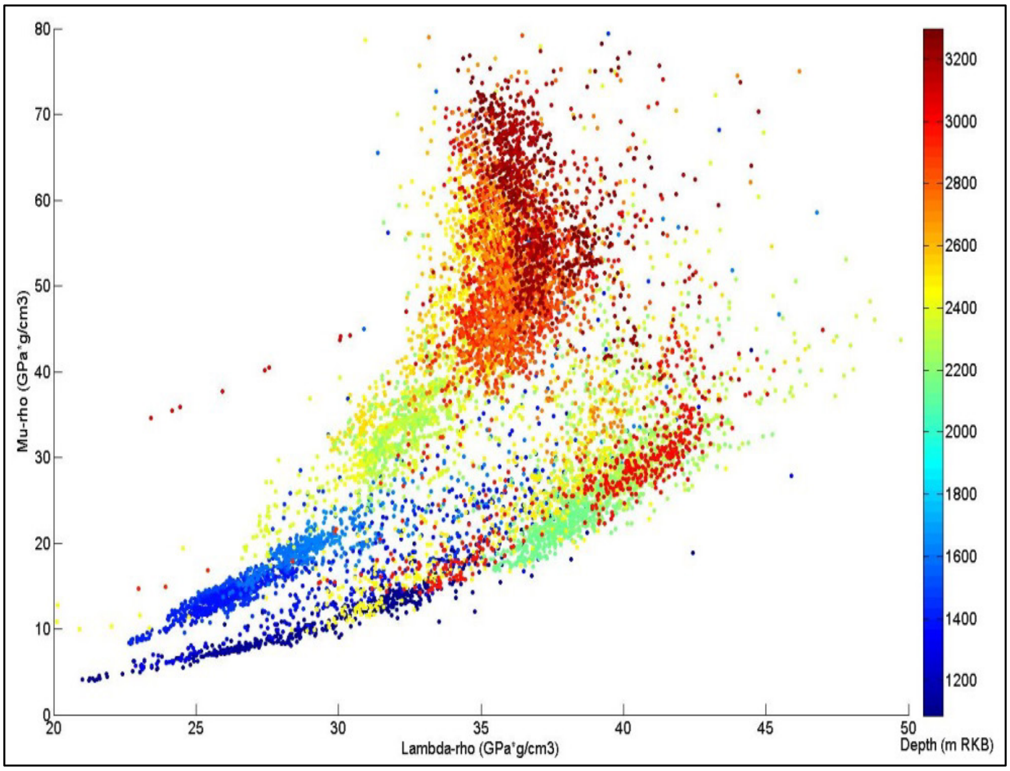

Figure Appendix-15 LMR cross plot of Knurr and Stø Formation data in all the wells available. The data are coloured coded by depth.

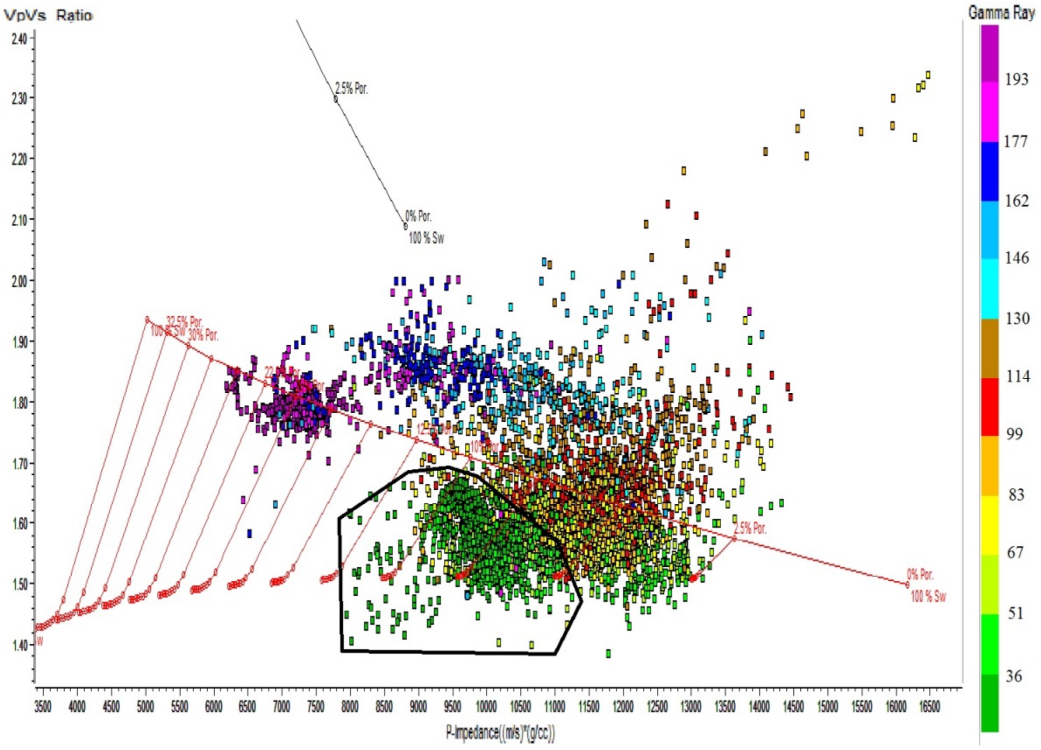

Figure Appendix-16 Vp/Vs-Ip cross plot of all the formations available in well 7119/12-4. Measured Vs values are used in this plot. The data are colour coded by GR values. Stø Formation sandstones are in the black polygon.

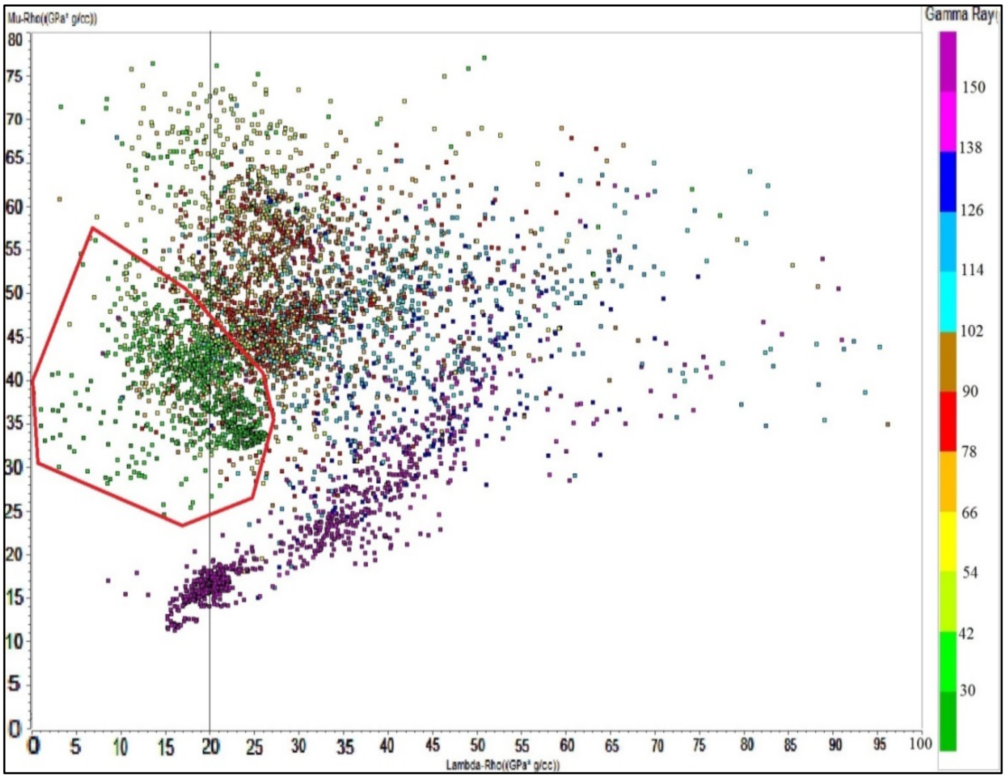

Figure Appendix-17 LMR cross plot of all the formations available in well 7119/12-4. Measured Vs values are used in this plot. The data are colour coded by GR values. Stø Formation sandstones are in the black polygon.

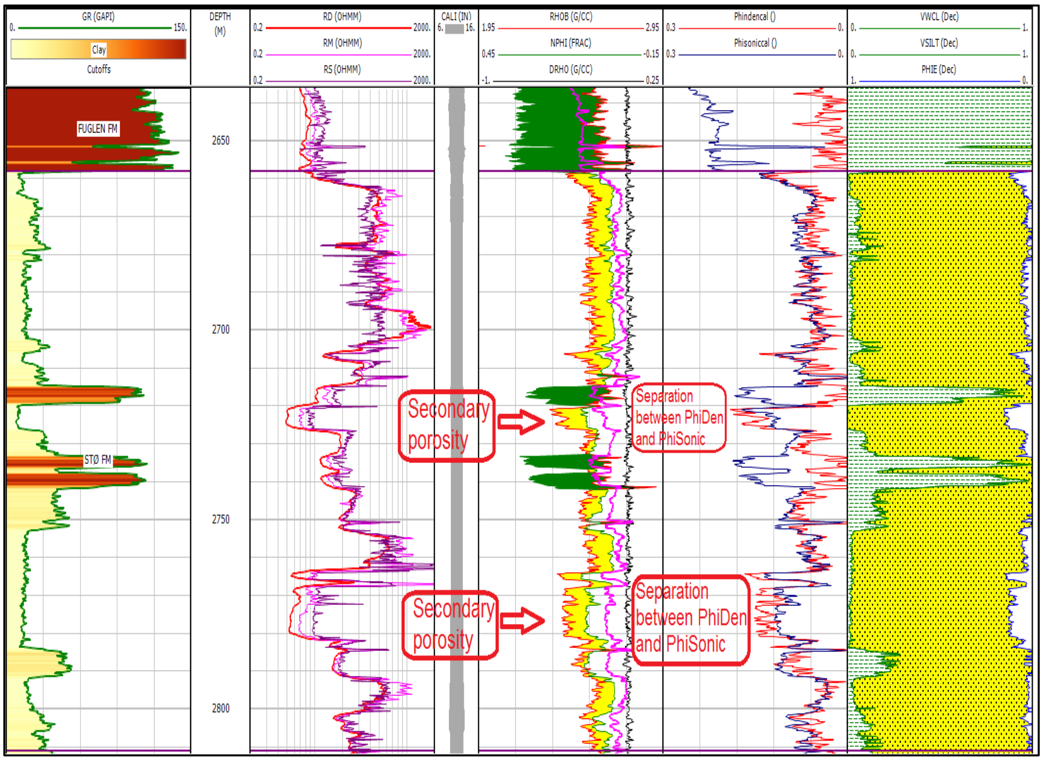

Figure Appendix-18 The composite interpretation plot of well 7119/12-1. The density porosity and sonic porosity curves separate in zones with secondary porosity.